
**Universidad Autónoma de Madrid**

**Departamento de Física Teórica**

# Calibration of the Electromagnetic ATLAS Calorimeter and search of the W' exotic boson

to obtain the title of

**PhD of Science**

Defended by

**Carolina GABALDÓN RUIZ**

Thesis Advisor: Jose DELPESO MALAGÓN

# Introducción

El LHC (**Large Hadron Collider**) representa el experimento más importante de física de partículas de altas energías, con una energía del centro de masas sin precedentes de 14 TeV y una luminosidad de $10^{34}$ $cm^{-2}s^{-1}$. Esta luminosidad tan alta nos permitirá el estudio de procesos de física con una sección eficaz tan pequeña como por ejemplo la producción del boson Higgs. Además, la alta energía del centro de masas permitirá el descubrimiento de nuevas partículas con masas en la escala del $TeV$.

El detector ATLAS (**A Toroidal LHC Apparatus**) es uno de los cuatro experimentos diseñados para el estudio de las colisiones proton-proton en el LHC. ATLAS ha sido evaluado desde 2006 mediante el uso de datos de cósmicos. Millones de cósmicos se han almacenado desde entonces permitiendo la calibración del detector. En Septiembre del 2008 un haz de protones circuló por primera vez en el LHC. La interacción de los protones del haz con los colimadores, que se encuentran a 200 metros de ATLAS, lo iluminó con una nube de partículas que impactaron con cada celda del detector permitiendo realizar estudios de calibración. Debido a un problema técnico, el LHC fue apagado por un año, reanudándose de nuevo en Noviembre de 2009.

Una gran parte de los canales de descubrimiento en ATLAS involucran electrones, positrones y fotones en el estado final. Por ejemplo, algunos de los más importantes son $Higgs \rightarrow \gamma\gamma$, $Higgs \rightarrow e^+e^-e^+e^-$, $Z' \rightarrow e^+e^-$ y $W' \rightarrow e\nu$. La medida de la energía y de la dirección de estas partículas finales establece unos requerimientos muy estrictos en la construcción y en la calibración del calorímetro electromagnético. En particular, una resolución en energía con un término constante menor que 0.7 % es necesaria para conseguir una resolución del 1 % en la medida de la masa en procesos tales como $Higgs \rightarrow \gamma\gamma$ y $Higgs \rightarrow e^+e^-e^+e^-$.

El experimento ATLAS tiene un calorímetro electromagnético de plomo y argón líquido (EMC) con forma de acordeón. Este detector ha sido construido con un alto nivel de precisión y ha sido sometido a una meticulosa cadena de calibración para alcanzar las metas impuestas por la física.

El trabajo expuesto en esta tesis se centra fundamentalmente en el calorímetro electromagnético de ATLAS y abarca casi todas las etapas desde la calibración de los $\sim 173000$ canales del EMC hasta el análisis de un prometedor canal de física con los primeros datos del LHC.

Después de la descripción de las principales características del calorímetro electromagnético (Capítulo 4) y del método utilizado para la reconstrucción de la señal (Capítulo 5), se presenta una detallada comparación entre la señal medida en cada celda con los datos del haz de protones y la señal predicha por dicho método de reconstrucción (Sección 5.4). Este análisis nos permitirá extraer importantes conclusiones sobre la calidad de la señal de reconstrucción en el

EMC y su influencia en la resolución de la medida de la energía.

La falta de uniformidad de la respuesta del calorímetro debe mantenerse por debajo del 0.6 % para cumplir con los requisitos de un término constante en la resolución de la energía del orden de 0.7 %. Durante la fase de construcción se midio un término constante por debajo del requerido utilizando un haz de electrones. Sin embargo, la uniformidad de la respuesta se debe evaluar en todo el calorímetro electromagnético, una vez instalado dentro del experimento ATLAS. En concreto, el gap entre los electrodos y los absorbes que componen el EM tiene una cierta influencia en la señal de salida. De manera que, las variaciones en el espesor del gap afectán la uniformidad de la respuesta del calorímetro. Una cantidad muy sensible a las variaciones del espesor del gap es el tiempo de deriva. En esta tesis, se presenta un método, independiente de la energía de la partícula, para la medida del tiempo de deriva (Capítulo 6). A partir de la obtención del tiempo de deriva somos capaces de determinar la uniformidad de la respuesta. Obtenemos una contribución al término constante menor del 0.6 %, resultado compatible con las medidas realizadas anteriormente.

Incluso con una perfecta calibración y uniformidad del calorímetro electromagnético, la medida de la energía de los electrones, positrones y fotones se ve afectada por la incertidumbre debida a la energía perdida cuando las partículas cruzan el material en frente del calorímetro. Un método para corregir la energía ha sido desarrollado en [1, 2]. Este procedimiento se basa en Monte Carlo y en el conocimiento de la distribución del material en frente del EMC. Un procedimiento para localizar y determinar la cantidad de material en frente del EMC ha sido desarrollado y documentado en [3]. En este analisis se usan simulaciones Monte Carlo con electrones de alto $P_t$ que vienen de la desintegración $W \rightarrow e\nu$. La idea es combinar la alta precisión del detector interno de ATLAS (ID) para la determinación de trazas con la información sobre la deposición de energía tanto longitudinal como transversal en el calorímetro electromagnético de alta granularidad.

Finalmente, una vez estudiada en profundidad la reconstrucción de la energía en el EMC, en el Capítulo 7 se estudiará el posible descubrimiento en ATLAS del boson pesado $W'$ de spin 1, mediante el proceso $W' \rightarrow e\nu$. El conocimiento de la energía de resolución del calorímetro electromagnético es aplicado para reconstruir la energía del electron (o positrón). Sin embargo, un nuevo ingrediente se suma en este analysis, la conocida como energía perdida inducida por la falta de interacción entre el neutrino y el detector. En esta tesis se estudiara el impacto en la reconstrucción de la masa del $W'$ usando diferentes procedimientos para reconstruir la energía perdida.

# Contents

# 1 Introduction

The Large Hadron Collider (LHC) represents the next major step in the high-energy frontier of particle physics, with an unprecedented center of mass energy of 14 TeV and design luminosity of $10^{34}$ cm$^{-2}$s$^{-1}$. Its high luminosity allows the study of physics processes with small cross-sections such as Higgs-boson production, while its high center of mass energy will allow the discovery of new particles with masses at the TeV scale.

The ATLAS detector is one of four experiments designed to study proton-proton collisions at the LHC. The ATLAS detector has been tested since 2006 using cosmic data. Millions of cosmic events have been accumulated since then. In September 2008 a single proton beam circulated in the LHC for the first time. Interactions of the single proton beam with collimators, placed at a distance of 200 meters from ATLAS, illuminated the detector with a particle flow sufficient for some calibration studies. An incident occurred requiring a shutdown of the LHC for one year. The LHC has resumed operation in November 2009.

Some of the ATLAS discovery channels involve electrons, positrons or photons in the final state. $Higgs \rightarrow \gamma\gamma$, $Higgs \rightarrow e^+e^-e^+e^-$, $Z' \rightarrow e^+e^-$ or $W' \rightarrow e\nu$ are some examples among them. The measurement of the energy and direction of these final state particles sets strict requirements on the construction and calibration of the Electromagnetic Calorimeter. In particular, an energy resolution, with constant term less than 0.7%, is required to achieve a 1% mass resolution on the $Higgs \rightarrow \gamma\gamma$ and $Higgs \rightarrow e^+e^-e^+e^-$ decay channels.

The ATLAS detector has a lead-liquid-Argon ElectroMagnetic Calorimeter (EMC) with accordion shape. The device has been built with a high level of precision and it has been subject to a meticulous calibration chain to achieve the physics goals.

The work in this thesis focuses on the ATLAS Liquid Argon (LAr) calorimeter and covers almost all stages, from the detector calibration of the $\sim$ 173000 EMC channels to the physics discovery potential.

After a description of the main characteristics of the EMC (see Chapter 4) and of the signal reconstruction procedure (see Chapter 5), the quality of the signal reconstruction is checked by comparing the measured signal from single LHC beam data with the predicted one from the reconstruction method (see Section 5.4). Agreement at the level of a percent is observed, fulfilling the physics requirements.

The non-uniformity of the response must be kept below 0.6% in order to fulfill the required 0.7% for the constant term of the energy resolution. During the construction phase, a few modules were tested with an electron beam resulting in a non-uniformity below the requirement. However, the uniformity of the response must be checked for the whole EMC after its installation in the ATLAS experiment. In particular, the gap between electrodes and absorbers influences the output signal, so that variations of the gap size with the position affect the uniformity of the calorimeter response. A very sensitive quantity to the gap size variations is the LAr drift time. A method to measure the drift time is presented in this thesis (see Chapter 6), which is independent of the particle energy, allowing it to be measured with cosmic data. The response uniformity measured from cosmic data through the drift time is compatible with previous measurements from beam tests, and is less than 0.6%.

Even with a perfectly calibrated and uniform EMC, the energy measurement of the electrons, positrons and photons is affected by uncertainties due to the energy lost when the particles cross the material in front of the EMC. A procedure to correct for these energy losses has been proposed [1, 2] which is based on Monte Carlo and the best knowledge of the amount and distribution of material in front of the EMC. A method to localize and determine the amount of material in front of the EMC have been performed [3] using Monte Carlo simulations with high $P_t$ electrons coming from the decay $W \rightarrow e\nu$. The method matches tracks, measured through the high precision Inner Detector (ID), with calorimeter deposits exploiting the high granularity of the EMC, both lateral as well as longitudinal [1].

Finally, Chapter 7 discusses a study of the ATLAS discovery potential for a new heavy charged spin 1 gauge boson ($W'$), through the decay mode $W' \rightarrow e\nu$. The knowledge of the energy resolution of the EMC is applied to reconstruct the electron (or positron) energy. However, a new ingredient is added namely the missing energy of the neutrino. The impact on the final results of different reconstruction procedures to obtain the missing energy is presented.

[1] Although the author of this thesis has contributed significantly to this topic, it is not included in this document.

# 2

# Theoretical background

This chapter gives an overview of the Standard Model [4] and of the Extended Gauge Model [5] that requires a new heavy $Z$ and $W$ bosons. The chapter covers, among others, those aspects of the theories which are useful as background to the studies presented in this thesis.

The Standard Model (SM) describes elementary particles and their interactions. This model has proven to be extremely successful, giving theoretical predictions that are in agreement with experimental observations. However, it is not a complete theory because it has left many important questions unanswered, such as why do quarks come in different flavors or why are quarks arranged in three generations? In addition the SM does not describe the force of gravity. New theories are being developed to address these and another questions.

## 2.1 Standard Model

The Standard Model (SM) of particle physics describes three fundamental interactions of nature: the electromagnetic, weak and strong interactions. It is based on Quantum Field Theory (QFT) and the Gauge Symmetry Principle. In the former, field operators are derived from a Lagrangian which can create and destroy particles. The latter is a procedure to introduce interactions from the free Lagrangian: an internal symmetry of the fields (gauge symmetry) is demanded to be satisfied locally, at each space-time point. This method introduces gauge bosons which mediate the forces. The gauge symmetry group of the SM is $SU(3)_C \times SU(2)_L \times U(1)_Y$. The sub-indices, $C$, $L$ and $Y$, stand for the conserved quantities, color (strong interaction) and isospin and hypercharge (electroweak interaction), respectively. The gauge bosons obtained from the gauge principle are always massless. This contradicts reality: W and Z bosons are massive. To solve this problem the SM introduces the Higgs mechanism (see Section 2.1.2).

The SM involves 12 fermions and their respective antiparticles, which are the constituents of matter and 5 bosons which carry the forces (see Figure 2.1). The SM describes all known forces of nature except gravity. All attempts to combine the force of gravity with the SM theory are still in an early stage. There is no model available which includes all four elementary forces and of which predictions have been verified in data. For example, in the last few years many models assuming a large number of extra space-time dimensions have been developed which explain the weakness of gravitation with respect to the other forces by the fact that only the gravitational force acts in all space-time dimensions while the other forces are restricted to the 3+1 space-time dimensions which we are familiar with. New experimental results at the LHC might give valuable hints on models where all known forces are combined.

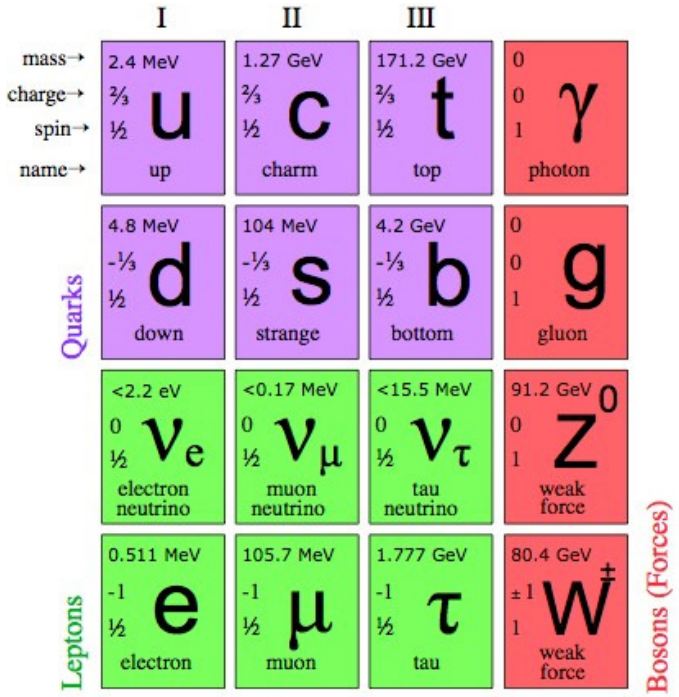


Figure 2.1: The three generations of leptons and quarks and the interaction carriers described in the Standard Model of particle physics.

The SM is a remarkably successful theory that describes the interactions of the presently known particles with excellent accuracy. However, to explain why the particles have masses, the SM requires the so called Higgs boson. The Higgs boson has the property that its coupling is proportional to the particle mass. The Higgs boson has not yet been observed, so finding the Higgs boson would complete the SM. In the context of the SM, there are several decay channels which could be exploited to discover the Higgs boson at the LHC depending on its mass. The mass of the Higgs boson is not predicted by theory but direct searches at LEP require a mass larger than 114 GeV, while from theoretical arguments it is expected to be smaller than 300 GeV.

For the light Higgs boson the most promising channel is the decay channel in two photons (despite its small branching ratio). If the Higgs boson mass is larger than twice the Z-boson mass, the most promising signature is the decay into two Zs, with the Zs decaying into four leptons. In both cases an excellent performance of the electromagnetic calorimeter is needed. The measurement of the hadronic energy in the form of jets becomes important at high Higgs masses, when W-boson pairs are produced that decay into jets. All these channels have to be isolated from an overwhelming background.

### 2.1.1 The Standard Model Lagrangian

In classical physics, a Lagrangian is constructed such that it reproduces the equations of motion, via the Euler-Lagrange equations. In Feynman's formulation of quantum mechanics, the Lagrangian appears in the *path integral*. The path integral gives the amplitude for a particle to move from point $A$ to point $B$ by integrating over all the possible paths, each of which is weighted by the action $S\left(S \equiv \int L d^4x\right)$ that belongs to that path.

The total number of possible paths is infinite, which makes the path integral ill defined. Thus, the integral needs to be regularized to obtain finite answers for quantities like cross sections. Many of these regularization procedures are done in the context of perturbation theory, where a saddle point approximation is performed on the path integral. Quantities like cross sections can then be expressed as a series expansion, where only the first few terms in the series need to be taken into account if the expansion parameter is small. Each term in the series can be represented by a *Feynman diagram*. The rules that relate the diagrams to the mathematical expressions, the *Feynman rules*, are derived from the Lagrangian.

The theories in the Standard Model are based on invariance principles, i.e. there exist sets of transformations (*symmetry groups*) that leave the Lagrangian L invariant. The complete symmetry group of the Standard Model is $SU(3) \times SU(2)_L \times U(1)_Y$. $SU(3)$ is the symmetry group associated with the strong interactions, while the $SU(2)_L \times U(1)_Y$ group is associated with the electroweak part of the theory. The gauge bosons in the theory of strong interactions are the gluons, which act on color charge. The electroweak counterparts of the gluon fields are the fields $W_\mu$ and $B_\mu$, which correspond to weak isospin (only affects left-handed fermions) and weak hypercharge respectively. These last two are the generators of the symmetry groups $SU(2)_L$ and $U(1)_Y$ (see Table 2.1).

| Interaction | symbol | spin | $Q(q_e)$ |
|---|---|---|---|
| electromagnetic | $\gamma$ | 1 | 0 |
| weak | $Z$ | 1 | 0 |
| | $W^\pm$ | 1 | $\pm 1$ |
| strong | $g$ | 1 | 0 |

Table 2.1: The gauge bosons in the Standard Model.

The symmetry group that is associated with quantum electrodynamics (QED) is $U(1)$, the group of complex numbers with modulus 1. The QED Lagrangian is ($\hbar = c = 1$):

$$L = \bar{\psi}\left(i\gamma^{\mu}D_{\mu} - m\right)\psi - \frac{1}{4}F_{\mu\nu}F^{\mu\nu} \tag{2.1}$$

where:

$$F_{\mu\nu} = \partial_{\mu}A_{\nu} - \partial_{\nu}A_{\mu} \tag{2.2}$$
$$D_{\mu} = \partial_{\mu} + ieA_{\mu} \tag{2.3}$$

The field $\psi$ is a fermion field [1], while $A_{\mu}$ is the photon field. The Lagrangian 2.1 is invariant under the transformation:

$$\psi \rightarrow e^{-ie\gamma(x)}\psi \tag{2.4}$$
$$A_{\mu} \rightarrow A_{\mu} + \partial_{\mu}\alpha \tag{2.5}$$

Note that $\alpha$ is supposed to depend on $x$, therefore the symmetry is called a *local symmetry*. Local gauge invariance is a stronger requirement than global gauge invariance. If $\alpha$ does not depend on $x$ then the covariant derivative $D_{\mu}$ would not be needed in Equation 2.1, the derivative $\partial_{\mu}$ would be sufficient. In other words, requiring local gauge invariance makes it necessary to replace ordinary derivatives with covariant derivatives. This introduces a term proportional to $\bar{\psi}A_{\mu}\bar{\psi}$, which represents the coupling between the fermions and the photon. The fermions ($\psi$) interact by exchanging gauge bosons (the photon ($A_{\mu}$)).

The kinematics of the fermions, and their interactions with the weak gauge fields, are given by the Lagrangian of electroweak interactions:

$$L_F = i\sum_A \left(\bar{\ell}_{A_L}\not{D}_L\ell_{A_L} + \bar{l}_{A_R}\not{D}_R l_{A_R} + \bar{q}_{A_L}\not{D}_L q_{A_L} + \bar{u}_{A_R}\not{D}_R u_{A_R} + \bar{d}_{A_R}\not{D}_R d_{A_R}\right) \tag{2.6}$$

where:

- The left- and right-handed fermions are grouped as follows:

$$\ell_{A_L} = \begin{pmatrix}\nu_A \\ l_A\end{pmatrix}_L, \qquad l_{A_R} \tag{2.7}$$
$$q_{A_L} = \begin{pmatrix}u_A \\ d_A\end{pmatrix}_L, \qquad u_{A_R}, \qquad d_{A_R} \tag{2.8}$$

with $\nu_A = (\nu_e, \nu_\mu, \nu_\tau)$, $l_A = (l_e, l_\mu, l_\tau)$, $u_A = (u, c, t)$ and $d_A = (d, s, b)$ (see Figure 2.1).

[1] Fermions are particles with spin $s = \frac{1}{2}$. Quarks and leptons are fermions.

- The operators $\not{D}_{L_\mu} = \gamma^\mu D_{L_\mu}$ and $D_{R_\mu} = \gamma^\mu D_{R_\mu}$ are the covariant derivatives for left and right-handed fermions:

$$D_{L_\mu} = \partial_\mu - ig_1 I \cdot W_\mu - ig_2 \frac{Y}{2} B_\mu \tag{2.9}$$

$$D_{R_\mu} = \partial_\mu - ig_2 \frac{Y}{2} B_\mu \tag{2.10}$$

  where $g_1$ is the weak isospin coupling, and $g_2$ is the weak hypercharge coupling. Note that the right-handed fermions do not couple to the fields W. Furthermore, the value of $Y$ (the weak hypercharge) is different for left-handed and right-handed fermions.

Finally, the Lagrangian for strong interactions that describes the gauge fields and their self interactions is given by:

$$L_G = -\frac{1}{4} F^a_{\mu\nu} F^{\mu\nu}_a - \frac{1}{4} F_{\mu\nu} F^{\mu\nu} \tag{2.11}$$

with:

$$F^a_{\mu\nu} = \partial_\mu W^a_\nu - \partial_\nu W^a_\mu + g_1 \varepsilon^{abc} W^b_\mu W^c_\nu \tag{2.12}$$

$$F_{\mu\nu} = \partial_\mu B_\nu - \partial_\nu B_\mu \tag{2.13}$$

Here $\varepsilon^{abc}$ is the Levi-Civita tensor, the structure constants of the group $SU(2)$.

### 2.1.2 The Higgs mechanism

The gauge fields $W_\mu$ and $B_\nu$ are massless. Adding mass terms for these fields by hand in the Lagrangian would break the gauge invariance of the theory, which would make the theory non-renormalizable. Such a theory cannot be used to compute observable quantities like cross sections, because of infinities that appear in the calculations. On the other hand, the $W$ and $Z$ bosons are clearly not massless, so mass terms in the Lagrangian are definitely needed.

A solution for this problem is provided by the Higgs mechanism [6], in which the gauge symmetry is spontaneously broken. Spontaneous symmetry breaking implies that the theory is still gauge invariant, but the ground state no longer exhibits this symmetry. To accomplish this, a complex scalar field $\phi$ is introduced, which (as it turns out) generates the masses of the gauge bosons and the fermions. The Lagrangian that corresponds with this field is:

$$L = \frac{1}{2} \partial_\mu \phi^\dagger \partial^\mu \phi + \frac{1}{2} \mu^2 |\phi|^2 - \frac{1}{4} \lambda^2 |\phi|^4 \tag{2.14}$$

The potential in this Lagrangian reaches a minimum at $|\phi| = \frac{\mu}{\lambda}$. Since one should expand around the ground state to perform perturbation theory, the fields $\rho = \phi_1 - \frac{\mu}{\lambda}$ and $\xi = \phi_2$ are

introduced, where $\phi_1$ and $\phi_2$ are the real and imaginary components of the field $\phi$. In terms of these fields the Lagrangian reads:

$$L = \frac{1}{2}(\partial_\mu \rho)(\partial^\mu \rho) - \mu^2\rho^2 + \frac{1}{2}(\partial_\mu \xi)(\partial^\mu \xi) + \lambda\mu(\rho^3 + \ \xi^2) - \frac{\lambda^2}{4}(\rho^4 + \xi^4 + 2\rho^2\xi^2) + \frac{\mu^4}{4\lambda^2} \quad (2.15)$$

This Lagrangian is no longer invariant under $U(1)$ transformations, but the symmetry is still there, it is merely hidden by the choice of ground state. The field $\rho$ is called the Higgs field. Its mass is $\sqrt{2}\mu$, while the field $\xi$ is massless. The field $\xi$ corresponds to motion along the valley of the Higgs potential, where the potential is constant. That the field $\xi$ is massless is no coincidence: according to Goldstone's theorem, a massless scalar state appears for every degree of freedom of a spontaneously broken continuous symmetry. The field $\xi$ is called a Nambu-Goldstone boson. It can be transformed away by choosing a suitable gauge (the *unitary gauge*).

The Lagrangian is now extended with the electroweak Lagrangian. The derivatives in Equation 2.14 are replaced by covariant derivatives, which yields coupling terms between the Higgs field and the gauge fields $W_\mu$ and $B_\mu$. After transforming the Higgs field to the minimum of its potential, these coupling terms generate masses for the following fields:

$$W_\mu^\pm = \frac{1}{\sqrt{\mu}}(W_{\mu,1} \mp iW_{\mu,2}) \quad (2.16)$$

$$Z_\mu = -sin\theta_W B_\mu + cos\theta_W W_{\mu,3} \quad (2.17)$$

where $\theta_W$ is the weak mixing angle. These fields are the familiar $W$ and $Z$ bosons. Their masses are:

$$m_{W^\pm}^2 = \frac{g_2^2 v^2}{4} \quad (2.18)$$

$$m_Z = (g_1^2 + g_2^2)\frac{v^2}{4} = \frac{m_W^2}{cos^2\theta_W} \quad (2.19)$$

where $v = \frac{\mu}{\lambda}$ is called the vacuum expectation value of the Higgs field. One combination remains massless:

$$A_\mu = cos\theta_W B_\mu + sin\theta_W W_{\mu,3} \quad (2.20)$$

which is the photon field. Since it is massless, the Lagrangian is still invariant under $U(1)_{EM}$ transformations, while the $SU(2)_L \times U(1)_Y$ symmetry has been broken.

The masses of the fermions are generated by introducing Yukawa couplings between the Higgs and fermion fields, which yield masses of the form $m_f = \frac{G_F v}{\sqrt{2}}$. The coupling $G_F$ is different for each fermion species, which explains why their masses are different.

### 2.1.3 The $W$ and $Z$ boson

The charged $W$ and the neutral $Z$ are the two mediators of the weak interaction. They were discovered in 1983 at the UA1 and UA2 experiments at CERN [7, 8, 9] and their properties were studied at LEP from 1989 up to 2000. The current world average for the masses are [10]:

$$m_W = 80.398 \pm 0.025 \text{ GeV} \quad (2.21)$$
$$m_Z = 91.1876 \pm 0.0021 \text{ GeV} \quad (2.22)$$

The accurate measurements will make it possible to use the boson masses for calibration of the ATLAS detector. To this end, the widths are important. These have been measured to be:

$$\Gamma_W = 2.141 \pm 0.041 \text{ GeV} \quad (2.23)$$
$$\Gamma_Z = 2.4952 \pm 0.0023 \text{ GeV} \quad (2.24)$$

The $W$ and $Z$ bosons can be created as daughter particles of heavier particles in channels such as the top quark decaying into a $W$ and $b-quark$, or the Higgs decaying into a $ZZ$ pair [2]. We note that W's as well as Z's can be produced in pairs, yet we restrict ourselves to the single boson production channels.

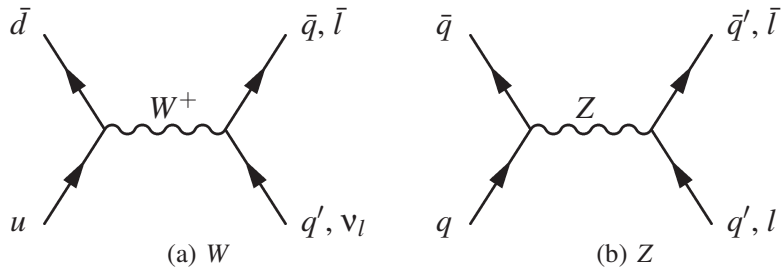


(a) $W$ (b) $Z$

Figure 2.2: Leading order $W$ (a) and $Z$ (b) production at the LHC.

The $W$ and $Z$ bosons can also be created directly in the hard interaction by quark-antiquark fusion, see Figure 2.2. Both bosons need an anti-quark to be produced; at the Tevatron this is present as valence quarks in the anti-proton, at the LHC it is only present as a sea quark. The two cross sections have been calculated up to NNLO and for the inclusive production at the LHC and are expected to be $\sigma_W = 20.5$ nb and $\sigma_Z = 2.02$ nb at 14 TeV center-of-mass energy [11]; this is including the branching ratio into one lepton generation. In this thesis the leptonic decay of the W plays an important role and we restrict ourselves to the decays into an electron plus $\nu_e$. The branching ratios for the W's and Z's to the leptonic channel are [10]:

$$W^+ \to l^+\nu : 10.80 \pm 0.09\% \ (3\times) \quad (2.25)$$
$$Z \to l^+l^- : 3.3658 \pm 0.0023\% \ (3\times) \quad (2.26)$$

[2] This channel is heavily suppressed if the Higgs mass is not large enough.

The Z boson cross section is lower than that of the $W$ boson because its branching ratio to one lepton generation is smaller, and because its coupling constants to the fermions are smaller.

#### 2.1.3.1 The $W$ production cross section

The cross section for inclusive $W$ production $pp \to W + X$ is derived from the quark subprocess in leading order (see Figure 2.2):

$$\hat{\sigma}(q_i\bar{q}_j \to W) = 2\pi|V_{ij}|^2 \frac{G_F}{\sqrt{2}} m_W^2 \delta(\hat{s} - m_W^2) \tag{2.27}$$

where $\hat{s} = x_p x_p s$ , with $x_p$ the Bjorken kinematic variable (for each proton), $s$ the square of the center of mass energy and $V_{ij}$ the Cabibbo-Kobayashi-Maskawa matrix. The inclusive production cross section is:

$$\sigma(pp \to W + X) = \frac{1}{3} \int_0^1 dx_p \int_0^1 dx_p \sum_{i,j} f_{q_i}(x_p, Q^2) f_{\bar{q}_j}(x_p, Q^2) \hat{\sigma}(q_i\bar{q}_j \to W) \tag{2.28}$$

where $f$ refers to the quark density functions inside the proton.

On the other hand, the calculation at leading order of the cross section for $W$ production and the subsequent decay into an electron and a neutrino gives:

$$\hat{\sigma}(q_i\bar{q}_j \to W \to e\nu) = \frac{|V_{ij}|^2}{3\pi} \left( \frac{G_F m_W^2}{\sqrt{2}} \right)^2 \frac{\hat{s}}{(\hat{s} - m_W^2)^2 + (\Gamma_W m_W)^2} \tag{2.29}$$

where $\Gamma_W$ is the total decay width.

## 2.2 Extensions to the Standard Model

Although the Standard Model predictions agree with existing experimental data, there are reasons to think it is not the ultimate theory. In particular, there are unresolved questions and problems as, for example, why the weak force distinguishes between left and right helicities or why such hierarchy of fermion masses ($m_t > m_b > m_c > m_s > m_d > m_u > m_t$ ; $m_\tau > m_\mu > m_e$). In addition, the SM contains many free parameters and it does not provide a unification of the electroweak and strong forces. A concern for cosmology is that no SM particle can be a candidate for the abundant dark matter.

A large variety of theories beyond the Standard Model, predict additional gauge bosons: Grand Unified Theories, various Left-Right Symmetric Models, Kaluza Klein Theories, Little Higgs Models, Dynamical Symmetry Breaking Models and models inspired by Superstrings. Any charged, spin 1 gauge boson which is not included in the Standard Model is called $W'$ boson and according to several predictions there is at least one $W'$ boson detectable at the LHC.

We pay our attention to the Left-Right Symmetric extension of the Standard Model, which was first proposed by Pati and Salam [12]. It is based on the gauge group $SU(3)_C \times SU(2)_L \times SU(2)_R \times U(1)_{\tilde{Y}}$ which has to break to recover the Standard Model $SU(2)_C \times SU(2)_L \times U(1)_Y$ below a certain scale. The new $SU(2)_R$ symmetry leads to additional gauge bosons ($W'$ and $Z'$ ). Singlets of right-handed fermions of the SM turn to doublets regarding $SU(2)_R$ which requires the introduction of right-handed neutrinos $\nu_R$:

$$\nu_R, l_R \rightarrow \begin{pmatrix} \nu \\ l \end{pmatrix}_R \tag{2.30}$$

The hypercharge has to be modified so that this quantum number is identical for left- and right-handed particles. Using the third component of the weak isospin for left- and right-handed particles, the following relation is derived

$$Q = I_{3L} + I_{3R} + \frac{1}{2}\tilde{Y} \tag{2.31}$$

where $\tilde{Y} = 1/2(B-L)$, with $B$ and $L$ the baryon and lepton number respectively.

In general, a new CKM mixing matrix ($V^R_{CKM}$) can appear in the right-handed quark sector which differs from the left-handed matrix ($V^L_{CKM}$). However in the so called *Manifest Left-Right Symmetric Model* these matrices agree: $V^R_{CKM} = V^L_{CKM}$.

A mixing ($\xi$) of the $W_L$ and $W_R$ eigenstates leads to the mass eigenstates $W_1$ and $W_2$, the first one corresponds to the SM $W$ boson whereas the second one to a new heavy $W'$ boson. Since the latter has not been observed yet, its mass must be large $m_{W'} \gg m_W$.

Due to the large variety of models which predict heavy gauge bosons a more general approach is considered called *Reference Model* which was introduced by Altarelli et al. [5]. In this model the new charged gauge boson $W'$ appears as a heavier version of the (left- handed) Standard Model $W$ boson. The couplings of the $W'$ boson to quarks, leptons and gauge bosons of the electroweak interaction are assumed to be identical to the Standard Model couplings. As a consequence, the decay channel $W' \rightarrow WZ$ is dominant for masses $m_{W'} > 2m_Z$ , with decay width:

$$\Gamma(W' \rightarrow WZ) \sim m_{W'} \frac{m^4_{W'}}{m^2_Z m^2_W} \tag{2.32}$$

This leads to widths of the $W'$ boson which are larger than the mass for $m_{W'} > 500$ GeV. (For a small mixing ($\xi$) this decay channel is suppressed.) The CKM matrix is assumed the same as in the SM.

Due to the close affinity to the Standard Model W boson, cross sections and widths related to $W'$ are merely marginal modifications of the SM ones. In particular, the decay mode into two fermions gives:

$$\Gamma(W' \rightarrow f_i \bar{f}_j) = \frac{N_c G_F m^2_W m_{W'}}{6\pi\sqrt{2}} \tag{2.33}$$

where $N_c = 3|V_{ij}|^2$ for quarks ($V$ = CKM matrix) and $N_c = 1$ for leptons. Comparing with the corresponding width for the SM $W$ boson, we have:

$$\Gamma(W' \to f_i \bar{f}_j) = \Gamma(W \to f_i \bar{f}_j) \frac{m_{W'}}{m_W} \tag{2.34}$$

This behavior translates also into the total width.

Particular attention is payed in this thesis on the decay into an electron and a neutrino. The following cross sections are obtained:

$$\hat{\sigma}(q_i \bar{q}_j \to W') = \frac{\pi |V_{ij}|^2}{4} g^2 \delta(\hat{s} - m_{W'}^2) \tag{2.35}$$

$$\hat{\sigma}(q_i \bar{q}_j \to W' \to e\nu) = \frac{|V_{ij}|^2}{192\pi} g^4 \frac{\hat{s}}{(\hat{s} - m_{W'}^2)^2 + (\Gamma_{W'} m_{W'})^2} \tag{2.36}$$

where $\hat{s} = x_p x_p s$ , with $x_p$ the Bjorken kinematic variable (for each proton) and $s$ the center of mass energy squared.

The total cross section for the inclusive $W'$ production is obtained by integration over the momentum fractions taken into account the Parton Density Functions (PDF):

$$\sigma(pp \to W + X) = \frac{1}{3} \int_0^1 dx_p \int_0^1 dx_p \sum_{i,j} f_{q_i}(x_p, Q^2) f_{\bar{q}_j}(x_p, Q^2) \hat{\sigma}(q_i \bar{q}_j \to W') \tag{2.37}$$

The $W'$ bosons in the Reference Model can be either left-handed or right-handed and the model is considered as a generalization of the Manifest Left-Right Symmetric Model with light right-handed neutrinos.

The analysis presented in this thesis is based on the Reference Model. The production and subsequent decay of such a new gauge boson ($W'^+, W'^-$, left- or right-handed) into an electron and a light, non-detectable neutrino is searched for. This channel provides a clean final state containing a highly energetic electron which is important for triggering. It is possible to reconstruct electrons up to highest energies with reasonable precision, unlike the muon channel ($W' \to \mu\nu$). In the latter one suffers from the momentum resolution of the muon spectrometer which deteriorates with increasing muon momentum.

## 2.3 Event generators

This section is devoted to briefly describe some of the most used Monte Carlo generator programs, linked to the previous processes described above. A successful way to produce hypothetical events with the distribution predicted by theory is through the so-called *event generators*. In the simulation of events both the hard interaction and the underlying event are taken into account. The physical concept that makes such simulations possible is factorization, the ability to isolate separate independent phases of the overall collision. These phases are dominated by

different dynamics, and the most appropriate techniques can be applied to describe each of them separately. For a detailed review on event generation we refer to [13]. In the following, we focus on the event generators which are used in the analysis for $W/W' \to e\nu$ and their backgrounds:

- **ALPGEN** [14] is a Monte Carlo generator for hard multi-parton processes in hadronic collisions. The algorithm performs leading order (LO) QCD exact matrix elements calculations for a large set of parton-level processes of interest in the study of LHC and Tevatron data. Parton-level events are generated providing full information on their color and flavor structure, enabling the evolution of the partons into fully hadronized final states. So, the development of partonic cascades, with the subsequent transformation of the partons into observable hadrons are carried out by Monte Carlo programs such PYTHIA (see below). The consistent combination of the parton-level calculations with the partonic evolution given by the shower MC programs is the subject of extensive work. In the case of $W/Z(\to ll)+N$ jets process, $N$ can reach for the moment, $N \leq 5$.

- **PYTHIA** [15] is a general purpose generator for hadronic events in $pp$, $e^+e^-$ and $e^+p$ high-energy colliders, comprising a coherent set of physics models for the evolution from a few-body hard processes to a complex multi-hadronic final state. In the generation of the basic partonic processes like $\gamma$, $Z^0$ and $W^\pm$ among others, initial and final-state showers are added to provide more realistic multipartonic configurations. New versions of PYTHIA has introduced major changes to the description of minimum bias interactions and the underlying event. There is a more sophisticated scenario for multiple interactions, new $p_T$-ordered initial- and final-state showers and a new treatment of beam remnants.

- **McAtNlo** [16, 17] event generator includes the full next-to-leading order(NLO) QCD corrections in the computation of hard processes. The package includes hadronic collisions, with the production of the following final states: $W^+W^-$, $W^\pm Z$, $ZZ$, $b\bar{b}$, $t\bar{t}$, $H^0$, etc. Incorporating the NLO matrix elements provides a better prediction of the rates while improving the description of the first hard hadron emission. As with any other parton shower based Monte Carlo, MCatNLO is capable of giving a sensible description of multiple soft/collinear emissions. One feature of MCatNLO as opposed to standard MC's is the presence of negative weights (which appear in higher order perturbative calculations, like NLO).

# 3

# LHC machine and ATLAS detector

The LHC is now the largest and most energetic hadron collider ever constructed. ATLAS is one of two multipurpose detectors designed to study proton-proton collisions. In this chapter, the main features of the Large Hadron Collider and some details of the ATLAS experiment will be briefly introduced.

## 3.1 The Large Hadron Collider

The LHC [18] is a proton-proton collider built at the European center for particle physics (CERN), located in the same tunnel that was used for the LEP [19] accelerator. The LHC will accelerate two counter-rotating proton beams to an energy of 7 TeV, which will collide head-on at four points along the ring. The resulting interactions have an unprecedented center of mass energy of 14 TeV, which will allow us to study a new field of physics. The acceleration of the protons starts at a dedicated linear accelerator (linac), which accelerates bunches of $10^{11}$ protons to an energy of 50 Mev. These bunches are then transferred to the PS Booster (PSB), where the energy is increased to 1.4 GeV. The energy is further increased to 26 GeV by the Proton Synchrotron (PS). The protons are then injected into the Super Proton Synchrotron (SPS) where they are accelerated to 450 GeV. Finally, the SPS injects the protons clockwise and counter-clockwise into the LHC ring, where they are accelerated to their final energy of 7 TeV. More than 1200 dipole magnets are installed along the LHC ring to keep the protons on track in the ring. The dipoles provide a magnetic field of up to 9 Tesla. The main parameters of the LHC accelerator are given in Table 3.1. Like its center of mass energy, the luminosity of the LHC is also unprecedented for a proton collider. The luminosity is defined as the number of protons crossing, per unit area, per unit time. The higher the luminosity, the more proton-proton interactions per second will occur. At the LHC, with a design luminosity of $10^{34}$ cm$^{-2}$ s$^{-1}$, on average about 27 interactions will occur per bunch crossing, with a bunch spacing of 25 ns.

Thus the number of proton-proton interactions per second will be around $10^9$. Such high luminosity is needed because many interesting physics processes at the LHC energy have very small cross sections, 1 pb or less (1 pb $= 10^{-36}$ cm$^2$).

| Parameter | Value | Unit |
|---|---|---|
| Circumference | 26659 | m |
| Beam energy | 7 | TeV |
| Injection energy | 0.45 | TeV |
| Dipole field at 450 GeV | 0.535 | T |
| Dipole field at 7 TeV | 8.33 | T |
| Helium temperature | 1.9 | K |
| Coil aperture | 56 | mm |
| Distance between apertures | 194 | mm |
| Luminosity | $10^{34}$ | cm$^{-2}$ s$^{-1}$ |
| Luminosity lifetime | 10 | h |
| Bunch spacing | 25 | ns |
| Particles per bunch | $10^{11}$ | |
| Bunches per beam | 2808 | |

Table 3.1: The design parameters of the LHC accelerator.

Figure 3.1 shows the geographical location of the LHC and the position of four experiments that have been built around the points where the beams collide: ALICE [20] (A Large Ion Collider Experiment), ATLAS [21] (A Toroidal LHC ApparatuS), CMS [22] (Compact Muon Solenoid) and LHCb [23] (A Large Hadron Collider beauty). ATLAS and CMS are general purpose detectors, i.e. they are designed to cover a wide range of physics. Their primary task will be to discover the Higgs particle (if it exists), but they will also explore the physics beyond the Standard model, like supersymmetry, extra dimensions, and even mini black holes. The ALICE experiment focus on the study of the quark-gluon plasma, by measuring the particles that are produced in heavy ion collisions. The quark-gluon plasma is a hadronic state where quarks and gluons are not in a bound state like protons anymore, but move freely in the plasma. The LHCb experiment is dedicated to the study of CP-violation in the B-system, it is therefore optimized for the detection of B-mesons. LHCb uses a low luminosity beam of about $10^{32}$ cm$^{-2}$ s$^{-1}$, by defocusing the proton beams near the interaction point. This is needed because the production and decay vertices of the B-mesons are difficult to reconstruct if there is more than one interaction per bunch crossing.

On 10 September 2008, proton beams were successfully circulated in the LHC ring for the first time. On 19 September 2008, the operations were halted due to a serious fault between two superconducting bending magnets [24]. On 18 December 2009, CERN Director General Rolf Heuer said:

> "The LHC circulated its first beams of 2009 on 20 November, ushering in a remarkably rapid beam-commissioning phase. The first collisions were recorded on 23 November, and a world-record beam energy was established on 30 November."

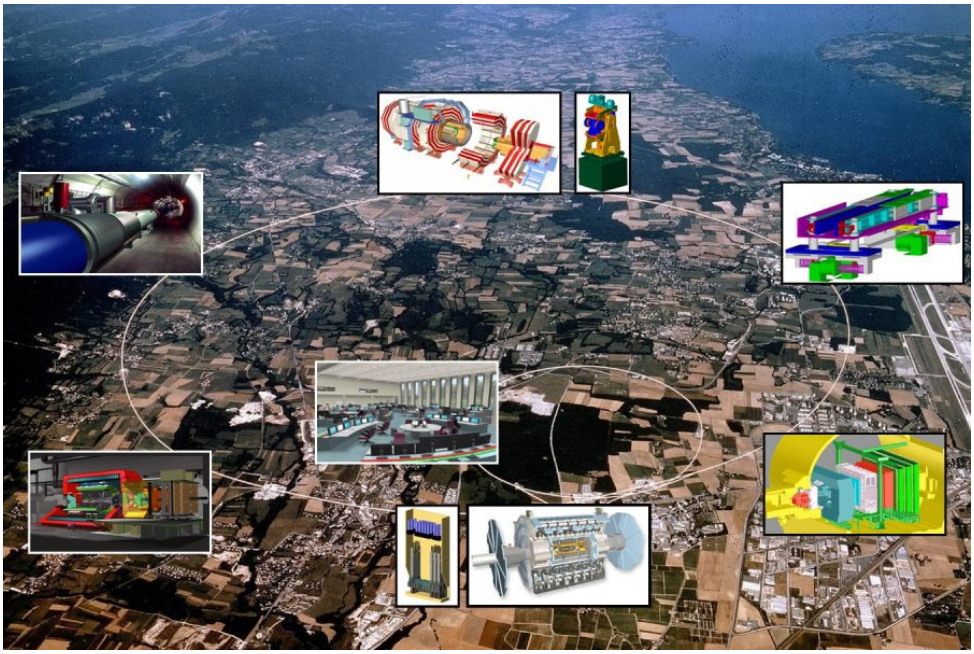

Figure 3.1: Geographical location of the 26.7 km long LHC tunnel indicating the four particle detector experiments placed along the accelerator ring.

## 3.2 The ATLAS experiment

The ATLAS experiment [21] is one of the two general purpose experiments at the LHC and is designed to explore the physics in the TeV region. Like most colliding beam experiments it has approximate cylindrical symmetry. The detector is organized in a central barrel where the detection elements form cylindrical layers around the beam pipe, and two endcaps organized in cylindrical wheels. Figure 3.2 gives an overall view of the detector.

The cylindrical symmetry makes a polar coordinate system useful. The direction of the proton beams is the z-axis, being zero the ATLAS center or nominal interaction point and positive $z$ values corresponds to the side where the endcap A is located. The origin for the azimuthal angle ($\phi$) points to the center of the LHC ring ($x$-axis), while the origin of the polar angle $\theta$ is the positive $z$-axis. Instead of the polar angle $\theta$, the pseudorapidity $\eta = -ln(tan(\theta/2))$ is used. The pseudorapidity is a convenient quantity because the particle multiplicity is approximately constant as a function of $\eta$.

ATLAS consists of several subdetector-systems, each with the purpose of measuring specific observables. The detector closest to the interaction point is the Inner Detector, which detects the track of charged particles. Next in ATLAS are two calorimeters, one to measure the energy from electromagnetic showers, i.e. the energy from electrons and photons, and second a calorimeter to measure all hadronic energy deposit. The outer layer of ATLAS is the muon spectrometer which measures the momenta of the muons deflected by a toroidal magnetic field. ATLAS is 45 meters long and 22 meters high, which makes its volume an order of magnitude larger than previous collider experiments. This is a direct consequence of the 14 TeV center of mass energy of the LHC beams.

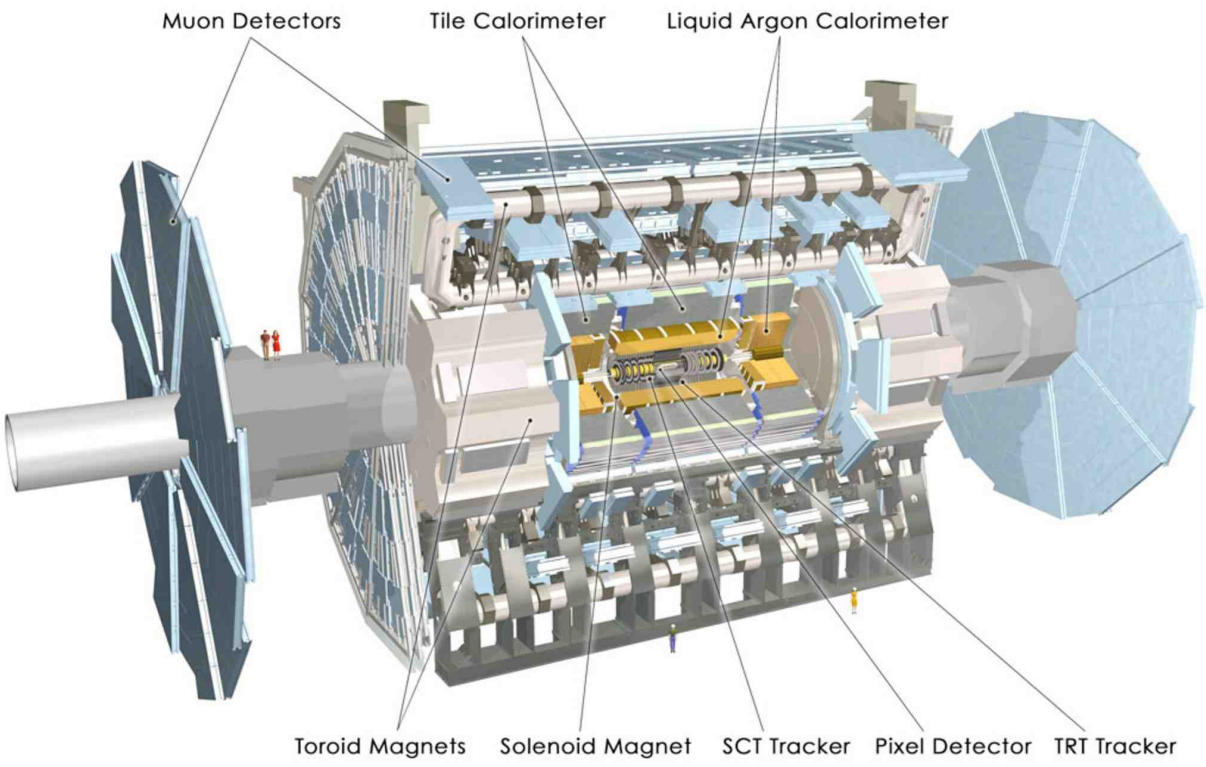


Figure 3.2: Overview of the ATLAS detector. The various subsystems have been indicated.

The basic design criteria of the ATLAS detector are:

- Efficient tracking at high luminosity for momentum measurement of high $p_T$ leptons, electron identification, $\tau$-lepton and heavy-flavor identification, and full event-reconstruction capability.

- Very good electromagnetic calorimeter for electron and photon identification and energy measurement, complemented by full-coverage hadronic calorimetry for accurate jet and missing traverse-energy measurements.

- High-precision muon momentum measurements, with the capability to guarantee accurate measurements at high luminosity using the external muon spectrometer.

- Large acceptance in pseudo-rapidity with almost full azimuthal angle coverage everywhere.

- Triggering and measurements of particles at low-$p_T$ threshold, providing high efficiency for most physics processes at LHC.

- Fast electronics are required to ”keep up” with the bunch crossing rate, which is also higher than in previous experiments.

### 3.2.1 Inner Detector

The lay-out of the ATLAS inner detector is illustrated in Figure 3.3. The Inner Detector(ID) system [25] covers the acceptance range $|\eta| < 2.5$, matching that of the rest of the ATLAS subdetectors for precision physics. The resolution on momentum and vertex location required for the physics studies and the very large track density expected at the LHC call for high-precision measurements with fine granularity and fast detectors. The ID, thanks to the tracks bending provided by the solenoid magnet, is responsible to measure the momentum of the charged particles coming from the interaction point. Together with the electromagnetic calorimeter, it provides the identification of electrons and photons.

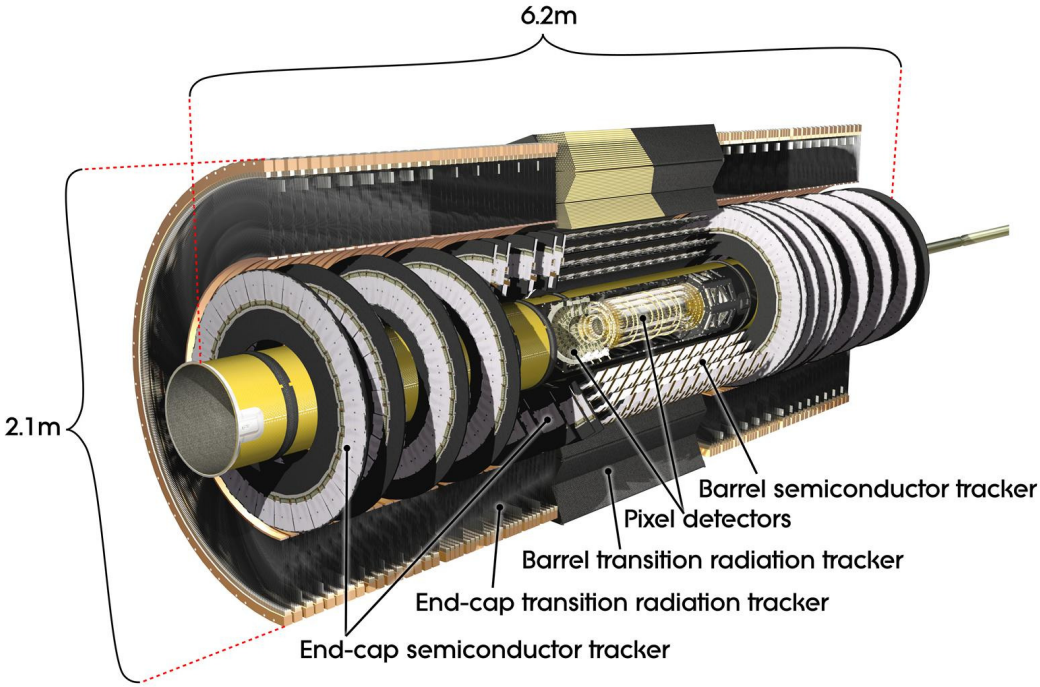


Figure 3.3: Tridimensional cut-away view of the ATLAS inner detector system.

The ATLAS ID tracking system (Figure 3.4) is composed of three different subdetectors layers:

- **The Pixel Detector (PD)** is a finely segmented silicon detector located in the radial range between 4 and 22 cm from the beam line. The PD consists of three concentric layers in the barrel and three disks in each endcap. Silicon modules of $2 \times 6$ cm$^2$ with a thickness of $285 \pm 15$ $\mu$m are segmented into small rectangles of $50 \times 400$ $\mu$m$^2$, the pixels. There are 47232 pixels per module and 1744 modules.

  Because of its closeness to the beampipe, the pixel detector determines mainly the resolution of the impact parameter. Its very high granularity makes it essential for the pattern recognition.

- **The Semiconductor Tracker (SCT)** is a silicon detector located in the radial range between 22 and 56 cm. It consists itself of three sub-parts, one barrel and two endcaps. The barrel consists of four cylindrical layers with its silicon modules mounted such that the strips run parallel to the beam axis. The two endcaps each have nine disks with the modules oriented such that the strips run radially. Each disk can have an inner and outer layer, mounted on the side of the disk facing the interaction point, plus a middle layer on the other side of the disk. The exact location of the disks and their occupation in modules are chosen such that any charged particle always hits at least four modules.

  Due to its high granularity, the SCT is important for the momentum resolution and the initial pattern recognition. It also contributes to the resolution of the impact parameter.

- **Transition Radiation Tracker(TRT)** is based on the use of straw tubes that can operate at very high rate. The straw tubes are filled with a gas mixture $X_e/CO_2/O_2$. The straws are bundled in triangular shaped modules that provides a $\phi$-coverage without any gaps.

  The TRT is important for particle identification and defines the momentum resolution, due to its long lever arm. The large number of measurements per particle allows for track-following, which enhances the performance of the pattern recognition and tracking.

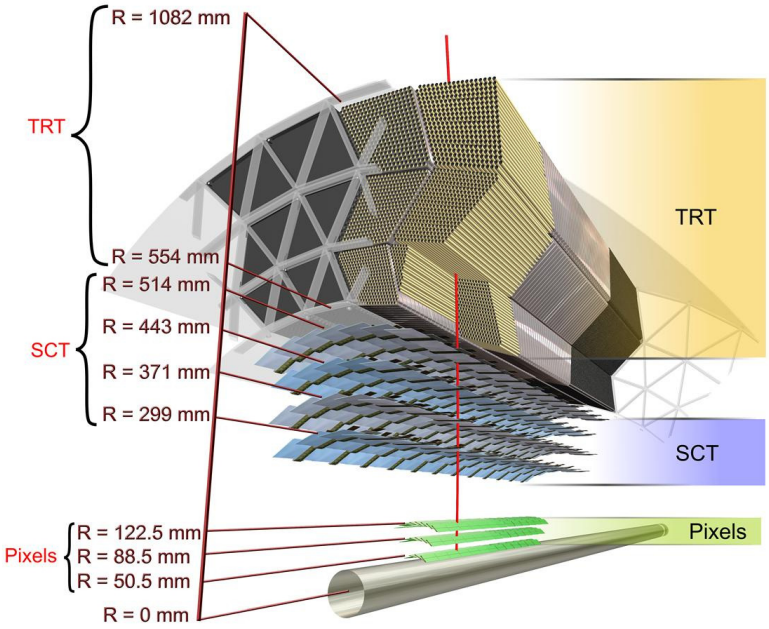


Figure 3.4: Tridimensional cut-away view of the ATLAS inner detector system.

#### 3.2.1.1 Dead material

Particles traversing the inner detector will interact with the dead material (sensors, cables, support structures etc.) causing them to lose energy and deviate from their trajectory. This will degrade the performance of the inner detector. Furthermore, the calorimeters, positioned behind the inner detector, need to measure precisely the energy of all, also neutral, particles. Therefore, the amount of material in the inner detector needs to be minimized. Figure 3.5 shows the amount of material expressed in number of radiation lengths [1] contributed by the different sub-detectors in the latest geometry version (ATLAS-CSC-03). This version used the most realistic material description, coming from precise weighting measurements of all its components.

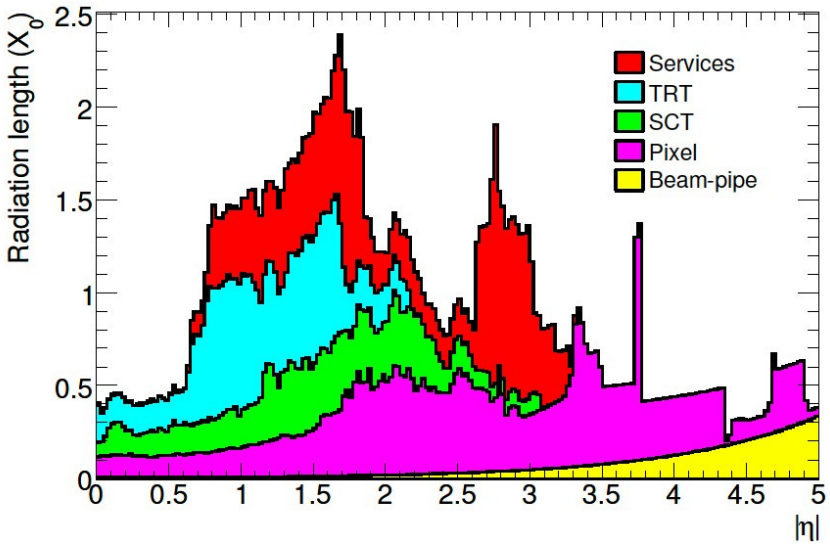


Figure 3.5: Material in the inner detector in term of radiation length $X_0$ at the exit of the ID envelope, including the services. The distribution is shown as a function of $\eta$ and averaged $\phi$ for the different sub-detectors and the various services in the latest version (ATLAS-CSC-03) used in [11].

### 3.2.2 The calorimeters

The calorimetry system in the ATLAS detector identifies and measures the energy of particles (both charged and neutral) and jets. It also detects missing transverse energy by summing all the measured energy deposit (see Equation 7.1).

The calorimeters contain dense materials (absorber), which cause an incoming particle to initiate a shower. Particles that are created in this shower are detected in the active material, which is interleaved with the absorbers. The total signal in the active material is proportional to the energy of the incoming particle. ATLAS uses two types of active material: liquid argon (LAr) and plastic scintillator. Charged particles traversing the liquid argon create charge

[1] One radiation length $X_0$ is defined as the distance over which a high-energy electron on average loses all but $1/e$ of its energy by Bremsstrahlung.

by ionization, which is collected on readout electrodes. The plastic scintillator is doped with fluorescent dye molecules, which emit light when the atoms in the plastic are excited by the crossing of a charged particle. This light is detected and amplified by photomultiplier tubes. For the absorbers several different types of material are used, depending on factors like space constraints and ease of manufacturing: lead, iron, copper and tungsten. The location of the calorimeters is shown in Figure 3.6. The pseudorapidity coverage by the whole calorimetry system is $|\eta| \leq 4.9$.

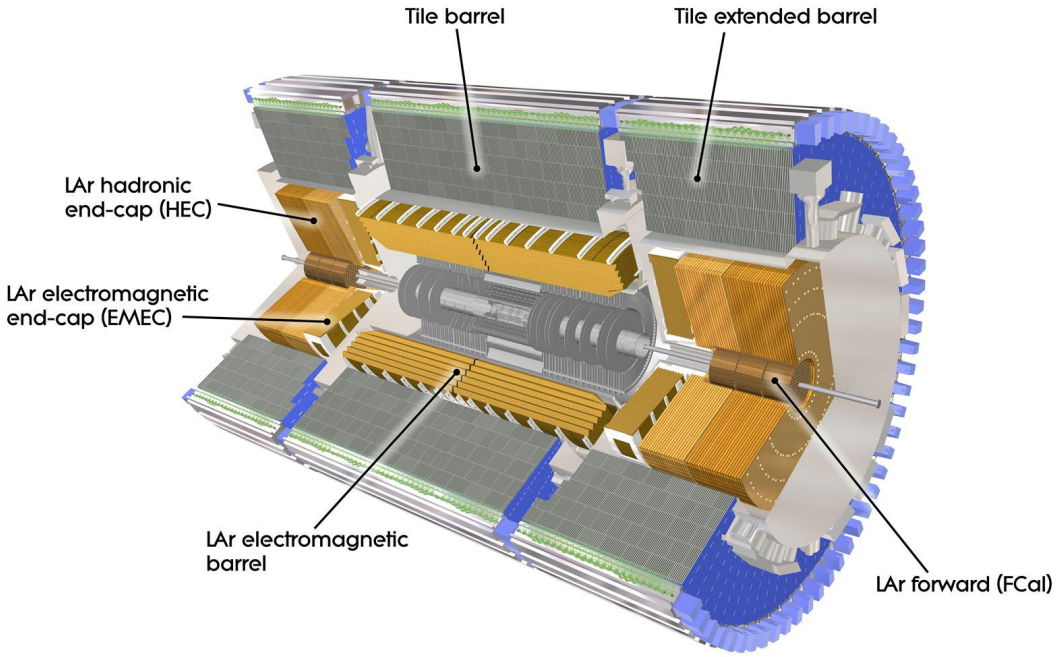


Figure 3.6: Overview of the ATLAS calorimeter. The various subsystems are indicated.

#### 3.2.2.1 The electromagnetic calorimeter

The electromagnetic calorimeter [26] identifies electrons and photons and measures their energy. It consists of a barrel ($0 < |\eta| < 1.475$) and two endcaps ($1.375 < |\eta| < 3.2$). It uses liquid argon as the active medium and lead absorber plates as the passive medium. The lead plates are folded into an accordion geometry providing complete $\phi$-coverage without azimuthal cracks. The readout electrodes, made of copper and kapton, are installed between the lead plates.

The electrodes are separated from the lead by spacer meshes. The remaining space is filled with liquid argon. The argon is cooled by a cryostat system; the barrel part shares the same cryostat vessel with the solenoid magnet. The barrel and endcap modules are divided into three longitudinal layers and a presampler layer that provides a measurement of the energy lost in front of the EM calorimeter. The front layer is finely segmented in $|\eta|$, which makes a good $\gamma/\pi_0$ and $e/\pi$ separation possible. The middle layer is the deepest, hence contains most of the

shower energy generated by incident electrons or photons. The last layer is used to complete the energy measurement of showers for higher energies and for estimations of leakage behind the calorimeter. To go into more details a separate chapter is devoted to the EM calorimeter, see Chapter 4.

One of the key ingredients for the description of the detector performance is the amount and position of the upstream material. Figure 3.7 shows the amounts of material in front of the electromagnetic calorimeters.

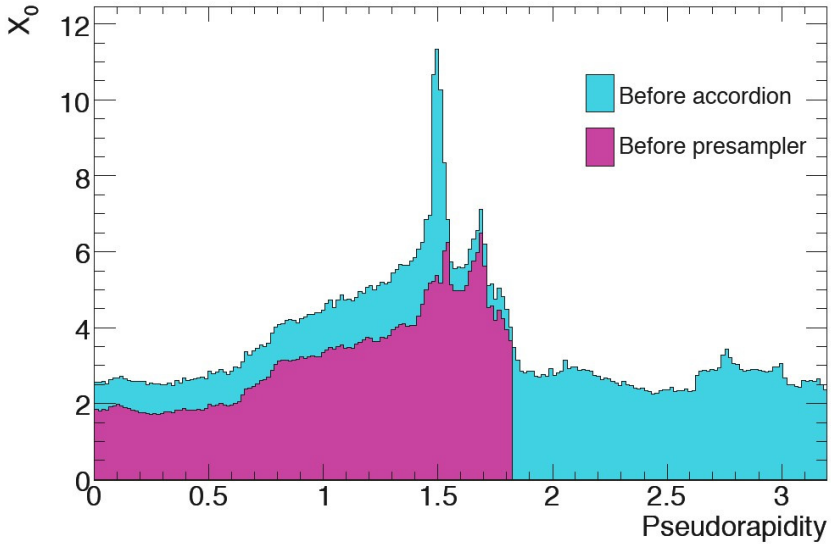


Figure 3.7: Dead material, in units of radiation length $X_0$ and as a function of $|\eta|$, in front of the electromagnetic calorimeters. The pink and blue distribution are the amount of material in front of the presampler layer and in front of the accordion itself, respectively.

#### 3.2.2.2 The hadronic calorimeter

The hadronic calorimeter [27] is built around the electromagnetic calorimeter. It will measure the energy and direction of jets of particles, formed by the hadronization of quarks and gluons, and by hadronically decaying $\tau-$leptons. The barrel part, called the Tile calorimeter, consists of a central barrel ($0 < |\eta| < 1.0$) and two extended barrels ($0.8 < |\eta| < 1.7$). The Tile calorimeter uses iron plates as the absorber, which also serve as the return yoke for the solenoid magnet. The active medium is formed by scintillator plastic tiles, which are read out on both sides by optical fibers. The tiles are placed radially, normal to the beam line, and are staggered in depth. Cells are formed by grouping tiles together. The calorimeter has three layers or samplings in depth which are read out independently. The readout cells are approximately projective to the interaction point, and have a granularity of $\delta\eta \times \delta\phi = 0.1 \times 0.1$ ( $0.2 \times 0.1$ in the third layer). The total number of channels is about $10,000$.

The Hadronic Endcap Calorimeter (HEC) uses liquid argon technology, because of its higher radiation tolerance. It uses 25 and 50 mm copper plates as the absorber material, arranged in a

parallel-plate geometry. The 8.5 mm gaps between the copper plates have three parallel electrodes, thus dividing the gap into four 1.8 mm drift spaces. Smaller drift spaces require a lower voltage (typically 2 kV instead of 4 kV) which reduces the risk of ion build-up and discharge currents. Hadronic showers are much longer than electromagnetic showers, and also much wider. Therefore the hadronic calorimeter needs to be much thicker than the electromagnetic calorimeter. The total thickness of the calorimeters is more than $10\lambda$, where $\lambda$ is the interaction length (the mean free path of a hadron between two interactions). This is sufficient to stop almost all the particles that are created in the shower, except muon and neutrinos. However, the calorimeters produce a large background for the muon detector, that consists mainly of thermalized slow neutrons and low-energy photons from the hadronic shower. The Hadronic endcap calorimeter is segmented longitudinally in 4 layers.

#### 3.2.2.3 The forward calorimeter

The forward calorimeter (FCAL) is a copper-tungsten calorimeter. It covers the region $3.1 < |\eta| < 4.9$. It is split longitudinally into an electromagnetic layer, and two hadronic layers. The copper and tungsten have a regular grid of holes that hold the tube- and rod-shaped electrodes. The space between the tubes and rods is filled with liquid argon. The FCAL is integrated in the same cryostat as the electromagnetic and hadronic endcap calorimeters. To avoid that neutrons are backscattered into inner detector volume, the forward calorimeter is placed 1.2 m further away from the interaction point, compared to the electromagnetic endcap calorimeter.

### 3.2.3 The muon spectrometer

The muon system [28] is by far the largest subdetector in ATLAS. High-$p_T$ muons are a signature of interesting physics, therefore the muon trigger and reconstruction is very important. The muon system is designed to achieve a momentum resolution of 10% for 1 TeV muons. Figure 3.8 gives an overview of the detector layout.

The magnet system in the muon detector is completely independent from the inner detector. It consists of eight superconducting coils in the barrel, and and eight coils for each toroid per endcap. The magnet is an air-core magnet system, i.e. the space between the coils is left open. Filling this space with iron would enhance the field strength and would also make the field more uniform, but it would also induce multiple scattering that would degrade the momentum resolution. The air-core system has an average field strength of 0.5 T. Four types of detection chambers are used in the muon system: Monitored Drift Tube (MDT) chambers, Resistive Plate Chambers (RPCs), Thin Gap Chambers (TGCs) and Cathode Strip Chambers (CSCs). The MDT chambers provide precise muon tracking and momentum measurement. The chambers consist of aluminum tubes with a 30 mm diameter and a central wire. A muon that crosses a tube will produce ionization clusters in the gas ($Ar/CO_2$), which will drift to the wire. The distance between the muon and the wire is determined by measuring the drift time of the first cluster that reaches the wire and passes over a threshold. The resolution on the drift distance is around 80 $\mu$m. In the inner-most ring of the inner-most endcap layer, CSCs are used instead of MDT chambers because of their finer granularity and faster operation. They are multiwire proportional chambers. The precision coordinate is read out with cathode strips, the second co-

ordinate is read out using strips which are parallel to the anode wires (orthogonal to the cathode strips). The spatial resolution on the precision coordinate is around 60 $\mu$m. The RPCs and TGCs are the muon trigger chambers in ATLAS. Their task is also to identify the bunch crossing to which a trigger belongs. Their adequate position resolution (about 1 cm) and excellent time resolution (about 2 ns) make them well suited for this task. The TGCs are multiwire proportional chambers. The position measurement in these chambers is obtained from the strips and the wires, which are arranged in groups of 4 to 20 wires.

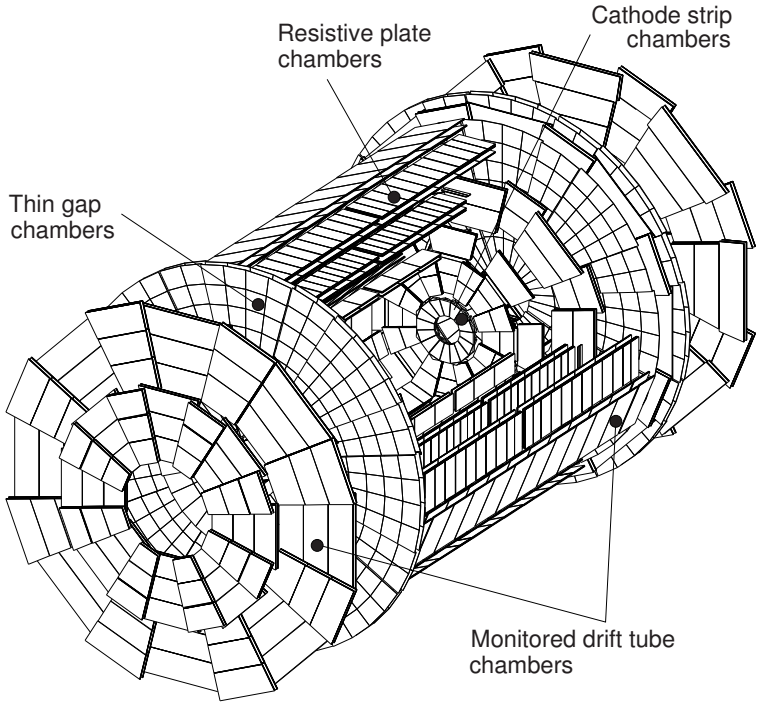


Figure 3.8: Three-dimensional view of the ATLAS muon spectrometer.

### 3.2.4 ATLAS trigger system

At the design luminosity of the LHC, of the order of $\sim 10^9$ interactions per second will occur inside the ATLAS detector, generating 1 PB/s of data. This means the amount of data measured in ATLAS is far too large to allow every event to be written to storage. To reduce the total data flow without losing interesting physics events, ATLAS uses a trigger system organized in three levels (see Figure 3.9). Each trigger level reduces the event rate by orders of magnitude. The final rate will be 200 events per second, which corresponds to an amount of $\sim$ 300 MB/s for data storage.

The three levels of the ATLAS trigger system are:

- **Level 1 trigger (LVL1)** is a hardware-based system that receives signals from the ATLAS calorimeter and muon detectors. It is designed to reduce the event rate to 75 kHz within

a latency of 2 $\mu$s. The detectors used for these searches are the calorimeter (`L1Calo`) and the trigger muon chambers (`L1Muon`), i.e. the RPC and the TGC chambers.

The LVL1 electronics are designed to look for high-$p_T$ muons, electrons, photons, jets and $\tau$-leptons decaying into hadrons, as well as large missing transverse energies.

- **Level 2 trigger (LVL2)** is a software trigger which uses the output of LVL1 and the full event information, which reduces the data rate to 2 kHz within a latency of 10 ms. LVL2 can access data from all subdetectores of ATLAS in the so called "Regions-of-Interest" (`ROIs`) that were identified by the LVL1 system. The `ROIs` are reduced granularity areas, i.e. in the calorimeter are regions of size $\Delta\eta \times \Delta\phi = 0.1 \times 0.1$ called "Trigger Towers" (see Figure 3.10).

- **Event Filter (EF)** is also based on software selection algorithms. In contrast to LVL2 it runs after the event building, such that the complete event information is available to the EF algorithms. The event filter further reduces the event rate to 200 Hz by using information of more complex reconstruction algorithms such as Bremsstrahlung recovery for electrons and vertex finding.

  Those events that have passed the selection criteria are tagged on basis of the results of the EF and sorted into data streams to be available for further analysis with the ATLAS offline software.

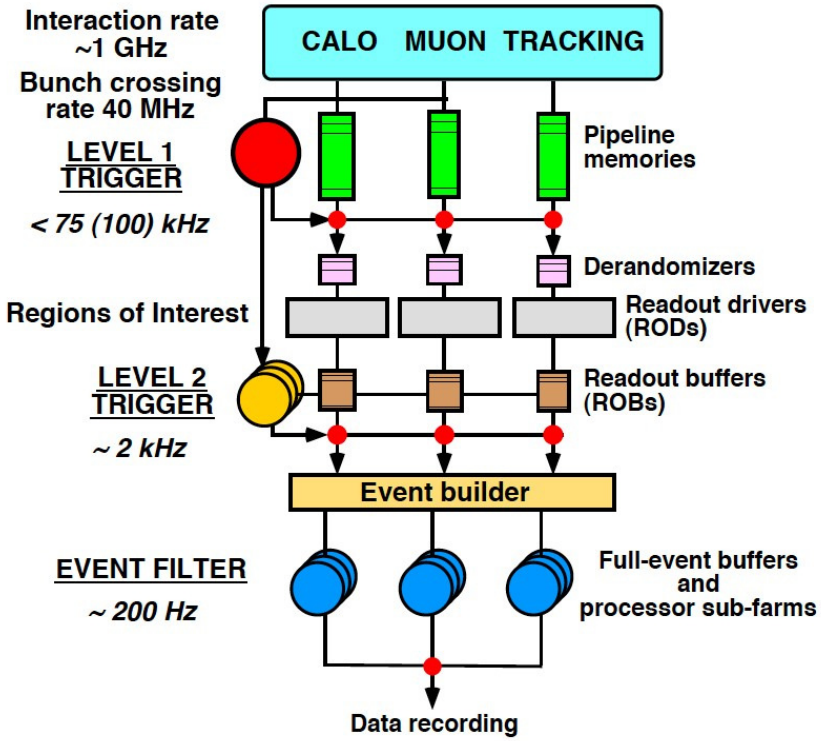


Figure 3.9: Schematic view of the ATLAS trigger system.

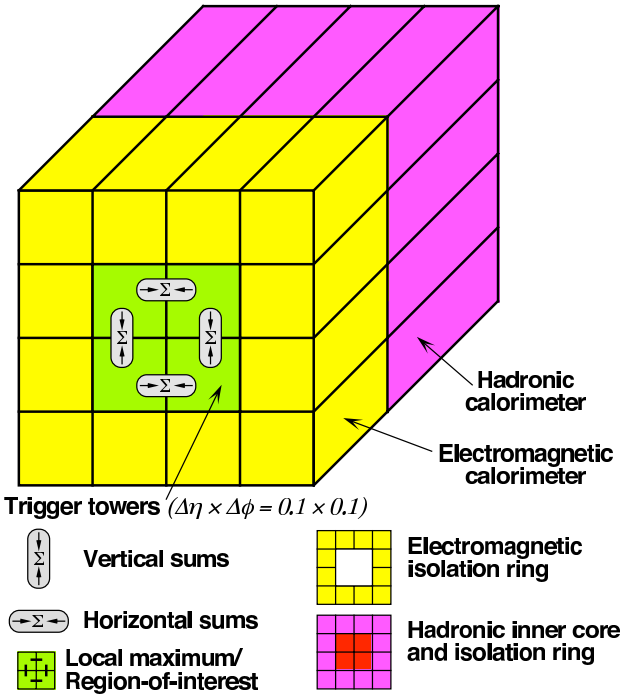


Figure 3.10: Trigger Towers of size $\Delta\eta \times \Delta\phi = 0.1 \times 0.1$ used for the $e/\gamma$ and $\tau/hadron$ algorithms and extensively used for commissioning with cosmic muon in the calorimeters.

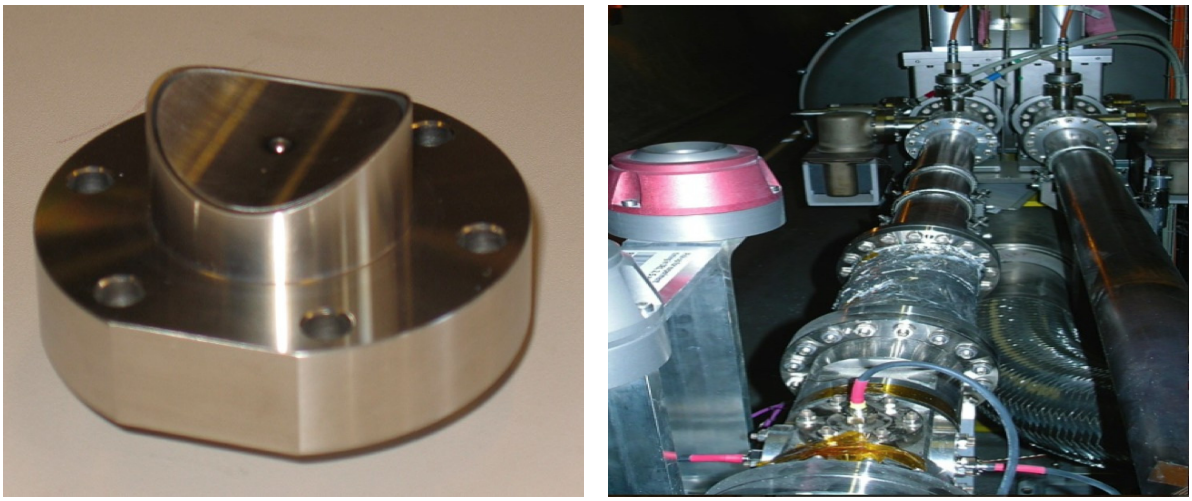

(a) (b)

Figure 3.11: (a) One electro-static button electrode for the BPTX. (b) A photograph of one of the two ALTAS BPTX stations.

#### 3.2.4.1 BPTX detectors

The ATLAS BPTX stations consist of electrostatic button pick-up detectors, located 175 m away along the beam pipe on both sides of ATLAS. The pick-ups are installed as a part of the LHC beam instrumentation and used by ATLAS for timing purposes.

One BPTX station consists of 4 electrostatic button electrodes (see Figure 3.11(a)) arranged symmetrically in the transverse plane around the beam pipe. Since the signal from a passing charge distribution is linearly proportional to distance, the signals from all four pick-ups are summed to cancel out potential beam position deviations. Figure 3.11(b) shows the BPTX station for beam 2, installed in the accelerator tunnel on the side C of ATLAS. At the bottom of the photograph, the cables from three of the four button pick-ups are visible.

The usage of the BPTX signals in ATLAS is twofold:

- By discriminating the signals from the BPTX detectors and compensating for the lengths of the transmission lines, BPTX detectors provides LVL1 trigger input signals synchronous when a bunch passes through ATLAS.
- The BPTX signals are also used in a standalone monitoring system for the LHC beams and timing signals. The system monitors the phase between the collisions and the LHC clock signals and measures the structure and uniformity of the LHC beams.

During the period with beam in 2008, the BPTX system was used extensively as a trigger to time in the readout windows of the sub-detectors of the ATLAS experiment.

# 4

# The ATLAS Electromagnetic Calorimeter

The UAM [1] has shared with CPPM [2] the responsibility for the design and construction of the LAr electromagnetic endcap calorimeter. The results presented in this thesis are part of the group contribution to the commissioning efforts.

In this chapter an overview of the principles, performance and main characteristics of the Electromagnetic Calorimeter are given, specially those relevant to the research work of this document.

## 4.1 Principle of operation

The electromagnetic calorimeters are basically blocks of matter in which charged particles lose partially or completely their energy. To understand the operating principles of a calorimeter we need to study first the interactions of particles with matter.

When electrons or positrons interact with matter, they lose energy in two different ways, each dominant in a defined energy range. These two process are:

- **Ionization.** For energies lower than 10 MeV, electrons lose their energy mainly by ionizing the medium they are traversing.
- **Breamstrahlung.** Above 10 MeV, bremsstrahlung (*braking radiation*) is the main source of energy loss.

[1] Universidad Autónoma de Madrid
[2] Centre de Physique des Particules de Marseille

Figure 4.1 shows the energy loss processes of photons and electrons as function of their energy. In what follows, we will explain in detail these processes with particular attention to those that occur within the electromagnetic calorimeter.

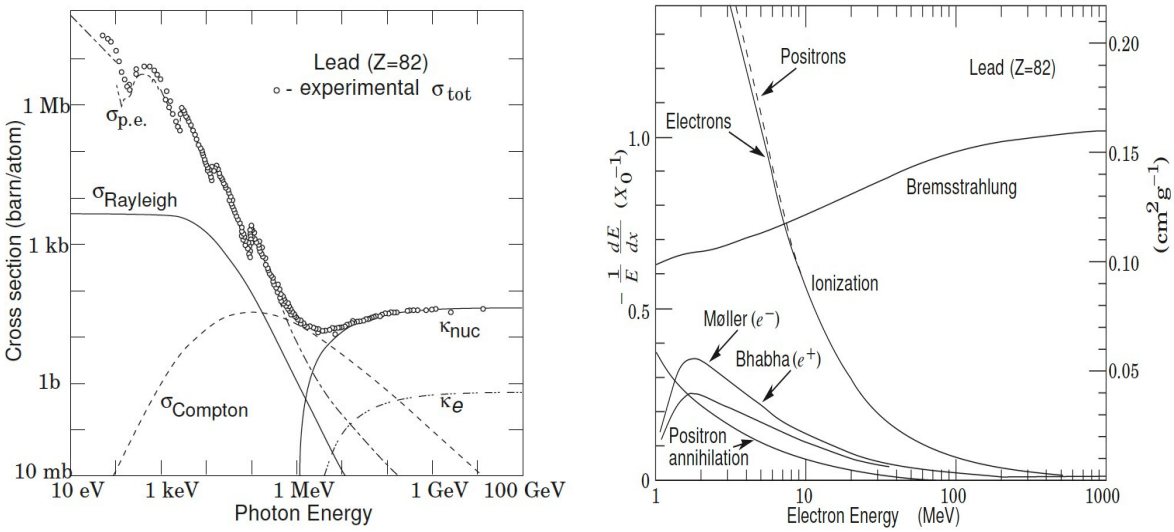


(a) (b)

Figure 4.1: (a) Photon cross section as function of the energy in lead. (b) Fractional energy loss of electrons and positrons per radiation length as function of the energy.

### 4.1.1 Electromagnetic shower development

When an electron or positron passes through matter it irradiates bremsstrahlung. The bremsstrahlung photon gives rise to electron–positron pair production. Thus, a cascade of many particles with lower and lower energy builds up until the energy of the particles falls below the threshold for pair production. The remaining energy is dissipated by excitation and ionization.

#### 4.1.1.1 Bremsstrahlung

If a charged particle is decelerated in the Coulomb field of a nucleus, a fraction of its kinetic energy will be emitted in form of photons. The electron and positron are the only particles for which energy loss by bremsstrahlung is significantly important (see Figure 4.1(b)).

In fact the semi–classical calculation for the bremsstrahlung cross section for any given particle of mass $M$ and velocity $v$ [29]:

$$\left(\frac{d\sigma}{dk}\right)_{rad} \simeq \frac{5e^2}{\hbar c} z^4 Z^2 \left(\frac{m_e c}{Mv}\right)^2 \frac{r_e^2}{k} \ln\left(\frac{Mv^2\gamma^2}{k}\right) \tag{4.1}$$

where:

- $k$ is the photon energy.
- $m_e$, $e$ are the mass and charge of the electron, respectively.
- $z$ is the charge of incident particle in units of $e$.
- $Z$ is the atomic number of absorbing material.
- $r_e$ is the classical electron radius ($2.817\times10^{-13}$ cm).
- $\gamma$ is the $1/\sqrt{(1-\beta)}$ and $\beta$ is the $v/c$ of the incident particle.

It can be seen that the dependence of the previous cross section with the particle mass $M$ is (neglecting the logarithm term):

$$\left(\frac{d\sigma}{dk}\right)_{rad} \propto \quad M^{-2} \tag{4.2}$$

Thus, the bremsstrahlung cross section for a muon, $M_\mu = 105.7$ MeV, is approximately $44,000$ times smaller than that for an electron, $m_e = 0.51$ MeV. Despite of this fact, bremsstrahlung of muons has been observed in the ATLAS EM calorimeter; actually these are the type of events mostly used in the commissioning period with cosmic rays.

We can also note in the Equation 4.1 that the cross section is proportional to $Z^2$, i.e. to the atomic number squared of the traversed material. This explains the use of high $Z$ materials ( Fe, Cu, Pb, U) as absorbers in sampling calorimeters, in order to get a bigger energy loss by radiation. Finally, the cross section becomes very large as the radiated photon becomes very soft ($k$ very small).

#### 4.1.1.2 Pair production

Photons with an energy of at least twice the electron rest mass can produce an electron–positron pair in the Coulomb field of a charged particle. The cross section for this process rises with energy and reaches an asymptotic value at very high energies ($>$ 1 GeV). For energies above some MeV (depending on the absorber material), pair production becomes the dominant photon interaction process.

#### 4.1.1.3 Compton and Rayleigh scattering

Rayleigh scattering is a coherent process; the photon is deflected by an atomic nucleus but does not lose any energy. In contrast, a photon that undergoes Compton scattering does transfer part of its energy and momentum to an atomic electron that is put into an unbound state. The process will result in a free electron and a scattered photon. For most absorber materials, Compton scattering is by far the most likely process for photons with energies between a few hundred keV and 5 MeV.

#### 4.1.1.4 Photoelectric effect

At even lower energies, the most likely process is the photoelectric effect, where a photon is absorbed by an atom that in turn emits an electron. The atom is put into an excited state by this process and will return into its ground state by emission of Auger electrons or X-rays. The cross section is strongly dependent on the number of available electrons and scales with $Z^N$, where $n$ is 4 to 5 and has an energy dependence like $E^{-3}$.

### 4.1.2 Energy loss due to ionization

Let us consider a heavy particle, with charge $ze$, mass $M$ and velocity $v$ traversing a block of matter. Let us assume that at a distance $b$ of the incident particle direction an atomic electron is found. One can use a semi–classical approximation assuming the electron to be free and at rest during the time the interaction takes place. One usually further assumes that the direction of the incident particle is not changed as it is much heavier than the atomic electron.

Within these approximations, Bohr obtained expressions for energy loss of heavy particles ($\alpha$ particles of heavy nuclei), which were found to properly describe experimental data. For lighter particles like protons a disagreement with experiment was found, because quantum effects were not taken into account. The correct quantum-mechanical calculation was first performed by Bethe and Bloch, obtaining this formula:

$$-\left(\frac{dE}{dx}\right)_{ioniz} = 2\pi N_a r_e^2 m_e c^2 \rho \frac{Z}{A}\frac{z^2}{\beta^2}\left[\ln\left(\frac{2m_e\gamma^2 v^2 W_{max}}{I^2}\right) - 2\beta^2\right] \tag{4.3}$$

where:

- $E$ is the incident particle energy and $x$ is the path length.
- $N_a$ is the Avogadro's number ($6.022 \times 10^{23}$ mol$^{-1}$).
- $\rho$, $A$ and $Z$ are the density, atomic weight and atomic number of absorbing material, respectively.
- $W_{max}$ is the maximum energy transfer in a single collision.
- $I$ is the mean excitation potential.

In practice, two more corrections are needed, the so called density effect and the shell effect [30]:

$$-\left(\frac{dE}{dx}\right)_{ioniz} = 2\pi N_a r_e^2 m_e c^2 \rho \frac{Z}{A}\frac{z^2}{\beta^2}\left[\ln\left(\frac{2m_e\gamma^2 v^2 W_{max}}{I^2}\right) - 2\beta^2 - \delta - 2\frac{\zeta}{Z}\right] \tag{4.4}$$

where:

- $\delta$: density effect correction, which arises from the fact that the electric field of the particle also tends to polarize the atoms along its path.

- $\zeta$: shell effect correction, which accounts for effects when the velocity of the incident particle is comparable or smaller than the orbital velocity of the bound electrons.

The maximum energy transfer occurs in head on collisions between the incident particle and the atomic electron and is given by the expression:

$$W_{max} = \frac{2m_e c^2(\beta\gamma)^2}{1+2s\sqrt{1+(\beta\gamma)^2}+s^2} \qquad \text{with} \quad s = m_e/M. \tag{4.5}$$

A semi-empirical formula can be used for the excitation potential, namely:

$$\frac{I}{Z} = 12 + \frac{7}{Z}\ \text{eV} \qquad Z < 13$$
$$\frac{I}{Z} = 9.76 + 58.8\, Z^{-1.19}\ \text{eV} \qquad Z \geq 13$$

which gives a reasonable approximation for most cases.

The energy loss per unit length depends on the energy of the incident particle. It exhibits a sharp fall off, proportional to $1/\beta^2$ for low $\beta$ values, it reaches a minimum known as the ionization minimum (around $\beta\gamma = 3$), and finally shows a logarithmic increase (relativistic rise) leading to a plateau (*Fermi plateau*), see Figure 4.2. For energies bigger than the ionization minimum, each particle shows a characteristic curve. It can be used to identify particles in this energy range.

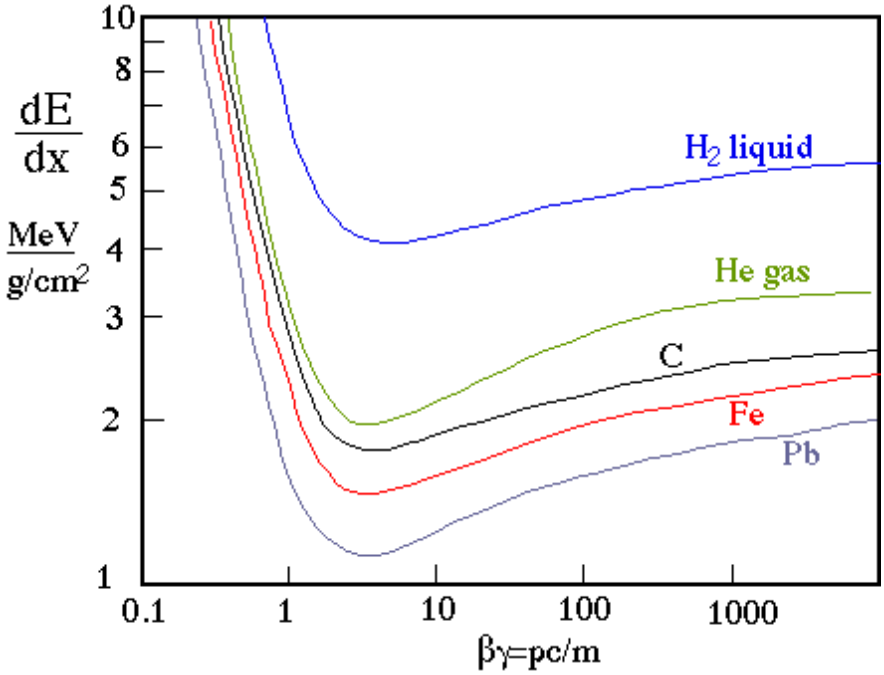


Figure 4.2: Ionization energy loss per unit of length in liquid hydrogen, gaseous helium, carbon, iron and lead.

Cosmic muons lose energy in the EM calorimeter primarily through ionization. The mean energy loss ($E$) is given by Equation 4.4, hence $E$ is proportional to the path length ($x$) crossed by the muon. Event by event this energy is subjected to stochastic fluctuations described by a Landau distribution. This function is not symmetric exhibiting a characteristic tail at high energy losses, hence the mean value of the distribution differs from the Most Probable Value (MPV). In practice, the MPV is more relevant than the mean value, for example for calibration studies, since the tail is often difficult to define with enough precision. It can be shown that the MPV is related to the path length through a relation of the type $MPV \sim x(a + \ln x)$, although the logarithm is usually much smaller than the term $a$, hence may be neglected in those cases. In addition, the ratio $\omega/MPV$, where $\omega$ is the full width at half maximum of the Landau distribution, decreases when $x$ increases.

### 4.1.3 Energy Resolution

Charged particles in the shower loose energy permanently by ionizing the material. For high-energy particles, the ionization loss rate rises approximately logarithmically with the energy.

Electron-Ion pairs created in the liquid argon are separated by an electric field and drift towards the electrodes inducing an electrical signal that is proportional to the number of electron/ion pairs and the energy deposited in the liquid argon gap (see Section 4.3).

In a sampling calorimeter like the ATLAS electromagnetic calorimeter, only a fraction of the total energy is deposited in the active part. The ratio of total energy deposit in the active region is called the **sampling fraction**:

$$f_s = \frac{E_{Active}}{E_{Passive} + E_{Active}} \tag{4.6}$$

The energy measured in a sampling calorimeter has to be multiplied with the inverse of the sampling fraction to obtain the total energy deposit.

However, the number of electrons and positrons in a shower produced by a particle with a given energy fluctuates statistically. Since the total ionization signal is proportional to the number of charged particles, the reconstruction energy fluctuates in the same way. Fluctuations in the deposited energy ($\Delta E$) can therefore be expressed like:

$$\frac{\Delta E}{E} \quad \propto \quad \frac{\Delta N}{N} \quad \propto \quad \frac{1}{\sqrt{N}} \quad \propto \quad \frac{1}{\sqrt{E}} \tag{4.7}$$

Therefore, the calorimeter energy resolution improves with increasing energy as $1/\sqrt{E}$. This estimation is based purely on statistical arguments. The actual energy resolution of a realistic calorimeter can be written as:

$$\frac{\sigma_E}{E} = \frac{a}{\sqrt{E}} \oplus \frac{b}{E} \oplus c \tag{4.8}$$

where:

- $a/\sqrt{E}$ is called **stochastic or sampling term**. It represents the fluctuations related to the physical development of the shower. Homogeneous calorimeters have a very small stochastic term because the whole shower is absorbed in the active material ($a$ about few percent). The sampling calorimeters have a much bigger stochastic term because the energy deposited in the active material can fluctuate on an event-by-event basis.
- $b/E$ is called **noise term**. This term depends on the noise of the electronic read-out chain. Methods like signal shaping and optimal filtering can help to reduce the noise term.
- $c$ is called **constant term**. This term summarizes all the contributions which do not depend on the particle energy. It includes material non-uniformities, imperfections of the mechanical structures, temperature gradients, etc.

For very high energies, the stochastic term becomes small and the resolution of the calorimeter is determined by instrumental effects.

## 4.2 Detector requirements

One of the challenges in building the ATLAS EMC is applying the same high precision mechanical techniques, used successfully in the building of previous electromagnetic calorimeters, on a scale that is an order of magnitude larger than before. Furthermore, calorimetry will be a crucial tool for the understanding of many physics processes which will manifest themselves through final states with electrons or photons (i.e. $H \rightarrow \gamma\gamma$ or $H \rightarrow 4e$). In this sense, the main requirements to fulfill the physics program are:

- **Rapidity coverage**. Searches for rare processes require an excellent coverage in pseudorapidity, as well as the measurement of the missing transverse energy of the event and the reconstruction of jets.
- **Excellent energy resolution**. To achieve a 1% mass resolution for the $H \rightarrow \gamma\gamma$ and $H \rightarrow 2e^+2e^-$ in the range $114 < m_H < 219$ for the standard model Higgs, the sampling term should be at the level of $10\ \%/\sqrt{E[GeV]}$ and the constant term should be below 0.7 %.
- **Electron reconstruction capability from** 1 GeV **to** 5 TeV. The lower limit comes from the need of reconstructing electrons from $b$ quark decay. The upper one is set by heavy gauge boson decays.
- **Excellent** $\gamma/jet$, $e/jet$, $\tau/jet$ **separation**, which requires again high transverse granularity and longitudinal segmentation.
- **Accurate measurement of the shower position**. The photon direction must be accurately reconstructed for the invariant mass measurement in $H \rightarrow \gamma\gamma$ decay. This implies a very good transverse and longitudinal segmentation, with a measurement of the shower direction in $\theta$ with an angular resolution of $\sim \frac{50\ \text{mrad}}{\sqrt{E(GeV)}}$.

- **Small impact of Noise**. The impact of noise on the calorimeter performance must be as small as possible. At LHC, contributions to the calorimeter resolution from noise arise from pile-up and from the electronic noise of the readout chain. These contributions are particularly important at low energy ($E < 20\ GeV$) where they can dominate the accuracy of the calorimeter energy and position measurements. Minimization of the pile-up noise requires fast detector response and fast electronics; minimization of the electronic noise requires high calorimeter granularity and high-performance electronics.

- **Resistance to radiation**. The EM calorimeters will have to withstand neutron fluencies of up to $10^{15}\ \frac{n}{cm^2}$ and radiation doses of up to 200 kGy (integrated over ten years of operation).

- **Time resolution**. The time resolution should be around 100 ps for background rejection and for the identification of some decay modes with non-pointing photons.

- **Linearity**. It is necessary to obtain a linearity better than 0.1 %.

In order to fulfill these requirements precise optimal filtering coefficients (OFC) must be determined, which imply an accurate knowledge of the pulse shape response of every calorimeter channel. This will be discussed in Chapter 5.

## 4.3 Description of the EM calorimeter

The EM calorimeter is a sampling calorimeter with lead as passive material (absorber) and liquid argon as an active material [26]. An accordion shape is given to all plates in order to avoid crack regions due to cables and boards of the readout. For the sake of clarity a photograph of the accordion shape corresponding to the EM endcap can be seen in Figure 4.3(a). Particles would be incident from left to right on the Figure.

The LAr ionization is collected by electrodes (at high voltage) situated in between two absorbers (see Figure 4.3(b)). To keep the electrode in the right place, honeycomb spacers are located in between the absorber and the electrode. Hence, the calorimeter is stacked as a sandwich of absorber, spacer, electrode, spacer, (next absorber), repeated along the azimuthal direction up to complete the whole coverage.

The EM Calorimeter covers the whole range along the azimuthal ($\phi$) direction and between -3.2 and 3.2 along the $\eta$ direction. It is divided in one barrel ($-1.475 < \eta < 1.475$) [31] (EMB) and two endcaps ($1.375 < |\eta| < 3.2$) [32] (EMEC) and is segmented in depth in three layers (see Figure 4.4). There is also a thin presampler detector in front of the calorimeter covering the region $|\eta| < 1.8$, whose task is to correct for the energy losses of electrons and photons in the upstream material (see Figure 3.7).

The Argon is kept liquid at a temperature of $\sim 89\ ^{o}$K through a cryogenic system, being the EM barrel and endcap calorimeters inside their respective cryostat vessels.

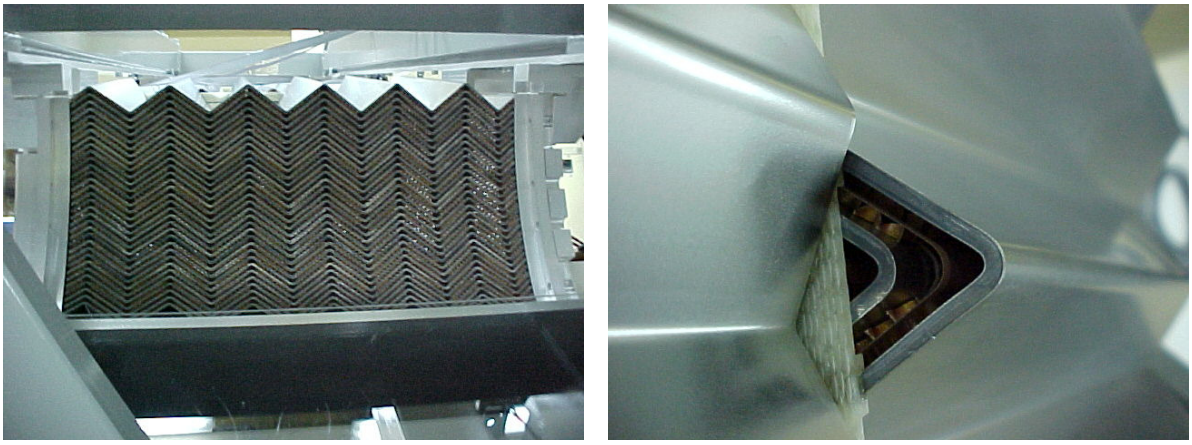

(a) (b)

Figure 4.3: (a) Accordion–shaped in EM endcap inner wheel. (b) Picture of an electromagnetic module during stacking.

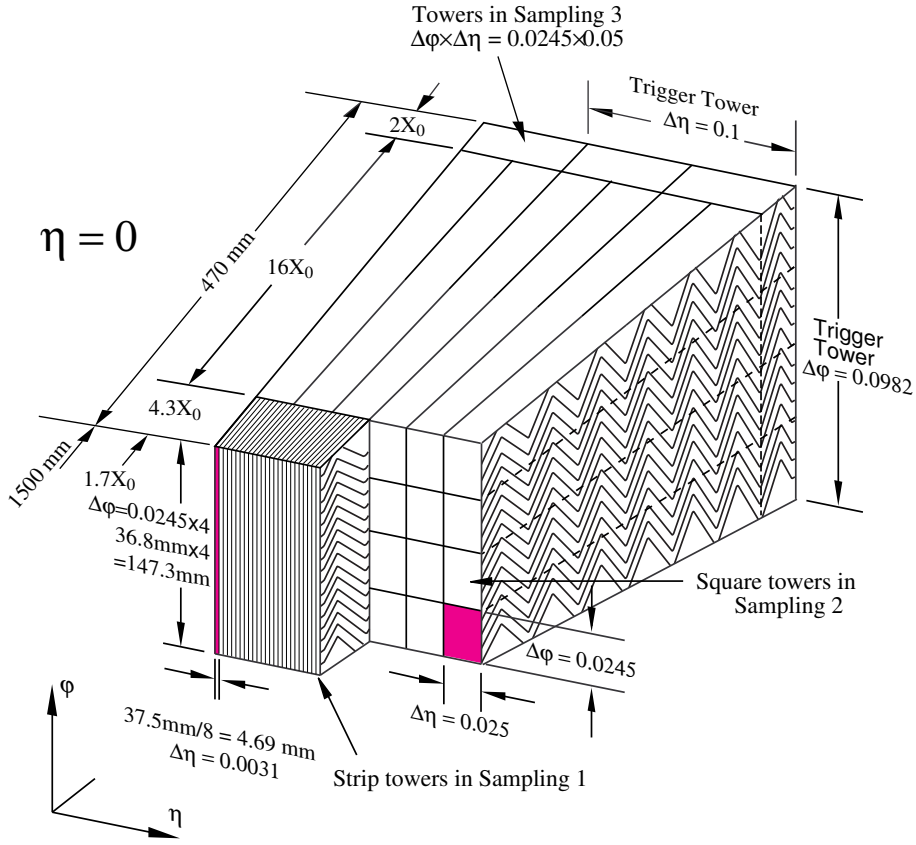


Figure 4.4: Schematic view of an accordion calorimeter piece. Sampling segmentation (three layers) and granularity of the EM calorimeter.

### 4.3.1 Barrel specific properties

The barrel electromagnetic calorimeter is made of two half-barrels, centered around the z-axis. One half-barrel covers the region $0 < \eta < 1.475$ and the other one the region $-1.475 < \eta < 0$. The length of each half-barrel is 3.2 m, their inner and outer diameters are 2.8 m and 4 m respectively.

Figure 4.5 shows a diagram of one half-barrel. The direction of the accordion waves is indicated pointing to the $z$ axis as well as the calorimeter cells which points to the ATLAS center or nominal interaction point. The calorimeter is inside the cryostat vessel which has two walls, warm and cold, separated with a vacuum gap for temperature isolation purposes. The cables pass from inside to outside of the cryostat vessel using special feedthrough connectors which keeps the temperature isolation. In the "warm" part (outside the cryostat) crates are connected to the feedthroughs, which contains some electronics boards: Front End Boards (FEB) and Calibration Boards. It can also be seen in Figure 4.5 a tube on top of the cryostat through which the cryogenic system injects the liquid Argon.

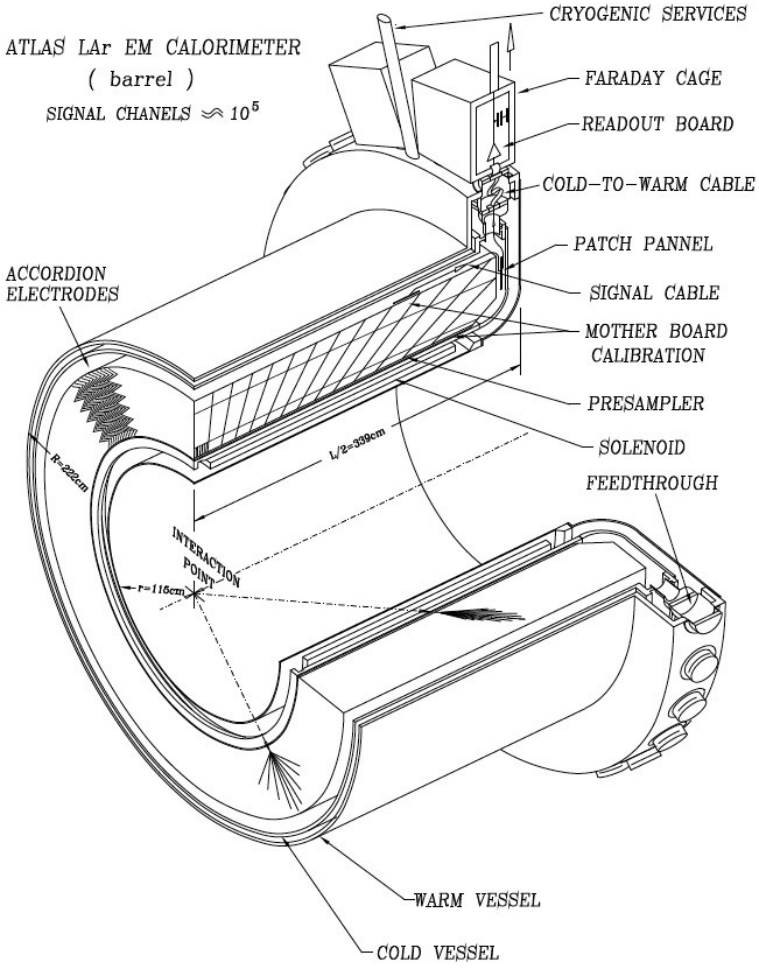


Figure 4.5: Diagram of a half of the EM Barrel.

The size of the LAr gap on each side of the electrode is 2.09 mm, which corresponds to a total drift time of about 450 ns for an operation voltage of 2000 V. For ease of construction, each half-barrel has been divided into 16 modules, each covering a $\Delta\phi = 22.5^o$. A picture of one EMB module is shown in Figure 4.6.

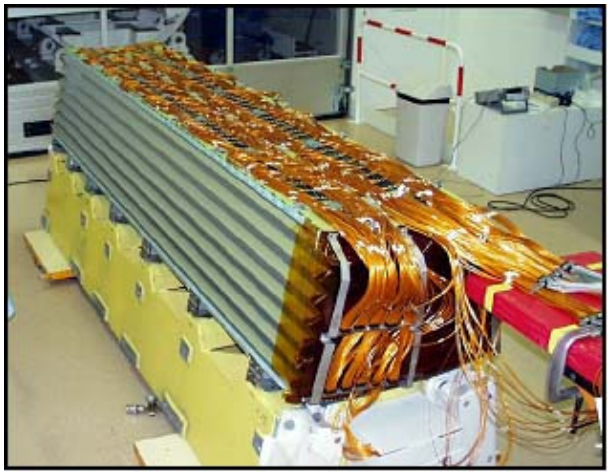

Figure 4.6: Picture of an EMB module.

### 4.3.2 Endcap specific properties

There are two EMEC cylinders in ATLAS located inside the endcap Cryostat at $z \sim \pm 350$ cm of the nominal interaction point. A picture of one EMEC inside the endcap cryostat can be seen in Figure 4.7(a). Since the EMEC is a cylindrical wheel, the amplitude of the accordion waves decreases when $\eta$ increases (when the radius decreases). Due to mechanical constraints demanded by this accordion shape, a second independent wheel is needed to extend the coverage to $\eta = 3.2$. Hence, there are two wheels, the outer wheel from $\eta = 1.375$ to $\eta = 2.5$ and the inner wheel from $\eta = 2.5$ to $\eta = 3.2$. The lead is cladded with 0.2 mm thick stainless steel jacket to give it enough rigidity. For the outer wheel, the thickness of the lead plates is 1.7 mm while the LAr gap thickness between the absorber and the electrode decreases continuously from 2.8 mm (at $\eta = 1.375$) to 0.9 mm (at $\eta = 2.5$) when $\eta$ increases (see Figure 4.8). For the inner wheel, the thickness of the lead plates is 2.2 mm while the LAr gap thickness between the absorber and the electrode decreases continuously from 3.1 mm (at $\eta = 2.5$) to 1.8 mm (at $\eta = 3.2$) when $\eta$ increases.

To facilitate handling and logistics, the EMEC cylinder is divided into 8 octants or modules (see Figure 4.7(b)). The 16 modules have been stacked at the CPPM and UAM clean rooms.

One module consists of 96 (32) layers for the outer (inner) wheel stacked one on top of each other. Each layer is a sandwich of absorber, spacer (gap), electrode, spacer (gap). The design is symmetrical in $\phi$ and projective to the interaction point in $\eta$. In particular the cells drawn in the electrodes point to the nominal ATLAS interaction point.

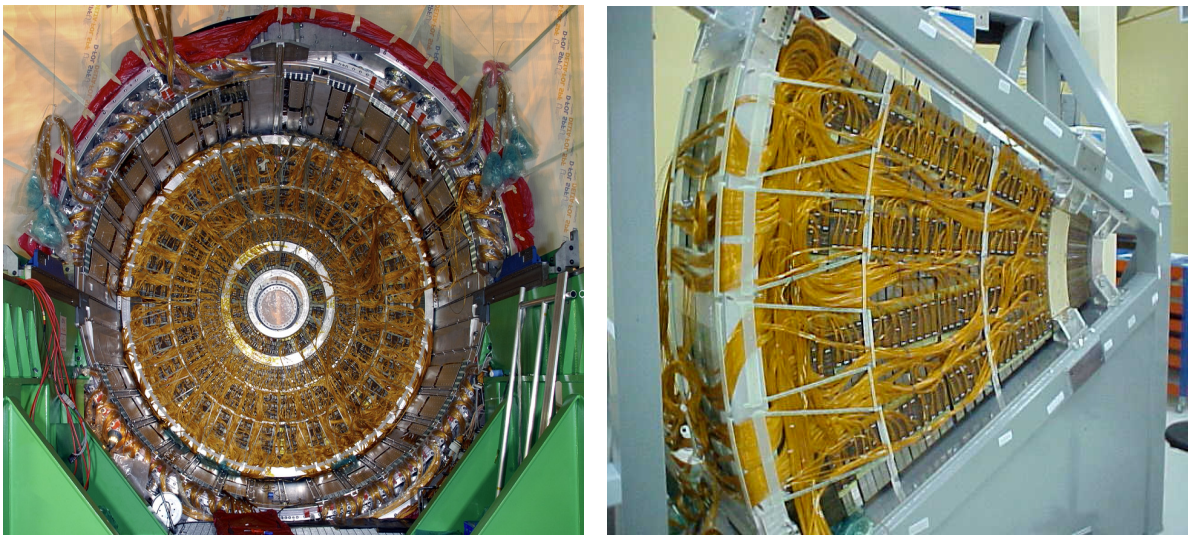

(a) (b)

Figure 4.7: (a) Picture of an EMEC wheel inside the endcap Cryostat. (b) Picture of an EMEC module or octant at the stacking frame of the UAM clean room.

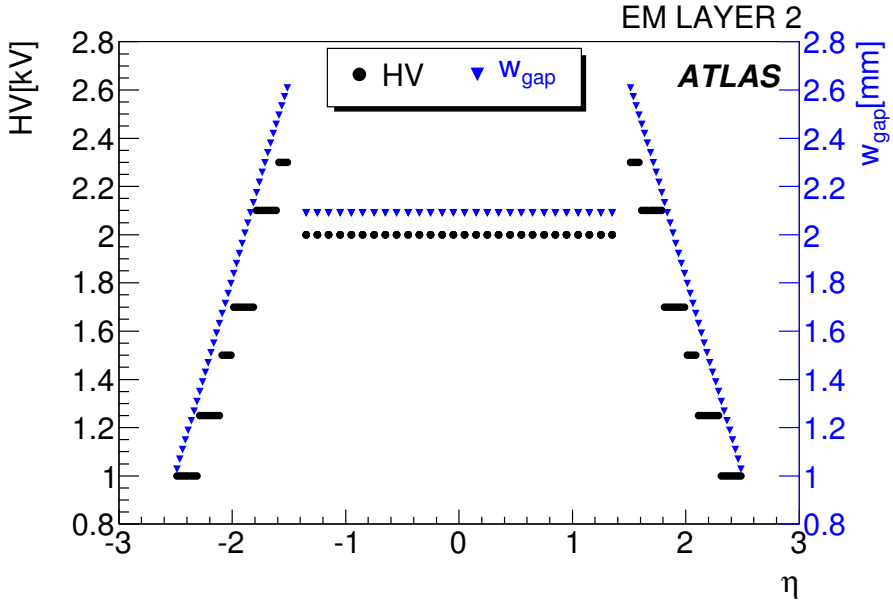


Figure 4.8: Nominal HV (black dots) and nominal gap width $w_{gap}$ (blue triangles) versus η in the $2^{nd}$ layer of the EM calorimeter.

### 4.3.3 Segmentation and granularity

The EM Calorimeter is segmented into cells along the two angular directions, $\eta$ and $\phi$, and the longitudinal direction (calorimeter depth). In depth, three layers are defined by reading out three electrode regions independently, namely: front (layer 1), readout from the calorimeter front side, middle (layer 2) and back (layer 3), both readout from the calorimeter back side (see Figure 4.4).

The granularity along $\eta$ is also defined in the electrodes as copper strips using kapton as electrical insulator between two strips. The size of such strips depends on the layer, being smallest in layer 1 to allow for the separation of the two photons from the decay of a $\pi^0$. A picture of an electrode for barrel and endcap is shown in Figure 4.9. The angular variable $\eta$ increases from right to left of the picture. The copper strips are clearly seen so defining the granularity along the $\eta$ direction. The three layers in depth can be clearly distinguished as the width of the strips changes from one layer to another.

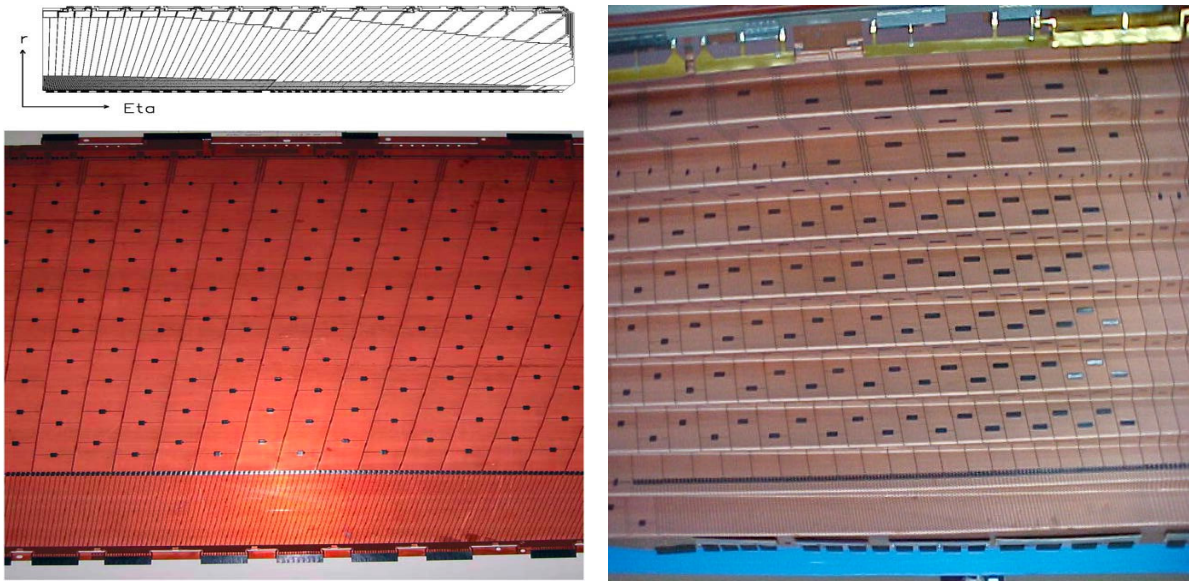


(a) EM barrel (b) EM endcap

Figure 4.9: Picture of an EMB (a) and EMEC (b) electrode of the outer wheel. The segmentation along $\eta$ and the three layers in depth front, middle and back, are clearly seen.

The granularity along the azimuthal $\phi$ direction is defined by connecting summing boards to the electrode connectors, hence grouping the signal in $\phi$. Each liquid argon electronic cell is built out of several gaps connected in parallel: for layers 2 and 3, there are 4 (3) consecutive electrodes in the barrel (endcap) respectively; there are four times as many gaps per cell in layer 1, given the coarser granularity of the readout in the azimuthal direction. Figure 4.10 shows some summing boards plugged in the electrode connectors for layer 1 of an EMEC module. The $\phi$ direction goes from bottom to top of the picture, while the $\eta$ direction increases from left to right. The electrode connectors can be distinguished in black between two absorbers. The summing boards grouped the signals of 12 electrodes together in this example.

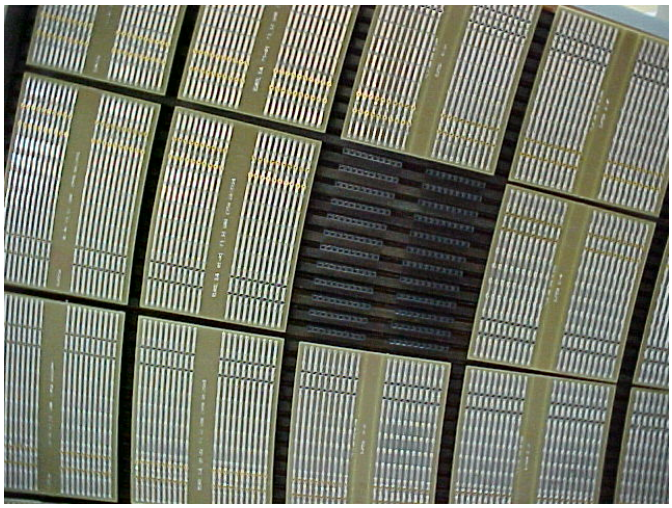

Figure 4.10: Picture of the summing boards plugged in the front face of an EMEC module.

The electromagnetic calorimeter granularity is detailed in Table 4.1. In total the number of cells or channels in the electromagnetic calorimeter is 173,312 (101760 in barrel, 62208 in endcaps and 9344 in presampler).

| | | Layer 1 | Layer 2 | Layer 3 |
|---|---|---|---|---|
| Barrel | $\|\eta\| \leq 1.35$ | $0.025/8 \times 0.1$ | $0.025 \times 0.025$ | $0.050 \times 0.025$ |
| | $1.35 \leq \|\eta\| \leq 1.4$ | $0.025/8 \times 0.1$ | $0.025 \times 0.025$ | – |
| | $1.4 \leq \|\eta\| \leq 1.475$ | $0.025 \times 0.025$ | $0.075 \times 0.025$ | – |
| Endcaps | $1.375 \leq \|\eta\| \leq 1.425$ | $0.050 \times 0.1$ | $0.050 \times 0.025$ | – |
| | $1.425 \leq \|\eta\| \leq 1.5$ | $0.025 \times 0.1$ | $0.025 \times 0.025$ | – |
| | $1.5 \leq \|\eta\| \leq 1.8$ | $0.025/8 \times 0.1$ | $0.025 \times 0.025$ | $0.050 \times 0.025$ |
| | $1.8 \leq \|\eta\| \leq 2.0$ | $0.025/6 \times 0.1$ | $0.025 \times 0.025$ | $0.050 \times 0.025$ |
| | $2.0 \leq \|\eta\| \leq 2.4$ | $0.025/4 \times 0.1$ | $0.025 \times 0.025$ | $0.050 \times 0.025$ |
| | $2.4 \leq \|\eta\| \leq 2.5$ | $0.025 \times 0.1$ | $0.025 \times 0.025$ | $0.050 \times 0.025$ |
| | $2.5 \leq \|\eta\| \leq 3.2$ | $0.1 \times 0.1$ | $0.1 \times 0.1$ | – |

Table 4.1: *Granularity* $\Delta\eta \times \Delta\phi$ *for each calorimeter layer (front, middle and back).*

### 4.3.4 High Voltage

The condition of projectivity to the nominal ATLAS interaction point in the construction of the EMEC makes that the Liquid Argon gap thickness (between absorber and electrode) decreases continuously when $\eta$ increases. The relation between the energy collected by the calorimeter ($E$) and the liquid Argon gap thickness ($w_g$) is [33]:

$$E \sim \frac{f_s}{w_g^{1+\alpha}} H V^{\alpha} \tag{4.9}$$

where $HV$ is the High Voltage applied on the gaps and $f_s$ is the sampling fraction defined in Equation 4.6 (which is a function of the gap thickness). The value of $\alpha$ has been determined to be $\alpha = 0.3$ at 88.5 K in [34].

The decrease of the liquid Argon gap thickness when $\eta$ increases implies an increase of the measured energy with $\eta$. This growth may be compensated by decreasing $HV$ continuously when $\eta$ increases. For practical reasons a decreasing stepwise function for $HV$ is chosen, thus defining seven HV sectors for the outer wheel and two sectors for the inner wheel. The growth of the measured energy with $\eta$ inside a HV sector is corrected by software in the reconstruction phase of the signal, keeping then the required uniformity of the calorimeter signal response. In contrast, for the EM Barrel Calorimeter this problem does not occur and, as a consequence, the High Voltage between electrodes and absorbers is kept constant, being the nominal value 2000 V. Figure 4.8 shows the nominal gap size and the nominal HV size used in the standard geometry simulation in the ATLAS EM calorimeter until $|\eta| < 2.5$.

The High-Voltage sector definitions, consequence of the endcap geometry, is given in Table 4.2.

| | **Barrel** | **End-cap Outer W.** | | | | | | | **End-cap Inner W.** | |
|---|---|---|---|---|---|---|---|---|---|---|
| **HV region** | 0 | 1 | 2 | 3 | 4 | 5 | 6 | 7 | 8 | 9 |
| **$\eta$ range** | 0-1.475 | 1.375-1.5 | 1.5-1.6 | 1.6-1.8 | 1.8-2.0 | 2.0-2.1 | 2.1-2.3 | 2.3-2.5 | 2.5-2.8 | 2.8-3.2 |
| **HV values** | 2000 V | 2500 V | 2300 V | 2100 V | 1700 V | 1500 V | 1250 V | 1000 V | 2300 V | 1800 V |

Table 4.2: The high voltage regions of the EM calorimeter.

### 4.3.5 Electronics

The electric signal from the ionization of the Liquid Argon produced by a charged particle has a triangular shape, when representing the intensity versus time, with typical duration of several hundreds nano-seconds. This signal pass through the electrode readout paths to the Summing Boards and the Mother Boards on top of them. Long cables connect the Mother Boards to the electronics outside the cryostat.

A simplified schematic view of the calorimeter readout inside the detector is shown in Figure 4.11. The detector cell is represented by a capacitance $C$ where a triangular ionization signal ($I_{inj}^{phys}(t)$) is generated by the detected particle. Also linked to a cell, there appears an inductance $L$ due to the electrode, the Summing-Board and a small portion of the Mother-Board. The signal travels through a 25 $\Omega$ cable in case of a middle or a back cell and a 50$\Omega$ cable in case of a front cell. Immediately after the feedthrough of the cryostat, the signal enters a Front-End-Board (FEB) and passes through a three gain shaper with gain factors 1, 9.3 and 93 corresponding to low, medium and high gain respectively. The measured shaped signal $g^{phys}(t)$ is sampled by a Switch Capacitor Array (SCA) located in the FEB at a frequency of 40 MHz (equivalent to a period of 25 ns), that is the nominal bunch crossing frequency of LHC beams. The samples are digitized by ADCs located in the FEB and the numbers are transmitted to the miniROD and the DAQ computing system in the control room.

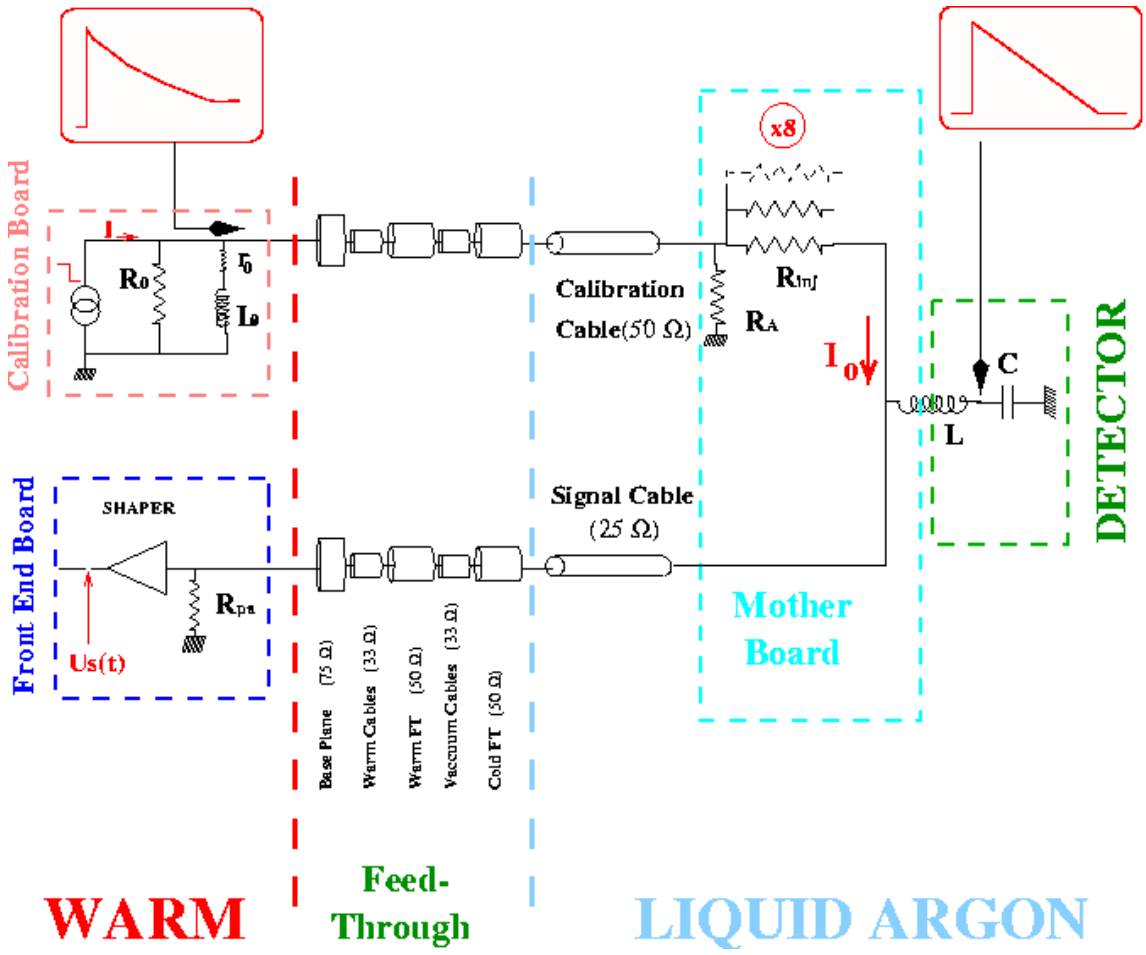


Figure 4.11: Diagram of the EM calorimeter readout inside the detector.

An exponential signal ($I_{inj}^{cali}(t)$) is generated in the Calibration Board playing the role of the triangular ionization signal of physics events. The signal $I_{inj}^{cali}$ passes the feedthrough to get into the cryostat and travels through a long cable up to the Mother-Board. The calibration signal sees the detector cell as a capacitance and an inductance as indicated in Figure 4.11. The response to this injection signal continues through the same readout line as the ionization signal to reach the SCA. The output is again seven samples of the shaped signal $g^{cali}(t)$ after being digitized by the ADC.

The calibration boards allow to set the amplitude of injected current $I_{inj}^{cali}$ numerically. A DAC unit, included in the calibration board, transforms this number into an analog amplitude. We will refer to this number as DAC value. The calibration board is equipped with a delay unit, which allows to delay the injection from 0 to 24 ns in steps of 1 ns with respect to the leading edge of the 40 MHz clock ($t_{delay}$). The calibration pulse $g^{cali}(t)$ is obtained by representing the sample heights as a function of $t_{delay}$ [3]. These delay runs were taken in between cosmic runs. Delay runs in high (medium, low) gain with a DAC value of 500 (4000, 40000) units are considered for the signal reconstruction studies.

[3]Every sample height is an average over 100 events taken for a given delay

### 4.3.6 Main differences between EM endcap and barrel

Some differences between EMEC and EMB relevant to the study of this document are summarized in the Table 4.3.

| | Barrel | Endcaps (outer wheel) |
|---|---|---|
| Gap (absorber-electrode) (mm) | 2.09 | 0.9 to 3.1 |
| Bending angle (°) | 70 to 90 | 60 to 120 |
| Drift time (ns) | 450 | 600 to 200 |
| dE/dX sampling fraction (%) | 25 or 28 | 30 to 14 |
| HV (V) | 2000 | 2500 to 1000 |
| Layer 2 Cell inductance *L* (nH) | 25 to 35 | 50 to 20 |
| Layer 2 Cell Capacitance at cold *C* (pF) | 1400 or 1900 | 1200 to 600 |

Table 4.3: Some geometrical and electrical characteristics of the barrel and endcap outer wheel EM calorimeter. In the former case, parameters may vary at $|\eta| = 0.8$. In the latter case, the variation is smooth and given for increasing $|\eta|$ from 1.375 to 3.2.

# 5

# Signal reconstruction performance

The ATLAS Liquid Argon electromagnetic calorimeter uses a digital filtering technique, called Optimal Filtering Method, to reconstruct the signal amplitude from samplings of the ionization pulse. Some weights, optimal filtering coefficients (OFC), are determined from the pulse shape and its derivative, such that the weighting sum of the samples gives the amplitude of the signal per cell. Each read-out channel can be calibrated by means of electronic pulses that mimic the ionization signal produced by an electromagnetic shower. The calibration and the ionization signal are slightly different in shape (exponential/triangular, respectively) and injection point (outside/inside the detector). It is necessary to know the electrical parameters of every cell in the detector to deduce the ionization signal from the calibration signal.

This chapter gives a brief description of the Optimal Filtering Method in Section 5.1 and a method to predict the ionization signal from the calibration signal in Section 5.2. Section 5.3 explains an algorithm to determine the electrical parameters of the calorimeter cell. Finally, in Section 5.4 a first global check of the signal reconstruction quality over the whole EM calorimeter coverage is performed with few tens of events created by the hit of LHC beams on collimators 200 meters before ATLAS on 2008.

## 5.1 Optimal filtering method

The LAr EMC signal is generated by the drift of the ionization electrons in the electric field provided by the High Voltage (HV) in the LAr gap. The current versus time has a triangular shape, being the peak proportional to the energy deposited by the electromagnetic shower. The ionization signal is pre-amplified and then shaped by a $CR - RC^2$ bipolar filter at the end of the readout chain. The bipolar signal is sampled every 25 ns (the LHC bunch crossing period) and 5 samples are digitized and used in the signal reconstruction procedure. For special runs more than 5 samples are digitized and recorded (typically 25 or 32). Figure 5.1 shows a comparison

between the original triangular signal generated inside the LAr gap and the output signal after passing the readout electronics. It corresponds to a cell of the layer 2 for high gain of the bipolar shaper. The maximum has been normalized to 1. The bipolar shaper is designed such that the maximum of the triangular signal corresponds to the maximum of the shaped pulse. Hence, the maximum amplitude of the shaped pulse is proportional to the energy deposited by the electromagnetic shower in that cell. The dots correspond to the samples each 25 ns.

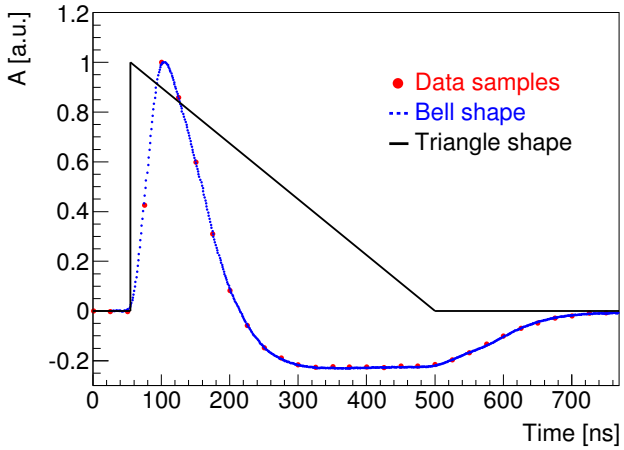


Figure 5.1: The triangle shape (black line) corresponds to the signal as a function of time just after the electrode, and the bell shape (blue line) corresponds to the signal after crossing the shaper. Red dots represent the recorded amplitudes separated by 25 ns.

From these samples two relevant quantities are deduced, using a digital filtering technique, namely the signal maximum amplitude ($A_{max}$), which is proportional to the energy deposited in the cell, and the time shift ($\Delta t$) of the signal maximum amplitude with respect to a reference value. The Optimal Filtering (OF) method is a digital filtering technique to determine such quantities. The inputs to the method are: the covariance or autocorrelation matrix of the samples, which contains the information of the noise, the pulse shape ($g^{phys}$), its maximum normalized to one, and its derivative ($dg^{phys}/dt$).

The outputs of the method are some weights or coefficients, $a_i,\ b_i\ \ i = 1,\ldots,n$, where $n$ is the number of samples, such that:

$$A_{max} = \sum_{i=1}^{n} a_i S_i \tag{5.1}$$

$$\Delta t = \frac{\sum_{i=1}^{n} b_i S_i}{A_{max}} \tag{5.2}$$

being $S_i\ i = 1,\ldots,n$ the measured samples (pedestal or zero is subtracted).

The Optimal Filtering coefficients (OFC), $a_i,\ b_i\ \ i = 1,\ldots,n$, are calculated by the method with the condition to minimize the noise contribution to the signal [35].

Two sources of noise are foreseen in the calorimeter during operation at LHC:

- **Thermal (or electronic) noise.** The amplitude of the thermal noise depends only upon the characteristics of the detector and the signal processing circuitry. Figure 5.2 shows the electronic noise measured in ADC counts at the cell level as a function of $\eta$ for every layer [1].
- **Pile-up (or physics) noise.** The minimum bias or soft scattering events will be superimposed to the hard scattering process. It is expected to have about 27 minimum bias events per bunch crossing at nominal LHC luminosity. In addition, events of previous bunch crossings will affect the signal of the present crossing, since the ionization time constant of the liquid Argon is several hundred nano-seconds. The overall effect is a small signal in the cells, fluctuating from event to event, which can be considered as a noise superimposed to the hard process physics event of interest. The level of pileup noise depends therefore on the luminosity of the machine and on the size of the calorimeter cells.

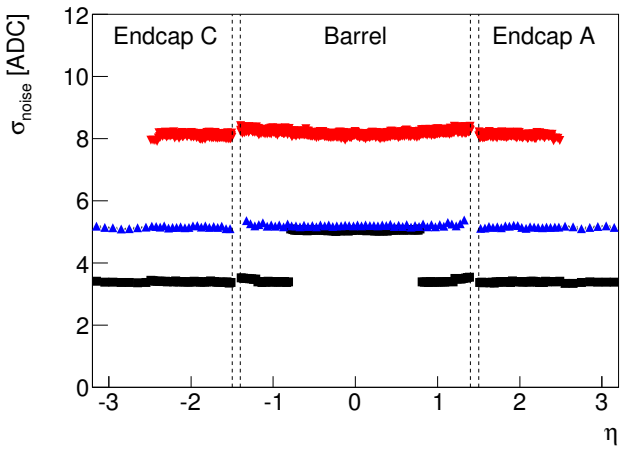


Figure 5.2: Electronic noise ($\sigma_{noise}$) computed with 5 samples OFC in high gain for each longitudinal layer of the EM calorimeter as a function of $\eta$. Results are averaged over $\phi$. Layer 1, 2 and 3 are represented with red down triangles, black squares and blue up triangles, respectively.

In the case of cosmics muon or single beam data, only the first source of noise enters in the analysis. In future, for the analysis of the LHC data we will need to take the pile-up noise contribution into account as well.

For ATLAS nominal operation with collision events, the bunch crossings and the readout clock are synchronous, hence the pulses get always sampled at the same position and one set of OFC is sufficient. However, in the cosmic test environment this is not the case since the cosmic signal is asynchronous to the readout clock. Depending on the phase shift between the clock

[1] unlike in the ATLAS standard convention, the two layers of the inner wheel are denoted layer 2 and layer 3 because they have similar geometrical and electrical characteristics as layer 2 and layer 3 of the outer wheel.

and the particle arrival, a different fraction of the pulse is sampled. To cope with this situation, multiple sets of OF coefficients are calculated by shifting the pulse shape $g^{phys}$ in steps of $\Delta_{phase}$. During the cosmic commissioning period, a set of $(a_i, b_i), i = 1, \ldots, n$ coefficients for each time phase were calculated, up to a total of 50 phases in 1 ns steps and for every gain. During the LHC single beam period in 2008, a different step was used $\Delta_{phase} = 3.125$ ns.

Given a certain asynchronous data event, with certain sample values $S_i, i = 1, \ldots, n$, the proper set of OFC is chosen such that the value of $\Delta t$ is minimum: $< 1$ ns or $< 3.125$ ns for cosmic or beam splash data respectively.

## 5.2 Prediction of physics pulse

As seen in the previous section, the pulse shape of the ionization (or physics) signal is needed to determine the Optimal Filtering Coefficients for each calorimeter cell. However this shape is unknown and must be predicted either by an analytical model of the EM readout [36] or directly from the cell response to a calibration pulse [37]. The second procedure is the standard ATLAS pulse shape prediction method and has been adopted in this work.

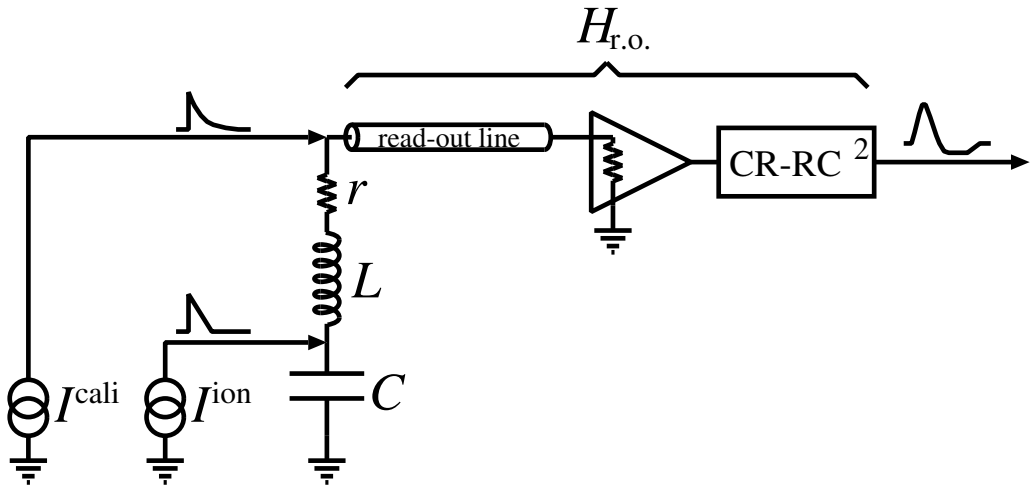


Figure 5.3: Basics electrical model of a LAr cell with schematic readout chain and simplified calibration network. Shapes of calibration and ionization signals are illustrated, as well as the output pulse.

Although the readout path and electronics are the same for physics and calibration inputs, there are two differences at the injection point, namely:

- the physics input signal is produced inside a gap of the detector, while the calibration input is generated outside the cryostat in a calibration board connected on a Front End Crate. This difference makes the calibration see the calorimeter cell as a different *RLC* circuit.
- the physics input signal has a triangular shape when represented as a function of time, while the calibration charge injection has an exponential shape.

In Figure 5.3 a simplified diagram of the electrical model for a LAr cell is shown. The calorimeter cell is seen as an *RLC* circuit: the capacitance $C$ of the LAr gap, an inductance $L$ which has two contributions, one from the electrode path between the gap and the Summing Board and the other one from the path inside the Summing Board itself added to a small portion of Mother Board, and a small resistance $r$ of the total path. The injection point of the ionization (physics) and calibration signals is indicated as well. Clearly these signals see the cell *RLC* circuit in a different way, *RL* in parallel with $C$ for physics injection signal and in serial in the case of calibration. The different shapes of the injection current between physics and calibration (triangular and exponential, respectively) is shown in Figure 5.4. These differences induces a different response amplitude to a normalized input signal. The resulting bias must be taken into account in order to correctly convert ADC counts into energy. This is achieved by using the ratio between the maximum amplitudes of physics and calibration pulses, called $M_{phys}/M_{cali}$.

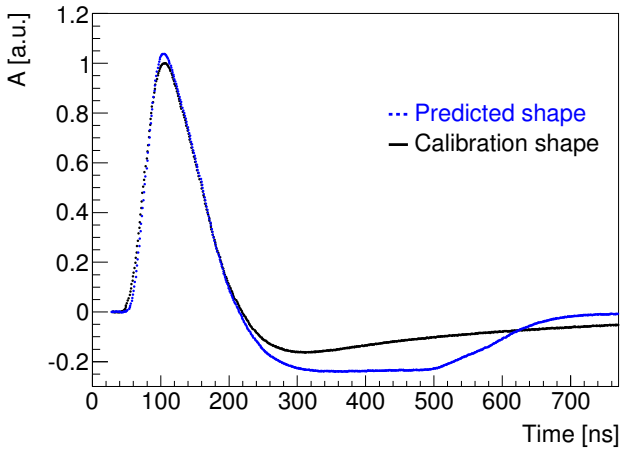


Figure 5.4: Typical predicted physic shape (blue line) compared with a calibration signal (black line). The calibration signal is normalized to 1.

The ionization electrons drift in the electric field inside the LAr gap, producing a current with amplitude proportional to the released energy. This current has the typical ionization-chamber triangular shape, with a fast rise time, of the order of 1 ns, followed by a linear decay for the duration of the maximum drift time $T_{drift}$. Neglecting the fast rise shape, such a signal at the input of the cell capacitor in time domain is given by:

$$I_{inj}^{phys}(t) = I_0^{phys}\theta(t)\theta(T_{drift}-t)\left(1-\frac{t}{T_{drift}}\right) \tag{5.3}$$

where $\theta$ is the *Heavyside* function and $I_0^{phys}$ is the amplitude of the ionization current. The drift time for the EM Barrel, 2.09 mm gap under a voltage of 2000 V, is close to 450 ns. In contrast it is a function of the pseudorapidity for the EMEC due to the change in the LAr gap and in the voltage, taking values in the range $200-600$ ns.

The output physics signal can be written as:

$$g^{phys}(t) = \int_{-\infty}^{+\infty} K_p(t-t')I_{inj}^{phys}(t')dt' \tag{5.4}$$

where $K_p$ contains the information of the readout circuitry.

In the Laplace domain and applying the **convolution theorem** [38]:

$$g^{phys}(s) = I_{inj}^{phys}(s)K_p(s) \tag{5.5}$$

where:

- $K_p(s)$ can be written as the product of a factor $H^{det}(s)$, which contains the electronics characteristics related to a detector cell (*RLC* circuit), and a factor $H^{readout}(s)$, which takes into account the readout chain (line+preamplifier+shaper) common for physics and calibration signals;
- $I_{inj}^{phys}(s)$ is the injected ionization signal 5.3 in the Laplace frequency domain, that is:

$$I_{inj}^{phys}(s) = I_0^{phys}\left(\frac{1}{T_{drift}s} - \frac{1-e^{-T_{drift}s}}{T_{drift}^2 s^2}\right) \tag{5.6}$$

Hence, the output physics signal can be written as:

$$g^{phys}(s) = I_{inj}^{phys}(s)H^{det}(s)H^{readout}(s) \tag{5.7}$$

The calibration charge injection aims to mimic the ionization signal, in order to be able to measure the actual gain and properties of each channel thus assuring the proper cell equalization. An exponential signal with decay time $\tau_{cali}$ is generated by the calibration boards (see section 4.3.5), whose pulser is based on a RL-circuit (see Figure 4.11). The values of the $R_0$ and $L_0$ components are selected such that to obtain the proper exponential decay constant $\tau_{cali}$, which has been chosen similar to the ionization signal decay slope. The non-ideal inductance $L_0$ of the calibration board pulser circuit has a resistive component $r_0$ that modifies the baseline of the exponential ($f_{step}$ parameter below). This exponential injection current can be written as:

$$I_{inj}^{cali}(t) = I_0^{cali}\theta(t)(f_{step} + (1-f_{step})e^{-t/\tau_{cali}}) \tag{5.8}$$

where $I_0^{cali}$ is the amplitude of the injected current, $\theta(t)$ is the *Heavyside* step function, $f_{step}$ (approximately 0.09) is the fraction

$$f_{step} = \frac{r_0}{r_0 + \frac{R_0}{2}} \tag{5.9}$$

and $\tau_{cali}$ is the effective exponential decay constant (which value is approximately 400 ns)

$$\tau_{cali} = \frac{L_0}{r_0 + \frac{R_0}{2}} \tag{5.10}$$

Similarly to the the ionization physics signal, the calibration signal at the output of the readout chain can be written in the Laplace frequency domain as:

$$g^{cali}(s) = I_{inj}^{cali}(s) H^{detcali}(s) H^{readout}(s) \tag{5.11}$$

where

- $H^{detcali}(s)$ is the detector part of the electronics circuit as seen by the calibration injection signal;
- $I_{inj}^{cali}(s)$ is the Laplace transform of the calibration injection signal (Equation 5.8), namely:

$$I_{inj}^{cali}(s) = I_0^{cali} \left( \frac{\tau_{cali}(1 - f_{step})}{1 + \tau_{cali} s} + \frac{f_{step}}{s} \right) \tag{5.12}$$

Dividing $g^{phys}(s)$ and $g^{cali}(s)$ the common part $H^{readout}(s)$ cancels out and we obtain:

$$\frac{g^{phys}(s)}{g^{cali}(s)} = \frac{I_0^{phys}}{I_0^{cali}} \frac{H^{det}(s)}{H^{detcali}(s)} \tag{5.13}$$

Hence, the physics signal or physics pulse shape can be obtain from the calibration pulse shape through the following expression in the Laplace frequency domain:

$$g^{phys}(s) = g^{cali}(s) \frac{I_{inj}^{phys}(s)}{I_{inj}^{cali}(s)} \frac{H^{det}(s)}{H^{detcali}(s)} \tag{5.14}$$

Or in the time domain as:

$$g^{phys}(t) = \left[ g^{cali} * \mathcal{L}^{-1} \left( \frac{I_{inj}^{phys}(s)}{I_{inj}^{cali}(s)} \right) * \mathcal{L}^{-1} \left( \frac{H^{det}(s)}{H^{detcali}(s)} \right) \right] (t) \tag{5.15}$$

where $*$ means convolution integral.

The second and third factors in the convolution take into account the differences in the injection signal and injection point respectively between the physics and the calibration signals.

### 5.2.1 Computation of $g^{phys}$

For computational purposes the Equation 5.15 can be written as:

$$\begin{aligned} g^{phys}(t) &= \left[ g^{cali} * \mathcal{L}^{-1} \left( \frac{(1+s\tau_{cali})(sT_{drift}-1+e^{-sT_{drift}})}{sT_{drift}(f_{step}+s\tau_{cali})} \right) * \mathcal{L}^{-1} \left( \frac{1}{1+s^2LC+sRC} \right) \right](t) \\ &= \left[ g^{cali} * g^{exp\to tri} * g^{MB\to det} \right](t) \end{aligned} \tag{5.16}$$

where the two different time-domain convolutions are:

$$\begin{aligned} g^{exp\to tri}(t) &= \delta(t) + \left[ \frac{1-f_{step}}{\tau_{cali}} e^{-f_{step}\frac{t}{\tau_{cali}}} - \frac{1-f_{step}}{f_{step}} \left( e^{-f_{step}\frac{t}{\tau_{cali}}} - 1 \right) \right] \theta(t) \\ &\quad + \frac{1-f_{step}}{f_{step}} \left( e^{-f_{step}\frac{t-T_{drift}}{\tau_{cali}}} \right) \theta(t-T_d) \end{aligned}$$

$$g^{MB\to det}(t) = \frac{2}{\tau_a} e^{(\tau_r/(2\tau_0^2))t} \theta(t) \tag{5.17}$$

where $\tau_r = RC$ and $\tau_0 = LC$.

The procedure requires the knowledge of the calibration pulse $g^{cali}$ (see Chapter 4) and of a set of five parameters, namely two related to the calibration board, $\tau_{cali}$ and $f_{step}$, two related to the cell electrical properties, $\tau_0$ and $\tau_r$, and one related to the ionization, $T_{drift}$. Their values may depend on the detector conditions, temperature, radiation dose, etc., hence it is important to monitor them on a regular basis. The parameter $T_{drift}$ has been measured with cosmic data (see Chapter 6), while the other four parameters can be extracted either from direct measurements or from the calibration pulse using the algorithm called Response Transformation Method (RTM).

## 5.3 Response Transformation Method

The RTM method was developed by the Milan Atlas group to be applied to the barrel EM calorimeter [37]. It has subsequently been adapted for the endcap EM calorimeter and tested with cosmic muon data [39].

The response to a calibration injection pulse can be written in the Laplace frequency domain as given in Equation 5.11. Let a generic current pulse $Y_{inj}(s)$ be injected on the system at the Mother Board level, as it is actually done with the real calibration pulse $I_{inj}^{cali}(s)$. The response $W_{out}(s)$ of the system to this signal would be:

$$\begin{aligned} W_{out}(s) &= Y_{inj}(s)\, H^{detcali}(s)\, H^{readout}(s) = \\ &= \frac{Y_{inj}(s)}{I_{inj}^{cali}(s)}\, I_{inj}^{cali}(s)\, H^{detcali}(s)\, H^{readout}(s) = \frac{Y_{inj}(s)}{I_{inj}^{cali}(s)}\, g^{cali}(s) \end{aligned} \tag{5.18}$$

or, in the time domain:

$$W_{out}(t) = \left[ g^{cali} * \mathcal{L}^{-1} \left( \frac{Y_{inj}(s)}{I_{inj}^{cali}(s)} \right) \right] (t) \tag{5.19}$$

The dependence on the circuit parameters has cancels out and only remains the ratio between the different injection functions.

The RTM bases its strategy to retrieve parameters on the computation and analysis of what would be the response to a signal different from the "exponential" calibration injection signal. The system response can in fact be sensitive to a particular injected waveform, the output showing in some cases easily recognizable characteristics. In the following steps, waveforms will be sought that minimize the signal tail of $W_{out}(t)$. For this purpose, a $\chi^2$-like quantity is built by summing the squares of the values of $W_{out}(t)$ along the tail, that is:

$$Q^2 = \sum_{t > t_{tail}} W_{out}^2(t) \tag{5.20}$$

the tail being defined as the signal portion after the time $t_{tail}$.

In particular, to obtain the calibration board parameters, $\tau_{cali}$ and $f_{step}$, a step function will be chosen for $Y_{inj}(t)$, and to extract $\tau_0$ a cosine function for $Y_{inj}(t)$ is more suitable.

### 5.3.1 Extraction of the calibration boards parameters: $\tau_{cali}$ and $f_{step}$

To obtain the calibration pulse parameters $\tau_{cali}$ and $f_{step}$ a Heaviside step function, $Y_{inj}(t) = \theta(t)$, is used with unit amplitude. The Laplace transform of the step function is $Y_{inj}(s) = 1/s$. On the other hand, the expression for $I_{inj}^{cali}(s)$ of Equation 5.12 can be written, for unit amplitude ($I_0^{cali} = 1$), as:

$$I_{inj}^{cali}(s) = \frac{\tau'_{cali} s + f'_{step}}{s(1 + \tau'_{cali} s)} \tag{5.21}$$

Hence, the ratio between both injection signals is:

$$\frac{Y_{inj}(s)}{I_{inj}^{cali}(s)} = \frac{1 + s\tau'_{cali}}{s\tau'_{cali} + f'_{step}} \tag{5.22}$$

and $W_{out}$ can be obtained as:

$$W_{out}(s) = \frac{1 + s\tau'_{cali}}{s\tau'_{cali} + f'_{step}} g^{cali}(s) \tag{5.23}$$

It can be shown that, for the correct values $\tau'_{cali} = \tau_{cali}$ and $f'_{step} = f_{step}$ of the calibration board parameters, $W_{out}(t)$ has the property of going to zero in the tail very rapidly. This is due to the fact that both $H^{det}$ and $H^{readout}$ functions contain only short time constants, hence $W_{out}(s) = Y_{inj}(s)\, H^{detcali}(s)\, H^{readout}(s)$ cannot have a long tail in the time domain.

This null-tail property of the step-response can be used to determine both calibration board parameters $\tau_{cali}$ and $f_{step}$ by minimizing the following quantity:

$$Q^2(\tau'_{cali}; f'_{step}) = \sum_{t>t_{tail}} W^2_{out}(t; \tau'_{cali}; f'_{step}) \tag{5.24}$$

The minimization procedure may in principle depend on the tail starting point value $t_{tail}$. A robust choice of $t_{tail}$ is given by $t_{tail} = t_{min} + 100$ ns, where $t_{min}$ is the minimum of the negative lobe of the shaped signal [2]. Using this criterion the systematic uncertainty introduced by $t_{tail}$ in the RTM procedure is small. The RTM values are in a good agreement (at the 5% level) with the values extracted from measurements in the production laboratories [40].

Figure 5.5 shows $\tau_{cali}$ (a) and $f_{step}$ (b) versus $\eta$ extracted with RTM method for every cell of the EM calorimeter in layer 2. The average value for $\tau_{cali}$ is 399.5 and $f_{step}$ is 0.089 in the outer wheel. From the dispersion of those scatter plot, an estimate of the uncertainty in the determination of $\tau_{cali}$ and $f_{step}$ can be inferred, namely 3% and 5%, respectively.

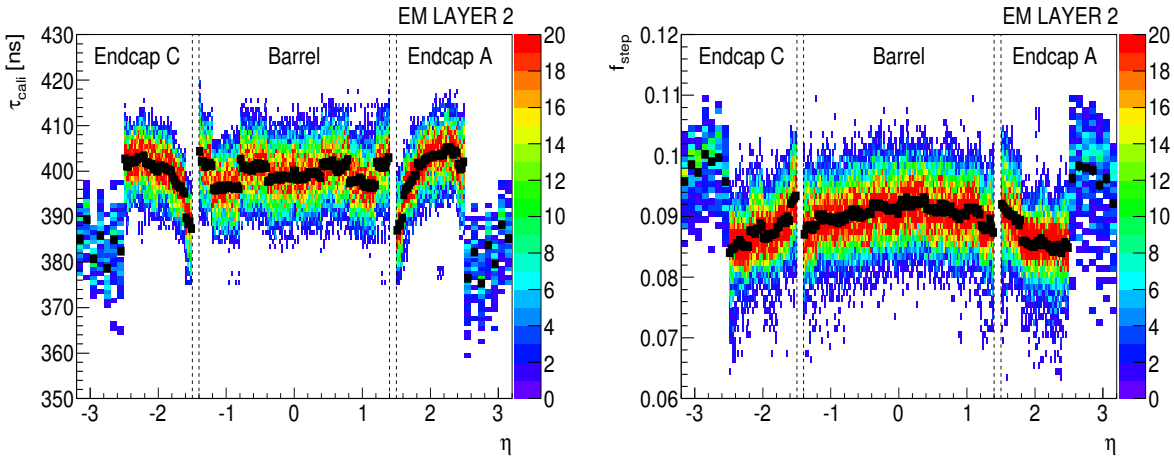


(a) $\tau_{cali}$ (b) $f_{step}$

Figure 5.5: Calibration board parameters ($\tau_{cali}$ (a) and $f_{step}$ (b)) as a function of $\eta$ in layer 2 of the EM calorimeter and in high gain.

### 5.3.2 Extraction of the detector parameters: $\tau_0$ and $\tau_r$

To extract $\tau_0$, or equivalently $\omega_0 = 1/\sqrt{\tau_0}$, the response to a monochromatic cosine pulse $Y_{inj}(t) = \theta(t)cos(\omega t)$ is studied, which, in the Laplace frequency domain, has the form:

$$Y_{inj}(s) = \frac{s}{s^2 + \omega^2} \tag{5.25}$$

[2] One can look at Figure 5.1 to see the negative lobe of the shape signal, although the pulse shape corresponds to a ionization signal instead of a calibration step function

The ratio between both "cosine-type" and calibration injection signals is:

$$\frac{Y_{inj}(s)}{I_{inj}^{cali}(s)} == \frac{s}{s^2+\omega^2}\frac{s(1+s\tau_{cali})}{s\tau_{cali}+f_{step}} \tag{5.26}$$

and $W_{out}$ can be obtained as:

$$W_{out}(s) = \frac{s}{s^2+\omega^2}\frac{s(1+s\tau_{cali})}{s\tau_{cali}+f_{step}}g^{cali}(s) \tag{5.27}$$

It turns out that the smallest amplitude for this function is obtained when $\omega = \omega_0$, hence this parameter is obtain by minimizing the following quantity:

$$Q^2(\omega) = \sum_{t>t_{tail}} W_{out}^2(t;\omega) \times \frac{(1+(\omega\tau_{sh})^2)^3}{(\omega\tau_{sh})^2} \tag{5.28}$$

where the last term introduces a shaper correction in this case, due to the fact that the shaper acts as a band-pass filter suppressing the high frequency components of the injected signals.

Finally the parameter $\tau_r$ can be extracted by injecting $Y_{inj} = I_{inj}^{cali}$, however at the physics injection point. This introduces a correction factor in the output signal, which depends on $\tau_r'$ as follows:

$$\frac{1}{1+s\tau_r'+s^2\tau_0'} \tag{5.29}$$

Hence,

$$W_{out}(s) = \frac{1}{1+s\tau_r'+s^2\tau_0'}g^{cali}(s) \tag{5.30}$$

If $\tau_0' \neq \tau_0$ or $\tau_r' \neq \tau_r$ the function $W_{out}(t)$ will have an oscillating behavior on the tail. We can assume that $\tau_0$ has been obtained before by the RTM method, as described in previous subsection, or by direct measurements. Hence, the quantity to minimize in order to obtain $\tau_r$ is defined as:

$$Q^2(\tau_r') = \sum_{t>t_tail} (W_{out}(t;\tau_r') - g^{cali}(t))^2 \tag{5.31}$$

Figure 5.6 shows $\omega_0$ and $\tau_r$ as a function of $\eta$ for layer 2. The values of both parameters are changed with pseudorapidity because of the capacitance variation. The dispersion of the $\omega_0$ values along azimuth $\phi$ can be considered an estimate of the parameter uncertainty, which turns at to be about 3%. The parameter $\tau_r$ includes a small resistance and other effects not included in the electronic model, hence it can be considered as an effective parameter. Its influence in the final result is a second order effect. Therefore, the dispersion of $\tau_r$ is not a concern.

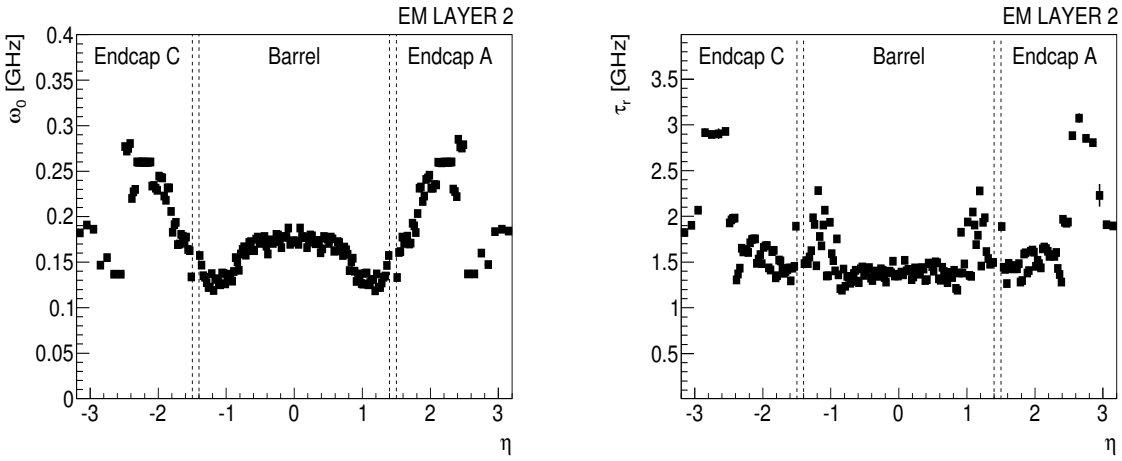


(a) $w_0$ (b) $\tau_r$

Figure 5.6: Cell resonance frequency $\omega_0$ (a) and $\tau_r$ extracted with RTM as a function of $\eta$ for layer 2 cells of the EM calorimeter. All points have been averaged over $\phi$.

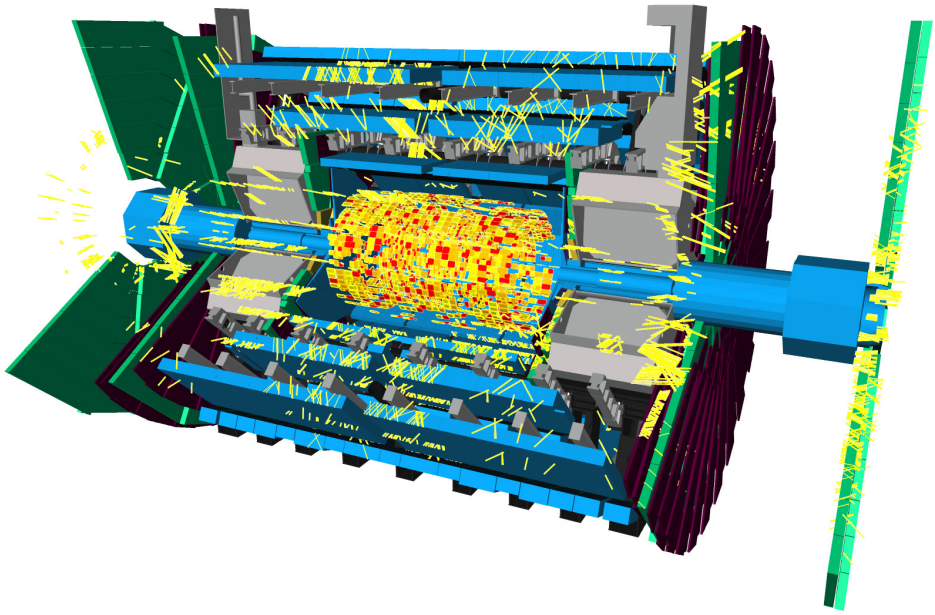

Figure 5.7: Atlantis display with a Splash event in the ATLAS experiment. Beam was initially directed at beam collimators just outside the detector, so that a splash of particles hit every cell of the detectors.

## 5.4 Validation of the signal reconstruction method

In September 2008, single beam circulated in the LHC for the first time. The presence of collimators 200 meters before ATLAS illuminated the detector with a particle flow which hit every channel of the calorimeter and depositing few PeV of energy in it. Figure 5.7 is an Atlantis display with a splash of particles later called **beam splash** on 10 September 2008.

In parallel with a stable and smooth running of the electronic calibration system, the detailed check of the signal reconstruction in each cell of the EM calorimeter is mandatory. The beam splash data have been used to perform a systematic and quantitative comparison between data and predicted physics pulse shapes (see Section 5.2) in the electromagnetic calorimeter (see Chapter 4). There is a clear benefit from the use of beam splash data with respect to cosmic data, namely the much higher number of events collected per run with sufficient energy for analysis.

In this section a procedure to check the quality of the signal reconstruction is performed by comparing the data samples recorded in each cell (25 ns step) with the predicted physics pulse shape. The method was already proven to be very useful to test the signal reconstruction with cosmic data [39, 41].

### 5.4.1 Beam splash data selection

On 10th of September 2008, first LHC beam circulated in ATLAS. Collimators, located in the beam pipe 200 meters in straight line from the ATLAS interaction point, were used to dump the beam. This produced a cascade of pions and muons, generating pulses in almost every cell of the EM calorimeter at the same time. The energy spectrum of the incoming particles is unknown but the flux of particle is so dense that the energy recorded per cell reflects roughly the volume of the cell. To perform a coherent analysis of the signal reconstruction over the whole coverage of the EM Calorimeter, a selection described in this section is applied.

A simple and robust beam-related trigger called BPTX is chosen in this analysis. The information about BPTX trigger can be found in Section 3.2.4.1. Only one run (86 events with 26 real beam splash events arriving from the C-side, $z < 0$) with stable enough data taking conditions is used afterwards. Integrating over all events, an approximate energy of 20 PeV is deposited almost uniformly in the EM calorimeter.

From this data period, EM calorimeter is functioning in a standard running mode:

- The nominal high voltage is applied everywhere (see Figure 4.8) except for 1% of cells with lower high voltage in the barrel.
- All the front–end boards (FEBs) are functioning except four of them (512 cells), which represents 0.3% of the total number of cells.

For each cell, 5 samples in ADC counts are recorded in free gain mode. Offline, optimal filtering coefficients (OFC), computed by step of 3.125 ns (see Section 5.1), are applied to the samples to calculate the maximum amplitude ($A_{max}$) in ADC counts, whenever the iterative procedure to find the correct OFC set is successful ($|\Delta t| < 3.125$ ns). Failing cases are mainly

due to a badly adjusted latency. When this happens, the sample with the highest amplitude is located in the first or fifth sample, preventing the iterative procedure to converge. Such cases are removed from our analysis. Finally, the maximum amplitude is converted in energy by applying a factor

$$E[GeV] = F(ADC-MeV) \times A_{max} \tag{5.32}$$

which includes details of the electronic chain, the sampling fraction and the absolute energy scale [42],

$$F(ADC-MeV) = f_{\mu A \to GeV}\ f_{DAC \to \mu A}\ \frac{M_{cali}}{M_{phys}}\ g_{ADC \to DAC} \tag{5.33}$$

The variation of $F(ADC-MeV)$ as a function of the layer and $\eta$ is illustrated in Figure 5.8 for high gain.

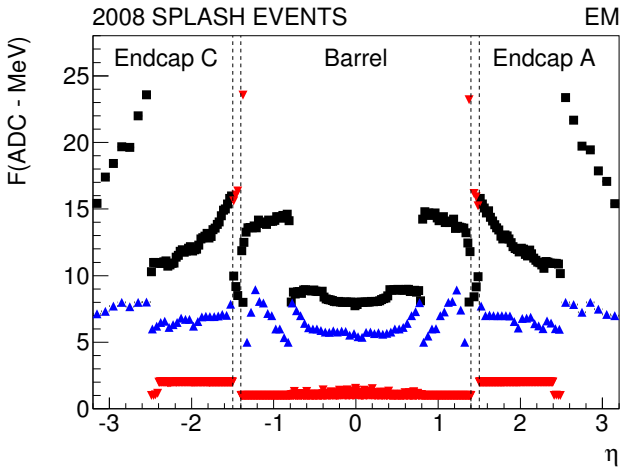


Figure 5.8: ADC to MeV conversion factor, $F(ADC-MeV)$, as a function of $\eta$ for front (red down triangles), middle (black squares) and back (blue up triangles) cells. All points have been averaged over $\phi$.

#### 5.4.1.1 Cell selection

The ATLAS "precision" region is defined by the inner detector coverage, $|\eta| < 2.5$. For completeness, we extend our study up to the EM calorimeter inner wheel acceptance, $2.5 < |\eta| < 3.2$. Cells from the region $1.4 < \eta < 1.5$ are removed in the following because the sample with the highest amplitude in the A-side data signals is located in the fifth sample, preventing the iterative procedure to converge. Although in the C-side the situation is different, the region $-1.4 < \eta < -1.5$ is not considered in the analysis for consistency.

To minimize the fluctuations in the signal reconstruction, the energy deposited per cell should be well above the noise. In a first step of the analysis, a lower energy cut is required,

$E > 500$ MeV. Finally, to decorrelate and understand the biases of the signal reconstruction from other effects, like abnormal noise level or uncorrect cell characteristics (abnormal cell capacitance or inductance, ...), an official list of "problematic" cells is established in the EM calorimeter (see Appendix A). It represents about 600 pulses in total, i.e. few per mill of the total number of hits. These pulses are rejected from the analysis.

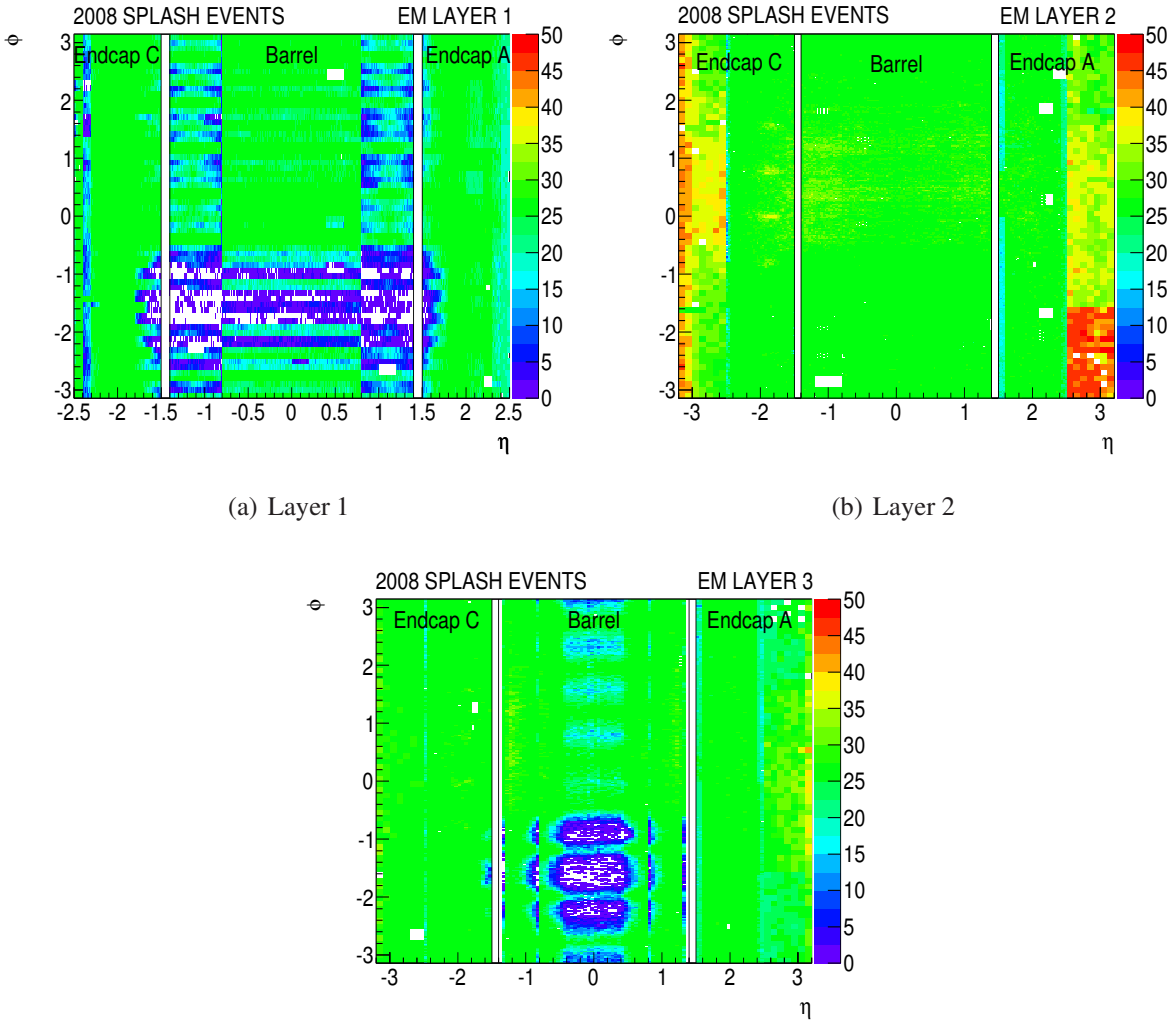


(a) Layer 1

(b) Layer 2

(c) Layer 3

Figure 5.9: $\eta - \phi$ map (1 bin = 1 cell) of hits in layer 1 (a), layer 2 (b) and layer 3 (c) after all selection criteria.

Table 5.1 shows the number of cells, hit at least once in the chosen run, after each step of the selection. All cells but 1(6)% are selected in layer 2 and 3 (layer 1). As one cell can be hit several times, it is also interesting to look at the $\eta - \phi$ map of those cells. Figure 5.9 shows that almost every functioning middle cells have recorded at least 26 pulses with energy larger than 500 MeV, corresponding to the number of beam splash events (Section 5.4.1). This is also true in layer 1 and 3 providing a total of 3.5 millions of data pulse shapes for the analysis. However

some regions of front and back [3] are less populated in the barrel because of the $\phi$-asymmetry of the LHC tunnel installation : particles coming downwards encountered more material than upwards. The eight-fold structure also visible in $\phi$ is due to the eight-fold structure of the endcap toroid material.

| Layer | Layer 1 | Layer 2 | Layer 3 | All |
|---|---|---|---|---|
| Total | 86400 | 52608 | 24960 | 163968 |
| + remove $1.4 < \|\eta\| < 1.5$ | 84352 | 50048 | 24960 | 159360 |
| Total functioning | 83968 | 49920 | 24960 | 158848 |
| + $\|\Delta t\| < 3.125$ ns | 78995 (94.1%) | 49907 (100%) | 24627 (98.7%) | 153529 (96.7%) |
| + E> 500 MeV | | | | |
| + Bad channels cut | 78762 (93.8%) | 49545 (99.2%) | 24564 (98.4%) | 152871 (96.2%) |

Table 5.1: Number of hit cells per layer of the EM calorimeter after the different selection criteria. The percentages in brackets correspond to the number of selected cells compared to the number of functioning cells.

It is also interesting to look at the energy distribution of the selected hits. This is shown in Figure 5.10 for the three layers of the barrel ( 5.10(a)) and of the endcap ( 5.10(b)). The energy deposited by the particle flow is proportional to the cell volume, explaining the higher energy in layer 2 compared to layer 3 and 1. It should be noticed that in more than 99% of the selected shapes, the energy range corresponds to the high gain mode.

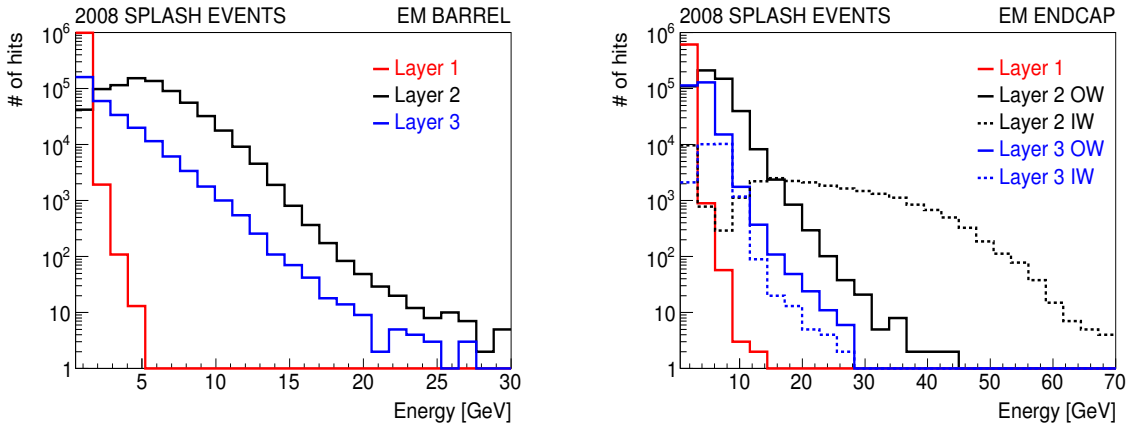


(a) Barrel

(b) Endcap

Figure 5.10: Energy distribution of selected hits in the barrel (a) and in the endcaps (b) of the EM calorimeter. Layer 1, 2 and 3 cells are represented with full red, black and blue lines, and inner wheels with dashed lines.

[3] This is also true in layer 2, but only visible when cutting at higher energies.

### 5.4.2 Matching data and predicted physics pulses

Compared to a normal LHC running, the pulses recorded in beam splash events are not correctly timed, i.e. the maximum of the pulse is almost never located in the third sample. This is mainly because the particles come asynchronously from a flow parallel to the LHC beam and not from the interaction point. Moreover, as it was the first run, the FEB timing was not adjusted over the whole calorimeter acceptance. The timing of the EM calorimeter in run analyzed is illustrated in Figure 5.11 which shows the sample with highest amplitude averaged over each FEB. It is in general on the second sample for side C ($z < 0$) and the fourth sample for side A ($z > 0$), but other situations can also occur.

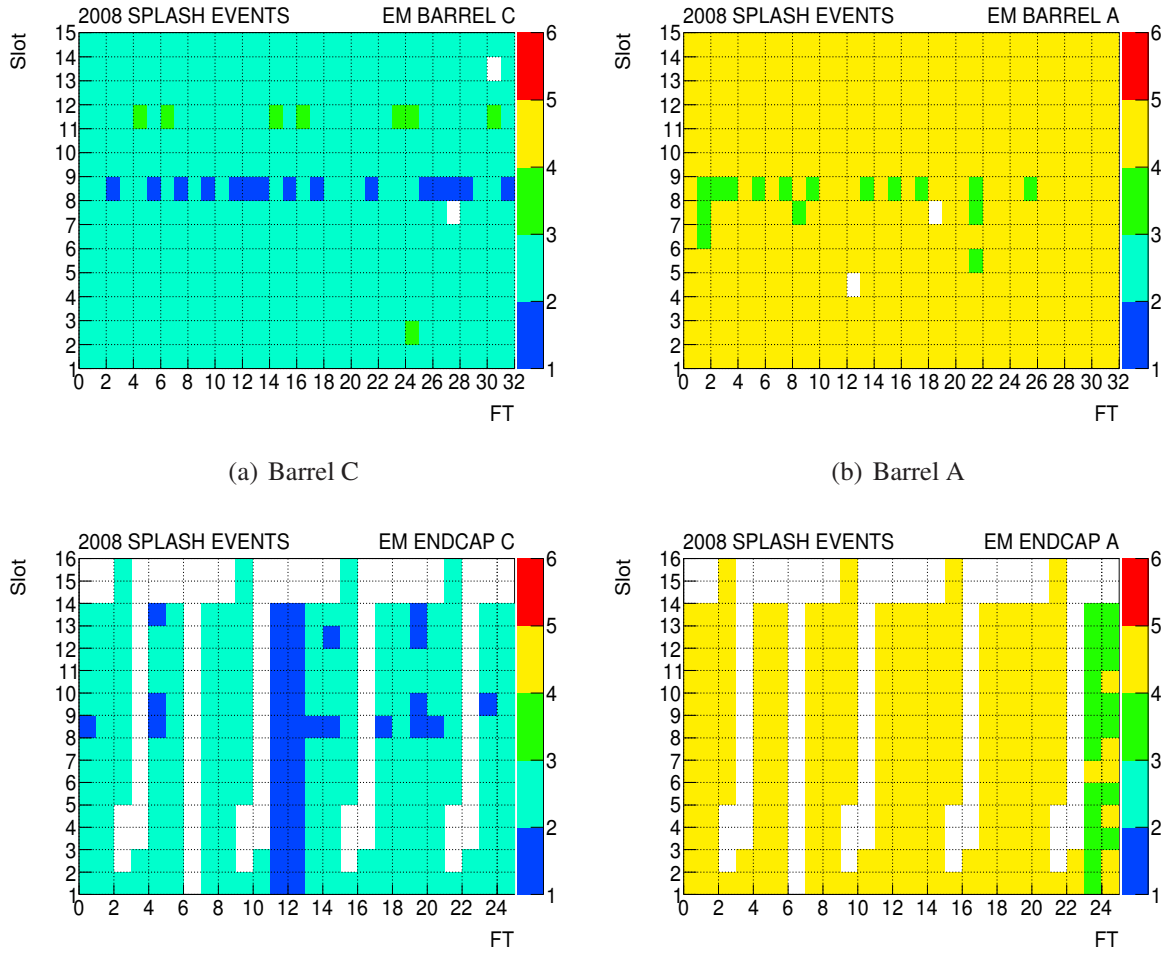


(a) Barrel C

(b) Barrel A

(c) Endcap C

(d) Endcap A

Figure 5.11: Sample with highest amplitude averaged over each FEB denoted with its Slot-FT location in the barrel C (a), barrel A (b), endcap C (c) and endcap A (d). The 5 samples from data are labeled from 1 to 5.

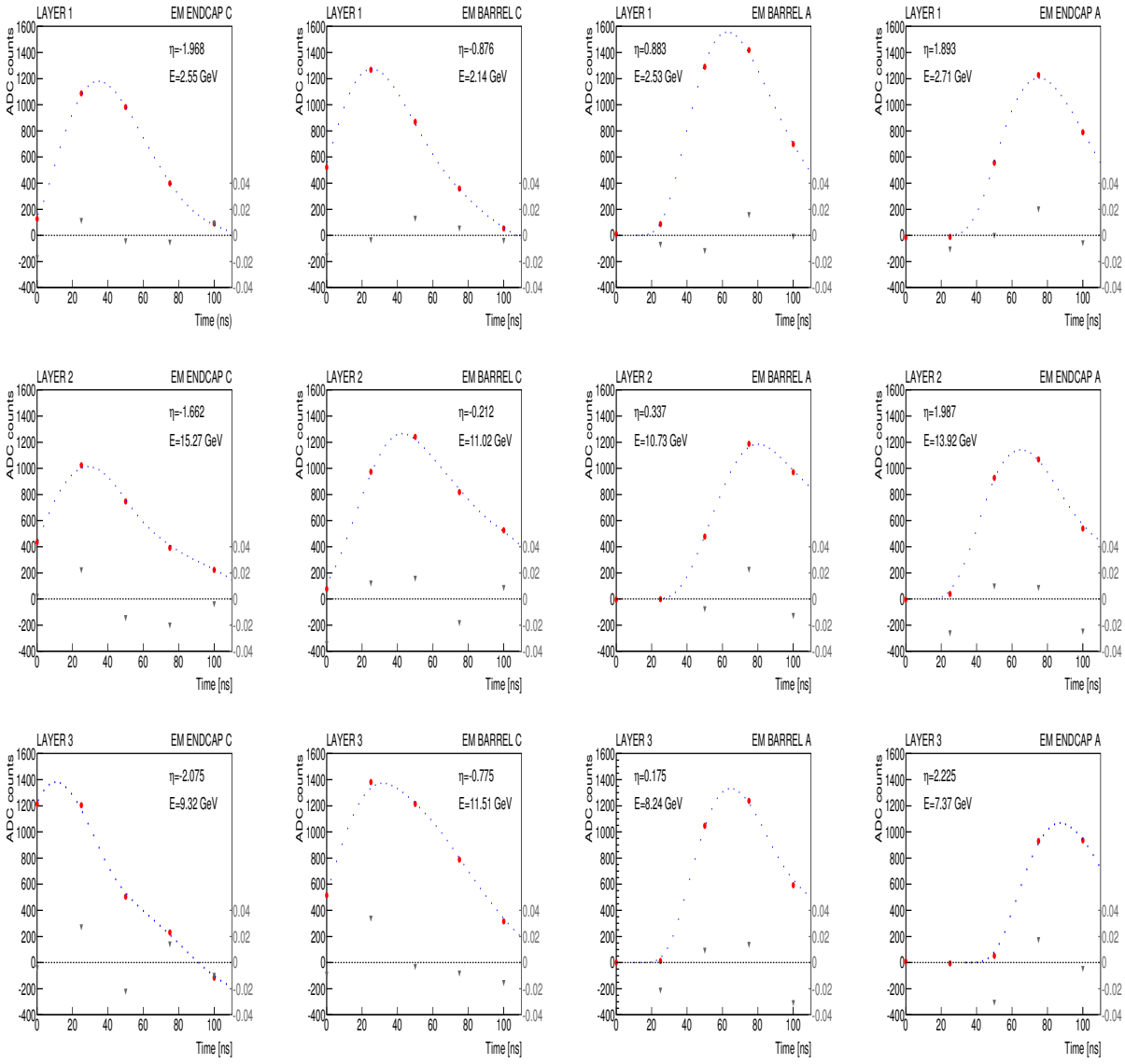


Figure 5.12: Typical cell response (5 red samples in ADC counts) in high gain to high energy deposits in the endcap C (left), barrel C (middle left), barrel A (middle right) and endcap A (right) for layers 1, 2 and 3 from top to bottom. The blue squares correspond to the predicted pulse shapes using 40 samples computed by step of 3.125 ns. The gray triangles, with the scale on the right, are the residuals, i.e. (data-prediction) normalized to the maximum amplitude. The $Q^2$-estimator is around 1 for all these cells. $Q^2$ is defined in Equation (5.34), where $k = 1\%$, 1.5% and 2% is used for layer 1, 2 and 3, respectively.

Because of the complex situation of the beam splash run, a dedicated method to match data and prediction is set-up. First, the predicted physics pulse shape (normalized to one) is multiplied by the maximum amplitude $A_{max}$ computed for each cell using the OFC. To cope with the timing situation, a global time adjustment between data and prediction is first performed by 25 ns steps through a simple $\chi^2$ minimization. This is then refined by using the OFC computation for the timing. Because of the 3.125 ns step between each point of the predicted shape, a linear interpolation is performed between predicted points closest to the data to compute the prediction at the data time phase.

Figure 5.12 shows typical physics shapes for each sampling (front, middle and back from top to bottom) in the barrel (center) and in the endcaps (sides). In all cases, the predictions agree qualitatively nicely with the data. The residuals, defined as (data-prediction) normalized to the maximum amplitude, are indicated with gray open circles, with the scale on the right of the plot. They are all contained within the $\pm 2\%$ (resp. $\pm 3.5\%$) band for layer 1 and 2 (resp. layer 3).

As only three significant samples are recorded in the A side (the two first samples are in the pedestal), quantitative comparisons between data and predicted shapes are based on the three highest samples for both A and C sides, to keep the same procedure in both.

### 5.4.3 Quality of the signal reconstruction

The distance between the predicted and the data pulse shapes can be estimated by the following quantity, which is a measure of the signal reconstruction quality:

$$Q^2 = \frac{Q'^2}{N_{dof}} = \frac{1}{N_{dof}} \sum_{i=1}^{N_{samples}} \frac{\left(S_i - A_{max} * g_i^{phys}\right)^2}{\sigma_{noise}^2 + (k * A_{max})^2} \tag{5.34}$$

where:

- $N_{samples} = 3$ is the number of samples used to estimate the quality of the pulse shape prediction as defined in Section 5.4.2.
- $S_i$ is the amplitude of each sample $i$.
- $A_{max}$ is the maximum amplitude calculated from the OFC (see Equation 5.2).
- $g_i^{phys}$ is the normalized predicted ionization shape.
- $\sigma_{noise}$ is the noise for a single sample in ADC counts (see Figure 5.2).
- $k$ is an effective parameter reflecting mainly the relative accuracy of the amplitude $A_{max}$, linked to the pulse shape residuals. The parameter $k$ is chosen such that $Q^2$ is independent of $A_{max}$ and close to one, as seen in Figure 5.13 for layer 2 of the barrel. The values chosen in a first iteration are 1%, 1.5% and 2% for layer 1, 2 and 3, respectively.
- $N_{dof} = 3$ is the number of degrees of freedom.

The $Q^2$ denominator reflects the numerator uncertainty : it is the quadratic sum of the data amplitude uncertainty (noise term) and of the predicted amplitude uncertainty. To extract stable results, the preferred situation correspond to $kA_{max} > \sigma_{noise}$, i.e. when the noise fluctuation for each sample is negligible compared to the uncertainty on the pulse shape prediction. This regime is guaranteed by requiring $A_{max} > 500$ ADC counts (high gain). This new selection cut reduces the statistics by a factor about 3, which means 1.1 millions of pulse shapes in the final sample.

After this selection, $Q^2 \sim p_0$ can be interpreted as a pulse shape prediction at the $k\sqrt{p_0}$ level. For example, in layer 2 of the Barrel $p_0 \sim 1.4$, hence the accuracy in the signal shape is $1.5\sqrt{1.4} = 1.8\%$.

It has been checked that the variable $Q^2$ follows a normalized $\chi^2$ distribution when rescaling $k$ to the level of accuracy. Figure 5.14 shows an example for layer 2 of the barrel where $k$ has been rescaled to $k = 1.8\%$. The distribution corresponds to $Q'^2$ instead of $Q^2$. The $\chi^2$ probability density function corresponding to three degrees of freedom agrees very well with the $Q'^2$ distribution.

Figure 5.15 shows the $Q^2$-estimator as a function of $\eta$ over the whole calorimeter acceptance, for the three layers of the EM calorimeter. The value of the $Q^2$-estimator is around 1 for central $\eta$ regions of every layer and it increases at high $|\eta|$ values reflecting the larger difficulty to describe the data pulses. The variation over $\eta$, excluding regions around cracks, is at most a factor 4 in some endcap regions. This means that the quality of the prediction is at most degraded by $\sqrt{4}$ in these regions. This is a proof of the quality of the ATLAS signal reconstruction in the endcaps, despite its challenging aspect.

The quality factor $Q^2$ can be used to detect bad behaved channels. Figure 5.16 shows the $Q^2$-estimator (colors) as a function of $(\eta, \phi)$. Blank regions means no event has hit those cells with a deposit above 500 ADC units. The red color indicate a high $Q^2$ value. For example, in layer 2 of the Barrel red spots are seen specially around $\eta = 1$. They corresponds to $Q^2 > 5.5$. The re-scaled value corresponding to a normalized $\chi^2$ distribution is $Q^2_{norm} > 5.5/1.4 \sim 3.9$. The probability to obtain such values is:

$$\int_{3.9}^{\infty} \chi^2(x)dx \sim 0.05 \tag{5.35}$$

Hence, the hypothesis that those are well-behaved channels is rejected at the 5% significant level.

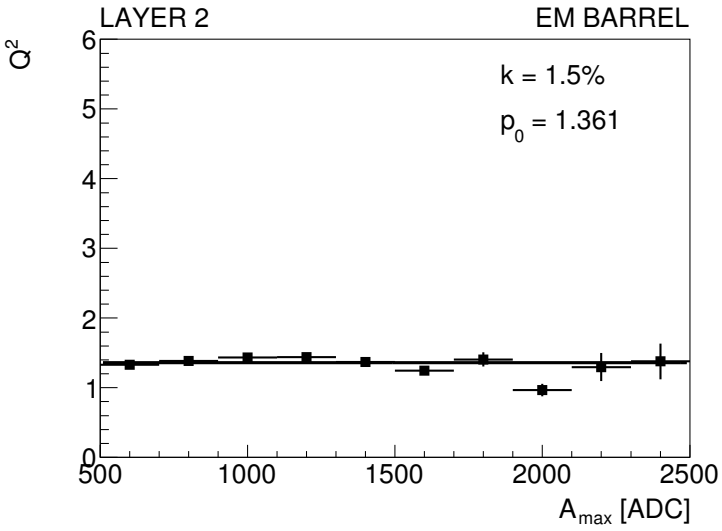


Figure 5.13: $Q^2$ as a function of the maximum amplitude ($A_{max} > 500$ ADC counts) for layer 2 of the barrel. $Q^2$ is defined in Equation (5.34), where 1.5% is used for layer 2. The results of a fit with a constant $p_0$ are superimposed.

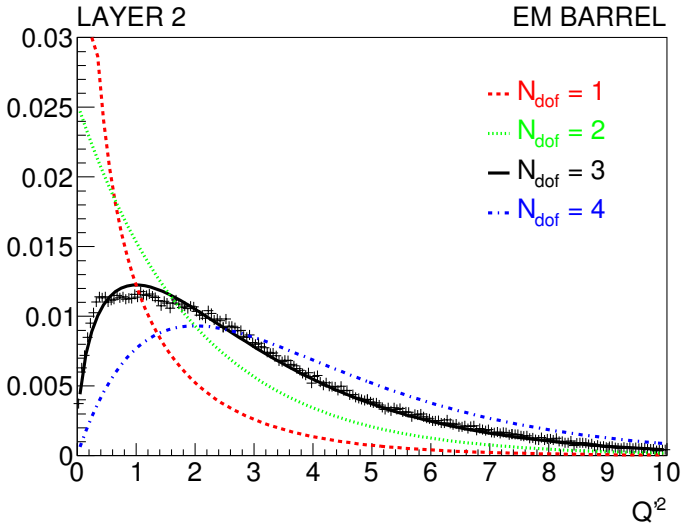


Figure 5.14: Normalized distribution of $Q'^2$ defined in Equation (5.34), using $k = 1.8\%$, for layer 2 cells in $|\eta| < 0.8$. A fit with a $\chi^2$ function is superimposed (full line), resulting in a number of degrees of freedom ($N_{dof}$) around 3. Dotted lines indicate $\chi^2$ functions with $N_{dof}$ fixed to 1, 2 and 4.

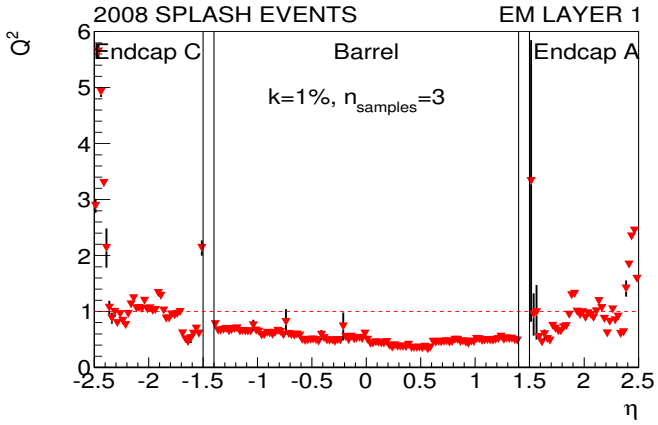


(a) Layer 1

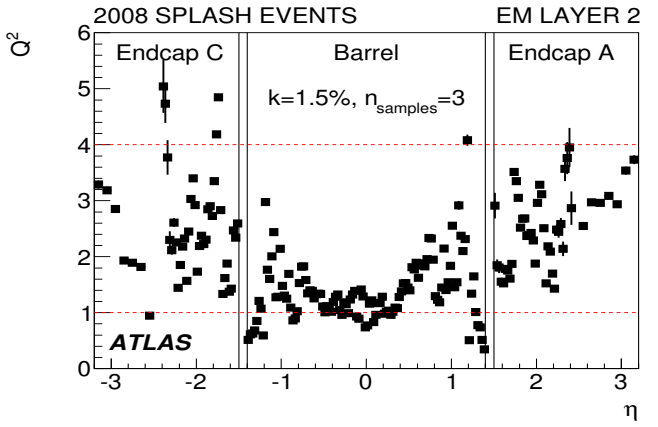


(b) Layer 2

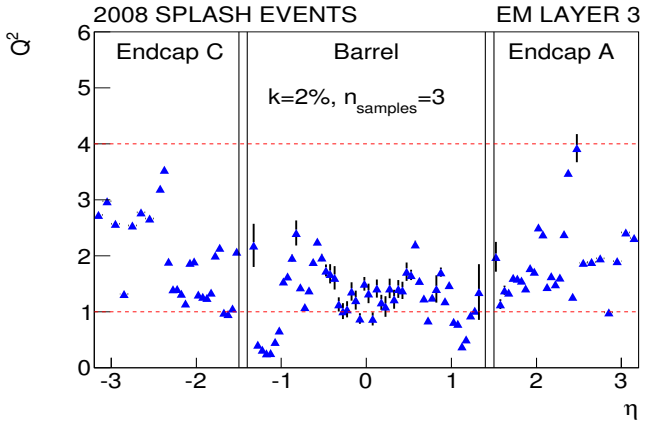


(c) Layer 3

Figure 5.15: Estimator $Q^2$, representing the quality of the physics pulse shape prediction, as a function of $\eta$ for layer 1 (a), 2 (b) and 3 (c). $Q^2$ is defined in Equation (5.34), where $k = 1\%$, 1.5% and 2% is used for layer 1, 2 and 3, respectively. Only cells with $A_{max} > 500$ ADC counts and 3 highest samples in high gain mode are selected. The number of selected hits are 397822 in layer 1, 502294 in layer 2 and 196487 in layer 3.

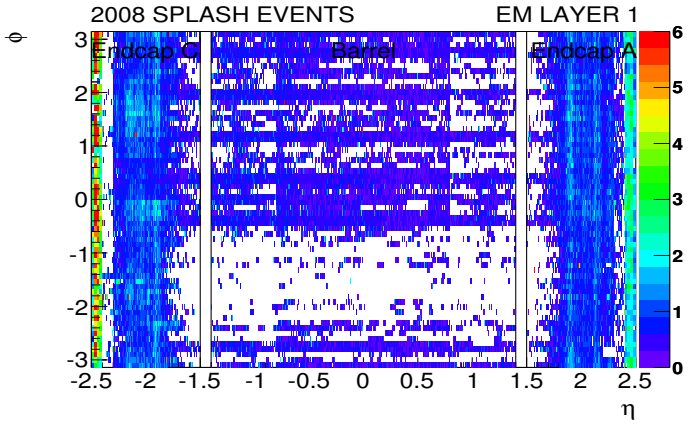


(a) Layer 1

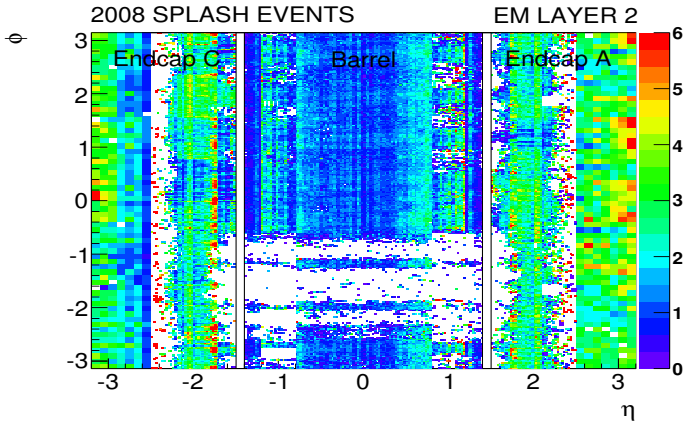


(b) Layer 2

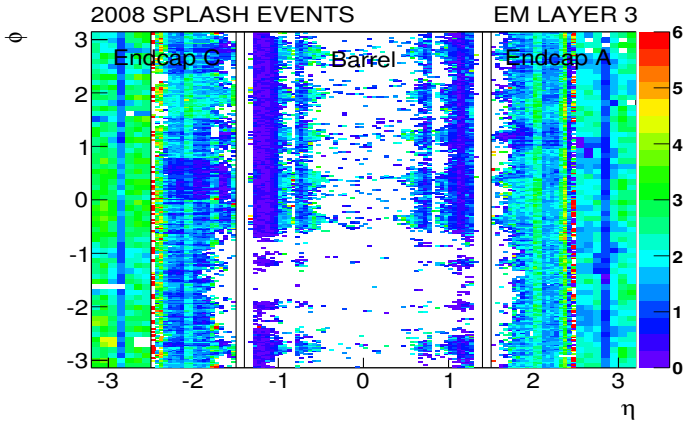


(c) Layer 3

Figure 5.16: η-ϕ maps (1 bin=1 cell) of estimator $Q^2$, representing the quality of the physics pulse shape prediction, in layer 1 (a), 2 (b), 3 (c). $Q^2$ is defined in Equation (5.34), where $k = 1\%$, $1.5\%$ and $2\%$ is used for layer 1, 2 and 3, respectively. Only cells with $A_{max} > 500$ ADC counts and 3 highest samples in high gain mode are selected.

### 5.4.4 Impact of the signal reconstruction on the constant term

It is possible to derive a rough estimate of the impact of the quality of the signal reconstruction on the constant term $c$ of the energy resolution. This constant term was measured around 0.5% for the barrel EM calorimeter using 250 GeV electron beam data on 10% of the modules and about 0.7% for the Endcap using 120 GeV electron beam on three modules [43]. The uncertainty on the signal reconstruction is only one of the contributions to the constant term, which will be labeled as $c_{SR}$ in the following. It has been demonstrated that an uncertainty of $k = 1\%$ in the determination of $A_{max}$ leads to a constant term in the range $0.1\% < c_{SR} < 0.3\%$ [37].

In electromagnetic showers, most of the energy is deposited in layer 2, hence the unknowns of the signal reconstruction in layer 2 dominates the contribution to the constant term, and the other layers will therefore be neglected. As shown in previous section the uncertainty on the signal reconstruction in the barrel layer 2 is about 1.8%. This value corresponds to a constant term in the range $0.2\% < c_{SR} < 0.5\%$. Applying this argumentation for the endcap gives $0.25\% < c_{SR} < 0.7\%$. Both ranges are compatible with test beam results. The slightly worse results obtained in the endcap reflects the greater unknowns on the pulse shape prediction.

## 5.5 Conclusions

The Optimal Filtering procedure used for the ATLAS EM Calorimeter has been described, which converts from digital samples to the maximum amplitude of each channel signal. The method requires the knowledge of the signal shape versus time, which is calculated from the calibration pulse shape using a modeling of the circuit which takes into account the differences between calibration and ionization. The four parameters entering the model, two of the calibration board and two related to the calorimeter cell, are determined using the Response Transform Method (RTM) from the calibration pulse shape. The values of these parameters are compatible with measurements for those cases such measurements exist. The value of the parameters has been studied as a function of pseudorapidity. Their spread along the azimuth ($\phi$) is at the few per cent level.

A first global check of the signal reconstruction quality over the whole EM calorimeter coverage is performed with few tens of events created by the hit of LHC beams on collimators 200 meters before ATLAS. Requesting that the energy deposited per cell is 100 times above the noise allows to select 1.1 millions of signal pulse shapes in high gain mode, covering all the EM calorimeter.

Using this high statistics, a systematic and quantitative $\chi^2$ comparison of data and predictions is performed in the three layers of the EM calorimeter. It was checked that results are independent of the deposited energy. The pulse shape prediction agrees with the data to better than 1% and 2% for the first and second/third compartments of the barrel. Due to a less refined description of the cell electronic chain in the endcaps, the situation is slightly degraded : the agreement is of 1% and better than 3% in first and second/third compartments, respectively. Only regions near the cracks at $|\eta| = 1.4$ and $|\eta| = 2.5$ give worse values. This gives confidence that the energy reconstruction is in good control over the complete calorimeter coverage $|\eta| < 3.2$.

From these results, a rough estimate of the impact of the quality of the signal reconstruction on the constant term of the energy resolution, $c_{sr}$, has been derived : $0.2\% < c_{sr} < 0.5\%$ in the barrel and $0.25\% < c_{sr} < 0.7\%$ in the endcaps. This first estimate can be refined with high energetic electrons during the LHC running, where it can probably be extended to medium gain.

# 6

# Drift time measurements

At the end of the summer and during autumn 2008 stable cosmic muon runs were taken with the detector fully operational and using various trigger menus. The main challenge was to extract the electron drift time in LAr that it is a powerful monitoring tool to measure the asymmetries and intrinsic non-uniformities of the calorimeter. The drift time, $T_{drift}$, can be obtained from the signal pulse shape resulting from ionizing particles that deposit sufficient energy above the intrinsic noise level in a calorimeter cell. In normal data taking only 5 samples around the pulse peak at 25 ns intervals are taken, but in order to accurately measure the drift time 32 samples are needed. The procedure to measure the drift time presented in this chapter can be applied to any type of events: cosmic data, beam splash, beam-beam interactions, since it is essentially based on signal pulse shapes.

In this chapter a measurement of the LAr EMC drift time using 32-samples cosmic data, taken in the period September - November 2008, is presented for the full ATLAS EMC (EMB and EMEC) in its final position. The $T_{drift}$ behavior along both pseudo-rapidity ($\eta$) and azimuth ($\phi$) is studied, as well as the measured values of $V_{drift}$ in the different detector regions.

## 6.1 Ionization signal in the calorimeter

Electrons and photons hitting the detector induce electromagnetic showers (Section 4.1.1). The fraction of the shower energy lost by ionization in the LAr gaps generates the device signal: the ionization electrons drift in the field produced across the LAr gap by the high voltage, generating a current with an amplitude proportional to the released energy. This current is then amplified, shaped, sampled at the LHC bunch-crossing frequency and digitized by the following readout chain [26].

In the straight section of the LAr gaps the ionization current has a typical ionization-chamber triangular shape with a fast rise time less than 1 ns followed by a linear decay for the duration

of the maximum drift time:

$$T_{drift} = \frac{w_{gap}}{V_{drift}}, \tag{6.1}$$

with $w_{gap}$ being the LAr gap width and $V_{drift}$ the electron drift velocity [44]. The ionization current, I, is then modeled as:

$$I(t; I_0, T_{drift}) = I_0 \left(1 - \frac{t}{T_{drift}}\right) \quad \text{for} \quad 0 < t < T_{drift} \tag{6.2}$$

where $I_0$ is the current at $t = 0$. The peak current amplitude,

$$I_0 = \rho V_{drift}, \tag{6.3}$$

is proportional to the drift velocity and the negative linear charge density $\rho$ along the direction perpendicular to the readout electrode. The charge density $\rho$ is proportional to the fraction of the shower energy deposited in the LAr gap: since the determination of this energy is based on the measurement of the current amplitude $I_0$, it is crucial to be able to precisely evaluate and monitor $V_{drift}$. While the LAr gap thickness $w_{gap}$ is in fact mechanically constrained, the drift velocity depends on the actual conditions of the detector; i.e. the LAr temperature and density and the local gap voltage.

For a fixed value of the high-voltage $HV$ applied to a LAr gap, the corresponding $V_{drift}$ depends on the magnitude of the electrical field $E = HV/w_{gap}$ as:

$$V_{drift} \sim V_{ref} \left[\frac{E}{E_0}\right]^{\alpha} = V_{ref} \left[\frac{HV}{HV_0} \cdot \frac{w_{gap0}}{w_{gap}}\right]^{\alpha} \tag{6.4}$$

where $\alpha = 0.3$ [34] (see Section 4.3.4). In this respect, the peak current in a LAr cell is weakly sensitive to a variation of the gap width, since (Equation 6.3):

$$I_0 \sim w_{gap}^{-\alpha} \simeq w_{gap}^{-0.3} \tag{6.5}$$

while the drift time is approximately four times more sensitive (Equation 6.1):

$$T_{drift} \sim w_{gap}^{1+\alpha} \simeq w_{gap}^{1.3} \tag{6.6}$$

The drift time $T_{drift}$ can be directly measured from samples of shaped ionization pulses that have been recorded over the full length of the pulse (see Figure 5.1): the dimension of the positive lobe of the EM calorimeter shaped pulses is in fact sensitive to the readout cell electrical properties, while the tail length reflects the drift time duration. The $T_{drift}$ measurements can be performed by fitting a pulse shape prediction to the physics signal from data containing 32 digitized samples, covering $\sim 800$ ns from the rising pulse edge to the end of the negative lobe. The measurement of $T_{drift}$ can then be used to:

- measure and monitor any variation of $V_{drift}$ with respect to the nominal value, thus keeping under control any change of LAr local temperature and electric field;

- asses the intrinsic uniformity of the calorimeter gaps, which has an impact on the constant term of the energy resolution (Section 4.1.3).
- improve the quality of the ionization pulse predictions, where the measured $T_{drift}$ values enter as an external parameter (Section 5.2), and thus improve the Optimal Filtering Coefficients (Section 5.1) computed from these predictions.

While some 32-sample physics data were recorded during past EMB test-beams, no such long pulses were ever acquired for the EMEC modules. The data collected during the ATLAS commissioning cosmic runs represent therefore the only opportunity to perform such a measurements before the LHC collisions data-taking.

## 6.2 Drift time measurement method

### 6.2.1 Effect of the accordion bend

The ionization current collected by a readout electrode has a main contribution from the straight part of the LAr accordion that can be accurately modeled by a triangle of drift time, as described by Equation 6.2.

However in the bends of the accordion electrodes the gap size and shape are different from the straight part ones, producing a different and varying electrical field. The current of the charge collected in these regions is better modeled by a triangular pulse $I(t;I_{bend},T_{bend})$ with a longer drift time $T_{bend} > T_{drift}$ than in the straight sections (see Section 6.3).

On average the total current seen in a LAr readout cell is then modeled by the superposition of the two triangular pulses, corresponding to the electron drift in the straight and bend regions of the accordion:

$$\begin{aligned} I(t) &= I(t;I_{nom},T_{drift}) + I(t;I_{bend},T_{bend}) \\ &= I_0 \left( f_{nom}\, I(t;1,T_{drift}) + f_{bend}\, I(t;1,T_{bend}) \right) , \end{aligned} \tag{6.7}$$

where $I_0 = I_{nom} + I_{bend}$ is the total current generated in the cell, and the weights $f_{nom} = \frac{I_{nom}}{I_0}$ and $f_{bend} = \frac{I_{bend}}{I_0}$ correspond to the straight and fold regions for the given cell, with $f_{nom} + f_{bend} = 1$.

The superimposition of the two pulses results in a combined pulse which has a triangular form for $t < T_{drift}$ with a drift time $T^{\mathrm{n+b}}_{drift} > T_{drift}$:

$$T^{\mathrm{n+b}}_{drift} = \frac{T_{drift}T_{bend}}{f_{nom}T_{bend} + f_{bend}T_{drift}} , \tag{6.8}$$

followed by the remnant of the longer current pulse in the bend for $T_{drift} < t < T_{bend}$ (see Figure 6.1).

The value of $T_{bend}$ and $f_{bend}$ for the different EMC layers and regions is determined using a Monte Carlo simulation (see Section 6.3), and they are kept fixed in the fitting procedure of the physics pulses (see Section 6.2.3).

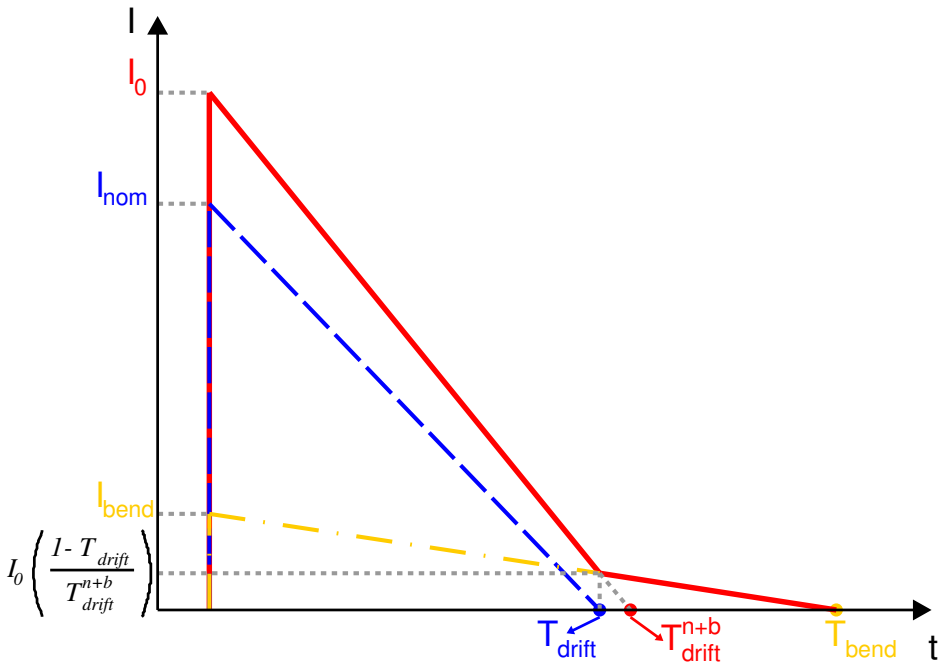


Figure 6.1: Schematic view of the superposition (red) of two triangular pulses of different drift time $T_{drift}$ and $T_{bend}$ (blue), corresponding to the current pulse contributions in the straight and bend regions of the LAr accordion.

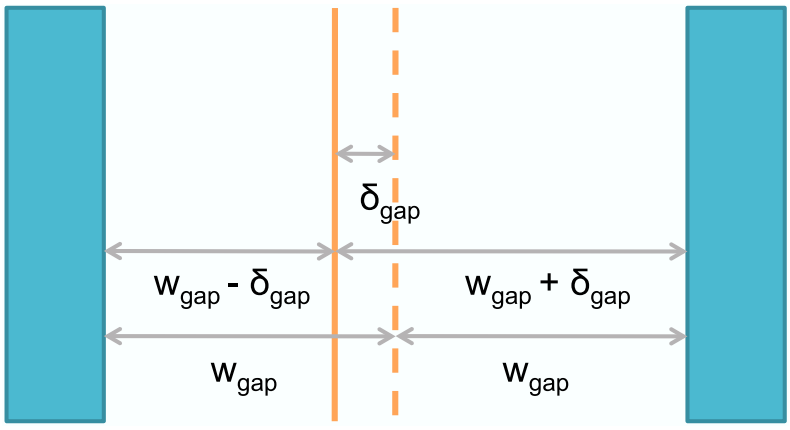


Figure 6.2: Schematic view of a LAr gap. The nominal position of the the readout electrode (dashed) is exactly at the middle in between the lead absorbers. Any shift with respect of the nominal position (solid) implies an increase of the gap width on one side of the electrode, and a decrease on the other side.

### 6.2.2 Effect of a readout electrode shift

Each EMC readout electrode is placed in between two lead absorbers, and has a LAr gap on either side. The ionization electrons drift toward the electrode in opposite directions in the two gaps. With an electrode centered between the absorbers the electron drift in the two gaps would have the same drift time, and then identical pulses.

However it is possible for the readout electrode to be slightly off-centered in the gap. Honeycomb spacers are used to maintain the electrodes centered between the absorbers, but the spacers were in fact sanded to a thickness slightly smaller than the nominal gap size in order to make possible the stacking of the modules, and additionally there is a certain tolerance on their final thickness.

For a shift $\delta_{gap}$ of the electrode position, the gap size is smaller on one side of the electrode, and bigger on the other (Figure 6.2):

$$w_{gap}^{\pm} = w_{gap} \pm \delta_{gap} = w_{gap}(1 \pm x) \tag{6.9}$$

where $x$ measures the shift relative to the gap width. The shift directly produces an asymmetry in the drift times in the gaps of the electrodes (Equation 6.6):

$$T_{drift}^{\pm} = T_{drift}(1 \pm x)^{1+\alpha} \simeq T_{drift}\,(1 \pm (1+\alpha)x) \tag{6.10}$$

and in the peak currents (Equation 6.5):

$$I_{drift}^{\pm} = I_0(1 \pm x)^{-\alpha} \simeq I_0\,(1 \mp \alpha x) \tag{6.11}$$

To take this effect into account, the current produced in the straight part of the accordion is split into two separated triangular contributions of amplitudes $\frac{I_{nom}}{2}\,(1 \mp \alpha x)$, each respectively with an increased (decreased) drift times $T_{drift}^{\pm}$.

The superimposition of two triangular pulses corresponding to a slightly larger (smaller) drift time $T_{drift}^{+}$ ($T_{drift}^{-}$) and slightly smaller (larger) peak amplitude results in a pulse composed by a faster triangle of drift time $T_{drift}^{x} < T_{drift}$:

$$T_{drift}^{x} = T_{drift}\left(\frac{1 - \frac{16}{9}x^2}{1 + \frac{8}{9}x^2}\right) T_{drift} \tag{6.12}$$

for $t < T_{drift}^{-}$, followed by the remnant of the longer current pulse for $T_{drift}^{-} < t < T_{drift}^{+}$.

Note that no electrode shift is assumed in the bend regions, since it represents a second order effect with respect to the one described in Section 6.2.1.

### 6.2.3 Global drift time fit

In order to account for the effects discussed in Sections 6.2.1 and 6.2.2, the ionization pulse generated in the LAr gap can be described by the superposition of three triangles:

$$\begin{aligned} I(t) &= I(t;I_{nom}/2,T^{+}_{drift}) + I(t;I_{nom}/2,T^{-}_{drift}) + I(t;I_{bend},T_{bend}) \\ &= I_0\left[\frac{f_{nom}}{2}\left(1-\frac{1}{3}x\right)I(t;1,T^{+}_{drift}) + \right. \\ &+ \left.\frac{f_{nom}}{2}\left(1+\frac{1}{3}x\right)I(t;1,T^{-}_{drift}) + f_{bend}I(t;1,T_{bend})\right], \end{aligned} \tag{6.13}$$

Since the readout system is linear, each of the three triangular contributions in Equation 6.13 can be separately computed at the end of the readout chain using Equation 5.16 for the different values of drift time $T^{+}_{drift}$, $T^{-}_{drift}$ and $T_{bend}$, and using a common set of $\tau_{\text{cali}}$, $f_{step}$, $rC$ and $LC$ parameters. The ionization pulse at the end of the readout chain is then:

$$\begin{aligned} g(t;f_{nom},T_{drift},x,f_{bend},T_{bend}) &= \frac{f_{nom}}{2}\left(1-\frac{1}{3}x\right)g^{\text{phys}}(t;T^{+}_{drift}) \\ &+ \frac{f_{nom}}{2}\left(1+\frac{1}{3}x\right)g^{\text{phys}}(t;T^{-}_{drift}) + f_{bend}g^{\text{phys}}(t;T_{bend}) \end{aligned} \tag{6.14}$$

This cumulative pulse prediction is scaled by an arbitrary amplitude $A_{\max}$ and shifted in time by an offset $t_0$ to fit the samples of the data pulses:

$$g_{\text{fit}}(t;A_{\max},t_0,T_{drift},x) = A_{\max}g(t;f_{nom},T_{drift},x,f_{bend},T_{bend}) \text{ for } \quad t > t_0 \tag{6.15}$$

The parameters $T_{bend}$ and $f_{bend}$ are fixed to the values obtained from the Monte Carlo simulation (see Section 6.3), whereas $T_{drift}$ and $x$ are left free to fit the data. The computational details of the fitting procedure are discussed in Section 6.4.

## 6.3 $T_{bend}$ and $f_{bend}$ from Monte Carlo simulations

### 6.3.1 EM barrel

The $T_{bend}$ and $f_{bend}$ parameters describing the drift time contribution in the accordion bend regions (Section 6.2.1) are calculated for the EMB assuming a uniform charge density in the LAr gap, corresponding to a muon flux. In the EMB simulation the current as a function of time is obtained by transporting the ionization electrons to the electrodes; the charge $q$ in a differential volume $dxdydz$ is computed from the energy deposited in that volume, and the current is determined as $qV_{drift}|E|/H$, where $E(x,y,z)$ is the local value of the electric field, and $H$ the high

voltage. The time is incremented in $\delta t$ steps and the spatial position as $V_{drift}\ \delta t\ \vec{E}/|E|$, in order to obtain the two triangular currents corresponding to the flat and bend parts.

The values obtained by the EMB simulation are given in Table 6.1; they are independent of pseudo-rapidity and azimuth.

| Layer | $T_{bend}$ (ns) | $f_{bend}$ (%) |
|---|---|---|
| Layer 1 | 820 | 4.9 |
| Layer 2 | 898 | 7.1 |
| Layer 3 | 941 | 8.5 |

Table 6.1: $T_{bend}$ and $f_{bend}$ for the three layers of the EMB.

### 6.3.2 EM endcap

The values of $T_{drift}$, $T_{bend}$ and $f_{bend}$ in the EMEC are obtained from a Monte Carlo (MC) simulation of the sub-detector response[1] to 10 GeV photons; photons are chosen since the selected cosmic data used later to fit Equation 6.15 are electromagnetic cascades from cosmic muons (see Section 6.4.2). The photons are generated with a projective direction pointing to the ATLAS Interaction Point, and a starting point (or initial vertex) at the beginning of the calorimeter. In reality the bremsstrahlung photons (or the $e^+e^-$ pairs) from cosmic muons are not projective: this could introduce a systematic difference when comparing data with simulation. About half a million photon events are generated.

The local drift velocity ($V_{drift}^{local}$) in LAr depends on the temperature and on the absolute value of the electric field, and is parameterized by an empirical formula [34]. The LAr temperature is set to the average value measured in the three EMEC modules exposed to beam tests in the past [45, 46], namely 88.16 K. For the computation of the electric field, nominal high voltage values are used as well as the local geometry of the accordion shaped electrodes and absorbers. The local value of the norm of the electric field at any point is obtained from a three-dimensional interpolation procedure, starting from the precisely computed electric field at different radial distances from the beam line.

Although the local drift velocity in the cells can not be measured, its average over a detector cell can be compared with real measurements. This average may depend on the geometry of the cell and on the distribution of the ionization energy within the cell: in order to check the effect of the latter, results for photons and muons are compared (see Section 6.3.2.2).

The distribution of the $V_{drift}^{local}$ within a shower is shown, for a EMEC Middle cell at $\eta = 1.650$, in Figure 6.3(a). Figure 6.3(b) shows the local drift time ($T_{drift}^{local}$) that it is obtained from the previously determined local drift velocity for every GEANT4 step according to Equation 6.1, where $w_{gap}$ is the average gap size over the GEANT4 step. The peaks in the distributions shown in Figure 6.3 correspond to the drift velocity and drift time in the flat part of the accordion, while the tails represent their values in the bend part. The electric field (gap) in the bend region is in fact lower (larger) than in the flat part, which leads to an increase of the drift time.

[1] This EMEC signal simulation is performed using Athena 14.2.23.1 with no magnetic field.

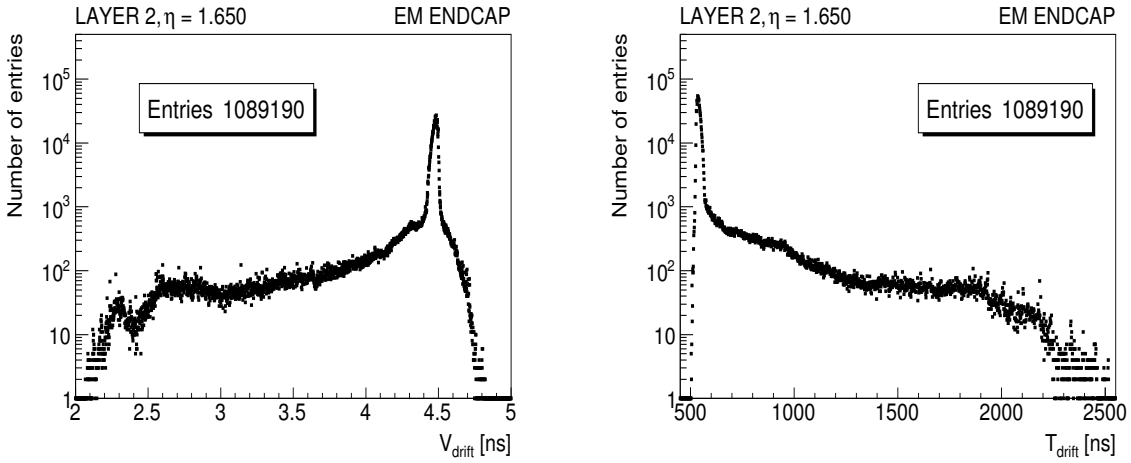


(a) $V_{drift}$ (b) $T_{drift}$

Figure 6.3: Distribution of the local drift velocity (a) and local drift time (b) in a Layer 2 of the endcap at $\eta = 1.650$, as obtained from the MC simulation of 10 GeV photons.

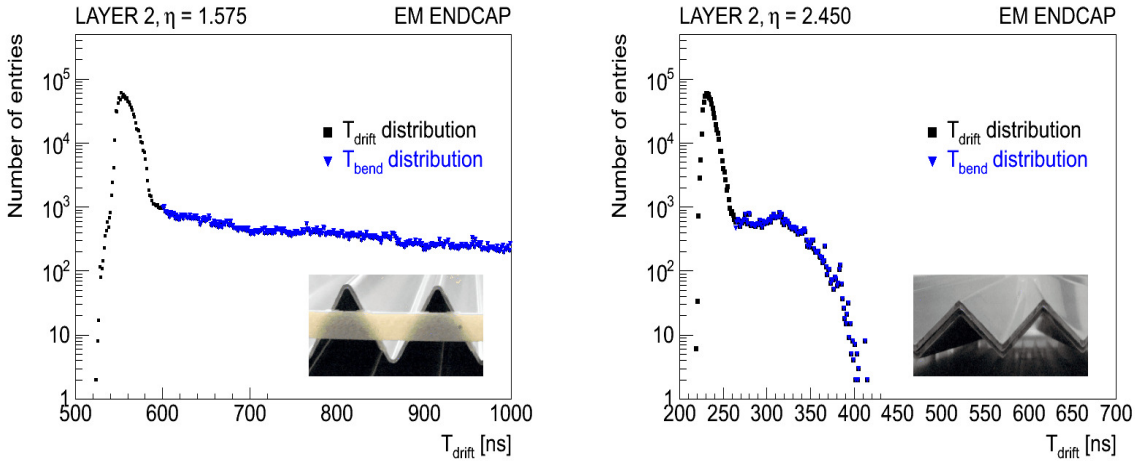


(a) $\eta = 1.575$ (b) $\eta = 2.450$

Figure 6.4: Local drift time distribution corresponding to a Middle cell of the endcap at $\eta = 1.575$ (a) and $\eta = 2.450$ (b). The contribution from the accordion bend is marked in blue.

#### 6.3.2.1 Determination of $T_{bend}$ , $f_{bend}$ and $T_{drift}$

The $T_{bend}$ and $T_{drift}$ values are obtained from the distribution of the local drift time (Figure 6.4). The right side tail (blue) is due to the bend part ($T_{bend}$ distribution) whereas the left part (black) corresponds to the flat part ($T_{drift}$ distribution). If $T_{cut}$ is the drift time value separating the two regions, one obtains:

$$T_{bend} = \int_{T_{cut}}^{\infty} T_{drift}^{(local)} \, f(T_{drift}^{(local)}) \, dT_{drift}^{(local)} \tag{6.16}$$

$$T_{drift} = \int_{0}^{T_{cut}} T_{drift}^{(local)} \, f(T_{drift}^{(local)}) \, dT_{drift}^{(local)} \tag{6.17}$$

where $f$ is the probability density function of $T_{drift}^{(local)}$, which is normalized to one:

$$\int_{0}^{\infty} f(T_{drift}^{(local)}) \, dT_{drift}^{(local)} = 1 \tag{6.18}$$

The function $f(T_{drift}^{(local)})$ is obtained from the distribution histogram dividing each bin contents by the total number of entries.

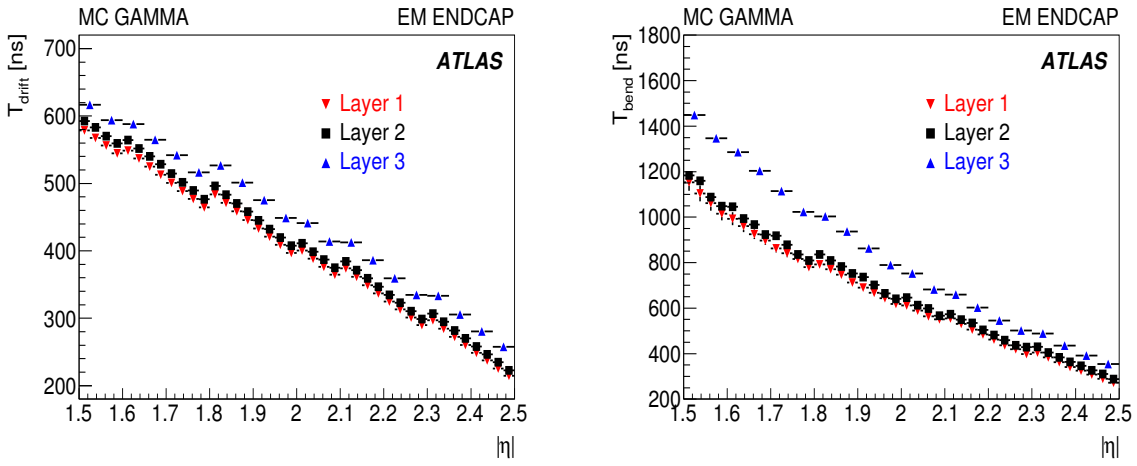


(a) $T_{drift}$ (b) $T_{bend}$

Figure 6.5: $T_{drift}$ (a) and $T_{bend}$ (b) versus η for the three EMEC layers.

The computed $T_{drift}$ and $T_{bend}$ values are shown in Figure 6.5(a) and 6.5(b) respectively as a function of pseudo-rapidity for the three EMEC layers. Both drift times decrease when η increases, following the reduction of gap size. The difference observed between the layers is due to a gap size variation with longitudinal depth: the gap size in the EMEC grows continuously at constant η from the Front up to the Back layers due to the projective geometry. The fact that the values for the Middle layer lie closer to the Front ones rather than to the Back ones is explained

by the energy distribution of the a 10 GeV photon shower: at this energy the maximum of the cascade is closer to the Front than to the Back layer.

As already mentioned in Section 6.2.1 the contribution of the bends to the total current is represented by a fractional weight $f_{bend} = I_{bend}/I_0$ for each calorimeter cell. This ratio can be obtained using the energy deposit ($E_d$), the drift velocity ($V_{drift}$) and the gap ($w_{gap}$) provided by GEANT4 for each hit or step inside a calorimeter cell. The local current on a differential volume $dxdydz$ of the cell is determined as $E_d/(w_{gap}/V_{drift})$. Therefore $f_{bend}$ can be calculated as:

$$f_{bend} = \frac{\int_{T_{drift}>T_{cut}} \frac{E_d}{w_{gap}/V_{drift}} dxdydz}{\int \frac{E_d}{w_{gap}/V_{drift}} dxdydz} \tag{6.19}$$

where $T_{drift} = w_{gap}/V_{drift}$ and the bend part is defined as all hits having $T_{drift} > T_{cut}$.

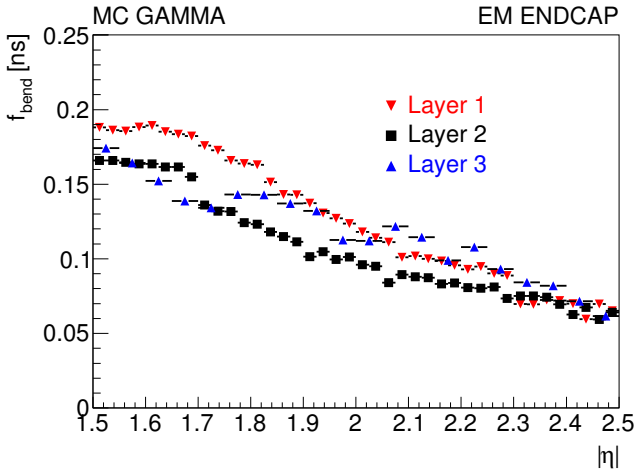


Figure 6.6: $f_{bend}$ versus η for the three EMEC layers.

The result of this calculation is shown in Figure 6.6 as a function of pseudo-rapidity for the three EMEC layers. The decreasing behavior of $f_{bend}$ for the three layers is again explained by two characteristics of the EMEC design: the accordion bend angle increases with pseudo-rapidity, and the gap size decreases when η grows; both effects lead to a decrease of the ratio between bend and flat part volumes, hence to the decrease of $f_{bend}$.

Another feature of the EMEC design is that both bend angle and gap size are independent of depth for a fixed radius. This implies they both change with depth for a fixed η value: the bend angle decreases while the gap size increases. One could thus expect a monotonous growth of $f_{bend}$ with the layer, its value being the smallest for the Front and the largest for the Back layers. In reality layer 1 shows a different trend (Figure 6.6). The reason for this behavior can be explained by the total volume of the bend part respect to the flat part: layer 1 ends in fact immediately after a bend crest, this fact unbalancing the equilibrium between the bend and flat part volumes. In the front layer there are in fact 4 bends and 3 flat parts in total.

A similar argument explains the lower values of three cells of the Back layer around $\eta = 1.65$ observed in Figure 6.6. For these EMEC cells the depth of the Back layer increases in such

a way that a flatter part of the accordion is added: this explains a smaller $f_{bend}$ value for these cells, and the opposite results for the corresponding Middle cells in this region.

#### 6.3.2.2 Difference between photons and muons

A muon flux parallel to the beam line and passing through the EMEC cells is simulated to compare the drift velocity and time with the ones obtained from the photon simulation. The muon energy is set to 30 GeV, hence it roughly behaves as a minimum ionizing particle.

The distributions of $V_{drift}$ and $T_{drift}$ for photons and muons are shown in Figure 6.7 for an EMEC Middle cell at $\eta$ = 1.650. A slight difference is systematically observed between the photons' and muons' distributions, to be attributed to the difference in the energy distributions of the two samples. Photon showers deposit in fact their maximum energy in the first part of the cell, whereas the muon energy deposition is uniform along the cell. Since the gap size increases with depth inside the cell, photons and muons see different electric fields and gap sizes.

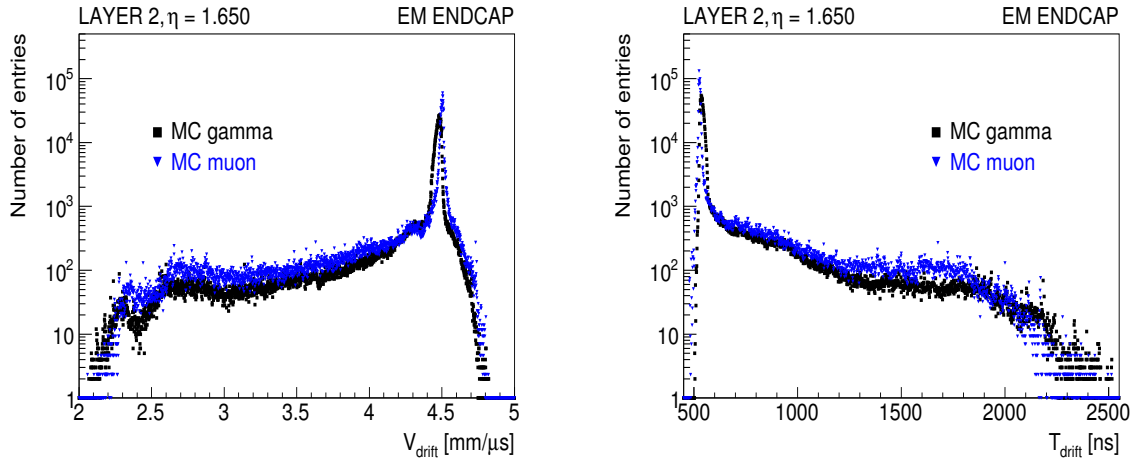


(a) $V_{drift}$ (b) $T_{drift}$

Figure 6.7: Drift velocity (a) and drift time (b) distributions for photons (squares black) and muons (down triangles blue), in a EMEC Middle cell at $\eta = 1.650$. The histograms are normalized to have the same number of entries.

The mean value of the drift velocity and time are computed for all Middle cells for the photon and muon samples. The relative difference of the mean values among the two samples, as averaged over all the cells, is 0.7 % for the drift velocity, and $-3.0$ % for the drift time. This difference is about four times larger for the drift time than the drift velocity. This is explained by the gap size dependence of the drift time and drift velocity (Equation 6.4 and 6.6):

$$\left\{ \begin{array}{rcl} \frac{1}{V_{drift}} \frac{\partial V_{drift}}{\partial w_{gap}} & \sim & -\alpha w_{gap}^{-1} \\ \frac{1}{T_{drift}} \frac{\partial T_{drift}}{\partial w_{gap}} & \sim & (1+\alpha) w_{gap}^{-1} \end{array} \right. \Rightarrow \left| \frac{\frac{1}{T_{drift}} \frac{\partial T_{drift}}{\partial w_{gap}}}{\frac{1}{V_{drift}} \frac{\partial V_{drift}}{\partial w_{gap}}} \right| \sim 4 \qquad (6.20)$$

## 6.4 Cosmic data selection

### 6.4.1 Data samples

Cosmic runs from the data taking period of September-November 2008 are used in this analysis, with the LAr data acquisition transmitting and saving 32 samples of the readout signals. Figure 6.8 shows an Atlantis picture of a cosmic with hits in all barrel detectors from a run taking in September 2008.

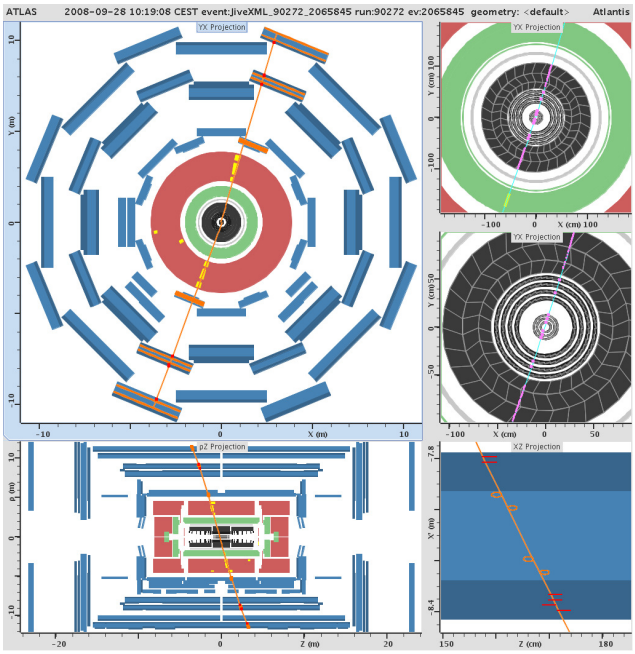


Figure 6.8: Atlantis display with a Cosmic event in the ATLAS experiment. Both solenoid and toroid were on during this run.

The first level trigger system [47] was tested during this period, which labeled different streams to be used for the different sub-detector commissioning. For the present analysis data streams marked with `L1Calo` or `L1CaloEM` are considered (see Section 3.2.4). The former refers to the general calorimeter trigger, which reads the energy deposits in towers of size $0.1 \times 0.1$ in the $\eta$, $\phi$ space for both hadronic and electromagnetic calorimeters. The latter is restricted to the electromagnetic calorimeter only. Since the trigger was fired by cosmic instead of LHC data, its thresholds were adjusted accordingly. Most of the signals correspond to an energy deposit smaller than 20 GeV, hence the LAr readout "High" gain is used throughout all this study.

Although the probability for bremsstrahlung emission is small because of the large muon mass, many events were taken during the run period, assuring sufficient statistics for most of the calorimeter regions [2]. However the EMEC Inner-Wheel could not be included in the analysis because the number of cosmic events was insufficient. Hence the pseudo-rapidity range in this study is restricted to be from $-2.5$ to 2.5.

[2] Similar argument for $e^+e^-$ emission

### 6.4.2 Energy cuts

Cells with high energy deposits - much larger than the energy lost by a minimum ionizing particle - are selected in order to minimize the effect of noise fluctuations on the pulse shape. This is especially important in the EMEC since the cosmic muons cross a small portion of the cells, because they do not follow the cell projectivity to the nominal ATLAS Interaction Point. The selected events correspond to electromagnetic cascades from cosmic muons, which guarantee sufficient energy deposit in the cells.

Figure 6.9 shows the energy distribution in barrel cells for two typical cosmic events selected for this analysis. The first one deposits most of its energy in the Front layer mostly along the $\eta$ direction, whereas the second one deposits most of its energy in the Middle layer mainly along the azimuthal direction. A cluster can be defined in both cases using the cells with energy deposit above the mean ionization energy lost by muons; the cluster size in both cases is compatible with an electromagnetic cascade.

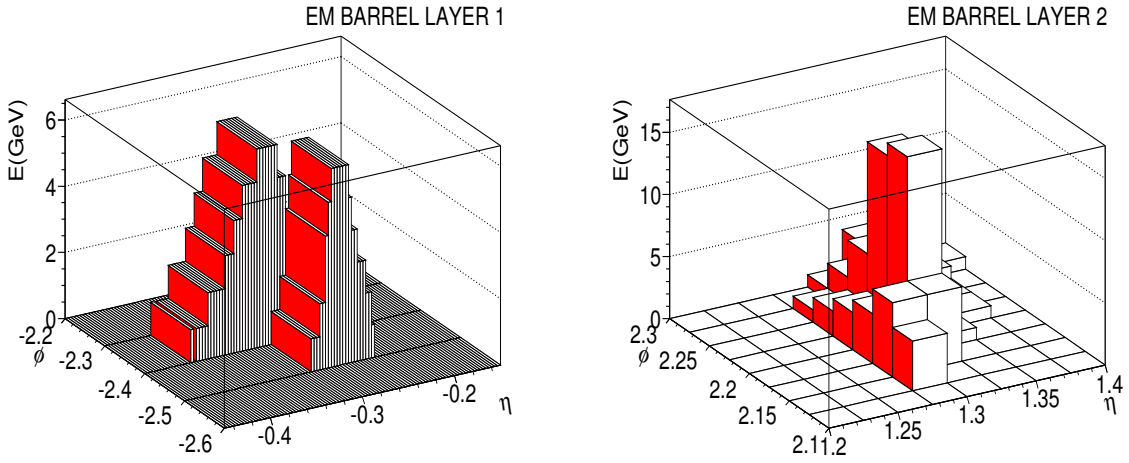


(a) (b)

Figure 6.9: Transverse energy profiles for two cosmic muon events: one crossing the layer 1 (a) (with 58 cells above the noise) and another one incident on layer 2 (b) (with 29 cells above the noise).

To minimize the distortion of the signal shape, the energy deposited in a cell should be well above its typical noise values. This is particularly important since the drift time is obtained on an event by event basis, many cells being hit only once. We denote by $S_{max}$ the amplitude of the most energetic sample of the data pulse. The minimum required values for $S_{max}$ are given in Table 6.2 for the three layers of EMB and EMEC. These values translate to a lower bounds for the energy between 1 and 2 GeV depending on the cell. The average noise is also quoted, which represents between 1 and 3.5 % of the minimum value for $S_{max}$. A different treatment is given to EMB electrode B region ($0.8 < |\eta| > 1.4$) in the Middle layer since it has a different gain.

| | Layer | $S_{max}$ lower limit | Noise |
|---|---|---|---|
| EM barrel | Front | 500 | 8 |
| | Middle ($\|\eta\| \leq 0.8$) | 160 | 5 |
| | Middle ($\|\eta\| > 0.8$) | 100 | 3.5 |
| | Back | 160 | 5 |
| EM endcap | Front | 500 | 7 |
| | Middle | 160 | 2 |
| | Back | 160 | 3.5 |

Table 6.2: Cut values for the most energetic sample of the data pulse in ADC units.

An upper limit of 3900 ADC counts for $S_{max}$ plus pedestal is also required to avoid saturation in High Gain. This cut is $3900/1.6$ ADC counts for the region of EMB electrode B.

### 6.4.3 Pulse quality cuts

A small fraction of the data pulses show a distorted shape, most likely related to large cross-talk contribution from the neighboring cells. In these cases the drift time cannot be determined accurately, hence only cells with a certain shape quality are considered in this analysis. The following notation is used here and in the rest of the document: $S_i$ ($i = 0,\ldots,n-1$) are the $n$ measured samples of the data pulse shape at time values $t_i$, where $t_i$ is increased by 25 ns between two consecutive samples ($t_{i+1} - t_i = 25$ ns), and $t_{max}$ is the time of the most energetic sample. The quality of the data pulse shape is assured by requiring the following selections:

- The tail of the pulse should not contain too many samples near zero. More explicitly, for $t_i > t_{max+5}$, there must be less than 12 samples for which $S_i > -0.1\ S_{max}$. This cut removes pulses which rise too fast due to cross-talk in the EMB. This condition cannot be applied to the EMEC because such shapes exist due to the expected low values of drift time at high pseudo-rapidity.

- The data should have a negative part of the pulse shape. For $t_i > t_{max}$ at least 5 samples with negative amplitude ($S_i < 0$).

- A measure of the difference between the prediction and the data samples for the last part of the pulse is defined as:

$$\Delta_{\text{last7}} = \sum_{i=25}^{32} \frac{S_i - g_{\text{fit}}(t_i; A_{\max}, t_0, T_{drift}, x)}{S_{max}} \tag{6.21}$$

  where $g_{\text{fit}}$ is the physics pulse prediction (Equation 6.15) after the fit (see Section 6.4.4). In order to guarantee that the data pulse tail, the portion of the signal that is more sensitive to the drift time values, is reasonably well described by the prediction, the $|\Delta_{\text{last7}}| < 0.15$ condition is required.

- Data pulses are required to be contained inside a "safety" envelope to avoid shapes with spikes (see Figure 6.10).

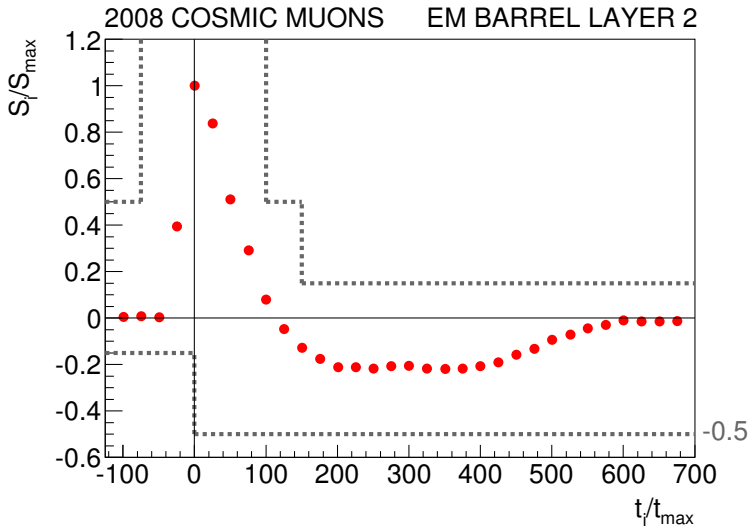


Figure 6.10: Envelope definition (grey line) and an example of a cosmic data pulse (red dots) in layer 2 of the barrel.

### 6.4.4 Fit quality cuts

The data pulse samples $S_i$ of every calorimeter cell selected by the criteria discussed above are fitted by the pulse prediction described by Equation 6.15 as a function of the drift time $T_{drift}$, the electrode shift $x$, the maximum amplitude of the pulse $A_{max}$ and the time offset of the data pulse $t_0$. The optimal set of $A_{\max}, t_0, T_{drift}, x$ parameters is estimated using the least squares method, by minimizing the quantity:

$$\chi^2_{\text{fit}} = \frac{1}{N_{dof}} \sum_{i=1}^{n} \frac{(S_i - g_{\text{fit}}(t; A_{\max}, t_0, T_{drift}, x))^2}{\sigma^2_{noise}} \tag{6.22}$$

where $N_{dof} = n - N_p$ is the number of degrees of freedom. The total number of data samples used in the fit, $n$, is usually $n = 32$, and $N_p = 4$ is the number of free parameters. This minimization is perform by employing the MINUIT package [48].

Under the assumptions that the samples $S_i$ are only distorted by the electronic noise, that the system is completely linear and that the $g_{\text{fit}}$ functional form is an accurate description of the normalized ionization pulse shape in the cell under study, the minimum of $\chi^2_{\text{fit}}$ is distributed according to a normalized $\chi^2$ probability density function. However, since the prediction of the pulse shape is accurate at the 2 % level but not perfect, more energetic events will have larger $\chi^2_{\text{fit}}$ values [49]. Figure 6.11 shows the dependence of the $\chi^2_{\text{fit}}$ variable as a function of the maximum data amplitude ($S_{max}$) for the Back layer of the EMEC: a clear increase of the $\chi^2_{\text{fit}}$ value is observed when $S_{max}$ increases. The same behavior is observed in the other calorimeter layers.

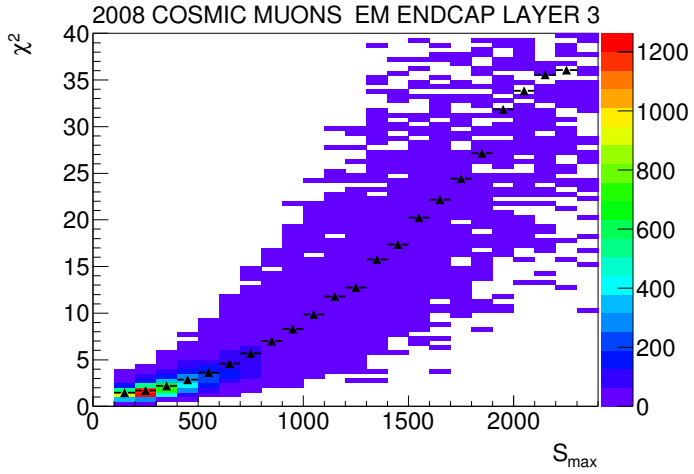


Figure 6.11: $\chi^2_{\text{fit}}$ variable as a function of $S_{max}$ for all cells of the EMEC Back layer.

In order to be able to apply a global selection on the fit quality independently on the data pulse amplitude, the modified quality estimator is defined following the proposal of Section 5.4.3:

$$Q^2 = \frac{1}{N_{dof}} \sum_{i=0}^{n} \frac{(S_i - g_{\text{fit}}(t; A_{\max}, t_0, T_{drift}, x))^2}{\sigma^2_{noise} + (kS_{max})^2} \tag{6.23}$$

where the value of $k$ is chosen such that $Q^2$ has no dependence on $S_{max}$. Figure 6.12 shows $Q^2$ as a function of $S_{max}$ for several values of $k$ for the Back layer of the EMEC. The one giving a flat dependence corresponds to $k = 1.3$ %. A similar procedure is applied to all the other calorimeter layers: the values of the corresponding $k$ values are given in Table 6.3.

| Calorimeter | Layer | $k$ |
|---|---|---|
| EMB | Front | 0.8 % |
| | Middle | 1.0 % |
| | Back | 1.0 % |
| EMEC | Front | 0.9 % |
| | Middle | 1.4 % |
| | Back | 1.3 % |

Table 6.3: $k$ values for the different calorimeter layers.

The $Q^2$ quantity represents a "normalized" $\chi^2$ per degrees of freedom, its denominator reflecting the numerator uncertainty, namely the quadratic sum of the data amplitude noise and of the predicted amplitude inaccuracy. The distributions of $Q^2$ for all EMB and EMEC layers are shown in Figure 6.13. They all have approximately a $\chi^2$-type shape with the Most Probable Value ($MPV$) near one. To avoid bad quality fits a $Q^2 < 3$ selection cut is applied for all layers of both EMB and EMEC.

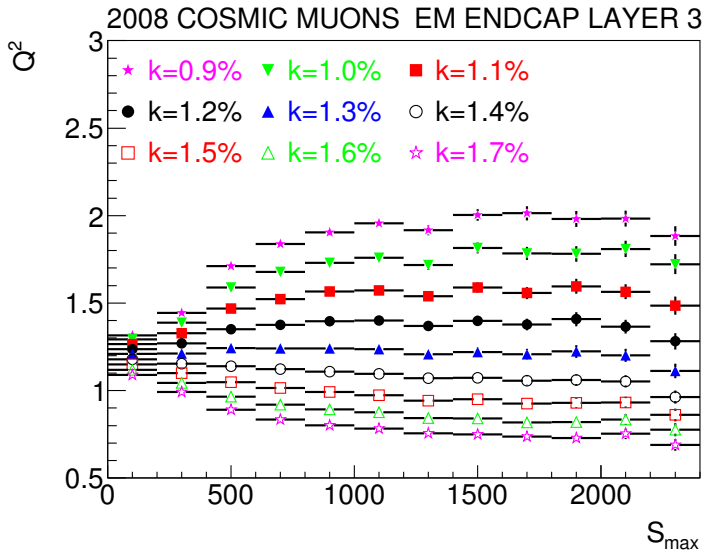


Figure 6.12: $Q^2$ as a function of $S_{max}$ for several values of $k$.

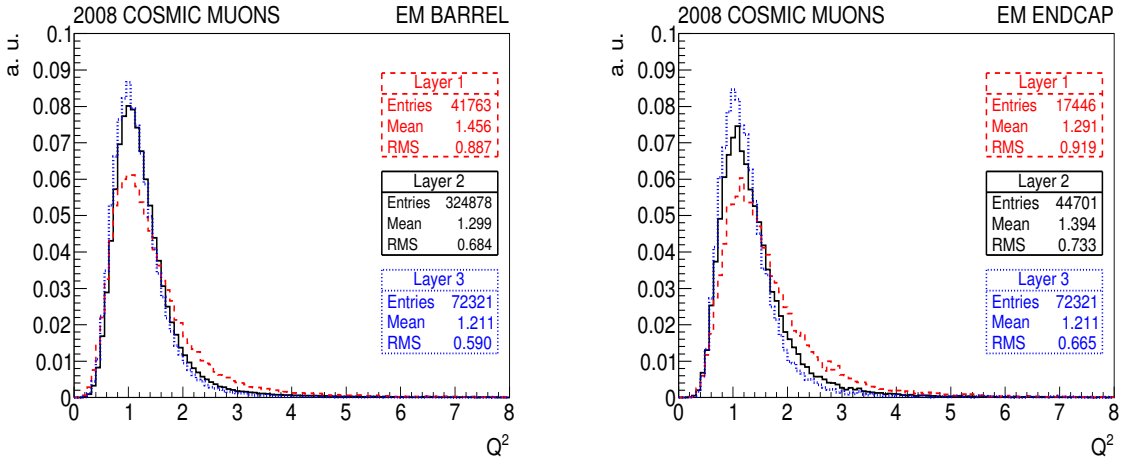


(a) EM barrel (b) EM endcap

Figure 6.13: Distributions of $Q^2$ for all layers of EMB (a) and EMEC (b).

The behavior of the $Q^2$ variable is studied as a function of pseudo-rapidity (Figure 6.14). Each point represents the average profile of the events in the corresponding $\eta$ bin. For all the three layers, cells near $|\eta| = 2.5$ show a larger value of $Q^2$, close to the selection cut of three. The reason for the pulse prediction not describing well the data in this region is still unclear, although it may partially be due to the difficulty to extract the RTM $\omega_0$ resonance frequency from the calibration pulse [39] when its value is too high and gets confused with the reflection-related frequencies.

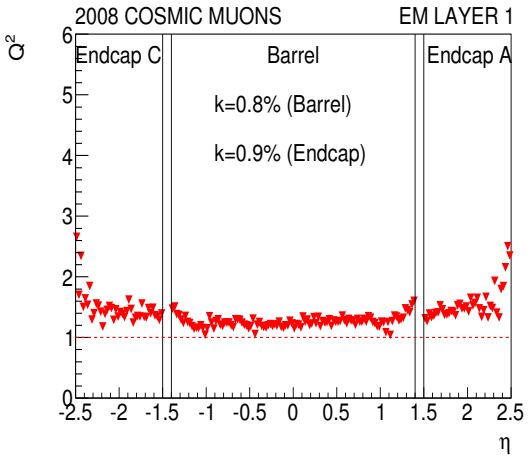


(a) Layer 1

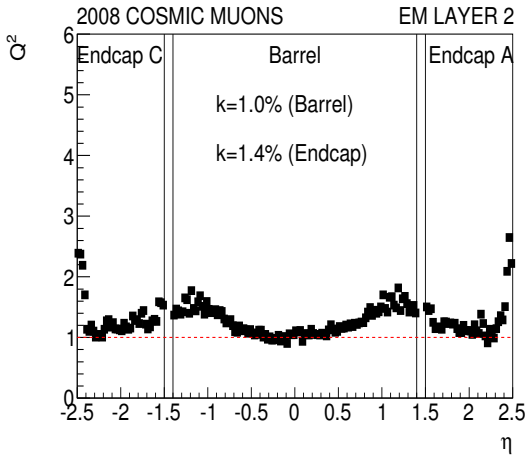


(b) Layer 2

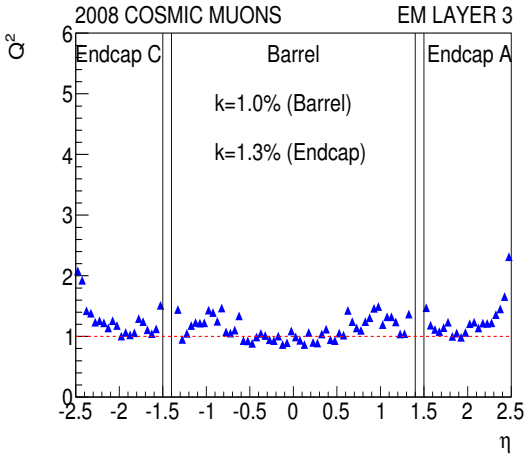


(c) Layer 3

Figure 6.14: Most Probable Value of the $Q^2$ distribution as a function of $\eta$.

In addition the region around $\eta = 0.8$ of the Middle layer have larger values of $Q^2$ than the average; this zone corresponds to the change from electrode A to electrode B of the EMB. No special attention has been paid to this effect since the values of $Q^2$ are still within reasonable limits.

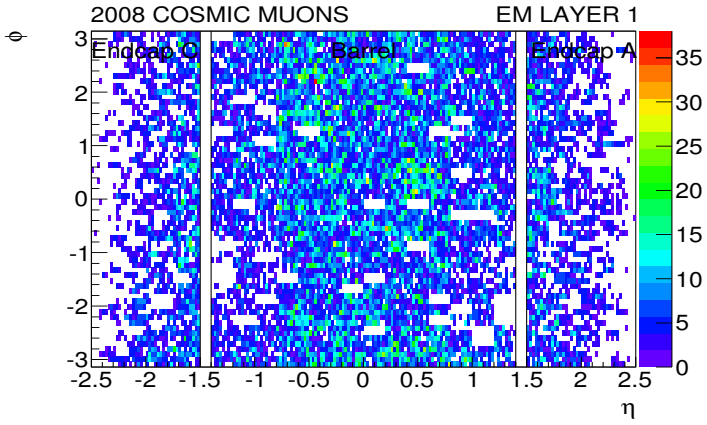


(a) Layer 1

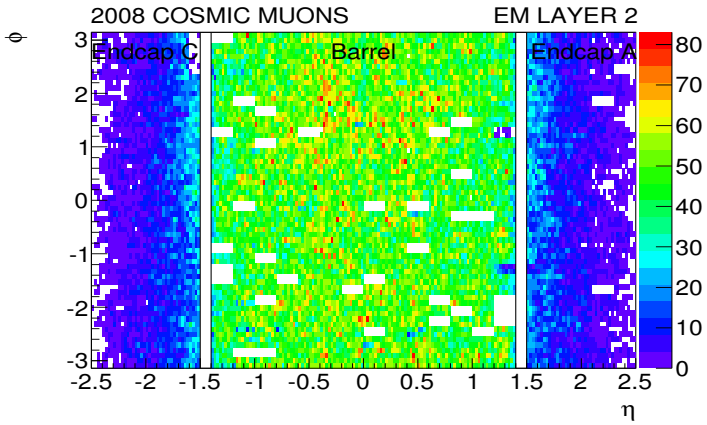


(b) Layer 2

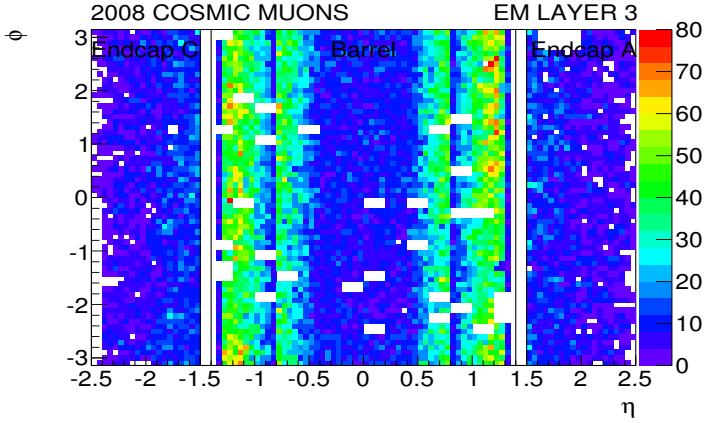


(c) Layer 3

Figure 6.15: Number of cells used in the analysis as a function of $(\eta, \phi)$ for the Front, Middle and Back layers. The white color indicates the absence of cells. The number of selected hits are $51,492$ in layer 1, $358,154$ in layer 2 and $87,920$ in layer 3.

### 6.4.5 Final statistics

The number of pulses above energy thresholds is given in the first columns of Table 6.4. Higher statistics is observed in the barrel than in the endcap due to a larger cross section offered to triggered cosmic muons and the better projectivity of cells. Table 6.4 also shows the efficiencies of the pulse and fit quality selections. The pulse quality requirements reduce the sample by about 20 %, whereas the fit quality selection removes roughly 5 % of the events.

| Calorimeter | Layer | Pulses above threshold | Pulse quality | Fit quality |
|---|---|---|---|---|
| EMB | Front | 55197 | 75.66 % | 94.72 % |
| | Middle | 400342 | 81.15 % | 97.06 % |
| | Back | 92851 | 77.89 % | 98.28 % |
| EMEC | Front | 15474 | 83.90 % | 91.91 % |
| | Middle | 55133 | 81.08 % | 95.83 % |
| | Back | 23161 | 75.32 % | 96.55 % |

Table 6.4: Number of pulses above energy thresholds and efficiencies of pulse and fit quality cuts.

The distribution of the selected pulses in the $\eta$, $\phi$ plane is shown in Figure 6.15 for the three calorimeter layers. The white color indicates the absence of pulses. The white regions in the EMB correspond to cells either disconnected from the readout chain or with a high voltage lower than nominal (2 KV) which are not considered in the analysis. The white zones in the EMEC corresponds to disconnected channels or the lack of cosmic events impacting those cells. The EMEC cells corresponding to $1.4 < |\eta| < 1.5$ are not included in the analysis because it is not possible to determine the drift time using only 32 samples on the data (see Section 6.5.1). The smaller number of pulses in the Front layer is due to the fact that the energy cut is approximately the same expressed in GeV for the three layers, despite the Front cells being smaller than the Middle and Back ones, which means they collect on average a smaller amount of energy.

## 6.5 Results and discussion

### 6.5.1 Quality of the pulse shape description

In order to visually present the general quality of the pulse description after the fits, six examples of pulse shapes are shown in Figure 6.16, corresponding to cells chosen at random among the results. The data samples in each plot correspond to a single cosmic event, thus fluctuations of the amplitude are still observed from sample to sample because of the noise contributions. The relative difference between the data and the prediction, $(S_i - g_{\text{fit}})/S_{max}$ is also shown. The data are globally well described at the 2 % level. The differences between the prediction and the data seem to be compatible with noise fluctuations on the data, although some systematic effects are not ruled out for certain cells.

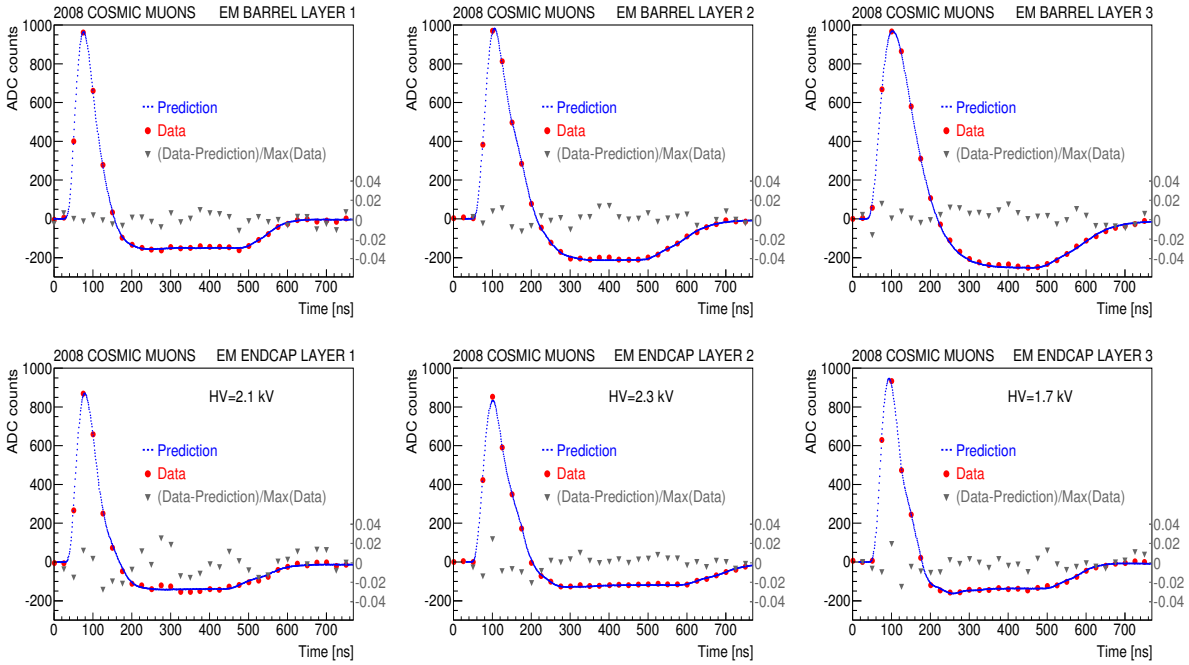


Figure 6.16: Pulse shapes for data (red points) and prediction (blue line) for the Front (left), Middle (center) and Back (right) layers for the EMB (top) and the EMEC (bottom) calorimeters. The green points correspond to the relative difference between data and the prediction in an enhanced scale.

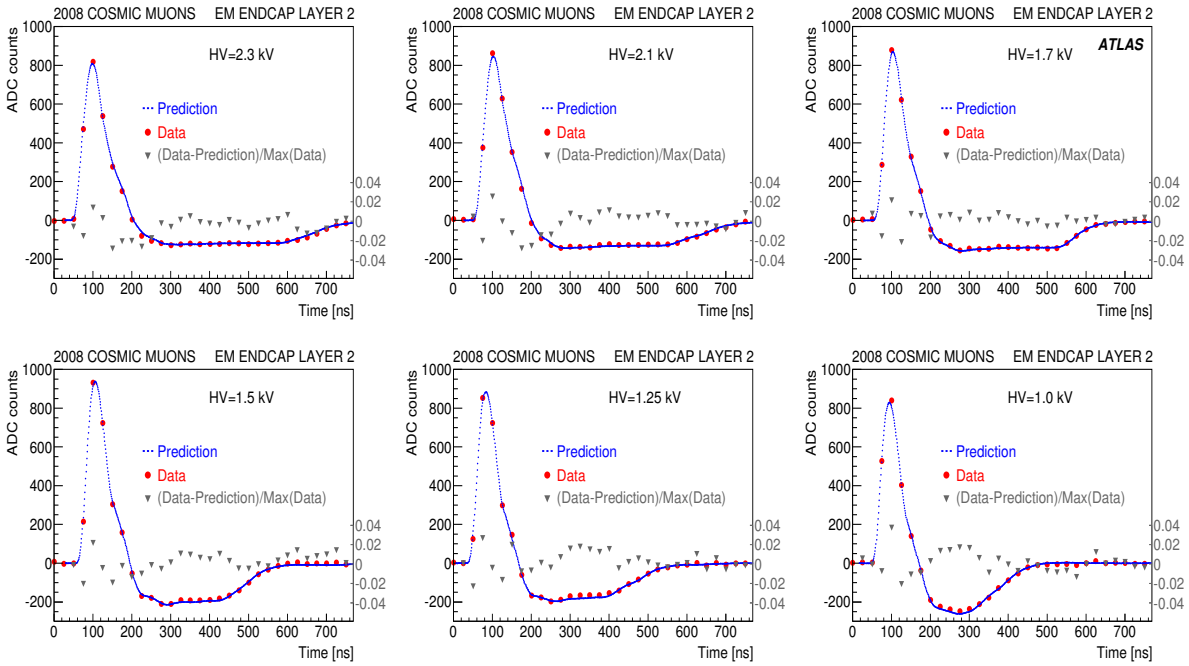


Figure 6.17: Pulse shapes for data (red points) and prediction (blue line) for EMEC middle cells belonging to different HV regions. The green points correspond to the relative difference between data and the prediction in an enhanced scale.

Because of the size variation of the gap with η in the EMEC, there are nine different high voltage regions defined to maintain an approximatively constant electrical field in η, seven of them in the outer-wheel (see Figure 4.8). The quality of the fit has been studied in each endcap region separately. As an example, Figure 6.17 shows the comparison between predicted and data pulse shapes for six cells, corresponding to six different high voltage regions for the EMEC Middle layer. No particular degradation of the fit quality is observed in any high voltage region.

Figure 6.17 nicely illustrates the variation of the EMEC pulse shape as a function of pseudo-rapidity because of the gap size change: the smaller the gap (larger η) the shorter the pulse undershoot is; as a direct consequence the EMEC drift time decreases when η increases. In particular at the lowest η values the drift time may become as long as 700 ns, a value which is barely covered by the time scale corresponding to 32 pulse samples. Because of this reason the fitting procedure of these pulses is less reliable, since the final portion of the pulse tail does not return to zero.

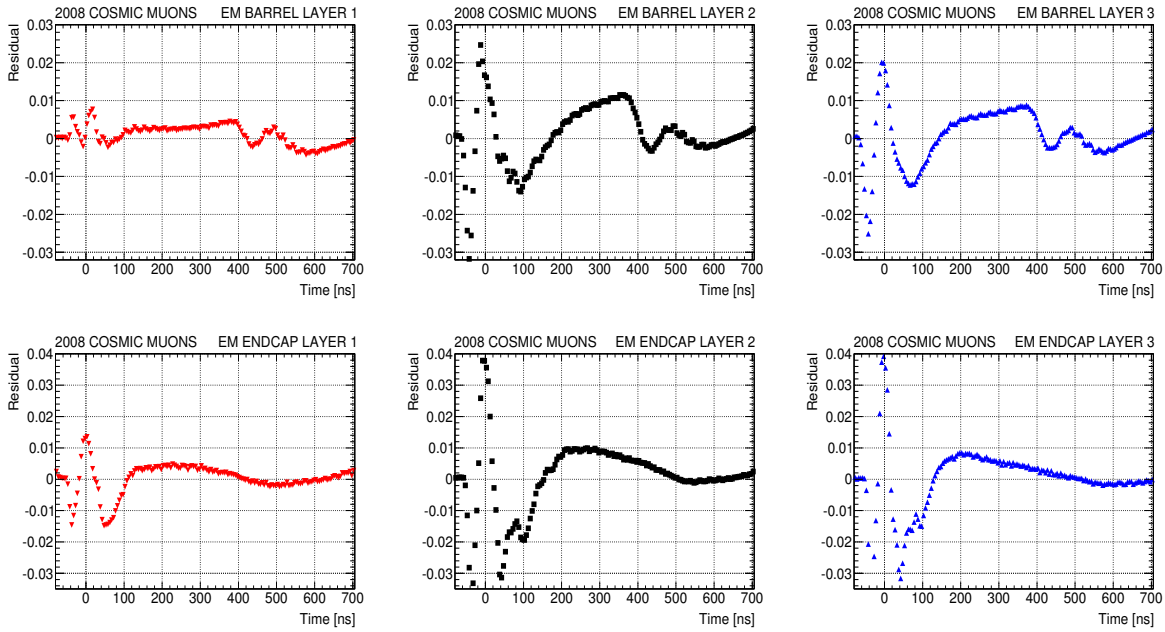


Figure 6.18: Average residual over all events for the Front (left), Middle (center) and Back (right) layers of the EMB (top) and the EMEC (bottom) calorimeters.

In order to investigate the global residuals between the pulse predictions and the data sample, the relative difference $(S_i - g_{\text{fit}})/S_{max}$ is averaged for all events and all cells in a given layer. Figure 6.18 shows the averaged residuals for each layer of the EM calorimeter: the data pulses of the Front layer seem to be better described than the pulses of the other two layers; additionally, the EMB pulses appear to be slightly better reproduced than the EMEC ones. The tail of the pulse, which is more sensitive to variations of the drift time, is described at the 1 % level or better. The time origin is chosen such that the maximum peaks of the pulses are at $t = 0$. The description at the maximum is about two or three times worst than for the tail, however, the use of Optimal Filtering Coefficients to obtain the signal amplitude may partially compensate for this difference, due to the oscillatory behavior of the residuals around the peak.

### 6.5.2 Drift time measurement along pseudo-rapidity

The drift time ($T_{drift}$) averaged over the azimuth ($\phi$) is studied as a function of pseudo-rapidity $\eta$ for the whole EM calorimeter. Figure 6.19 shows the distribution of the values and the behavior of their mean as a function of $\eta$. An expected variation in the EMEC is observed: due to the decrease of the gap size as $|\eta|$ increases, the EMEC drift time also decreases (see Figure 4.8). However, because of the constant gap size, $T_{drift}$ is constant in the barrel. No significant differences are observed between layers, despite the fact that the number of events collected is different for each one.

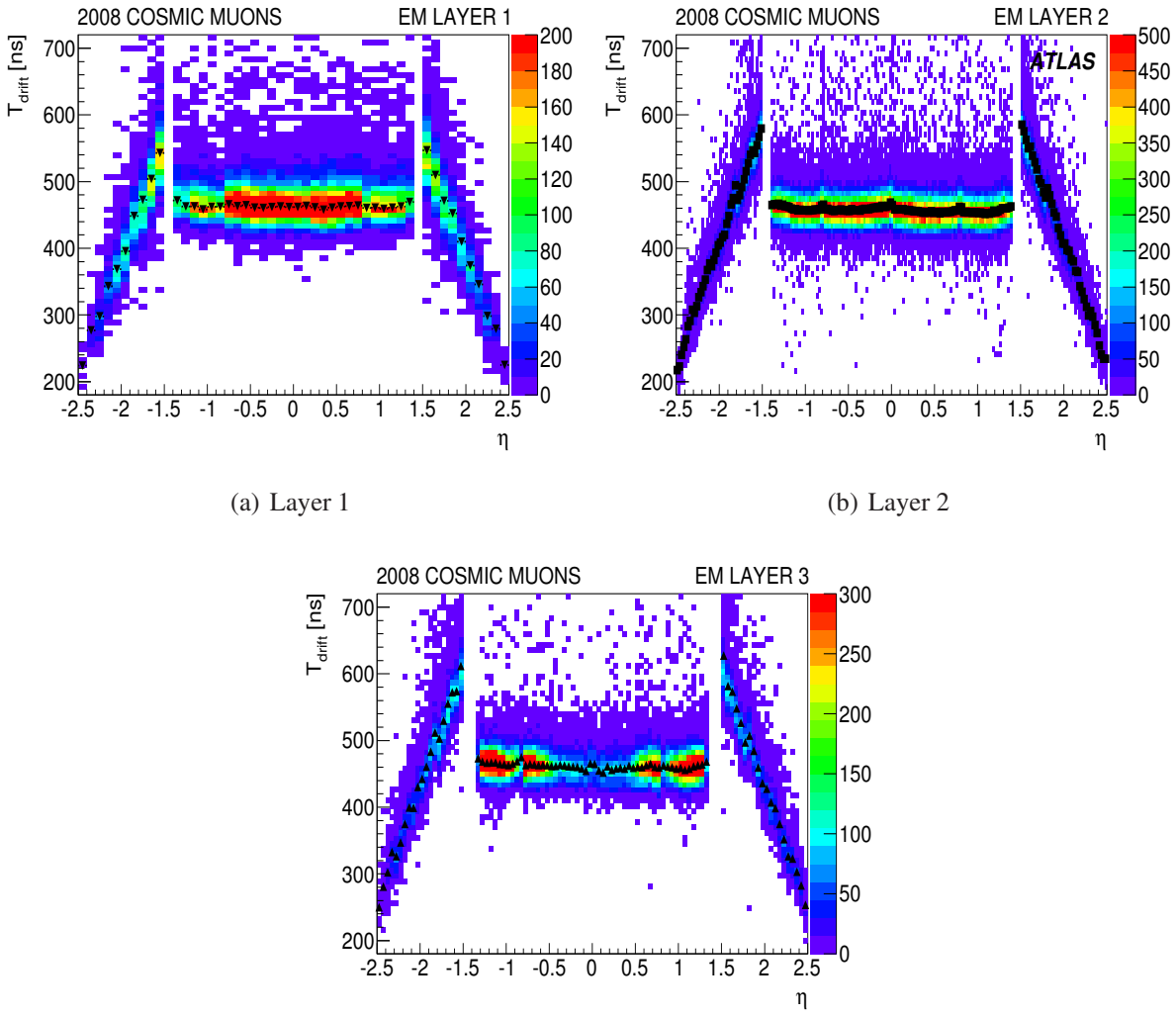


(a) Layer 1

(b) Layer 2

(c) Layer 3

Figure 6.19: Drift time versus pseudorapidity for the Front (a), Middle (b) and Back (c) layers of the electromagnetic calorimeter. Profile values (black points) are obtained by a weighted average, being the weight = $S^2_{max}$.

#### 6.5.2.1 EM barrel

In the EMB the LAr gap size is designed to be constant (2.09 mm) independently of $\eta$. The drift time is then expected to be constant, except for the presence of local non-uniformities. Figure 6.20 shows $T_{drift}$ as a function of $\eta$ for the EMB Front, Middle and Back layer. Differences from the average behavior are mostly observed at $\eta = \pm 0, \pm 0.8, 1.4$, where $\eta = 0$ corresponds to the transition between two barrels, $\eta = 0.8$ is the boundary between Electrode A and Electrode B and at $\eta = 1.4$ the crack region end of the Barrel. In all of these cases the electric field is lower, hence the drift time increases with respect to the average values.

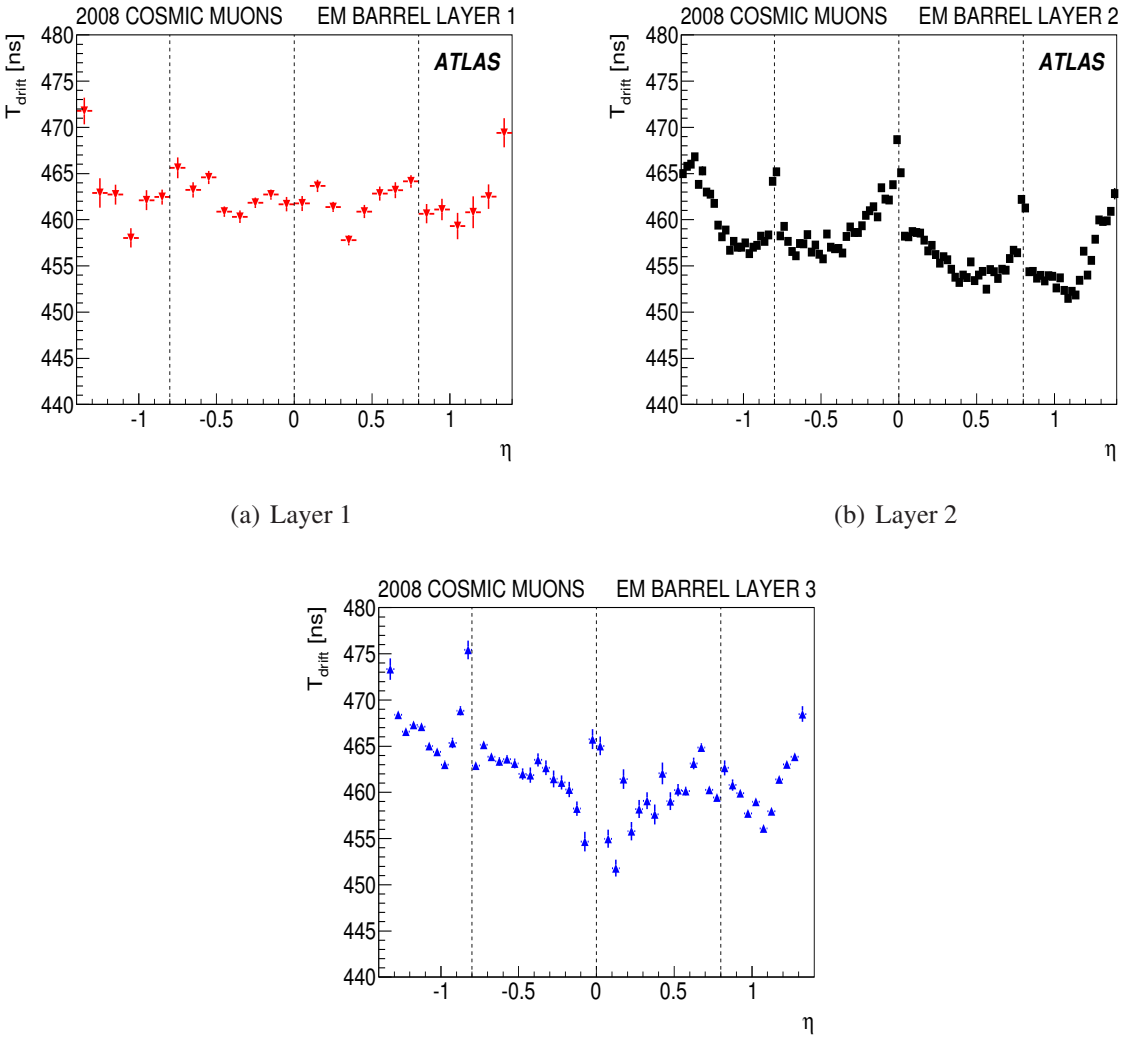


(a) Layer 1

(b) Layer 2

(c) Layer 3

Figure 6.20: Drift time versus pseudo-rapidity for front (a), middle (b), and back (c) cells of the EMB. Profile values are obtained by a weighted average, being the weight = $S^2_{max}$. The number of selected hits are 39,558 in layer 1, 315,317 in layer 2 and 71,075 in layer 3.

A positive-negative η effect is also observed: $T_{drift}$ is higher for $\eta < 0$ than for $\eta > 0$ half barrel. In particular, for layer 2 a difference in the average values between $\eta < 0$ (459.8 ns) and $\eta > 0$ (455.9 ns) can be noticed in Figure 6.20(b). This may be due to the existence of small modulations with opposite phases in the two half-barrels that appear to be more visible in the $(\eta, \phi)$ map of layer 3 (see Section 6.5.4).

In the EMB the value of $T_{drift}$ is supposed to be independent of the layer, because all layers share the same gap sizes. Figure 6.21 shows a reasonable agreement between the drift time values of the three layers.

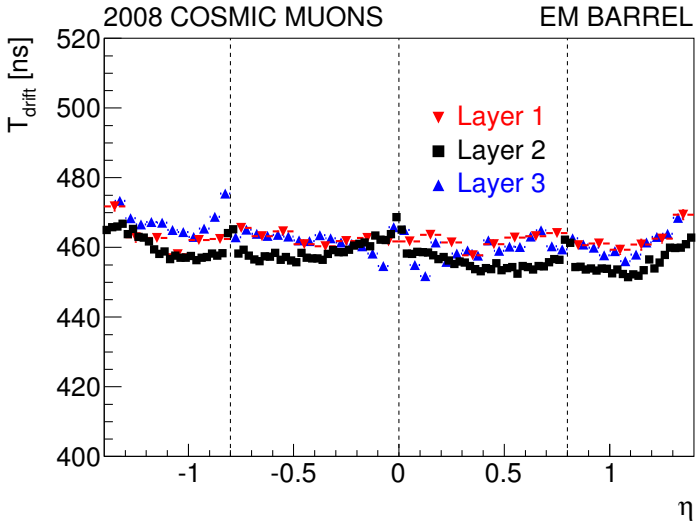


Figure 6.21: Drift time versus pseudo-rapidity for the three layer of the EMB: Front (down triangles), Middle (squares), Back (up triangles).

Table 6.5 shows the RMS and mean values for the drift time in η direction. The relative effect between the two half-barrels can be extracted for the middle layer: $0.9\% \pm 0.1\%$.

| Layer | η region | Mean | RMS |
|---|---|---|---|
| Front | $\lvert\eta\rvert < 1.4$ | $462.5 \pm 0.5$ | $2.8 \pm 0.4$ |
| | $\eta < 0$ | $462.9 \pm 0.8$ | $3.0 \pm 0.6$ |
| | $\eta > 0$ | $462.1 \pm 0.7$ | $2.6 \pm 0.5$ |
| Middle | $\lvert\eta\rvert < 1.4$ | $457.8 \pm 0.3$ | $3.7 \pm 0.2$ |
| | $\eta < 0$ | $459.8 \pm 0.4$ | $3.3 \pm 0.3$ |
| | $\eta > 0$ | $455.9 \pm 0.4$ | $3.0 \pm 0.3$ |
| Back | $\lvert\eta\rvert < 1.4$ | $462.3 \pm 0.6$ | $4.3 \pm 0.4$ |
| | $\eta < 0$ | $464.4 \pm 0.8$ | $4.1 \pm 0.5$ |
| | $\eta > 0$ | $460.1 \pm 0.6$ | $3.4 \pm 0.5$ |

Table 6.5: Summary of the RMS and mean values for the drift time in η direction for all layers of the EMB.

### 6.5.2.2 EM endcap

The measured drift time in the EMEC cells is shown in Figure 6.22, where the data from both the A and C wheels are combined. The points for the Middle layer are more stable due to the higher statistics. In all layers regular steps are observed at $\eta = 1.6, 1.8, 2.0, 2.1, 2.3$, corresponding to the location of the boundaries between high voltage regions (Figure 4.8). When the high voltage decreases from one region at lower $\eta$ to the next one at higher $\eta$, drift electrons take more time to reach the electrode, hence the drift time increases.

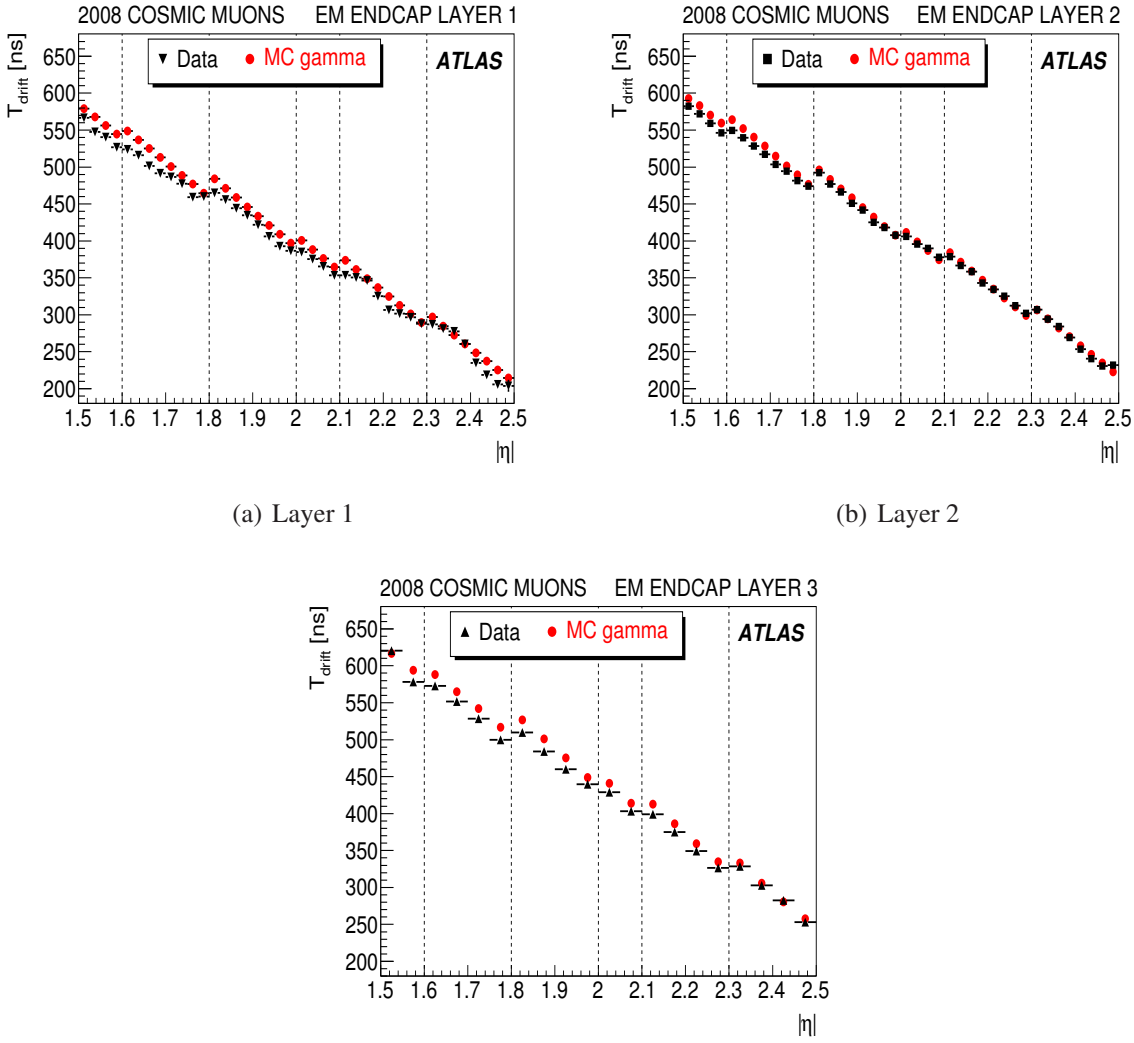


(a) Layer 1

(b) Layer 2

(c) Layer 3

Figure 6.22: Drift time versus pseudo-rapidity for front (a), middle (b), and back (c) cells of the EMEC. Red points are the data and black points corresponds to the Monte Carlo for photons. The data values are obtained by a weighted average, being the weight = $S^2_{max}$. The number of selected hits are 11,934 in layer 1, 42,837 in layer 2 and 16,845 in layer 3.

In Figure 6.22 the data is compared with the Monte Carlo calculation described in Section 6.3. A good agreement is observed for the Middle and Back layers, despite the fact that there are several effects which are not modeled in the Monte Carlo simulation (e.g. the gravitational deformations). However, the Monte Carlo points are slightly higher ($\sim 3$ %) than the data ones at low $\eta$ for the Front layer. This may be due to the difference in the direction of incidence between the simulated photons and the cosmic muons. The former are projective to the nominal ATLAS interaction point, whereas the latter enter the calorimeter almost perpendicular to the $z$ axis. The simulated photon showers have their maximum deposition of energy near the last bend of the Front layer, hence larger drift time, while cosmic photon showers are more evenly distributed in the Front layer.

A comparison of the averaged $T_{drift}$ for the three layers is shown in Figure 6.23. An increase of the drift time with the cell gap size is clearly observed, with $T_{drift}$ being smallest for the Front layer and highest for the Back layer. The drift time for the Middle layer lies half way between the Front and Back layers in contrast to the Monte Carlo simulation (Figure 6.5(a)) where the values for the Middle are closer to the values of the Front layer. This can be explained by the highly non-projectivity of cosmic muons, which leads to photon showers more evenly distributed across the cells than the Monte Carlo photons.

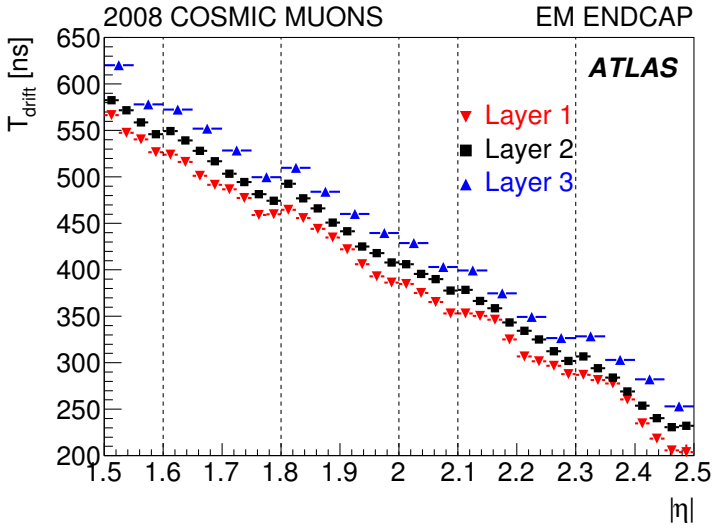


Figure 6.23: Drift time versus pseudo-rapidity for the three layers of the EMEC: Front (down triangles), Middle (squares), Back (up triangles).

Ideally the drift time should be the same for both EMEC wheels, however a difference is observed in the present data. To obtain any conclusion about this difference, sufficient statistics are needed in the whole $\eta$ range, hence only the Middle layer is considered. It turns out that the profile points of the Middle layer for $\eta > 0$ are mostly above those for $\eta < 0$ (see Figure 6.19). To unfold fluctuations, the drift time variation in each wheel can be fitted by a first order polynomial $T_{drift}(|\eta|) = a + b|\eta|$. The relative difference $(T_{drift}(A) - T_{drift}(C))/T_{drift}(A)$ obtained by subtracting the two polynomials is about $(0.5 \pm 0.5)$ % independent of pseudo-rapidity. The drift time for wheel A is larger than for wheel C: this difference can be attributed to the difference of the LAr temperature between the wheels, that has been measured to be 300 mK

higher in endcap A (88.7 K) than in endcap C (88.4 K). This temperature difference approximately corresponds to a 0.5 % difference in drift velocity and hence in drift time. Although the precision of the $(T_{drift}(A) - T_{drift}(C))/T_{drift}(A)$ measurement does not permit a quantitative statement, the fact that $T_{drift}(A) > T_{drift}(C)$ is endorse by the drift velocity extracted from $T_{drift}$ (see Figure 6.30 of Section 6.5.5), since $V_{drift} \sim \frac{1}{T_{drift}}$.

### 6.5.3 Drift time uniformity along azimuth

The drift time $T_{drift}$ obtained from the fitting procedure correspond to the contribution from the flat part of the accordion. Ideally this quantity is symmetric in azimuth; however two mechanical effects can break the symmetry: a modulation of absorber thickness, and the positioning or deformation of the calorimeter due to gravity. The study of the drift time as a function of $\phi$ may detect such effects, which could be unfolded during the signal reconstruction procedure, thus improving the global response uniformity of the calorimeter.

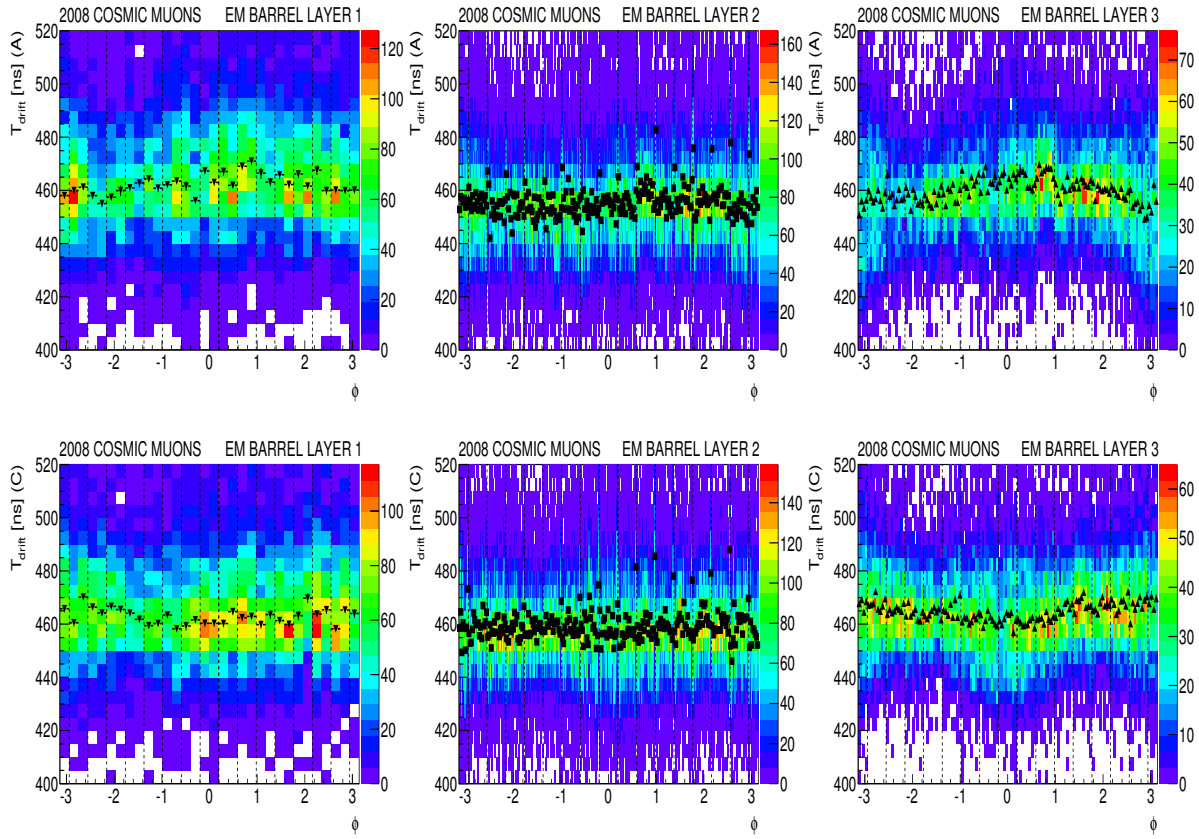


Figure 6.24: Drift time vs $\phi$ for Front(left), Middle(center) and Back(right) layers of the EMB calorimeter. Profile values (black points) are obtained by a weighted average, being the weight $= S^2_{max}$.

Figure 6.24 for the EMB and Figure 6.25 for the EMEC wheels show the drift time $T_{drift}$ as a function of azimuth for the Front, Middle and Back layers. The two half-barrels as well as the two EMEC wheels are shown separately. Bin sizes are chosen such that the number of

events per bin is approximately the same for all plots. For the EMEC wheels the values of $T_{drift}$ for each given pseudo-rapidity have been normalized to the average in order to cancel the dependence with $\eta$. An asymmetry is observed between positive and negative values of $\phi$: $T_{drift}(\phi > 0)$ is larger than $T_{drift}(\phi < 0)$. This effect is clearly observed in the two EMEC wheels, and it is also present in the EMB although is smaller. Since $\phi < 0$ is the lower half of the calorimeter, gravity may compress this part leading to slightly smaller gaps than in the upper half $\phi > 0$: this could explain the different $T_{drift}$ values for the EMEC. The vertical dashed lines indicate the boundaries between modules. Larger values of $T_{drift}$ are observed between EMB modules which correspond to higher gap sizes (see Figure 6.24 Middle). A clear modulation is observed in the EMB Back layer with opposite phases in the two half-barrels.

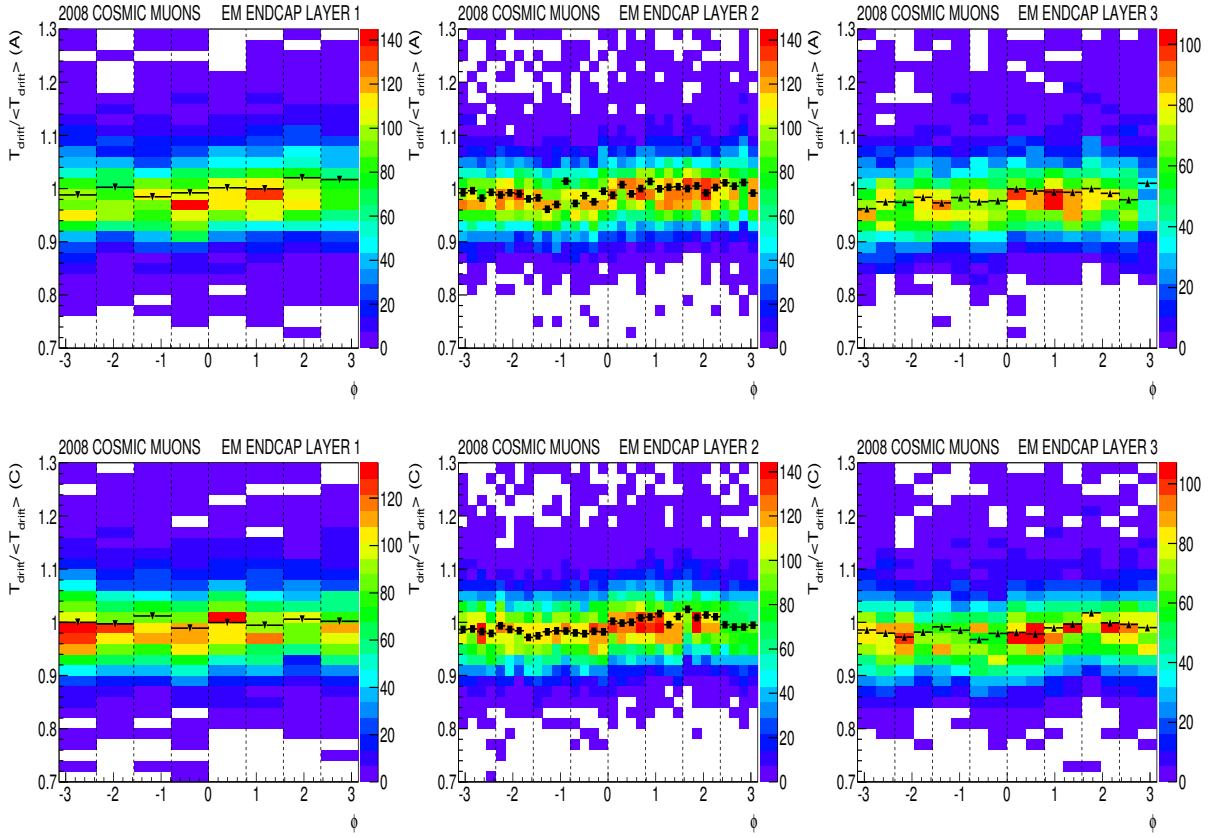


Figure 6.25: Drift time vs $\phi$ for Front(left), Middle(center) and Back(right) layers of the EMEC calorimeter. Profile values (black points) are obtained by a weighted average, being the weight $= S^2_{max}$.

Part of the observed fluctuations can be attributed to the finite number of events used in the fits. In particular in the EMEC the presence of highly non-projective cosmic events may influence the drift time value, because of the variation of the gap size with depth. This effect is enhanced by the fact that there is typically only one event per cell. This effect is less critical in the EMB because the gap size does not depend on depth, most cosmic events have a good projectivity and the global number of events is much higher than in the EMEC. Table 6.6 shows the RMS and mean values for the drift time in $\phi$ direction, joining the two sides of the calorimeter.

| Calorimeter | Layer | $\eta$ region | Mean | RMS |
|---|---|---|---|---|
| | | $\lvert\phi\rvert < \pi$ | $462.6 \pm 0.3$ | $1.6 \pm 0.2$ |
| | Front | $\phi < 0$ | $461.8 \pm 0.3$ | $1.1 \pm 0.2$ |
| | | $\phi > 0$ | $463.4 \pm 0.4$ | $1.7 \pm 0.3$ |
| | | $\lvert\phi\rvert < \pi$ | $457.6 \pm 0.2$ | $3.9 \pm 0.2$ |
| EMB | Middle | $\phi < 0$ | $456.8 \pm 0.3$ | $3.1 \pm 0.2$ |
| | | $\phi > 0$ | $458.3 \pm 0.3$ | $4.0 \pm 0.3$ |
| | | $\lvert\phi\rvert < \pi$ | $462.6 \pm 0.2$ | $2.0 \pm 0.1$ |
| | Back | $\phi < 0$ | $462.1 \pm 0.2$ | $1.9 \pm 0.2$ |
| | | $\phi > 0$ | $463.2 \pm 0.2$ | $2.0 \pm 0.2$ |
| | | $\lvert\phi\rvert < \pi$ | $1.001 \pm 0.003$ | $0.007 \pm 0.002$ |
| | Front | $\phi < 0$ | $0.995 \pm 0.001$ | $0.003 \pm 0.001$ |
| | | $\phi > 0$ | $1.006 \pm 0.004$ | $0.006 \pm 0.002$ |
| | | $\lvert\phi\rvert < \pi$ | $0.993 \pm 0.002$ | $0.012 \pm 0.001$ |
| EMEC | Middle | $\phi < 0$ | $0.980 \pm 0.002$ | $0.007 \pm 0.001$ |
| | | $\phi > 0$ | $0.996 \pm 0.001$ | $0.005 \pm 0.001$ |
| | | $\lvert\phi\rvert < \pi$ | $0.986 \pm 0.002$ | $0.010 \pm 0.002$ |
| | Back | $\phi < 0$ | $0.978 \pm 0.002$ | $0.005 \pm 0.001$ |
| | | $\phi > 0$ | $0.994 \pm 0.002$ | $0.006 \pm 0.002$ |

Table 6.6: Summary of the RMS and mean values for the drift time in $\phi$ direction for all layers of the EM calorimeter.

In order to disentangle the sources of the non-uniformities of the $T_{drift}$ values, the $T_{drift}$ measurements are converted into gap variations. The drift time $T_{drift}$ is in fact approximately proportional to the gap size:

$$\frac{T_{drift}}{T_{drift0}} = \left(\frac{w_{gap}}{w_{gap0}}\right)^{(1+\alpha)} \tag{6.24}$$

From the ratio $T_{drift}/T_{drift0}$, where $T_{drift0}$ is a certain reference value, the relative variation of the gap size $w_{gap}/w_{gap0}$ can then be extracted using the relation:

$$\frac{w_{gap}}{w_{gap0}} = \left(\frac{T_{drift}}{T_{drift0}}\right)^{\frac{1}{(1+\alpha)}} \tag{6.25}$$

Figure 6.26 shows the distribution of $w_{gap}/w_{gap0}$ for the EMEC and the EMB. The widths of the distributions are 2 % and 1 % for the EMEC and EMB respectively. These values are of the order of the absorber thickness tolerance (about 1 %), being a bit higher for the EMEC due to the larger fluctuations in the data discussed above.

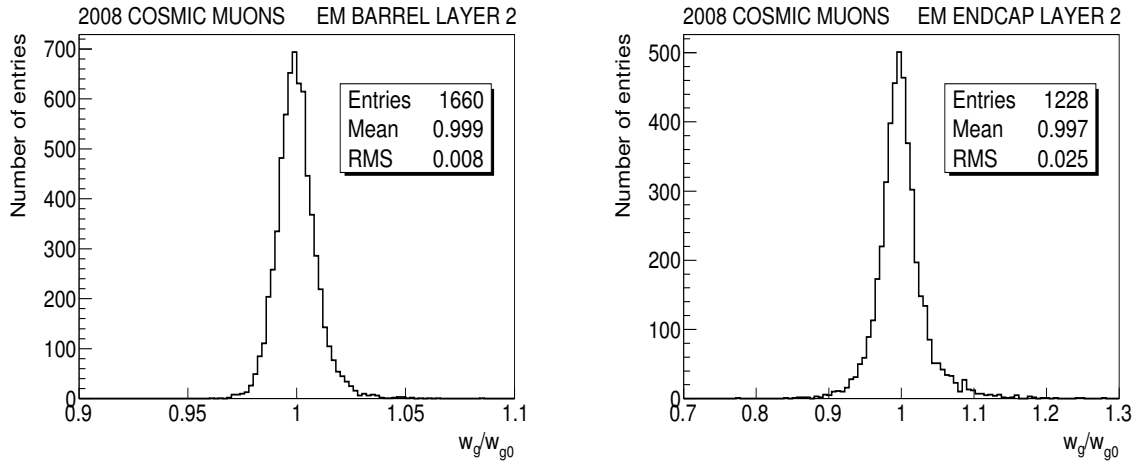


(a) EM barrel (b) EM endcap

Figure 6.26: Distribution of $w_{gap}/w_{gap0}$ for middle layer of the barrel (a) and endcap (b) calorimeter.

### 6.5.4 Response uniformity

When an electron or a photon coming from any physics process impact the calorimeter, a cluster of cells is built to contain most of its shower energy. The reconstructed cluster energy should be independent of the impact position on the calorimeter. The non-uniformity coming from intrinsic fluctuations of the calorimeter can be determined using the drift time measurements.

The measured drift time per cell is integrated over regions of size $0.1 \times 0.1$ - the nominal size of a trigger tower in the EMC - on the $(\eta, \phi)$ plane, and shown in Figure 6.27 for the different layers. These plots can be used to identify malfunctioning regions as well as unusual patterns. For instance, an unexpected pattern is observed in the Back layer of the EMB as a modulation along $\phi$ (blue regions). The fact that the modulations in the two half-barrels are in opposite phase may be related to a mechanical property, since the two half-barrels are mechanically identical, but were placed into the cryostat after a $180^0$ rotation around the vertical axis with respect to each other.

Figure 6.28 shows the distribution of $T_{drift}$ in clusters $0.1 \times 0.1$ for the EMEC (a) and EMB (b) for the Middle layer. In the case of the EMEC, first order polynomials are fit to the average drift time in each high voltage region (see Figure 6.23), which are used to normalize the drift time in order to cancel the variation with eta due to the design gap size variation. This study is carried out only for the Middle layer since it contains most of the shower energy (typically $> 70$ %) for ordinary LHC electrons and photons. In addition, more cosmic events have been recorded in the Middle than in the other layers, which lowers the statistical error of the measurement.

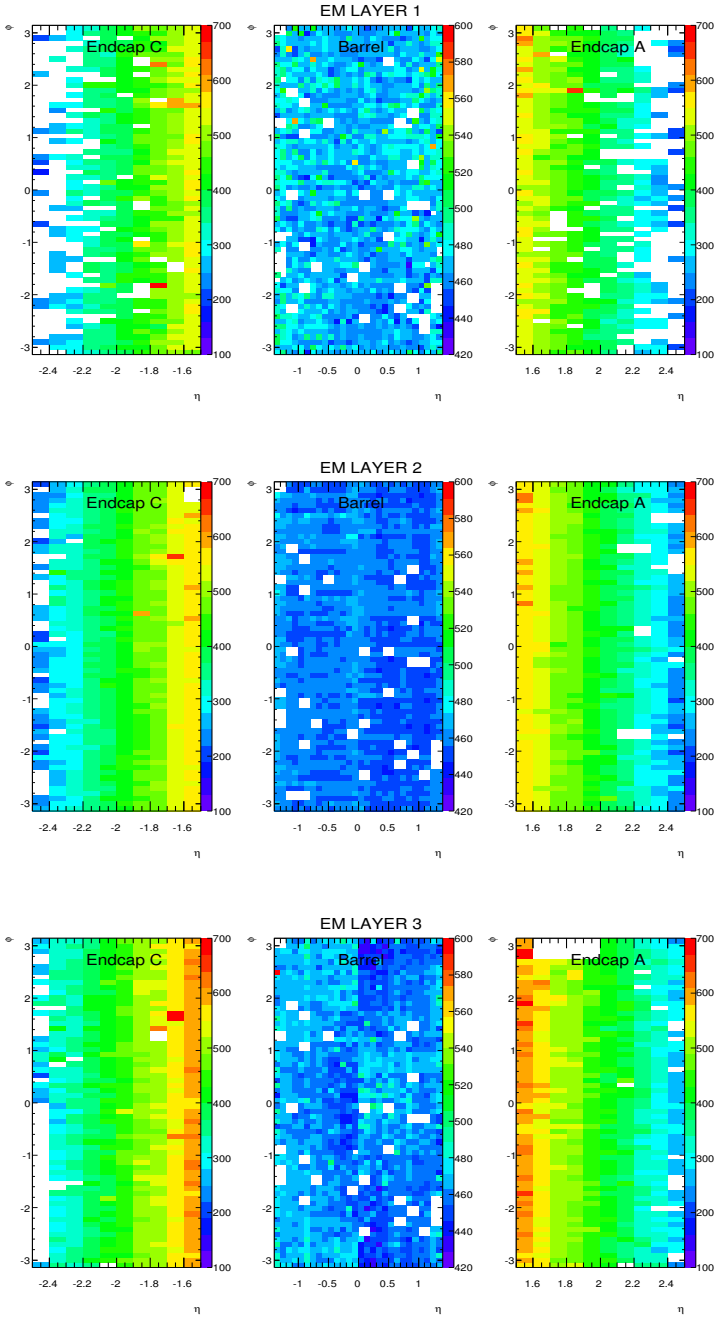


Figure 6.27: Mapping η -ϕ of the drift time measurement for front(top), middle(center) and back(bottom) for the EM calorimeter

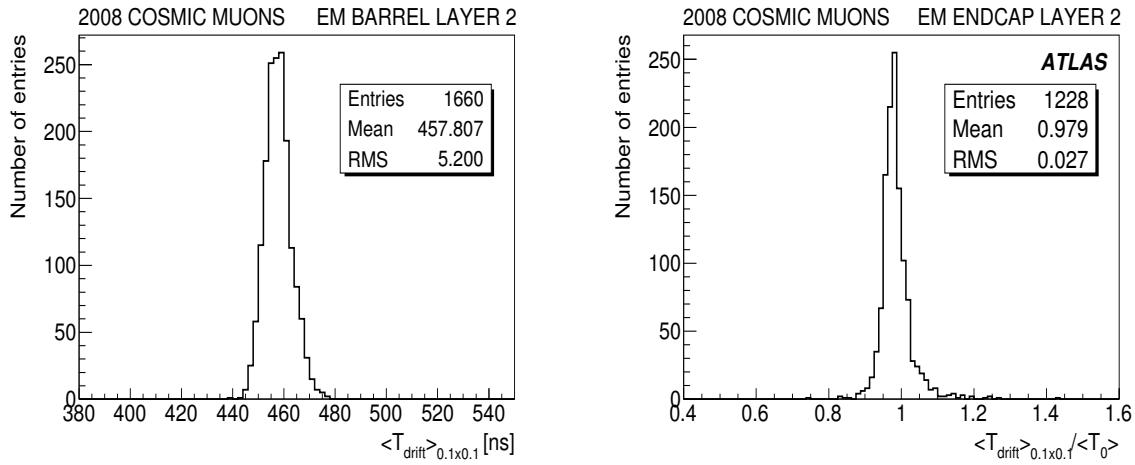


(a) EM barrel (b) EM endcap

Figure 6.28: Drift time uniformity within a cluster $0.1 \times 0.1$ in ($\Delta\eta \times \Delta\phi$ ) plane for barrel (a) and endcap (b) middle layer.

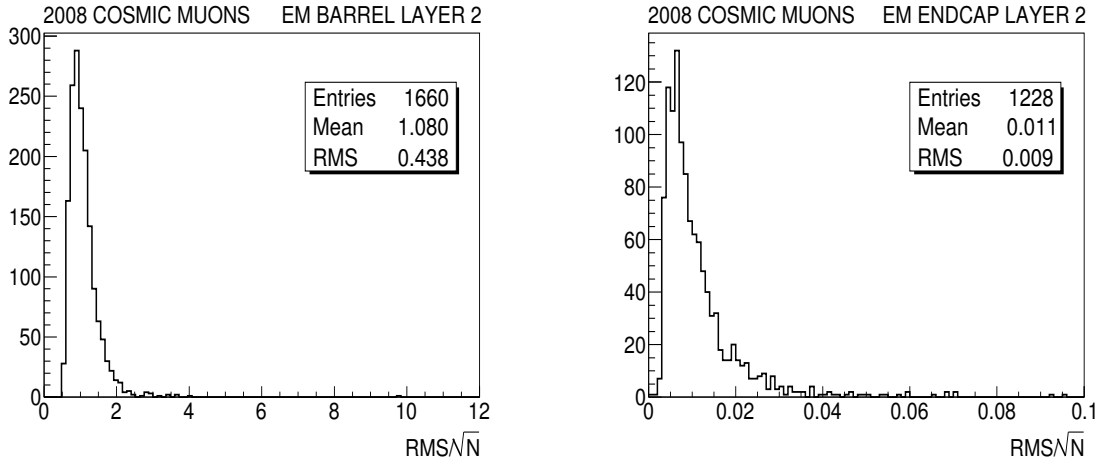


(a) EM barrel (b) EM endcap

Figure 6.29: $RMS/\sqrt{N}$ within a cluster $0.1 \times 0.1$ in ($\Delta\eta \times \Delta\phi$ ) plane for barrel (a) and endcap (b) middle layer.

To obtain the non-uniformity from the RMS of the $< T_{drift} >_{0.1\times0.1}$ distribution the contribution from pure statistical fluctuations must be subtracted. Figure 6.29 shows the distribution of RMS/$\sqrt{N}$ within a $0.1 \times 0.1$ cluster, namely

$$e_k = \frac{1}{N}\sqrt{\sum_{i=1}^{N}(T_{drift}^{(i)} - < T_{drift} >_{0.1\times0.1})^2} \tag{6.26}$$

for a given cluster $k$, where $N$ is the number of cells in the cluster. The square of the RMS, from the distribution of Figure 6.29, is

$$S^2 = \frac{1}{N_c}\sum_{k=1}^{N_c} e_k^2 - m^2 \tag{6.27}$$

where $N_c$ is the number of clusters.

The mean of the $< T_{drift} >_{0.1\times0.1}$ distribution is $\frac{1}{N_c}\sum_{k=1}^{N_c} < T_{drift} >_k$ which error is $\frac{1}{N_c}\sqrt{\sum_{k=1}^{N_c} e_k^2}$. Hence the RMS of the $< T_{drift} >_{0.1\times0.1}$ distribution, assuming pure statistical fluctuations only, is:

$$\sqrt{N_c}\frac{1}{N_c}\sqrt{\sum_{k=1}^{N_c} e_k^2} = \sqrt{S^2 + m^2} \tag{6.28}$$

Therefore, the drift time uniformity is $\frac{\sqrt{(5.2)^2-(1.08)^2-(0.438)^2}}{457.807} = (1.11 \pm 0.03)\%$ for the EMB and $\frac{\sqrt{(0.027)^2-(0.011)^2-(0.009)^2}}{0.979} = (2.3 \pm 0.1)\%$ for the EMEC.

This figures translate [3] to an uniformity of the calorimeter response due to intrinsic gap variations of $(0.26 \pm 0.01)\%$ and $(0.53 \pm 0.02)\%$ for the EMB and EMEC respectively, compatible with results obtained from beam test using electrons of known energy [45, 46].

### 6.5.5 Drift Velocity

The drift velocity can be obtained from the drift time measurement using Equation 6.1 where the nominal values for $w_{gap}$ are used. While $w_{gap}$ is constant for the EMB, it depends on $\eta$ for the EMEC where in addition there are different high voltage regions; a comparison of the drift velocity between different calorimeter sectors is then not possible since they may have different electric fields. In order to compare $V_{drift}$ for barrel and endcap, a "universal" determination must instead be adopted. Due to the fact that the drift velocity is approximately proportional to the electric field to the power $\alpha$ (Equation 6.4), the actual drift velocity can be scaled to a reference field of 1 kV/mm:

$$V_{drift}(1\ \mathrm{kV/mm}) = \frac{\mathrm{w_{gap}}}{\mathrm{T_{drift}}}\left[\frac{1000\,\mathrm{V}}{1\,\mathrm{mm}}\ \frac{\mathrm{w_{gap}}}{\mathrm{HV}}\right]^{\alpha} \tag{6.29}$$

[3] $\sigma(T_{drift})$ is about four times $\sigma$ of the response, since $T_{drift}$ is about four times more sensitive to gap variations than the signal

Hence, the drift velocity $V_{drift}$ for an electric field of 1 KV/mm can be used on equal footing for both barrel and endcap. As a consistency check the universal quantity $V_{drift}$ must be uniform along the whole EM calorimeter. It should also be similar for the three layers Front, Middle and Back.

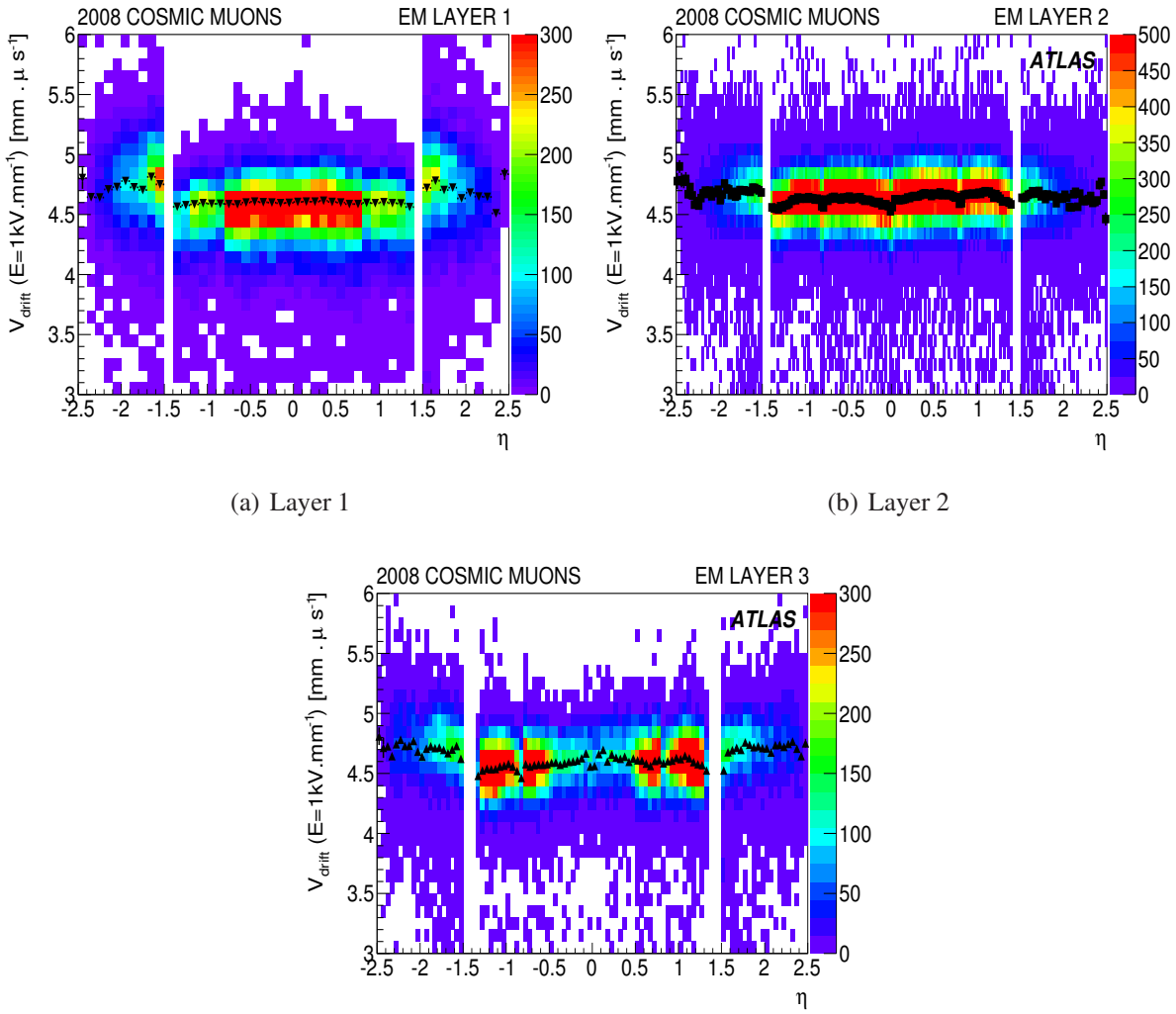


(a) Layer 1

(b) Layer 2

(c) Layer 3

Figure 6.30: Drift Velocity (at $E = 1$ kV/mm) as a function of $\eta$ for front (a), middle (b) and back (c) layers of the EM calorimeter.

Figure 6.30 shows $V_{drift}$ for the whole electromagnetic calorimeter as a function of $\eta$ for the three layers. A rather flat behavior is observed as expected. The values of $V_{drift}$ (at $E = 1$ kV/mm) for EMEC wheel C are higher than for wheel A. This can be interpreted as a difference in the LAr temperature between the wheels, as it has been explained already in Section 6.5.2. The deviation from a perfect horizontal line may be explained as local non-uniformities within a cell which are not canceled out in the computation of $V_{drift}$. In fact, both $w_{gap}$ and $T_{drift}$ are average quantities inside the whole volume of a cell.

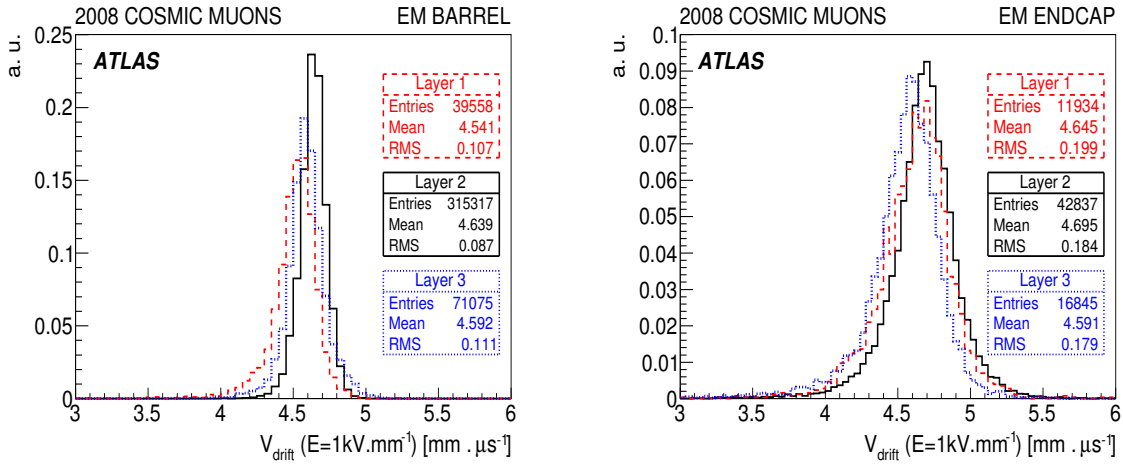


(a) EM barrel (b) EM endcap

Figure 6.31: Drift Velocity distribution for the Front, Middle, Back layers for barrel (a) and endcap (b).

Figure 6.31 shows the comparison of $V_{drift}$ for the three different layers. The mean values of the distributions are also quoted; the statistical errors on these means are much smaller than the systematic uncertainties. According to Equation 6.29, $V_{drift}$ uncertainty depends both on uncertainties on the gap size and on the drift time. The former can be extracted from Figure 6.26, being about 1 % and 2 % for the EMB and EMEC respectively. The latter is about 0.5 % (see Section 6.5.8). Hence, a systematic error of 1.1 % and 2.1 % for EMB and EMEC respectively is expected for the mean value of $V_{drift}$. The drift velocity mean values for the different layers of the EMB and EMEC are given in Table 6.7. They all agree within these errors.

| | EMB | EMEC |
|---|---|---|
| Front | $4.54 \pm 0.05$ | $4.65 \pm 0.10$ |
| Middle | $4.64 \pm 0.05$ | $4.69 \pm 0.10$ |
| Back | $4.59 \pm 0.05$ | $4.59 \pm 0.10$ |

Table 6.7: Average drift velocity $< V_{D1} >$ in $mm/\mu s$ for the three layers of EMB and EMEC.

The average of the layer 2 values of the barrel and endcap, for which most of the systematics are uncorrelated (see Section 6.5.8), is:

$$V_{drift0} = (4.66 \pm 0.07)\ \mathrm{mm}/\mu\mathrm{s} \tag{6.30}$$

for the reference electric field of 1 kV/mm and a LAr temperature of $88.5K$, which corresponds to the average value measures during the cosmic run period.

The empirical formula obtained in [34], for the same electric field and LAr temperature, gives $4.65\mathrm{mm}/\mu\mathrm{s}$, in good agreement with the present measurement.

### 6.5.6 Direct determination of local gap and drift velocity at operating point

Using Equation 6.1 and Equation 6.4 it is possible to express the gap size as a function of the measured $T_{drift}$, namely:

$$\begin{aligned} &\frac{w_{gap}}{T_{drift}} = V_{drift} = V_{drift0}(\frac{HV}{HV_0}\frac{w_{gap0}}{w_{gap}})^{\alpha} = V_{drift0}(\frac{HV}{HV_0})^{\alpha} w_{gap0}^{\alpha} \frac{1}{w_{gap}^{\alpha}} \\ &\Rightarrow w_{gap}^{1+\alpha} = T_{drift} V_{drift0}(\frac{HV}{HV_0})^{\alpha} w_{gap0}^{\alpha} \Longrightarrow w_{gap} = \left(T_{drift} V_{drift0}(\frac{HV}{HV_0})^{\alpha} w_{gap0}^{\alpha}\right)^{\frac{1}{1+\alpha}} \end{aligned} \tag{6.31}$$

This formula can also be obtained from Equation 6.25 replacing $T_{drift0}$ by its relation with $V_{drift0}$. The analysis presented below corresponds to layer 2 only, which has the highest number of events. The gap size should not depend on the reference, which has been taken as $w_{gap0} =$ 1 mm, $HV_0 = 1$ kV and $V_{drift0} = 4.66$ mm/$\mu$ for both Barrel and Endcaps. Data for the endcaps have been corrected for the temperature difference, and rescaled to 88.5 K.

Figure 6.32 shows the relative difference between the calculated gap sizes from previous formula and the design values as a function of pseudorapidity. In general, a reasonable agreement is observed apart from some local effects at "transition regions", $\eta = 0$, $\pm 0.8$ and $\pm 1.4$, already discussed in Section 6.5.2.1. It is also observed that the gap size is a bit lower in the Barrel for positive values of $\eta$ than for negative values of $\eta$. The same effect was observed in Figure 6.20(b) and was attributed to possible modulations with opposite phases in the two half-barrels. In the endcaps the statistical power is unfortunately lower giving rise to larger fluctuations, but no significant trend is observed.

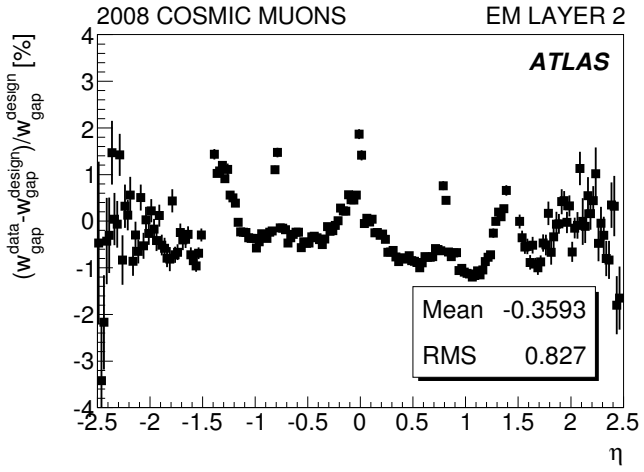


Figure 6.32: Relative difference between the design gap values and the values extracted from $T_{drift}$ measurements.

The drift velocity can be obtained from Equation 6.1 using as gap size the one calculated from Equation 6.31. The result is plotted in Figure 6.33 as a function of pseudorapidity. As opposed to Figure 6.30, which gave the speed at a reference field of 1kV/mm, Figure 6.33

shows the drift speed at the local operating field, which is directly related to the peak current associated with an energy deposition.

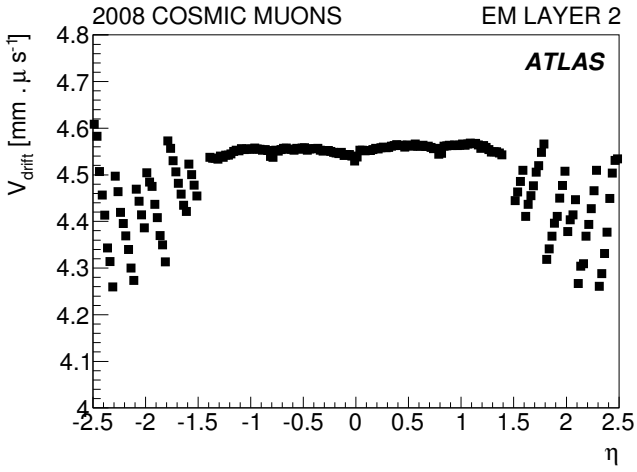


Figure 6.33: Drift velocity versus η in the layer 2 at the operating point extracted from $T_{drift}$ measurements.

In the barrel region, the drift velocity is essentially flat, with a slight modulation reflecting the variation of the absorber thickness with pseudorapidity. In the endcap region, one observes the 6 sawteeth on each side resulting from the finite granularity of the HV distribution (see Figure 4.8). Corrections are made in the energy reconstruction to normalize the response of each strip in pseudorapidity to the response of the strip in the center of the HV sector, using the power law dependence. Beside these modulations, one observes that:

- the average speed in the endcaps is smaller than in the barrel. In the energy reconstruction this is accounted for by a global normalization factor (which also takes into account the fact that the lead thicknesses are different) determined from beam and implemented in the detailed Monte Carlo simulation of the full ATLAS detector.

- the measured speed averaged over an HV sector somewhat diminishes with increasing pseudorapidity. This effect goes in the same direction (lowering the response) as the reduced contribution of liquid argon to showering/conversion effects at large pseudorapidities (small gaps). Both effects are qualitatively counterbalanced by the fact that the relative contribution of bends as compared to flat parts is lower at high pseudorapidity, resulting in an increased response. As already mentioned, detailed Monte Carlo simulations normalized with test beam scans were used to determine the HV values optimizing the uniformity of response of the endcaps. This will be cross checked when enough $Z^0 \rightarrow e^+e^-$ decays become available.

### 6.5.7 Electrode shift

The honeycomb spacers were cut with a thickness lower than the nominal gap size. This effect, combined with their mechanical thickness tolerance, gives some freedom to the electrodes to be displaced with respect to the geometrical center between two consecutive absorbers. This displacement is expected to be less than 400 $\mu$m except perhaps in the transition regions between modules.

The electrode shift is left as a free parameter in the fitting procedure to cosmic data (see Section 6.2.2), to obtain a value per calorimeter cell. Only the absolute value of the movement is accounted for. Since a cell consists of several electrodes (3 for the Middle, 12 for the Front layers in the EMEC for example) an effective value is obtained which encompasses the real absolute movement of each electrode within a cell.

The distributions of the electrode shift are shown in Figure 6.34 for the three layers of the EMB and EMEC. The average, about 145 $\mu$m, is rather independent of the layer and very similar for EMB and EMEC. The peak at zero represent events where the minimization program could not find a clear minimum for this shift parameter. These events are kept in the global $T_{drift}$ determination because the drift time fit values are anyway reasonable.

For high energy deposits (more than 800 ADC counts) the noise fluctuations are negligible and the fit quality is generally better. In particular the spike at zero is significantly decreased, as can be seen from Figure 6.35. The shift distributions of the three layers are superimposed in Figure 6.35: the average values of the different layers agree very well in the EMB while they show some differences for the layer 1 of the EMEC for which no explanation has been found.

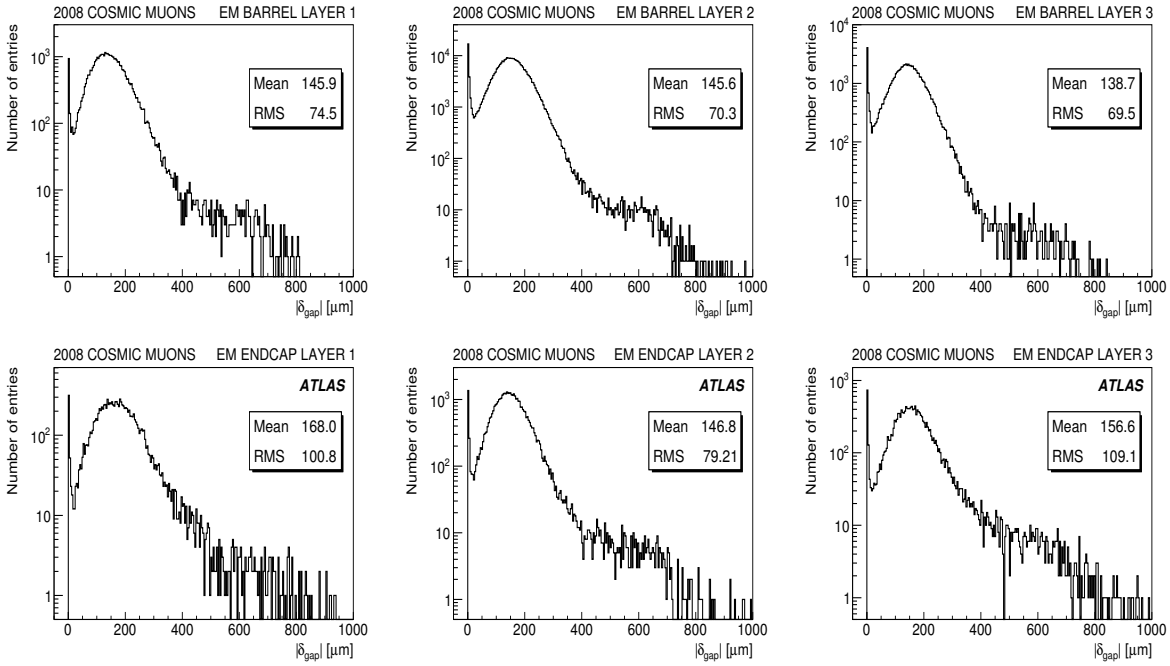


Figure 6.34: Electrode shift distributions for front(left), middle(center) and back(right) for the EMB (top) and EMEC(bottom) calorimeter.

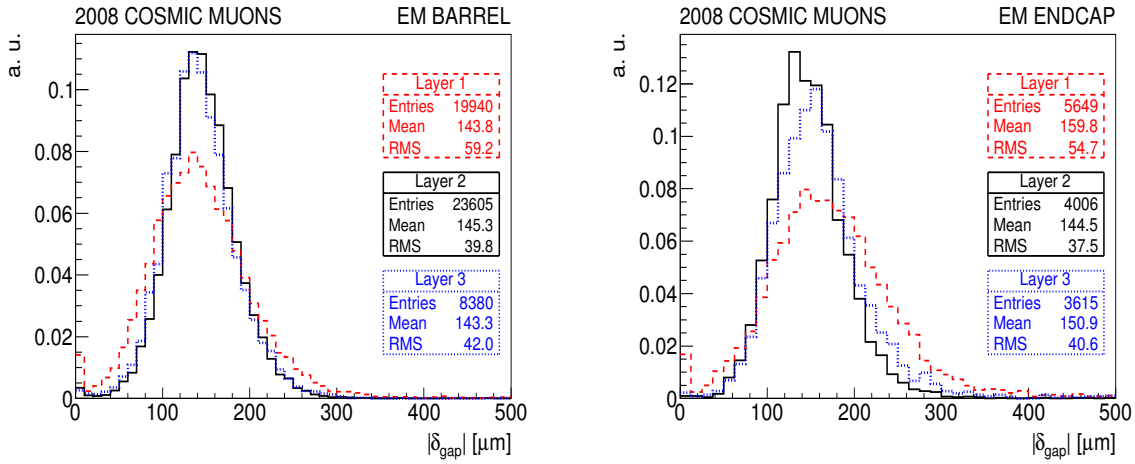


(a) EM barrel (b) EM endcap

Figure 6.35: Electrode shift distributions for cells with more than 800 ADC counts for the Front (red), Middle (black) and Back (blue) layers of the EMB (a) and the EMEC (b) calorimeters.

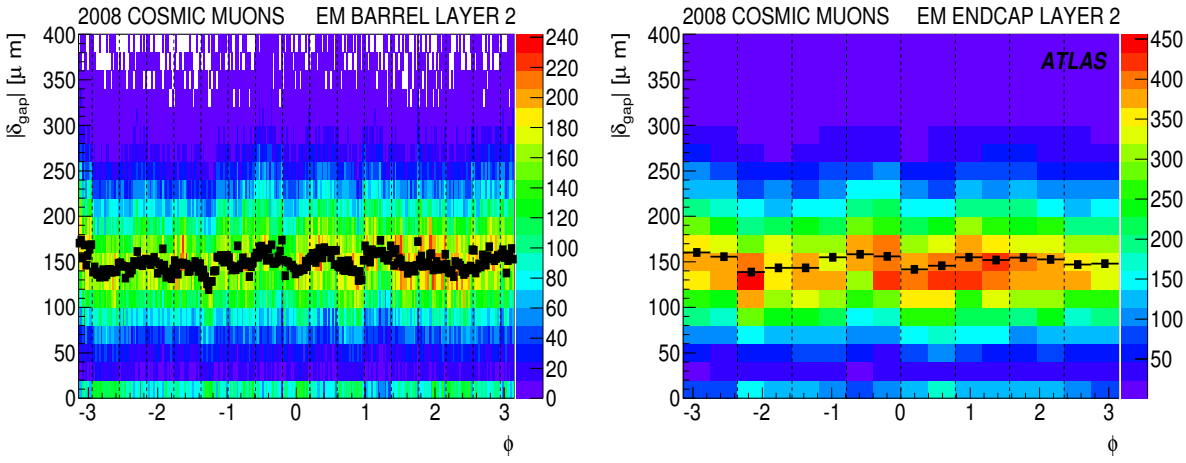


(a) EM barrel (b) EM endcap

Figure 6.36: Shift along ϕ for EMB (a) and EMEC (b) middle layer. Profile values are obtained by a weighted average, being the weight = $S^2_{max}$.

The behavior of the electrode shift along azimuth is studied in Figure 6.36, only for the Middle layer,for both EMEC and EMB. A rather flat behavior is observed. Vertical dashed lines correspond to the boundaries between consecutive modules. No particular increase of the shift is observed at these transitions, even extending the scale to 1000 $\mu$m.

In principle the measured values of the drift time and of the electrode shift should be uncorrelated. Figure 6.37 shows the scatter plots of these two fit quantities for the Middle layer in the EMEC and the EMB. In general an absence of correlation is observed, aside from few events with high or lower values of both shift and drift time parameters showing a large positive correlation.

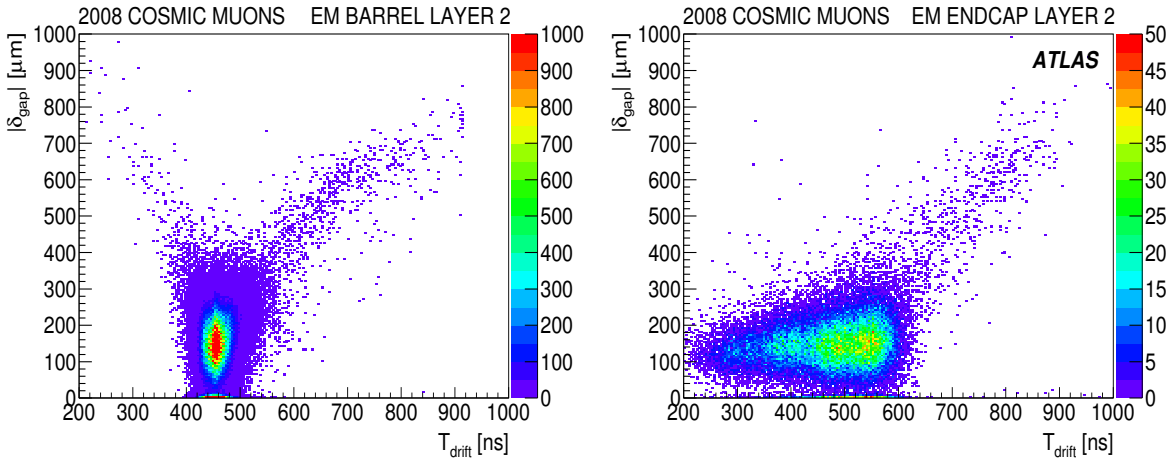


(a) EM barrel

(b) EM endcap

Figure 6.37: Shift versus drift time for all Middle cells of the EMB (a) and the EMEC (b).

The region in Figure 6.37(a) with a drift time $T_{drift}$ comprised between 380 and 550 ns corresponds to the expected range for the drift time in the barrel given the resolution of the measurement. The low drift time region $T_{drift} < 380$ ns of Figure 6.37(a) (0.05 % of the pulses) is dominated by low-amplitude pulses. A closer examination shows that large signals ($S_{max} >$ 1500 ADC) are found as first neighbors in about 80 % of cases for the layer 2 barrel, which corroborates a crosstalk hypothesis.

In the region $T_{drift} > 550$ ns of Figure 6.37(a) (0.25 % of the pulses), some pulses are still significantly negative, more than 700 ns after the time of signal maximum. A possible explanation is that the energy deposit originates from a photon emitted along a bent section, thus having an abnormally enhanced $f_{bend}$ contribution. Unfortunately the runs taken with 32 samples do not contain information from the inner tracker which would have allowed this hypothesis to be validated by a projectivity study. Aside from these extremely large drift time pulses, there is a larger class of pulses which are only somewhat longer than normal. They are distributed along specific $\eta$ and $\phi$ directions: in the transition regions at $|\eta| = 0.8$ and between the two half-barrels at $\eta = 0$ (see Figure 6.19(b)) where a slight dilution or leakage of the electric field lines yields a larger drift time; in the intermodular regions in $\phi$ in the upper part of the detector (see Figure 6.24), where mechanical assembly tolerances allow for a slightly

increased gap at the interface between modules due to gravity effects.

In the endcap, the cloud of points corresponding to the expected $T_{drift}$ is broader than in the barrel, as can be seen in Figure 6.37(b): it ranges from 300 to 600 ns. This is a consequence of the gap size variation with $\eta$ of the endcap design. The fact that the dispersion of $|\delta_{gap}|$ is larger at higher values of $T_{drift}$ is explained as a consequence of the larger gap size: the larger the gap width, the larger the displacement of the electrode can be. A few events (0.9 % of the pulses) are observed at very high values of both $T_{drift}$ and $|\delta_{gap}|$. They are located at low $|\eta|$ where the drift time is very large by construction (see Figure 6.5(a)). Their pulse shape cannot be completely readout using 32 samples, and in particular the rise following the undershoot is partially absent, which leads to unphysical values of the shift above 400 $\mu$m.

### 6.5.8 Systematic uncertainties

The effect of some systematic uncertainties on the final $T_{drift}$ result has been studied. In general, a small impact on the final results is observed.

- The physics pulse shape $g^{\text{phys}}$ is predicted from the calibration signal $g^{\text{cali}}(t)$ following Equation 5.16. The calibration pulse $g^{cali}(t)$ is not a continuous function but rather samples every $\sim$ ns. This implies the use of a numerical calculation of the convolutions in Equation 5.16, with a step of $\sim 1$ ns. The finite precision of these numerical convolutions can be propagated to the drift time value obtained by the fitting procedure. In fact, the parameter $\chi^2_{\text{fit}}$ of Equation 6.22 appears to be a discontinuous function of $T_{drift}$ due to the staggered function $g^{cali}(t)$. This fact makes more difficult to calculate the error on $T_{drift}$ from the fit, which is estimated $< 1$ ns by using a smoothing procedure.

  The other systematic uncertainties discussed in the following points which gives about $\sim 0.2$ %, cannot be distinguished from the one discussed here since it corresponds to about 1 *ns*.

- The drift time $T_{bend}$ in the accordion bends and its relative weight to the total current $f_{bend}$ are determined for the EMEC using a Monte Carlo simulation of 10 GeV photon showers. The Monte Carlo prediction for the drift time distribution contains both $T_{drift}$ of the flat and $T_{bend}$ of the bend regions (Figure 6.4), with $T_{cut}$ the inflection point separating both regions. The uncertainty on the value of $T_{cut}$ is smaller than 2 % for the Middle and Front layers and $\sim 4$ % for the Back layer.

  Using a fit to obtain $T_{drift}$ from cosmic data while changing the value of $T_{cut}$ according to the previous interval changes the values of $T_{drift}$ for each $\eta$ cell of the Middle layer (Figure 6.22) by about 0.2 % (0.4 %) for the Middle and Front (Back) layers.

  For the EMB, the $T_{bend}$ and $f_{bend}$ values are obtained using Monte Carlo assuming a uniform charge distribution along the cell. However the longitudinal profile of photon showers is not uniform: this may introduce a difference in the value of $f_{bend}$ since the bend angle changes with depth inside an EMB cell. The estimated change in $f_{bend}$ is about 3 % in the Middle layer which leads to an uncertainty of less than 0.2 % in $T_{drift}$.

- The electrical circuit parameters needed in Equation 5.16 to predict the physics pulse shape were extracted from the measured calibration pulse $g^{cali}(t)$, cell by cell using the RTM method (see Section 5.3). The estimated uncertainty for the $\tau_{\text{cali}}$ and $\omega_0$ parameters is assumed to be $\sim 3$ %. The determination of $T_{drift}$ is repeated after having modifying these parameters within their quoted uncertainty. The values of $T_{drift}$ are affected by about 0.5 % from the $\tau_{cali}$ uncertainty, and less than 0.1 % from the $\omega_0$ variation.

- A correction of the calibration pulse for the skin-effect on the calibration line is added to the algorithm to predict the physics pulse. The effect on the final result for $T_{drift}$ is found to be negligible.

- Throughout this work a relation between the drift velocity and the electric field is assumed (see Equation 6.4), which differs slightly from the empirical formula of [34]. The neglected terms contribute less than 0.2 %.

- During the beam test of the Module 0 calorimeter prototype for the EMEC, the energy reconstructed for 120 GeV electrons in a $5 \times 5$ cluster of cells was studied as a function of the high voltage [50]. This represented a measurement of the power $\alpha$ relating the drift velocity and the electrical field. The result was $\alpha = 0.39$. This value differs from the one obtained in [34]. The reason could be related to the gap size variation in the EMEC. A Monte Carlo calculation of the drift velocity as a function of the gap (see Equation 6.4) seems to confirm this explanation: the averaged $V_{drift}$ over the whole volume of a Middle cell yields larger values of $\alpha$ (and close to 0.39) than the average over a small sector covering only a portion of the flat part of the accordion.

  For the present study, the value $\alpha = 0.3$ is used for both EMB and EMEC. In the case of the EMB this value is optimal, hence the impact in the results of a possible wrong value for $\alpha$ is studied only for the EMEC. The drift time resulting from the fit procedure using $\alpha = 0.39$ is compared with $T_{drift}$ obtained employing $\alpha = 0.3$. The difference is found about 1 ns ($\sim 0.2$ %), at the level of the precision of the measurement.

  The power $\alpha$ has been used in Equations 6.25 and 6.29 for the gap non-uniformities and the drift velocity respectively. The effect of changing the power from 0.3 to 0.39 leads to a tiny effect in the results at the level of 0.2 %.

## 6.6 Conclusions

The average electron drift time in each cell of the highly granular LAr electromagnetic calorimeter of ATLAS, is measured from the samples of shaped ionization pulses induced by high energy deposits from cosmic muons recorded during the 2008 commissioning run. The pulses were recorded in a wide time window (32 samples) to assure the required precision of the measurement.

The drift time measurement has shown to be a powerful tool to detect asymmetries and intrinsic non-uniformities along the calorimeter. Transition regions are clearly distinguished both along: i) the $\eta$-direction, i.e. between the two barrel wheels, at the transition from electrode A to B of the barrel, in the zone between barrel and endcap, and at the boundaries between

the high voltage regions in the endcap, and ii) the $\phi$-direction, i.e. at the boundaries between modules.

The drift time is $\sim 4$ times more sensitive to gap variations than the drift velocity and thus the recorded energy. Taking advantage of these fact, an intrinsic non-uniformity of response due to gap size variations has been inferred, namely $\sim 0.26\%$ and $\sim 0.53\%$ respectively for the barrel and the endcaps. The other main contribution to the intrinsic non-uniformity of the calorimeter is the dispersion of the thickness of the lead absorbers which contributes 0.18 % for both barrel and endcaps [31, 32].

The drift velocity at 1 kV/mm is extracted from the drift time measurement, resulting in $4.59 \pm (0.05)_{\text{syst}}$ mm/$\mu$s and $4.65 \pm (0.10)_{\text{syst}}$ mm/$\mu$s for the barrel and endcap respectively. These results are in good agreement with the expectation corresponding to the average LAr temperature of 88.5 K measured during the run period.

The analysis method used to derive the drift time provides as another parameter the average absolute value of the amount the electrodes are off center between their two neighboring absorbers. Electrodes are found to be shifted with respect to their nominal central position by $\sim 146$ $\mu$m on average in both barrel and endcap, with a RMS of $\sim 40$ $\mu$m.

Since the actual value of the drift time enters the LAr electronic calibration in several points (e.g. OFC, current-to-energy conversion factors), the measurements presented in this analysis can be used to improve the EM calorimeter energy reconstruction. At the same time, these measurements will be used to correct for the measured gap variations in order to eventually reduce the constant term of the energy resolution.

# 7

# $W' \rightarrow e\nu$ discovery with early data

The ATLAS discovery potential of a new heavy charged spin 1 gauge boson, denoted $W'$, has already been studied in [11], using full potentiality of ATLAS detector with 14 TeV LHC data. Recent studies [51], repeating the CSC [1] analysis and taking into account the reduced LHC center-of-mass energy of 7 TeV in the first months of data taking early 2010, show that an integrated luminosity around 50 pb$^{-1}$ should be sufficient to discover a $W'$ slightly beyond the actual 1 TeV Tevatron limit [52]. This study shows that the expected number of signal events is $S \sim 20$ with a signal-to-background ratio of $S/B > 50$. This is therefore a straightforward analysis provided electron and $\not\!\!E_T$ reconstruction are under control. The subject of this chapter is to include realistic detector conditions of the setup foreseen for the earliest data taken, for the performance of both the electron and the missing transverse energy ($\not\!\!E_T$ ) reconstruction, and study their impact on the $W' \rightarrow e\nu$ discovery potential.

The complexity of the $\not\!\!E_T$ reconstruction in the early data is mainly due to the Monte Carlo dependence of the calibration and of the cryostat (rear wall between the electromagnetic and hadronic calorimeters) contribution, and to the muon reconstruction efficiency, which will need some time and data to be fully mastered ($e.g.$ to minimize fake muon contribution to $\not\!\!E_T$ tails). We therefore consider in this analysis a $\not\!\!E_T$ measurement based on calorimeter information only and discuss the impact of such a choice on the $W' \rightarrow e\nu$ discovery potential. This term is already well under control in present commissioning data (random data and cosmics), as explained in Section 7.2, while Section 7.1 recalls the simulation data set used in the analysis. Sections 7.4 and 7.5 is dedicated to the evaluation of the discovery potential of $W' \rightarrow e\nu$ when using the calorimetric definition of $\not\!\!E_T$ , which is compared to an analysis based on the full potentiality of ATLAS detector. We use the well known standard $W \rightarrow e\nu$ as control sample and perform a similar selection comparing $W$ and $W'$ results at each stage of the analysis.

[1] Computing System Commissioning executed during 2008. Millions of Monte Carlo events of different physics channels were produced on the ATLAS Grid which were useful for physics analysis.

## 7.1 Monte Carlo Samples

Several models predict a $W'$ : Grand Unified Theories, various Left-Right Symmetric Models, Kaluza Klein Theories, Little Higgs Models, Dynamical Symmetry Breaking Models and models inspired by Superstrings. In this analysis, the study is restricted to a 1 TeV $W' \rightarrow e\nu$ predicted by the Extended Gauge Model (see Section 2.2), where the W' has "Standard Model like" couplings to fermions and does not decay in WZ bosons. Its cross section at $\sqrt{s} = 10$ TeV is predicted to be around 4.7 pb. It should be noted that 1 TeV is a compromise between what the ATLAS could be sensitive to at LHC startup (first year at $\sqrt{s} = 7$ TeV) and the Tevatron current exclusion region [52].

All the samples used in this analysis are generated for a center-of-mass energy of 10 TeV. A full detector simulation, based on a distorted and misaligned geometry (ATLAS-GEO-02-01-00) is used and the ATLAS software corresponds to version 14.5.0. Associated cross sections, number of simulated events and the corresponding integrated luminosities, for both signal and background, are summarized in Table 7.1.

| Process (Generator) | Filter (efficiency) | $\sigma$ in pb (k-factor) | Events ($\times 10^3$) | L (pb$^{-1}$) |
|---|---|---|---|---|
| $W' \rightarrow e\nu$ (P) | none | 4.678 (1.37) | 48 | 104000 |
| $W \rightarrow e\nu$ (P) | $200 < M_T < 500$ | 12.6 (1.22) | 50 | 4000 |
| $W \rightarrow e\nu$ (P) | $M_T > 500$ | 0.39 (1.22) | 50 | 120000 |
| Dijet J0 (P) | $8 < \hat{p_T} < 17$ | $1.17 \times 10^{10}$ | 1000 | $8 \times 10^{-5}$ |
| Dijet J1 (P) | $17 < \hat{p_T} < 35$ | $8.67 \times 10^{8}$ | 1000 | $11 \times 10^{-4}$ |
| Dijet J2 (P) | $135 < \hat{p_T} < 70$ | $5.60 \times 10^{7}$ | 1000 | $17 \times 10^{-3}$ |
| Dijet J3 (P) | $70 < \hat{p_T} < 140$ | $3.28 \times 10^{6}$ | 1400 | 0.4 |
| Dijet J4 (P) | $140 < \hat{p_T} < 280$ | $1.528 \times 10^{5}$ | 1000 | 6.4 |
| Dijet J5 (P) | $280 < \hat{p_T} < 560$ | $5.12 \times 10^{3}$ | 1400 | 271.4 |
| Dijet J6 (P) | $560 < \hat{p_T} < 1120$ | $1.12 \times 10^{2}$ | 400 | 4000 |
| Dijet J7 (P) | $1120 < \hat{p_T} < 2240$ | 1.075 | 400000 | 400 |
| Dijet J8 (P) | $\hat{p_T} > 2240$ | $1.112 \times 10^{-3}$ | 400 | 44000000 |
| $W \rightarrow e\nu$ inclusive (P) | $\mid \eta \mid < 2.7$ (0.88) | 11754.4 | 4000 | 350 |
| $W \rightarrow \tau\nu$ (P) | $\mid \eta \mid < 2.7$ (0.87) | 4160.0 | 400 | 30 |
| Dijet JF17 (P) | $E_T^{cone} > 17\ GeV$ (0.0706) | $1453.6 \times 10^{6}$ | 7000 | 0.004 |
| $t\bar{t}$ semi-leptonic (Mc) | none | 205.28 | 1700 | 8500 |
| $t\bar{t}$ full hadronic (Mc) | none | 168.12 | 1000 | 5500 |

Table 7.1: Characteristics of fully simulated mc08 data samples at center-of-mass energy of 10 TeV for W' and its backgrounds (Upper part of the Table), W and its backgrounds (Center part) and the common backgrounds (Lower part) reconstructed with version 14.5.0 of the ATLAS software. $\hat{p_T}$ is the transverse momentum of the partons in their rest frame, while $M_T$ is the transverse mass of the electron and neutrino. $k-factor$ is the ratio between: $\sigma^{NLO}/\sigma^{LO}$ and $E_T^{cone}$ refers to the transverse energy in a cone of size $\Delta\eta \times \Delta\phi = 0.12 \times 0.12$. Different generator are used to produce these MC samples: Pythia (P), McAtNlo (Mc) and Alpgen (Al) (see Section 2.3).

Backgrounds to the $W' \rightarrow e\nu$ considered in the present analysis include processes with the following final states: $W \rightarrow e\nu$, $W \rightarrow \tau\nu$ , QCD dijets and $t\bar{t}$, where dijets corresponds to all quarks except the Top. The first one has the same final state as the signal, however with a different kinematics due to the much smaller mass: $M_w << M_{w'}$. Two special samples have been generated for this purpose, namely $200 < M_T < 500$ and $M_T > 500$, to populate the region of transverse masses of the $W'$ decay products, in order to minimize the computing time of the Monte Carlo production. At the generator level $M_T$ refers to the invariant mass of the electron and neutrino on the transverse plane. The corresponding cross sections quoted on Table 7.1 take into account the efficiencies. The last three may have real or fake electron and missing transverse energy ($\not\!\!E_T$ ). For example, muons in the final state give rise to a $\not\!\!E_T$ if only the calorimeter information is considered in the reconstruction, since muons deposit only part of its energy in the calorimeter. The Dijet sample is split in nine bins of the transverse momentum of the partons in their rest frame ($\hat{pT}$) which are labeled as $J_i$ with $i$ =0,8.

Apart from background to the heavy boson signal, the standard $W \rightarrow e\nu$ is also considered as a control sample, since it has the same final state as the $W'$ and similar backgrounds, despite the mass region is quite different. Therefore, results for both $W'$ and $W$ will be carried out in parallel along this chapter. The following backgrounds to the $W \rightarrow e\nu$ have been taken into account: $W \rightarrow \tau\nu$ , QCD dijets and $t\bar{t}$. A dedicated sample for Dijets is used, namely: events which have at least one cluster of energetic final state particles in a cone of size $\Delta\eta \times \Delta\phi = 0.12 \times 0.12$, such that the transverse in the cone ($E_T^{cone}$) is greater than 17 GeV. This filter is applied at the generator Pythia level to minimize the computing time. The efficiency of the filter, 0.0706, has to be multiplied by the cross section quoted on Table 7.1 to compared with the signal.

## 7.2 Measurement of the missing transverse energy

In the Standard Model the only particle which goes undetected through ATLAS is the neutrino. Its presence can be derived by measuring the missing transverse energy $\not\!\!E_T$ , that is the unbalanced energy in the transverse plane. Assuming a hypothetical detector covering perfectly the entire ($\eta$,$\phi$) plane, the $\not\!\!E_T$ is the $p_T$ of the missing particles. Complications start when multiple neutrinos are present, there is no way of deriving the different $p_T$'s from one $\not\!\!E_T$ measurement. An accurate measurement of the $\not\!\!E_T$ is needed to fully reconstruct the event and lead to a good signature for new physics. The following definitions are used along this chapter, the first one being the total transverse energy and the last one the missing transverse energy for each event:

$$\begin{cases} \sum E_T = \sum_{i=1}^{N_{cell}} E_i.sin\theta_i \\ \not\!\!E_x = -\sum_{i=1}^{N_{cell}} E_i \sin\theta_i \cos\varphi_i, \\ \not\!\!E_y = -\sum_{i=1}^{N_{cell}} E_i \sin\theta_i \sin\varphi_i, \\ \not\!\!E_T = \sqrt{(\not\!\!E_x)^2 + (\not\!\!E_y)^2}. \end{cases} \tag{7.1}$$

where $N_{cell}$ is the total number of calorimeter cells, each centered at $(\theta_i, \phi_i)$ and with an energy $E_i$ above a certain threshold (see Section 7.2.1).

There are two methods in ATLAS to determine the $\not\!\!E_T$ . The **Object-based** algorithm starts from the reconstructed, calibrated and classified objects in the event, taking also into account the deposits outside these objects. The **Cell-based** algorithm starts from the energy deposits in the calorimeter cells. The last procedure is expected to be robust even for the initial data taking and it is therefore used throughout this analysis.

As it is explained in Section 4.3, the calorimeter is designed such that it covers as much as possible of the ($\eta$,$\phi$) plane. However the beam-pipe hole makes unfeasible the measurement of the longitudinal energy present in the hard-scattering, hence we are restricted to a transverse energy measurement.

The method to reconstruct the energy in the cells of the calorimeter system is based, as a first step, on a digital filtering algorithm of the readout signal (see Section 5.1). Even with a stable calorimeter operation and good control of problematic cells (see Appendix A), a bias in the energy scale reconstructed in a cell can alter the $\not\!\!E_T$ performance. However, we have demonstrated in this thesis (see Chapter 5) that the impact of the energy reconstruction accuracy on the constant term of the energy resolution is below 0.7 % over the full EM calorimeter coverage and similar results are extracted for the hadronic calorimeter [53]. Therefore, the impact of such uncertainty on the $\not\!\!E_T$ can be considered negligible.

The main contribution to fake $\not\!\!E_T$ , that is missing transverse energy which is not lead by neutrinos, are:

- **Noise**: The electronic noise in the EM and Tile calorimeters is in the range $10-50$ MeV depending on the layer, while it is typically a factor 10 greater in the endcap hadronic and forward calorimeters. Another crucial issue for the $\not\!\!E_T$ computation is the pedestal stability. As an example, a variation of the cell pedestals by 1 MeV (negligible compared to the noise) in the EM calorimeter, where 92 % of the calorimeter cells are located, may lead to a variation of $\sum E_T$ of about 10 GeV [54]. Figure 7.1 shows the pedestal stability in the front-end electronic board (128 channels) of the LAr EM calorimeter over a period of 6 months. Pedestal variation follows a Gaussian distribution with a standard deviation of 0.02 ADC counts, i.e. of the order of 0.1 MeV. As residual cell-to-cell variation can still occur, pedestals will be taken between fills during LHC running to be confident.

- **Missed and fake muons**: Muons can sometimes escape detection, especially in the gap regions of the muon spectrometer. Fake muons can be caused for example by high $p_T$ jet punch-through from the calorimeter to the muon spectrometer.

- **Jet leakage**: This is a jet energy which is not deposited in the calorimeter, but for example in the muon spectrometer (without faking a muon) or in the cryostat. The reconstruction algorithm can compensate on average for the latter, but the large fluctuations in these deposits can still cause fake $\not\!\!E_T$ .

- **Mismeasured jets**: Due to mis-calibration of jets, or because of jets passing through the gaps in the calorimeter. Although some corrections are applied in the measured jet energies, the resolution in these areas is worse.

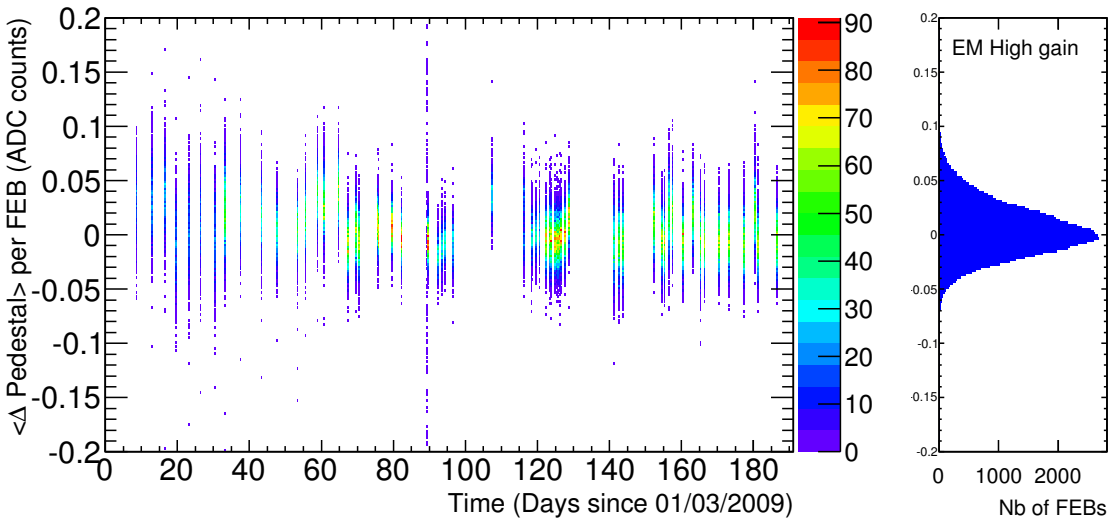


Figure 7.1: Pedestal time stability in LAr EM calorimeter over 6 months. Each entry is averaged of pedestal over 128 cell of a front-end electronic board (FEBs).

Most of these contributions can be kept to a minimum by a good selection and calibration of calorimeter cells. Fake muons are kept to a minimum by using information from the Inner Detector, missed muons are however more difficult to compensate for.

### 7.2.1 Cell-based reconstruction

The cell-based $\not{E}_T$ reconstruction method accounts for several contributions, as sketched in Figure 7.2 : one from the energy depositions in the calorimeter system ($\not{E}_T^{Calo}$), one from measured muons in the muon spectrometer and the ID ($\not{E}_T^{Muon}$) and one from losses in dead material, mainly the cryostat ($\not{E}_T^{Cryo}$) rear walls. The component in the $x$ and $y$ direction are thus given by:

$$\not{E}_{x,y}^{Final} = \not{E}_{x,y}^{Muon} + \not{E}_{x,y}^{Cryo} + \not{E}_{x,y}^{Calo} \tag{7.2}$$

The $\not{E}_T^{Muon}$ is calculated from all muons measured in the rapidity range $|\eta| < 2.7$. To reduce the amount of fake muons, the muon has to be matched to a track in the ID. With the ID covering the range up to $|\eta| < 2.5$, muons with $2.5 < |\eta| < 2.7$ are free of this requirement.

The cryostat between the LAr EM barrel and the Tile calorimeter is thick enough for hadronic showers to loose non-negligible amounts of energy. The $\not{E}_T^{Cryo}$ recovers this loss of energy in the cryostat using the correlation of energies between the layer 3 of the LAr calorimeter and the layer 1 of the hadronic calorimeter. A similar correction for the endcap cryostats is applied, see [11].

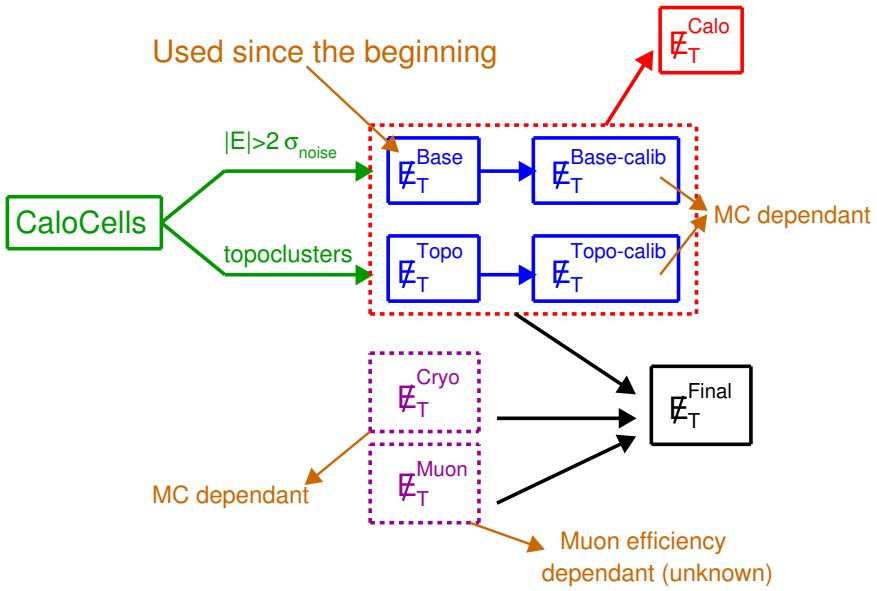


Figure 7.2: Scheme of the ATLAS $\not\!\!E_T$ reconstruction in the cell-based approach.

The calorimeter contribution, $\not\!\!E_T^{Calo}$ , sums the calibrated energy (currently with Monte Carlo weights taking into account the non-compensation of the calorimeters and the energy losses in dead regions of the calorimeters [11]) of all the cells passing a noise suppression cut. Because of the high granularity of the calorimeters it is crucial to suppress noise contributions to $\not\!\!E_T$ . In ATLAS, this is done with two methods:

- **cell-based method** ($\not\!\!E_T^{Base}$) selecting cells above a noise threshold of two standard deviations ($|E| > 2 * \sigma_{noise}$).
- **cluster-based method** ($\not\!\!E_T^{Topo}$) taking cells belonging to topological clusters built around $|E| > 4\sigma_{noise}$ seeds, gathering neighboring cells with $|E| > 2\sigma_{noise}$.

In ATLAS, useful commissioning have been performed using events triggered randomly [55, 53] that allow to compare the two noise suppression methods explained above. For example, Figure 7.3 shows the $\not\!\!E_T$ distributions for these data with the comparison of the two methods with the Gaussian noise model [2]. For the cell-based method ($\not\!\!E_T^{Base}$), a good agreement is observed between the data and the simple model. For the cluster-based method ($\not\!\!E_T^{Topo}$) the agreement between the data and the model is not as good as for the cell-based method, reflecting the higher sensitivity of this method to the noise description. The understanding and good control of the $\not\!\!E_T^{Base}$ (the most simple calorimeter $\not\!\!E_T$ ) makes this a more suitable option to computed the $\not\!\!E_T$ with early data, despite the larger reduction for the noise contribution to $\not\!\!E_T$ of the cluster-based method.

[2]The $\not\!\!E_T$ distribution can be compared with a Gaussian noise model (where no pedestal shift or coherent noise is present) obtained by randomizing the cell energy according to the Gaussian cell noise.

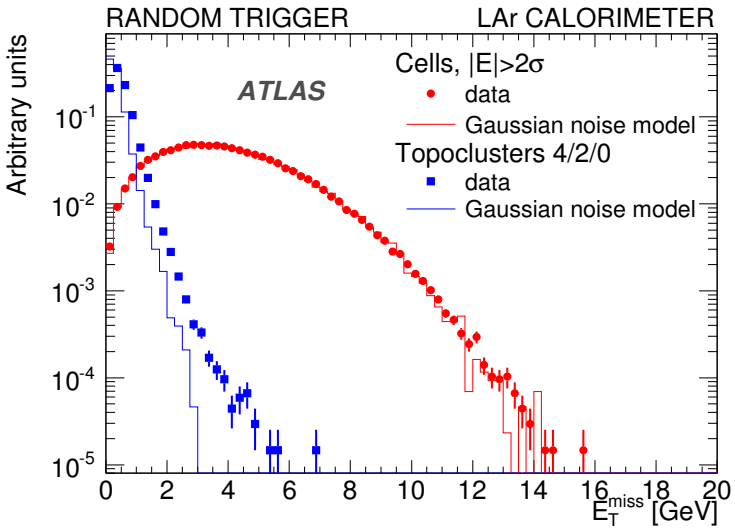


Figure 7.3: $\not{E}_T$ distribution with LAr calorimeter cells for 135,000 randomly triggered events in June 2009. $\not{E}_T^{Base}$ (dots) and $\not{E}_T^{Topo}$ (squares) are compared with the equivalent distributions for the Gaussian noise model (line).

The contribution of the three terms (see Equation 7.2) to the $\not{E}_T$ measurement in $W' \rightarrow e\nu$ channel are shown in Figure 7.10(a). The contributions from muons and losses in dead material are negligible (peaks near 0) compared to the calorimetric term, because the $W' \rightarrow e\nu$ event signature consists in a very high energetic calorimetric deposit due to a high $p_T$ electron and some hadronic activity. Moreover, as the real energy deposits in the calorimeter are well above the noise, the two types of noise reduction ($\not{E}_T^{Base}$ and $\not{E}_T^{Topo}$), are completely equivalent (red and green histograms on the figure). We observe on Figure 7.10(a) that the calorimeter term, with a calibration based on Monte Carlo weights (described on [11]), induces a 0.7 % shift in the $\not{E}_T$ distribution (compare Base-calib with Base). It will be shown later on this chapter that, in absence of this calibration, staying at the EM scale, induces a 6 % shift in the $W'$ transverse mass reconstruction but does not degrade the peak width and therefore the discovery potential.

This overall picture remains valid for the control sample $W \rightarrow e\nu$ events, even if the calorimetric deposit is lower. This is illustrated in Figure 7.10(b), the $\not{E}_T^{Calo}$ , where it can be noticed, that the contribution from the calorimeter Base-calib accounts for about 99 % to the total $\not{E}_T$ .

## 7.3 Electron Reconstruction

Electron candidates are built starting from clusters of calorimeter cell energy depositions, which are matched to a track from the inner detector. The energy of each cell included in the cluster definition is determined at the one percent level (see Chapters 5 and 6). The optimal cluster size depends on the particle type being reconstructed and the calorimeter region. The electron need larger clusters than photons due to their larger interaction probability in the upstream material and also due to the fact that they bend in the magnetic field.

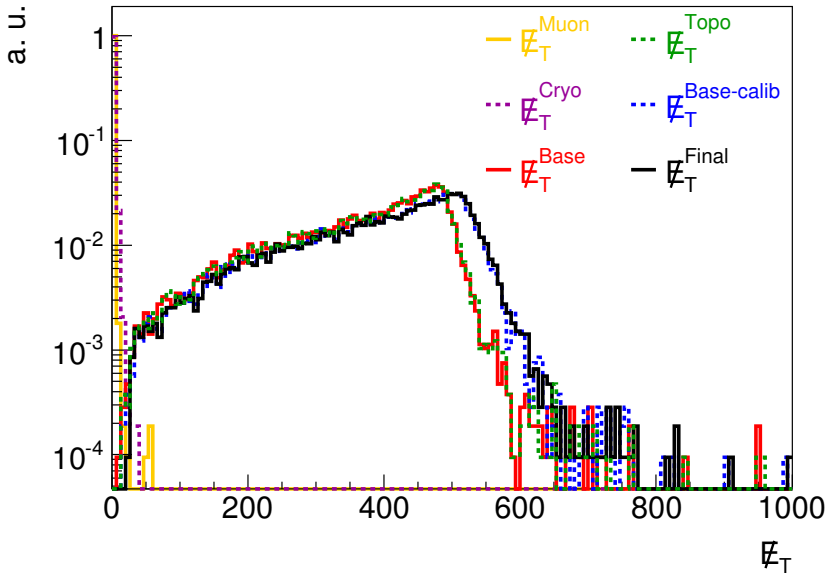


(a) $W' \rightarrow e\nu$

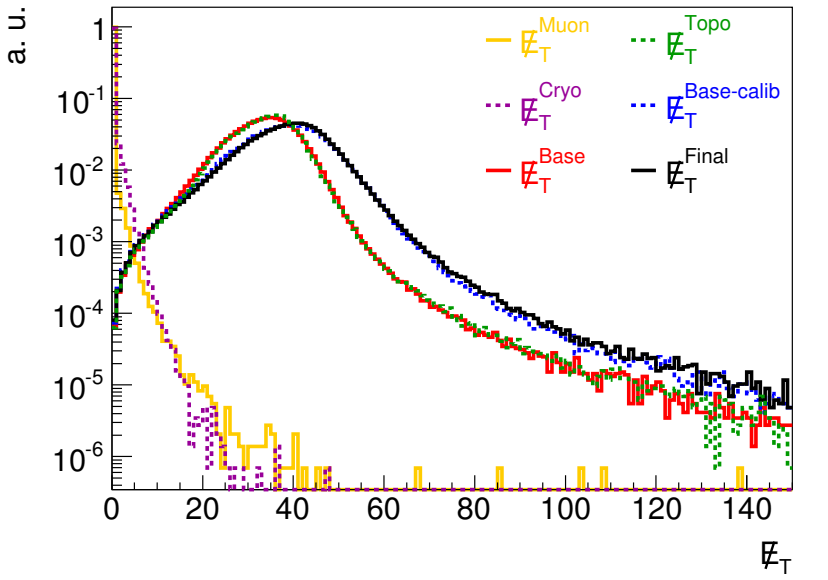


(b) $W \rightarrow e\nu$

Figure 7.4: Distributions of the different contributions to the ATLAS $\not\!\!E_T$ measurement in the cell-based approach, as sketched in Figure 7.2, for 1 TeV $W' \rightarrow e\nu$ (a) and $W \rightarrow e\nu$ (b) events.

Most of the energy of an electromagnetic interacting particle is deposited in the volume of the calorimeter, including the lead absorbers and the liquid argon gaps. A small fraction is deposited in non-instrumented material in the inner detector, the cryostats, the solenoid, and the cables between the presampler and the first EM calorimeter layer (see Figures 3.5 and 3.7). Energy also escapes from the back of the calorimeter in case of very high energetic electrons.

The cluster energy is calculated as a weighted sum of the energy in each of the three calorimeter layers plus the presampler [1, 2]. The purpose of these weighted factors is to correct for the energy losses, providing optimum linearity and resolution.

After electron candidates have been selected, some cuts can be applied to assure the electron purity. The standard identification of high-$p_T$ electrons in ATLAS uses the following categories of requirements:

- **Loose cuts**: simple electron identification based only on information from the calorimeters. The cuts are applied on the hadronic leakage and on shower-shape variables from the middle layer of the EM calorimeter. This set of cuts provides an excellent identification efficiency of about 88 %, but low background rejection.

- **Medium cuts**: Improvement by adding cuts on the strips in the first layer of the EM calorimeter with a finer granularity (see Figure 4.4) and on the tracking variables. Strip-based cuts are effective in the rejection of $\pi^0 \to \gamma\gamma$ decays. The energy deposit pattern from $\pi^0$'s is often found to have two maxima, which can be used to distinguish from the energy deposit pattern of an electron. Track quality cuts are also added as for example: at least one hit in the pixel detector, at least nine hits combining the pixel and the SCT, and the transverse impact parameter lower than 1 mm. The medium cuts increase the jet rejection by a factor of $3-4$ with respect to loose cuts set, while reducing the efficiency to about 77%. More information can be found in [11].

- **Tight cuts**: Use of all the particle-identification tools available for electrons. In addition to previous cuts, cuts are applied on the number of vertexing-layer hits (rejection of electrons from conversions), on the number of hits in the TRT, on the ratio of high-threshold hits to the number of hits in the TRT (rejection of the dominant background from charged hadrons, which radiate much less than electrons), on the difference between the cluster and the extrapolated track positions in $\eta$ and $\phi$, and on the ratio of cluster energy to track momentum. It increases the jet rejection up to $\sim 10^5$ and decreases the efficiency down to $\sim 62$ %.

The present study uses the loose and medium set of selection requirements for the electron reconstruction. Table 7.2 and 7.3 show the standard set of cuts applied on the $W'$ and $W$, respectively. Those cuts are compared with the analysis perform within the ATLAS collaboration in [11], using full potentiality of ATLAS detector with 14 TeV LHC data. The first set of three cuts will be referred to as "kinematic cuts".

| Type | Analysis with 10 TeV | Standard analysis with 14 TeV |
|---|---|---|
| One electron with | $p_T > 25$ GeV<br>$\mid \eta \mid \notin [1.3;1.6], \mid \eta \mid < 2.5$ | $p_T > 50$ GeV<br>$\mid \eta \mid < 2.5$ |
| Missing Transverse Energy | $\not{E}_T^{Final} > 25$ GeV | $\not{E}_T^{Final} > 50$ GeV |
| Electron Identification | medium cuts | medium cuts |
| Lepton Isolation | none | yes |
| Lepton Fraction | none | yes |
| Invariant Transverse Mass | $700 < M_T^{W'}(\text{ GeV}) < 1400$ | $700 < M_T^{W'}(\text{ GeV}) < 1400$ |

Table 7.2: Event selection cuts of the $W'$ analysis and comparison with a reference (Standard) analysis.

| Type | Analysis with 10 TeV | Standard analysis with 14 TeV |
|---|---|---|
| One electron with | $p_T > 25$ GeV<br>$\mid \eta \mid \notin [1.3;1.6], \mid \eta \mid < 2.5$ | $p_T > 25$ GeV<br>$\mid \eta \mid \notin [1.37;1.52], \mid \eta \mid < 2.4$ |
| Missing Transverse Energy | $\not{E}_T^{Final} > 25$ GeV | $\not{E}_T^{Final} > 25$ GeV |
| Electron Identification | medium cuts | medium cuts |
| Invariant Transverse Mass | $40 < M_T^W(GeV) < 120$ | $40 < M_T^W(GeV)$ |

Table 7.3: Event selection cuts of the $W$ analysis and comparison with a reference (Standard) analysis.

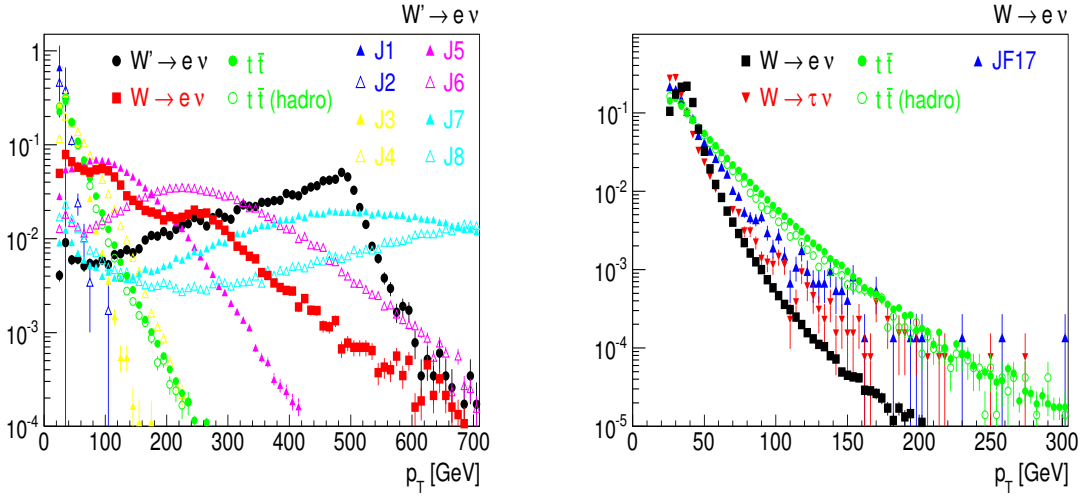


(a) $p_T$

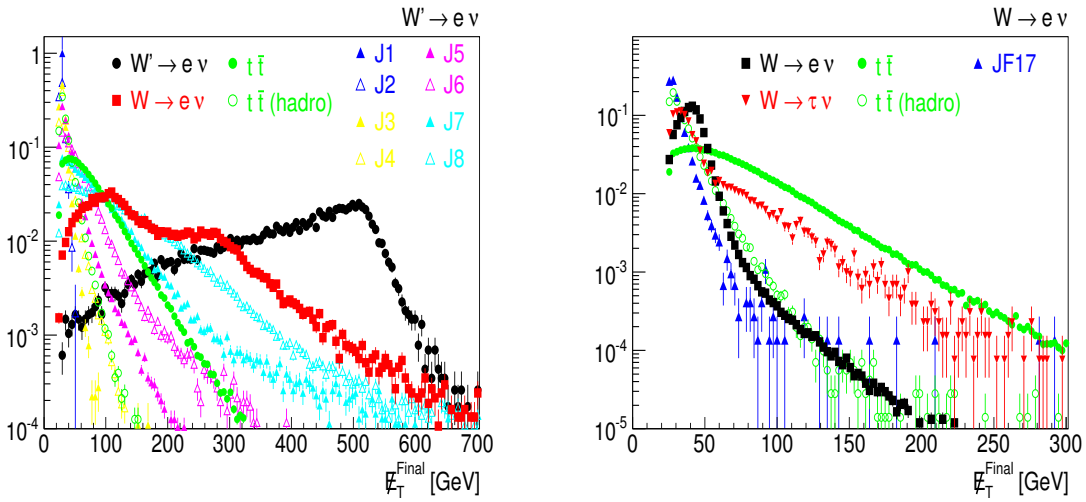


(b) $\not{E}_T^{Final}$

Figure 7.5: Kinematics distributions of all processes: $p_T$ distribution of the electron container that passed the kinematic cuts (a) and distribution of $\not{E}_T^{Final}$ (b) for $W'$ and $W$ signal and their corresponding background.

## 7.4 $W' \rightarrow e\nu$ analysis with standard $\not\!\!E_T$

The standard missing transverse energy, $\not\!\!E_T^{Final}$ , uses all ingredients of the detector to calculate $\not\!\!E_T$ , which are sketched in Figure 7.2. Throughout this section results for both $W'$ and the control sample, $W$, will be shown in parallel.

Figure 7.5 shows, the electron candidate $p_T$ distribution (a) and $\not\!\!E_T$ final distribution (b) for $W' \rightarrow e\nu$ and $W \rightarrow e\nu$ together with their corresponding backgrounds. A simple electron selection requires exactly one electromagnetic cluster loosely matched to a track. Only kinematics selection cuts have been applied, that is, the first three cuts of Tables 7.2 and 7.3, namely: $p_T > 25$ GeV , $|\eta| \notin [1.3;1.6]$, $|\eta| < 2.5$ and $\not\!\!E_T^{Final} > 25$ GeV . Every histogram is normalized such that the integral is equal to one, in order to focus on their shapes. The mean of the $p_T$ and $\not\!\!E_T$distribution is around 500 GeV for $W' \rightarrow e\nu$ decay, while for the $W \rightarrow e\nu$ is about ten times smaller. The kinematic requirement of a minimum value of 25 $GeV$ for both the electron transverse momentum and the missing transverse energy, reduces the number of events in 24 % and 4 % for $W' \rightarrow e\nu$ and $W \rightarrow e\nu$ respectively. Large $p_T$ electrons are identified in the background sample which shadow the distribution for $W' \rightarrow e\nu$. In contrast, the $\not\!\!E_T^{Final}$ distribution is more recognizable due to its increase at about half of the generated $W'$ mass.

Figure 7.6 shows the correlation between the electron $p_T$ and the $\not\!\!E_T$for $W'$ and their corresponding backgrounds in the $p_T$ region with high statistic (80 – 520 GeV). A clear correlation is observed for $W' \rightarrow e\nu$ between both variables, in contrast to the quark base backgrounds. However, this two dimensional variable cannot distinguish the signal from the $W \rightarrow e\nu$ background.

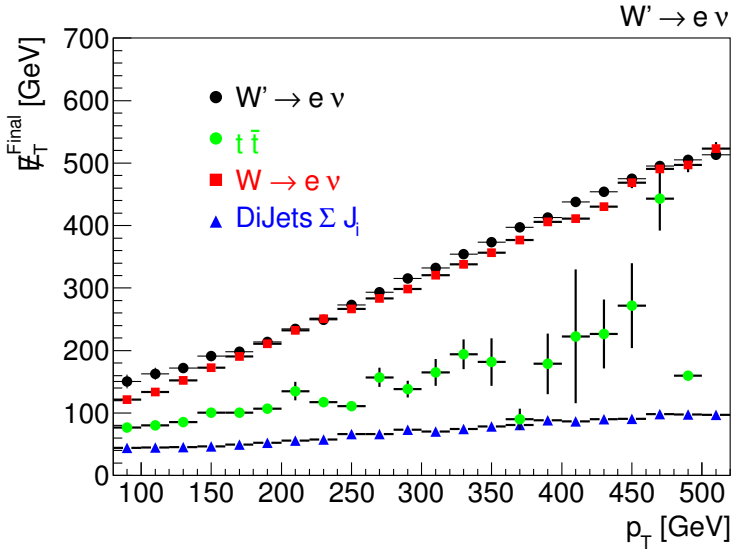


Figure 7.6: Standard missing transverse energy vs electron transverse momentum for the W' signal.

The invariant mass on the transverse plane (or simply transverse mass), $M_T$, is calculated from the transverse momentum of the electron, the missing transverse energy and the azimuth angle difference between the directions of the electron and $\not{E}_T$ via:

$$M_T = \sqrt{2 p_T \not{E}_T (1 - cos(\varphi_{electron} - \varphi_{\not{E}_T}))} \tag{7.3}$$

The $M_T$ differential cross sections are shown in Figure 7.7 for $W'$ (a) and $W$ (b) with their respective backgrounds, after kinematic cuts. The dijets contributions are added, as well as the semi-leptonic and hadronic $t\bar{t}$ for clarity. The $W'$ peak appears clearly above the background at 1 $TeV$ despite no electron identification criteria is applied. In contrast, the $W$ signal of the control sample needs a more refined selection criteria to discriminated from the Dijets background. Adding the "Medium Cuts" of the electron identification criteria to the kinematic cuts, both $W' \rightarrow e\nu$ and the control sample $W \rightarrow e\nu$ are more than one order of magnitude above the backgrounds at the peak (see Figure 7.8).

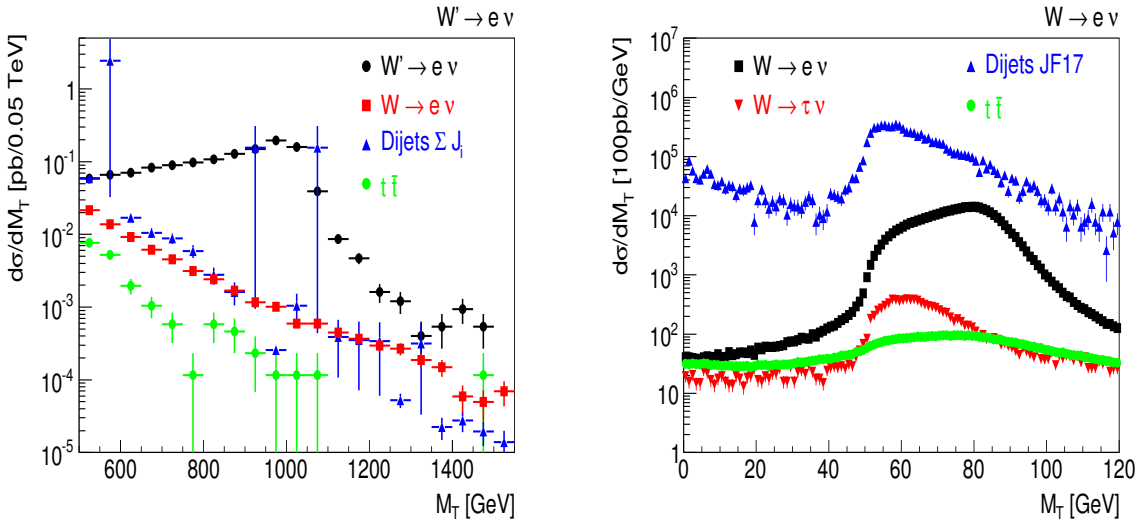


(a) $W' \rightarrow e\nu$ (b) $W \rightarrow e\nu$

Figure 7.7: Transverse invariant mass for W' (a) and W (b) after kinematics cuts on the electron and $\not{E}_T^{Final} < 25$ GeV.

These signal and background spectra are in good agreement with those obtained in the reference analysis at 14 TeV center of mass energy [11]. The selection cuts used are similar but not strictly identical (see Table 7.2). To quantify the comparison, cross sections (in $pb$) for the $W'$ signal and its backgrounds are given in Table 7.4. They correspond to the following integral after selection cuts:

$$\sigma = \int_{700\ GeV}^{1200\ GeV} \frac{d\sigma}{dM_T}\, dM_T \tag{7.4}$$

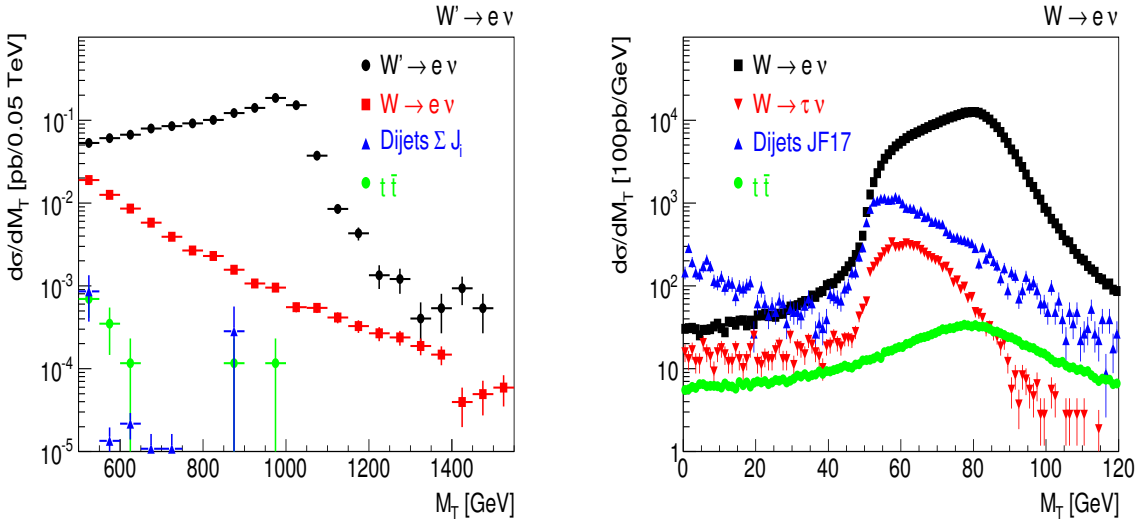


(a) $W' \rightarrow e\nu$ (b) $W \rightarrow e\nu$

Figure 7.8: Transverse invariant mass for W' (a) and W (b) after kinematics cuts on the electron, $\not\!\!E_T^{Final} < 25$ GeV and electron identification (medium cuts).

The factor two between both analysis is due to the different center of mass energy. Re-scaling by this factor the small differences, at the percent level, are due to the different $p_T$ , $\not\!\!E_T^{Final}$ thresholds (see Table 7.2). The signal over background ratio, S/B, is about 60, which is a measure of the discovery potential for this new boson.

| Process | This Analysis (10 TeV) | CSC results (14 TeV) |
|---|---|---|
| $W' \rightarrow e\nu$ | 0.927 | 1.860 |
| $W \rightarrow e\nu$ | 0.014 | 0.032 |
| $t\bar{t}$ + dijets | 0.000 | 0.000 |
| S/B | 62.44 | 58.68 |

Table 7.4: Comparison between the present analysis and the reference results, for the cross section in the transverse mass window 700 GeV $< M_T(\text{GeV}) <$ 1200 GeV for W' signal, its main backgrounds and the signal over background ratio $S/B$. A factor $\sim 2$ in the number of events is expected from the cross section ratio between 14 and 10 TeV.

## 7.5 $W' \rightarrow e\nu$ analysis with calorimetric $\not\!\!E_T$

In this section, the possibility of using an unweighted calorimetric definition of the missing transverse energy ($\not\!\!E_T^{Base}$) for the $W' \rightarrow e\nu$ and the control sample $W \rightarrow e\nu$ is investigated. This quantity is much simpler than the standard $\not\!\!E_T^{Final}$ commented in previous section, since on the one hand it contains only information from the calorimeters and on the other hand it does not include Monte Carlo weights on the cells to correct for energy losses in inactive parts and for the non-compensation of the calorimeters for hadronic cascades. Hence, $\not\!\!E_T^{Base}$ can be kept more under control, specially for the first LHC data when the Monte Carlo is not perfectly tuned.

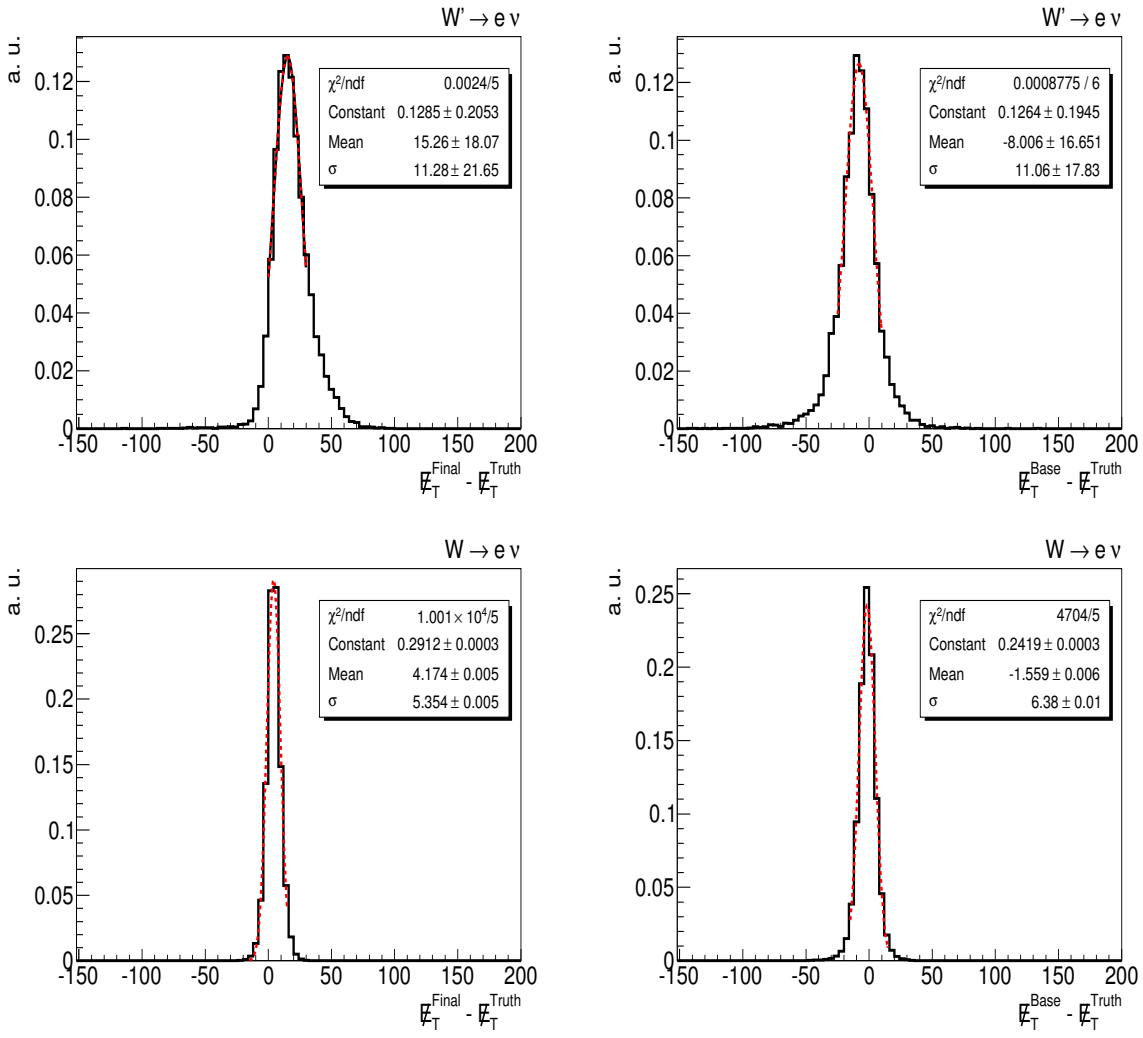


Figure 7.9: $\not\!\!E_T^{Final}$ (a) and $\not\!\!E_T^{Base}$ (b) resolutions distributions (black line) with fit (red line) for W' (top) and W (bottom).

Figure 7.9 shows the distributions of $\not\!\!E_T^{Final}$ and $\not\!\!E_T^{Base}$ relative to the value at the generator level or Monte Carlo Truth. An underestimate, of 8 GeV and 1.5 GeV, is observed when using $\not\!\!E_T^{Base}$ for $W'$ and $W$ respectively. This can be understood by the energy loss in inactive parts

of the detector, which decreases the value of $\not\!\!E_T^{Base}$(see Equation 7.1). The effect of this underestimate affects more to the $W$, since the percentage variation relative to the mass is more than twice larger for the $W$ than for the $W'$. In contrast, using $\not\!\!E_T^{Final}$an overestimate is observed, which amounts to 15 GeV and 4 GeV for $W'$ and $W$ respectively. In addition, the distributions deviates from a gaussian at high values. This indicates a problem in the standard procedure which may come from the Monte Carlo dependent parts of the corrections. On the other hand, the widths of the distributions are 11 GeV and 6 GeV for $W'$ and $W$ respectively, which represents about 1 % (8 %) of the $W'$ ($W$) mass [3]. A more visible effect on the gauge boson width is then expected for the $W$ than for the $W'$.

Figure 7.10 shows the transverse mass $M_T$ for $W' \rightarrow e\nu$ and $W \rightarrow e\nu$ after kinematic and electron identification medium cuts are applied. Three distributions are represented corresponding to Monte Carlo truth (black circles), unweighted calorimetric (red squares) and standard (blue triangles) missing transverse energy calculation. The transverse mass at the peak is about 1 % underestimated when using $\not\!\!E_T^{Base}$as transverse energy for the $W' \rightarrow e\nu$. This effect increases to about $7-8$ % for the $W$ case, where, in addition, the distribution is clearly broader than the Monte Carlo Truth.

The next step is to quantify the effect of a calorimetric definition of the missing transverse energy on the backgrounds. Figure 7.11 (left column) shows the distributions of $M_T$ for the different backgrounds to $W' \rightarrow e\nu$ signal. A good agreement is observed with the Monte Carlo Truth except for the Dijets background that increases, still being negligible compared to the signal.

The number of events for an integrated luminosity of 100 pb$^{-1}$ in the transverse mass window $700 < M_T^{W'}$( GeV) $< 1400$ is given in Table 7.5. A signal to background ratio (S/B) of almost 70 is obtained on a total of 89 $W'$ selected.

| Process | $\not\!\!E_T^{Truth}$ | $\not\!\!E_T^{Final}$ | $\not\!\!E_T^{Base}$ |
|---|---|---|---|
| $W' \rightarrow e\nu$ | 90.09 | 92.68 | 88.7 |
| $W \rightarrow e\nu$ | 1.27 | 1.43 | 1.22 |
| Dijets | 0.00 | 0.03 | 0.06 |
| $t\bar{t}$ | 0.02 | 0.02 | 0.02 |
| S/B | 70.94 | 62.62 | 68.23 |

Table 7.5: Number events for of W' and its backgrounds for $100 pb^{-1}$ of data in a transverse invariant mass window $700 < M_T(GeV) < 1200$ for $\not\!\!E_T^{Truth}$, $\not\!\!E_T^{Final}$and $\not\!\!E_T^{Base}$.

Another concern raised by the use of calorimetric $\not\!\!E_T$ is the the possibility that new backgrounds become significant when using $\not\!\!E_T^{Base}$. In particular, the situation that is more likely to fake calorimetric $\not\!\!E_T$ is the presence in the final state of jets or muons. For this purpose, events of $W \rightarrow \mu\nu$ + 1 or 2 jets has been studied. For an integrated luminosity of $100 pb^{-1}$, no events survived after selection cuts in the W' $M_T$ window of $700 < M_T^{W'}$( GeV) $< 1400$. A poissonian limit predicts less than 2.3 events at 90 % CL, which is negligible compared with the number of $W'$ selected (see Table 7.5).

[3] These values are consistent with the expected resolution for the hadronic calorimeters, which gives for the $W'$ on average: $50\ \%\sqrt{<\Sigma E_T>} = 50\ \%\sqrt{600} \sim 12$ GeV

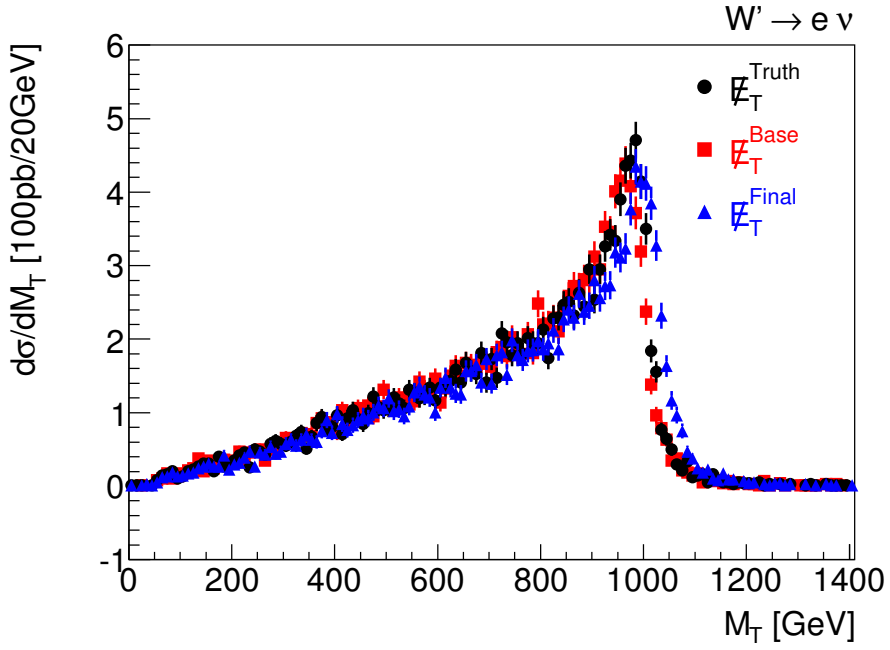


(a) $W' \rightarrow e\nu$

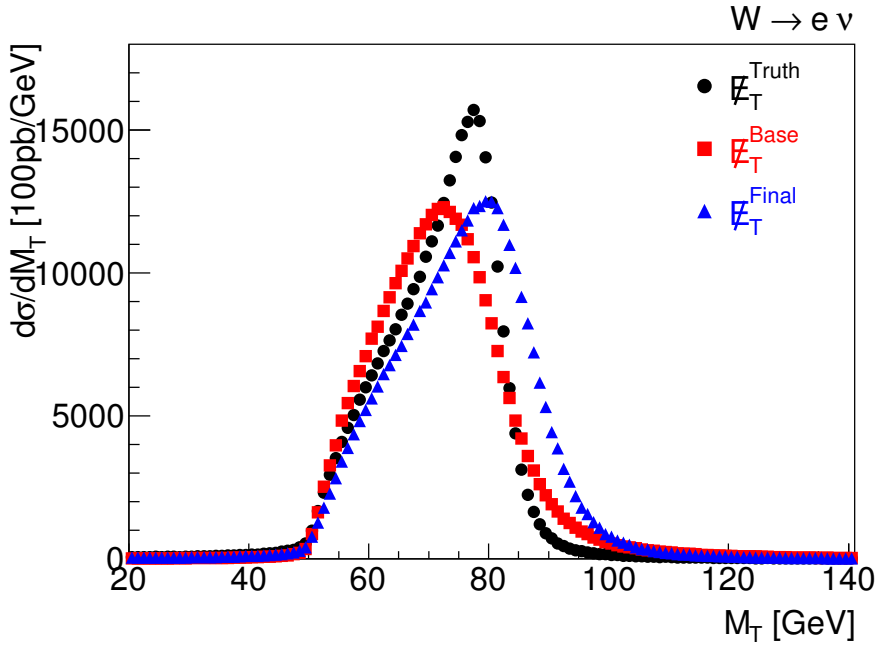


(b) $W \rightarrow e\nu$

Figure 7.10: Invariant transverse mass $M_T$ (Equation7.3) with $\not{E}_T$ truth (black), final (blue) and base (red) for W' (a) and W (b).

The much higher statistics in the control sample $W \rightarrow e\nu$ allows for a better quantitative study of the backgrounds. Figure 7.11 (right column) shows the distributions of $M_T$ for the different backgrounds to $W \rightarrow e\nu$ signal. It confirms the good agreement with the Monte Carlo Truth except for the Dijets background, which is still negligible compared to the signal. Table 7.6 contains the number of events for an integrated luminosity of 100 pb$^{-1}$ in the transverse mass window $700 < M_T^{W'}(\text{ GeV}) < 1400$. There is more than $300,000$ $W \rightarrow e\nu$. The number of $W \rightarrow \mu\nu$ + 1 or 2 jets events that survive after the selection cuts in the window $40 < M_T^{W'}(\text{ GeV}) < 120$ is 60 which represents less than 2 in ten thousand of the signal. This percentage applied to the $W'$ case will give rise to less than 0.02 events.

Figure 7.12 serves as a summary of the performance of the present analysis using the $\not{E}_T^{Base}$ definition for the missing transverse energy, where signal and backgrounds are compared as a function of $M_T$. The calorimetric definition $\not{E}_T^{Base}$ does not spoil the discovery potential of the new gauge boson $W'$, being suitable for the early data taken.

| Process | $\not{E}_T^{Truth}$ | $\not{E}_T^{Final}$ | $\not{E}_T^{Base}$ |
|---|---|---|---|
| $W \rightarrow e\nu$ | 316000 | 340148 | 319123 |
| $W \rightarrow \tau\nu$ | 5523 | 6889 | 5410 |
| Dijets JF17 | 9968 | 27149 | 33008 |
| $t\bar{t}$ | 1418 | 1483 | 1399 |
| S/B | 18.7 | 9.57 | 8.02 |

Table 7.6: Number of events for W and its backgrounds for $100 pb^{-1}$ of data in a transverse invariant mass window $40 < M_T(GeV) < 120$ for $\not{E}_T^{Truth}$, $\not{E}_T^{Final}$and $\not{E}_T^{Base}$.

## 7.6 Conclusions

The main goal of this analysis was to evaluate the discovery potential of a 1 TeV $W' \rightarrow e\nu$ using a robust definition of $\not{E}_T$ . In this prospect, a pure calorimetric $\not{E}_T$ definition was chosen since it is already well under control and can be quickly crosschecked with first data (Section 7.2).

Simple kinematic selection cuts on the electron $P_T$ and missing transverse energy are sufficient to distinguish the $W'$ boson against the background from Standard W, Dijets and $t\bar{t}$.

An overestimate of the W' mass of $+1.5$ % has been found when using a complete weighted definition of the missing transverse energy, while a degradation of $-1.5$ % has been observed instead when using an unweighted calorimetric definition of missing transverse energy.

A signal over background of 68 has been found in a window of the $W'$ transverse mass of $700 < M_T(GeV) < 1200$ around the mass peak.

The analysis has been performed in parallel for the standard $W \rightarrow e\nu$ which became useful as control sample, in particular for the precised evaluation of background shapes, due to the much larger number of events in the standard $W$ samples.

Due to the simple discrimination of backgrounds, new heavy gauge bosons will be one of the first particles to search for with early data.

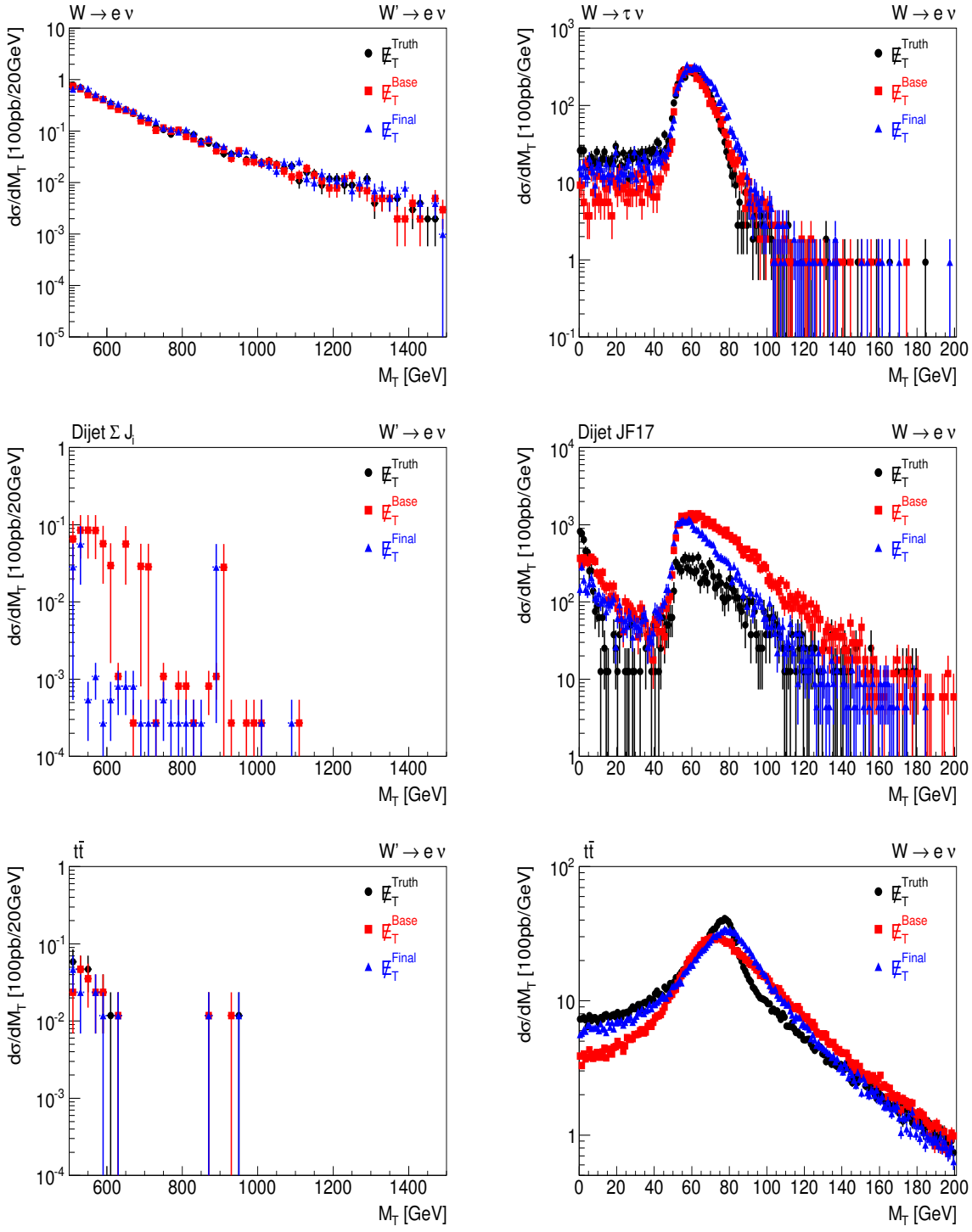


Figure 7.11: Invariant transverse mass $M_T$ (Equation7.3) with $\not{E}_T^{Truth}$(black circles), $\not{E}_T^{Final}$(blue triangles) and $\not{E}_T^{Base}$(red squares) for $W \rightarrow e\nu$ in the W' mass window (top left), $W \rightarrow \tau\nu$ the W mass window (top right), the dijet background in the W' mass window (middle left), the dijet background in the W mass window (middle right), $t\bar{t}$ in the W' mass window (bottom left) and $t\bar{t}$ in the W mass window (bottom right)

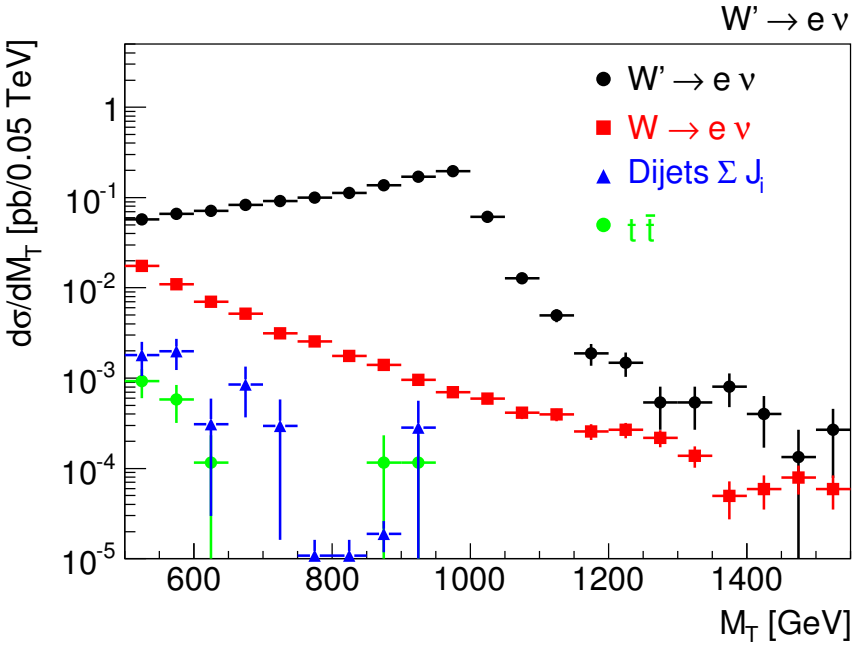


(a) $W' \rightarrow e\nu$

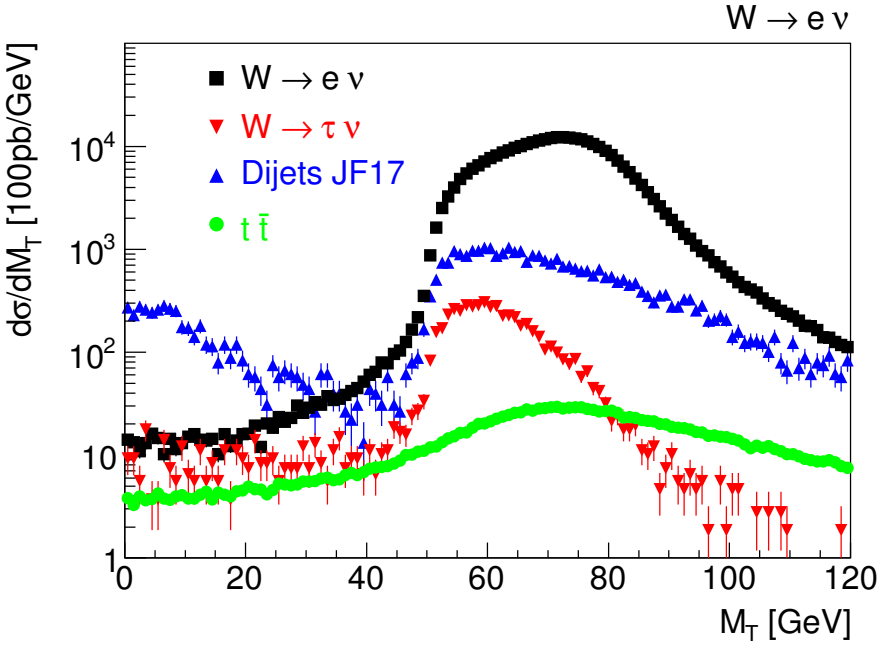


(b) $W \rightarrow e\nu$

Figure 7.12: Distribution of transverse invariant mass $M_T$ (Equation 7.3) of W' (a) and W (b) and their backgrounds after all the event selection and with a $\not{E}_T^{Base}$. .

# Summary

At the CERN laboratory, the Large Hadron Collider (LHC) has been built under the french-swiss border near Geneva, Switzerland. The LHC is designed to create proton-proton collisions with an unprecedented luminosity of $10^{34}$ cm$^{-2}$s$^{-1}$ and a center of mass energy of 14 TeV. The LHC takes particle physics research to a new frontier. On September $10^{th}$ 2008, the first single beam of $2 \times 10^9$ protons was circulated successfully through the entire LHC, with an energy of 0.45 TeV per proton.

ATLAS is one of the two general-purpose experiments at the LHC accelerator to search for particles with masses up to several TeV. One of its main goals is to study the Standard Model and look for possible new physics beyond this model. One of the greatest expectations lie in the discovery of the Higgs boson, the last of the fundamental particles in the Standard Model which remains undiscovered. Also in different extensions of the Standard Model new particles are predicted with masses lying in the kinematic window of ATLAS discovery potential. Events with electrons and photons in the final state are important signatures for many physics analyses conceived at the LHC.

The ATLAS Liquid Argon Calorimeter is one of the largest and most sophisticated calorimeters ever built. It is designed to provide a precise measurement of electrons, photons, jets and missing transverse energy. In particular, the EM calorimeter has to match challenging requirements in order to satisfy the physics goals, such as an energy resolution of $10\ \%/\sqrt{E} \oplus 0.7\ \%$ for electrons or photons of energy $E$, a linearity at the per mil level and a good control of the signal for the more than 170 thousands channels.

An important part of the work presented in this thesis focuses on the calibration and commissioning of the EM calorimeter. In particular, the signal reconstruction in every cell of the EMC and its performance are described extensively in this work. The data collected during the cosmic ray and beam splash runs in the fall 2008 have been very useful to commission this subdetector in its final position in ATLAS (see [55] and [56]).

Optimal Filtering weights (OFC) have been obtained to convert from digital data samples to the maximum amplitude for each calorimeter channel. The determination of these weights depends on the modeling of the readout line, in particular of four parameters which are determined by the ATLAS standard Response Transform Method (RTM) from the calibration pulse shape.

A first global check of the signal reconstruction quality over the whole EM calorimeter coverage is performed using events created by the hit of LHC beams on collimators 200 meters before ATLAS. The pulse shape prediction agrees with the data to better than 1 % and 2 % for the first and second/third compartments of the barrel. Due to a less refined description of the cell

electronic chain in the endcaps, the situation is slightly degraded : the agreement is of 1 % and better than 3 % in first and second/third compartments, respectively. A rough estimate of the impact of the quality of the signal reconstruction on the constant term of the energy resolution, $c_{sr}$, has been derived : $0.2\ \% < c_{sr} < 0.5\ \%$ in the barrel and $0.25\ \% < c_{sr} < 0.7\ \%$ in the endcaps.

The average electron drift time in each cell of the highly granular LAr electromagnetic calorimeter of ATLAS, is measured from the samples of shaped ionization pulses induced by high energy deposits from cosmic muons recorded during the 2008 commissioning run. The signals were recorded in a wide time window (32 samples) to assure the required precision of the measurement.

The drift time measurement has shown to be a powerful tool to detect asymmetries and intrinsic non-uniformities along the calorimeter. Its great sensitivity to gap variations made possible to determine the intrinsic non-uniformity of the response due to gap size variations, namely $\sim 0.26$ % and $\sim 0.53$ % respectively for the barrel and the endcaps.

From the measurement of the drift time the drift velocity has been infered, which resulted $4.59 \pm (0.05)_{\text{syst}}$ mm/$\mu$s and $4.65 \pm (0.10)_{\text{syst}}$ mm/$\mu$s for the barrel and endcap respectively, at 1 kV/mm electric field and an average LAr temperature of 88.5 K measured during the run period.

The analysis method used to derive the drift time provides as another parameter the average absolute value of the amount the electrodes are off center between their two neighboring absorbers. Electrodes are found to be shifted with respect to their nominal central position by $\sim 146$ $\mu$m on average in both barrel and endcap, with a RMS of $\sim 40$ $\mu$m.

Since the actual value of the drift time enters the LAr electronic calibration in several points (e.g. OFC, current-to-energy conversion factors), the measurements presented in this analysis can be used to improve the EM calorimeter energy reconstruction. At the same time, these measurements can be used to correct for the measured gap variations in order to eventually reduce the constant term of the energy resolution.

A Monte Carlo analysis of the potential of discovery of ATLAS for a new gauge $W'$ boson has been carried out. The mass was assumed of 1 TeV whereas the search has been focussed on the decay mode $W' \rightarrow e\nu$. The performance using a pure unweighted calorimetric definition for the missing transverse energy has been compared with a standard definition. Both leading to similar results in terms of signal to background significance of about 70, makes the former definition suitable for the first LHC data.

# Appendix A: Problematic channels in the EMC.

Figure 7.13 show the number of anomalous EM calorimeter channels discovered using cosmic data. They can be classified according to the type of problem:

- `P1`: dead channel at the readout level.
- `P2`: dead channel at the detector level.
- `P3`: channel whose calibration pulse is distorted.
- `P4`: channel with another typo of distorted problems.
- `P5`: noise channel which is more than around 5 standard deviations from expected noise.
- `P6`: channel with some features unstables with respect to time.
- `P7`: channel with sporadic bursts of noise.
- `P8`: channel with a short.

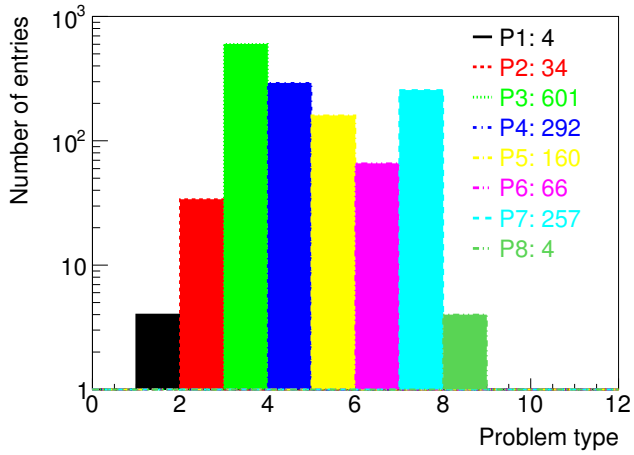


Figure 7.13: Problematic channels in the EM calorimeter.

In total, the ratio of unrecoverable channels is 0.02 % which comes from `P1`, `P2` and `P8` problem types, and those which are usable but should be masked represents 0.8 % of the full number of channels in the EM calorimeter.

# Bibliography


[1] D. Banfi, L. Carminati, L. Mandelli, *Calibration of the ATLAS electromagnetic calorimeter using calibration hits*, ATLAS Note (2007) ATL–LARG–PUB–2007–012.

[2] J. del Peso, E. Nebot, *Electron energy reconstruction for the EM Endcap Calorimeter using calibration hits*, ATLAS Note (2008) ATL–LARG–INT–2008–001.

[3] C. Gabaldon, M. Kuna et al., *Study of material in front of the EM calorimeter with high pT electron shower shapes and tracks*, ATLAS Note (2008) ATL–PHYS–INT–2008–026.

[4] F. Halzen and A.D. Martin, *Quarks and Leptons: An Introductory Course in Modern Particle Physics*. 2001.

[5] G. Altarelli, B. Mele and M. Ruiz-Altaba, *Searching for new heavy vector bosons in $p\bar{p}$ colliders*, Z. Phys. C Particles and Fields **47** (1990) 676.

[6] P. Higgs., *Broken Symmetries, Massless Particles and Gauge Fields*, Phys. Lett. **12** (1964) 132.

[7] UA1 Collaboration, *Experimental observation of isolated large transverse energy electrons with associated missing energy at $\sqrt{s} = 540$ GeV*, Phys. Lett. B **122** (1983) 103–116.

[8] UA1 Collaboration, *Experimental observation of lepton pairs of invariant mass around 95 GeV/c$^2$ at the CERN SPS collider*, Phys. Lett. B **126** (1983) 198–410.

[9] UA2 Collaboration, *Evidence for $Z0 \rightarrow e^+e^-$ at the CERN $p\bar{p}$ collider*, Phys. Lett. B **126** (1983) 198–410.

[10] C. Amsler et al., *Review of Particle Physics*, Phys. Lett. B **667** (2008) 1.

[11] ATLAS Collaboration, *Expected performance of the ATLAS experiment : detector, trigger and physics*, CERN Note (2008) CERN–OPEN–2008–020.

[12] J.C. Pati and A. Salam, *Lepton number as the fourth "color"*, Phys. Rev. D **10** (1974) 275–289.

[13] M.L. Mangano and T.J. Stelzer, *Tools for the simulation of hard hadronic collisions*, Ann. Rev. Nucl. Part. Sci. **55** (2005) 555–588.

[14] M.L. Mangano et al., *ALPGEN, a generator for hard multiparton processes in hadronic collisions*, JHEP **07** (2003) 001.

[15] T. Sjostrand et al., *PYTHIA 6.4 Physics and Manual"*, JHEP **0605** (2006) 026.

[16] S. Frixione and B.R. Webber, *Matching NLO QCD computations and parton shower simulations"*, JHEP **06** (2002) 029.

[17] S. Frixione,P. Nason and B.R. Webber, *Matching NLO QCD and parton showers in heavy flavour production"*, JHEP **08** (2003) 007.

[18] P. Lefevre and T. Pettersson, *The Large Hadron Collider: conceptual design*, CERN Note (1995) CERN–AC–95–05–LHC.

[19] LEP Collaboration, *LEP Design Report, The LEP injector chain*, CERN Note **1** (1983) CERN–LEP/TH/83–29.

[20] ALICE Collaboration, *ALICE: Technical proposal for a large ion collider experiment at the CERN LHC*, CERN Note (1995) CERN–LHCC–95–7.

[21] ATLAS Collaboration, *The ATLAS Experiment at the CERN Large Hadron Collider*, JINST **3** (2008) S08003.

[22] CMS Collaboration, *The compact muon solenoid: Technical proposal*, CERN Note (1994) CERN–LHCC–94–38.

[23] S. Amato et al., *LHCb technical proposal*, CERN Note (1998) CERN–LHCC–98–04.

[24] CERN Director General, *Summary of the analysis of the 19 September 2008 incident at LHC*, CERN Preprint (2008) 1135729.

[25] ATLAS/Inner Detector Collaboration, *Inner Detector Technical Design Report*, CERN Note (1997) CERN–LHCC–97–16.

[26] ATLAS/Liquid Argon Calorimeter Collaboration, *Liquid Argon Calorimeter Technical Design Report*, CERN Note (1996) CERN–LHCC–96–41.

[27] ATLAS/Tile Calorimeter Collaboration, *Tile Calorimeter Technical Design Report*, CERN Note (1996) CERN–LHCC–96–42.

[28] ATLAS/Muon Spectrometer Collaboration, *Muon Spectrometer Technical Design Report*, CERN Note (1998) CERN–LHCC–98–14.

[29] D.J. Griffiths, *Introduction to Electrodynamics*, vol. 3th Edition. 1998.

[30] D.H. Perkins, *Introduction to High Energy Physics*, vol. 4th Edition. 2000.

[31] B. Aubert et al., *Construction, assembly and tests of the ATLAS electromagnetic barrel calorimeter*, NIM A **558** (2006) 388–418.

[32] M. Aleksa et al., *Construction, assembly and tests of the ATLAS electromagnetic end-cap calorimeter*, JINST **3** (2008) P06002.

[33] O. Martin, E. Monnier, S. Tisserant, *Update of some Geometrical Parameters for the ATLAS EM End-Cap Calorimeter*, ATLAS Note (1996) ATLAS–LARG–NO–47.

[34] W. Walkowiak, *Drift Velocity of Free Electrons in Liquid Argon*, NIM A **449** (2000) 288–294.

[35] W.E. Cleland and E.G. Stern, *Signal processing considerations for liquid ionization calorimeter in a high rate environment*, NIM A **338** (1994) 467–497.

[36] C. Collard, D. Fournier, S. Henrot-Versillé, L. Serin, *Prediction of signal amplitude and shape for the ATLAS electromagnetic calorimeter*, ATLAS Note (2007) ATL–LARG–PUB–2007–010.

[37] D. Banfi, M. Delmastro and M. Fanti, *Cell response equalization of the ATLAS electromagnetic calorimeter without the direct knowledge of the ionization signals*, JINST **1** (2006) P08001.

[38] Y. Katznelson, *An introduction to harmonic analysis*, vol. 3th Edition. 2004.

[39] C. Gabaldon et al., *Signal reconstruction in the EM end-cap calorimeter and check with cosmic data in the region* $0 < \eta < 3.2$, ATLAS Note (2008) ATL–LARG–PUB–2008–001.

[40] S. Baffioni et al., *Electrical Measurements on the ATLAS electromagnetic barrel calorimeter*, ATLAS Note (2007) ATL–LARG–PUB–2007–005.

[41] C. Gabaldon, *Electronic calibration of the ATLAS LAr calorimeter and commissioning with cosmic muon signals*, J.Phys.:Conf. Ser. **160** (2009) 012050.

[42] W. Lampl et al., *Digitization of LAr calorimeter for CSC simulations*, ATLAS Note (2007) ATL–LARG–PUB–2007–011.

[43] J. Colas et al., *Response uniformity of the ATLAS liquid argon electromagnetic calorimeter*, NIM A **582** (2007) 429–455.

[44] W. Willis and V. Radeka, *Liquid Argon ionization chamber as a total absorption detector*, NIM A **120** (1974) 221–236.

[45] C. Oliver and J. del Peso, *Outer Wheel Uniformity of the ElectroMagnetic Endcap Calorimeter*, ATLAS Note (2005) ATL–LARG–PUB–2005–002.

[46] F. Hubaut and C. Serfon, *Response uniformity of the ATLAS electromagnetic endcap calorimeter*, ATLAS Note (2004) ATL–LARG–2004–015.

[47] R. Achenbach et al., *The ATLAS Level-1 Calorimeter Trigger*, JINST **3** (2008) P03001.

[48] F. James and M. Roos, *Minuit: A System for Function Minimization and Analysis of the Parameter Errors and Correlations*, Comput.Phys.Commun. **10** (1975) 343–367.

[49] M. Delmastro, *Quality factor analysis and optimization of digital filtering signal reconstruction for liquid ionization calorimeters*, Nucl. Instrum. Meth. **A600** (2009) no. 3, 545–554.

[50] B. Aubert et al., *Performance of the ATLAS electromagnetic calorimeter barrel module 0*, NIM A **500** (2003) no. 1-3, 202–231.

[51] N. Vranjes et al., *$W'$ discovery and exclusion potential @ 7 TeV*, talk at the August 24th 2009 ATLAS Lepton+X meeting.

[52] D0 Collaboration, *Search for W' Bosons Decaying to an Electron and a Neutrino with the D0 Detector*, Phys. Rev. Lett. **100** (2008) 031804.

[53] F. Hubaut et al., *Testing calorimetric Missing Transverse Energy and jet reconstruction with random and cosmic data*, ATLAS Note (2009) ATL–PHYS–INT–2009–045.

[54] F. Hubaut et al., *Testing calorimetric Missing Transverse Energy and jet reconstruction with random and cosmic data*, ATLAS Note (2009) ATL–PHYS–INT–2009–045.

[55] ATLAS Collaboration, *Readiness of the ATLAS Liquid Argon Calorimeter for LHC Collisions*, submitted for publication in EPJC (2010) arXiv:0912.2642v2.

[56] ATLAS Collaboration, *Drift Time Measurement in the ATLAS Liquid Argon Electromagnetic Calorimeter using Cosmic Muons*, submitted for publication in EPJC (2010) arXiv:1002.4189v1.

# Resumen

En el laboratorio del CERN, se ha construido el **Large Hadron Collider** (LHC) debajo de la frontera franco-suiza cerca de Ginebra. El LHC está diseñado para producir colisiones protón-protón con una luminosidad de $10^{34}$ cm$^{-2}$s$^{-1}$ y una energía en el centro de masas de 14 TeV sin precedentes. Con el LHC se alcanzarán nuevos retos en la física de partículas. El 10 de septiembre del 2008, el primer haz de $2 \times 10^9$ protones circuló satisfactoriamente a través del LHC, con una energía de 0.45 TeV por protón.

ATLAS es uno de los dos experimentos de propósito general en el LHC que será empleado para registrar partículas con masas del orden del $TeV$. Uno de sus principales objetivos será el estudio del modelo estandar y la búsqueda de nueva física más allá de este modelo. Una de sus mayores expectativas es el descubriento del bosón Higgs, la última partícula fundamental en el Modelo Standard que queda por descubrir. Además, diferentes extensiones del Modelo Standard predicen nuevas particulas con masas dentro de la ventana cinemática de descubrimiento de ATLAS. Eventos con electrones y fotones en el estado final son de gran importancia para muchos análisis de física concevidos en el LHC.

El calorímetro del argón líquido de ATLAS es uno de los más grandes y sofisticados calorímetros jamás construido. Está diseñado para proveer medidas precisas de electrones, fotones, jets y energía perdida. En particular, el calorímetro electromagnético (EMC) tiene que cumplir una serie de requisitos a fin de satisfacer los objetivos de la física, tales como una resolución en energía de $10\ \%/\sqrt{E} \oplus 0.7\ \%$ para electrones y fotones de energía $E$, un linearidad del uno por mil y un buen control de la señal para los más de 170 mil canales que componen el EMC.

Una parte importante del trabajo presentado en esta tesis está focalizado en la calibración y puesta a punto del calorímetro electromagnético. En particular, la reconstrucción de la señal en cada celda del EMC y su comportamiento se describe detalladamente en este trabajo. Los datos almacenados de muones cósmicos y haces de partículas en el otoño del 2008 han sido muy útiles para la puesta a punto de este subdetector en su posición final dentro de ATLAS (ver [55] y [56]).

Los coeficientes de **Optimal Filtering** (OFC) han sido obtenidos para convertir la señal digital muestreada en un valor para la amplitud máxima de cada celda del calorímetro. La determinación de estos pesos depende de la modelización de la electrónica de lectura, en particular de los cuatro parametros que son determinados usando el método estandar en ATLAS llamado RTM (**Response Transform Method**) a partir de la señal de calibración.

En un primer check global se ha comprobado la calidad de la reconstrucción de la senñal a lo largo de todo el calorímetro, empleando sucesos en los que un haz de protones del LHC

colisionan con colimadores situados 200 metros inmediatamente delante del detector ATLAS. El método de predicción de la señal está de acuerdo con los datos recogidos con una precision mejor del 1 % (2 %) para el primer (segundo/tercer) compartimento del EMC Barrel. Debido a una descripción menos precisa de la cadena electrónica en el los EMC end-caps, la situación se degrada ligeramente en este subdetector: el acuerdo en este caso es mejor del 1 % (3 %) en el primer (segundo/tercer) compartimento del calorímetro. El impacto de la calidad de reconstrucción la señal en el término constante de la resolución de energía , $c_{sr}$, ha sido estimada con estos datos : $0.2\% < c_{sr} < 0.5\%$ en el EMC barrel y $0.25\% < c_{sr} < 0.7\%$ en los EMC end-caps.

El tiempo de deriva de electrones en el Argón Líquido para cada una de las celdas del calorímetro electromagnético de ATLAS se ha determinado a través de las señales de ionización producidas por altos depósitos de energía de muones cosmicos recogidos durante 2008. Runes especiales de 32 muestras (32 samples) fueron requeridos para asegurar una precisión adecuada en esta medida.

Se ha demostrado que el tiempo de deriva es una potente herramienta para la detección de asimetrías y no uniformidades intrínsecas a lo largo del calorímetro. Su gran sensibilidad a las variaciones del gap de argón lquido ha hecho posible la medida de no uniformidades intrínsecas en la señal debidas a variaciones del gap, que resultan ser $\sim 0.26$ % y $\sim 0.53$ % para barrel y los end-caps respectivamente. De la medida del tiempo de deriva se ha inferido también la velocidad de deriva, que es una cantidad directamente proporcional a la energía de respuesta de cada celda. El resultado ha sido, $4.59 \pm (0.05)_{\text{syst}}$ mm/$\mu$s y $4.65 \pm (0.10)_{\text{syst}}$ mm/$\mu$s para barrel y end-cap respectivamente, a un campo electrico de 1 KV/mm y temperatura promedio del Argón líquido de 88.5 K.

El método utilizado para la medida del tiempo de deriva proporciona la posibilidad de medir el desplazamiento efectivo de los electrodos respecto a su posición nominal entre cada dos absorbers. El resultado de tal medida es que dicho desplazamiento es $\sim 146$ $\mu$m en promedio para ambos barrel y end-caps, con un RMS de $\sim 40$ $\mu$m.

Dado que el valor del tiempo de deriva entra en la modelización de la electrónica de lectura y en varios puntos de la cadena de calibración, como los OFC y la conversión a energía, las medidas presentadas en este analisis pueden usarse para mejorar el procedimiento de reconstrución de la energía de las celdas del EMC. Al mismo tiempo estas medidas pueden ser utilizadas para corregir no-uniformidades observadas y, de esta manera, mejorar la resolución en energía.

Finalmente, se ha realizado un análisis con sucesos Monte Carlo sobre el potencial de ATLAS para el descubrimento de nuevos bosones gauge $W'$. La masa de dicho bosón se asumió de 1 TeV y el canal de desintegración estudiado ha sido $W' \to e\nu$. Se ha comparado el funcionamiento de la definición estandar de energía transversa perdida con definiciones basadas en depósitos de energía en las celdas del calorímetro no corregidas. Ambos métodos han dado lugar a significancias estadisticas, razón señal a fondo, en torno a 70. La mayor simplicidad y control del segundo método le hace más apropiado para las búsqueda de este boson con los primeros datos del LHC.

# Acknowledgments

Este trabajo no se habría podido realizar sin la colaboración de muchas personas que me han brindado su ayuda, sus conocimientos y su apoyo. Quiero agradecerles a todos ellos cuanto han hecho por mí, para que este trabajo saliera adelante de la mejor manera posible.

En primer lugar, quiero expresar mi agradecimiento a mi tutor Jose del Peso. Gracias Jose porque me llevastes de la mano al CERN y me enseñastes todo lo que debía hacer con increible paciencia. Has sabido dirigir mi trabajo en estos dos años y enfocarlo con éxito. He aprendido contigo que si quieres algo lo puedes conseguir, solo tienes que esforzarte.

De igual manera, mi más sincero agradecimiento al director del grupo Fernardo Barreiro a quien debo el realizar el doctorado en el grupo de Altas Energías de la Universidad Autónoma de Madrid. Gracias por la confianza que has depositado en mi y por tu interés por mi trabajo.

A toda la gente del grupo de Altas Energías, gracias por haberme aceptado como parte del grupo. En particular, muchas gracias a Eduardo, le agradezco profundamente su apoyo en los momentos difíciles y por compartir conmigo tantas alegrias y tristezas durante tantos años de mi vida. A todos los del laboratorio, y en especial a Juanjo por su paciencia conmigo en el campo de la informática y como amigo.

La mayor parte de estos cuatro años he estado en el CERN. Ha sido increible para mi a nivel profesional y personal compartir mi trabajo con físicos como Pascal, Marco, Isabelle, Daniel, Martin, Emmanuele y tantos otros. Un mención especial a Pascal y Marco que me ha ayudado tanto en el CERN y me han enseñado realmente que es física de partículas, siempre recordaré todos los momentos compartidos y la alegría que se siente cuando después de tanto esfuerzo las cosas se entienden.

Por supuesto, a todos mis amigos del CERN. Mi mejor amiga, Maaike, con la que siempre comparto todo y ella comparte todo conmigo, espero que siempre estemos juntas en todos los momentos importantes de nuestra vida. Quiero darle las gracias por todas las agradables conversaciones, la felicidad, las risas, las cenas juntos a Louis, Gustavo, Caroline, Jochem, Nigel, Jacopo, Manouk, Barbara, Samuelle y la pequeña Justine.

Agradecer hoy y siempre a toda mi familia, a mis padres y a mi hermano, por haberme brindado su comprensión y apoyo. Mama gracias porque sin ti no habría podido empezar, ni terminar la carrera y porque siempre has estado conmigo en los malos y buenos tiempos, al final hemos conseguido todo lo que nos proponiamos.

Nicola gracias por tu inmensa paciencia, gracias por no enfadarte conmigo por estar trabajando todo el tiempo, gracias por el desayuno de las mañanas y porque tienes la facultad de convertir todas las cosas malas en buenas.